University of Massachusetts Amherst

ScholarWorks@UMass Amherst

Doctoral Dissertations | Dissertations and Theses

November 2017

Guiding the Self-Assembly of Block Copolymers in 2D and 3D with Minimal Patterning

Jaewon Choi

Follow this and additional works at: https://scholarworks.umass.edu/dissertations_2

Part of the Nanoscience and Nanotechnology Commons, and the Polymer and Organic Materials Commons

Recommended Citation

Choi, Jaewon, "Guiding the Self-Assembly of Block Copolymers in 2D and 3D with Minimal Patterning" (2017). *Doctoral Dissertations*. 1026.
https://scholarworks.umass.edu/dissertations_2/1026

This Open Access Dissertation is brought to you for free and open access by the Dissertations and Theses at ScholarWorks@UMass Amherst. It has been accepted for inclusion in Doctoral Dissertations by an authorized administrator of ScholarWorks@UMass Amherst. For more information, please contact scholarworks@library.umass.edu.

GUIDING THE SELF-ASSEMBLY OF BLOCK COPOLYMERS IN 2D AND 3D WITH MINIMAL PATTERNING

A Dissertation Presented

by

JAEWON CHOI

Submitted to the Graduate School of the
University of Massachusetts Amherst in partial fulfillment
of the requirements for the degree of

DOCTOR OF PHILOSOPHY

September 2017

Polymer Science and Engineering

© Copyright by Jaewon Choi 2017

All Rights Reserved

GUIDING THE SELF-ASSEMBLY OF BLOCK COPOLYMERS IN 2D AND 3D WITH MINIMAL PATTERNING

A Dissertation Presented

by

JAEWON CHOI

Approved as to style and content by:

____

Thomas P. Russell, Chair

____

Kenneth R. Carter, Chair

____

Mark Tuominen, Member

____

E. Bryan Coughlin, Department Head
Polymer Science and Engineering

DEDICATION

To my loving family

ACKNOWLEDGMENTS

This doctoral dissertation could not be achieved without the advice and support of many people, including my advisors, colleagues, friends, and family. Without them, I am certain that this PhD journey would have been quite a lonely process and much harder. I am truly grateful for being at the receiving end of so much strength and encouragement.

First of all, I am deeply indebted to my thesis advisors, Professor Thomas P. Russell and Professor Kenneth R. Carter, for being my mentor and guiding me through my PhD career. During the PhD journey, occasionally, I faced up to an unexpected difficulty or lost my way. However, whenever I met these difficult times, they turned the flashlight on and showed me the map and compass to guide the road to getting a PhD. I have greatly benefited from their scientific insight, technical resources, and expertise in the field of polymer science and engineering. I could learn how to approach research problems in different perspectives. At the same time, I could learn how to engage, develop, and work with the collaborators. I am particularly grateful for their warm encouragement, support, patience, and guidance because I believe that these allowed me to grow up to become more mature as an independent researcher. To Tom, I have always been inspired by your endless passion for research, and truly appreciate that you gave me the opportunity to apply for Samsung Scholarship and the motivation and confidence beyond the research advisor. To Ken, I have always been inspired by your enthusiasm for research, and sincerely appreciate for your invaluable comments and feedback on my research. I will never forget our SCRUM Meeting that helped me to develop the ability to quickly summarize thoughts in my head and present before time runs out. I would also like to thank my thesis committee

member, Professor Mark Tuominen for providing invaluable comments and helpful suggestions on my research, guiding me in the right direction.

I would also like to express my sincere gratitude to Professor Sang Eun Shim, who was my research advisor in the graduate school at Inha University. He introduced me to Polymer Research World, always encouraged me, and generously gave me freedom and independence in my research by letting me approach and resolve the scientific problems in my own way, but he was always available when I asked for advice. Without him, I would have a much harder time adapting the research at UMass Amherst. Also, I would like to thank Professor Du Yeol Ryu (Yonsei University), who provided me invaluable comments on my research, and advised me on his sabbatical year at UMass Amherst.

I would like to thank all of the Russell group members both past and present, Dr. Sung Woo Hong, Dr. Jung-Keun Kim, Dr. Ilja Gunkel, Dr. Huarong Nie, Dr. Ryu Takeko, Dr. Sermet Koyuncu, Dr. Ji Xu, Dr. Yao Liu, Professor Zhenbin Chen, Dr. Joseph Paulsen, Dr. Deepak Kumar, Dr. Joe Forth, Dr. Yu Chai, Wei Zhao, Kamil Bugra Toga, Daniel Miranda, Kathleen McEnnis, Sirinya Chantarak (Packy), Sunzida Ferdous, Xiaodan Gu, Yu Gu, Weiyin Gu, Feng Liu, Xiaobo Shen, Kyle Bryson, Paul Kim, Mengmeng Cui, Hsin-Wei Wang, Tao Feng, Zhiwei Sun, Gajin Jeong, Hongrui Guo, Caili Huang, Jooyoung Chang, Hyeyoung Kim, Duk Man Yu, Yige Gao, Yao Wu, Satyam Srivastava, Anju Toor, Yufeng Jiang, Jae Woong Jung, Jea Woong Jo, Hyungju Ahn, Yong Hoon Lee, and Carl Gunther Schirmeister, for their friendship and assistance. In addition, I would like to thank our previous group secretaries, Sandi Harris Graves and Laurie Banas for assisting in many things.

I would like to thank all of the Carter group members both past and present, Dr. Jin Young Park, Dr. Jacob John, Dr. Shuxi Dai, Dr. Fatma Koyuncu, Dr. Charlotte Mallet, Dr. Sachin Bhaladhare, Nicholas Hendricks, Samuel Pendergraph, Andrew Davis, Mikhail Kuchuk, Yinyong Li, Soeun Kim, Jared Harris, Kara Martin, Yilliang Zhou, Laura Parker, Allen Chang, Carmen Fischer, Kim Garth, Olga Linker, Daniel Ohm, and Eleni Tzeiranidou, for their friendship and assistance. Also, I would like to thank our group secretary, Trouble Mandeson, for assisting in many things.

I would like to express my thanks to all of the outstanding faculty at the PSE, who have taught me in the classes. Also, I am grateful for all of the help I received from the great staff members at the PSE. In particular, I would like to thank Lisa Groth, Maria Farrington, Jessica Skrocki, Lisa McNamara, Cheryl Kehoe, and Alyssa Kristek for assisting with all of the work related to my graduation. In addition, I would like to express my gratitude to technical staff members, John Nicholson, Dr. Sekar Thirunavukkarasu, Dr. Alex Ribbe, Lou Raboin, and Jack Hirsch for their helpful discussions and assistance in my research.

I would also like to acknowledge my collaborators both inside and outside the PSE, Dr. Sung Woo Hong, Dr. Jacob John, Xiaodan Gu, Yinyong Li, Paul Kim, Zhiwei Sun, Hyeyong Kim, Duk Man Yu, Shuang Pi (ECE, UMass Amherst), Professor Costas Grigoropoulos (UC Berkeley), Dr. Sangmo Koo (UC Berkeley), Dr. Junyeob Yeo (UC Berkeley), Zhengliang Su (UC Berkeley), Dr. Ilja Gunkel (ALS, LBNL), Dr. Feng Liu (ALS, LBNL), and Dr. June Huh (Korea University). None of the work would have been possible without them.

I would like to thank my fellow classmates of PSE 2011, Zhiwei, Nakul, Mike, Joel, Minchao, Connor, Sveta, Madhura, Piril, Patrick, Daniel E. Acevedo, Daniel Leibig, Alex, Hongrui, Gajin, Alper, Jana, and Greta for their help and friendship during the PhD journey. I wish you the best of luck in your future research endeavors.

I would also like to thank friends in Amherst, Hyun Suk Kim, Dr. Dong Yun Lee, Cheol Hee Lee, Dr. Soonyong So, Dr. Kyuyoung Heo, Dr. Junhee Na, Kwanyeol Paek, Jung-Won Keum, Hyunki Kim, Yongjin Kim, Byoung-Jin Jeon, Dr. Hyunbok Lee, Dr. Seog-Jin Jeon, Hyunkyu Sang, Seokhyoung Kim, Dr. Young-Kwan Kim, Dr. Woo Jin Choi, Dr. Hyeonjun Kim, Minjung Lee, Dr. Jaejoon Kim, Shuang Pi, Hao Jiang, and Peng Lin.

The work for this dissertation could never have been completed without the research fund. This work was supported by the National Science Foundation (NSF) supported Center for Hierarchical Manufacturing (CMMI-1025020) at the University of Massachusetts, Amherst. GISAXS experiments were performed at the Beamline 7.3.3 of the Advanced Light Source supported by the Director of the Office of Science, Office of Basic Energy Sciences, of the U.S. Department of Energy under Contract No. DE-AC02-05CH11231.

I would like to acknowledge Samsung Scholarship from the Samsung Foundation for financial support during my PhD course. Especially, I am grateful all of the help I received from the people, who are involved with Samsung Scholarship.

I would like to express my sincere gratitude, respect, and love to my parents, grandparents, sister, and family-in-law. Finally, and most importantly, I would like to give

my sincere heart and gratitude to my lovely wife, Jinhye, for her encouragement, understanding, and unconditional love.

ABSTRACT

GUIDING THE SELF-ASSEMBLY OF BLOCK COPOLYMERS IN 2D AND 3D WITH MINIMAL PATTERNING

SEPTEMBER 2017

JAEWON CHOI, B.S., INHA UNIVERSITY

M.S., INHA UNIVERSITY

M.S, UNIVERSITY OF MASSACHUSETTS AMHERST

Ph.D., UNIVERSITY OF MASSACHUSETTS AMHERST

Directed by: Professor Thomas P. Russell and Professor Kenneth R. Carter

Directed self-assembly (DSA) of block copolymers (BCPs) based on topographic patterns is one of the most promising strategies for overcoming resolution limitations in the current lithographic process and fabricating the next generation data storage devices. While the DSA of BCPs with deep topographic patterning has been extensively studied both experimentally and theoretically over the past two decades, less attention has been paid to the development of the DSA process using minimal topographic patterning. This dissertation focuses on understanding the effect of minimal topographic patterning on guiding the self-assembly of BCPs in 2D and 3D. We demonstrate that minimal trench patterns can be used to achieve highly ordered hexagonal arrays or unidirectionally aligned line patterns over large areas. By preparing BCP thin films on a series of minimal single trench with different dimensions, we study the minimum amount of topographic patterning necessary to successfully guide the self-assembly of BCPs. This approach provides insight into the minimum pitch of the trench necessary to fully order BCP microdomains. We develop a simple and robust method for the generation of macroscopically ordered

hexagonal arrays from the DSA of BCPs based on minimal trench patterns with solvent vapor annealing. The use of minimal trench patterns allows us to elucidate the morphological characteristics and lateral ordering of hexagonal array using grazing incidence small angle X-ray scattering (GISAXS). Moreover, using minimal trench patterns, we describe the generation of BCP line patterns oriented orthogonal to the trench direction over arbitrarily macroscopic distances. Beyond 2D BCP nanostructures, we explore the fabrication of 3D BCP architectures over large areas using simple woodpile structures as 3D guiding templates. We can also produce 3D networks of metallic nanostructures within the woodpile structures using a metal salt infiltration technique. In the last part, we conclude this dissertation and propose an outlook.

TABLE OF CONTENTS

Page

ACKNOWLEDGMENTS v

ABSTRACT..x

LIST OF TABLES xvi

LIST OF FIGURES xvii

CHAPTER

1. INTRODUCTION 1
    1.1 Overview...1
    1.2 Introduction to Block Copolymers..2
    1.3 Control of Interfacial Interactions..4
    1.4 Graphoepitaxy...7
        1.4.1 Fabrication of Topographic Patterns..8
        1.4.2 Topographic Patterns with Deep Patterning 10
            1.4.2.1 Deep Trench Patterns..11
            1.4.2.2 Deep Post Patterns 19
            1.4.2.3 Other Patterns...21
        1.4.3 Topographic Patterns with Minimal Patterning............................22
            1.4.3.1 Faceted Substrates..23
            1.4.3.2 Minimal Trench Patterns...26
    1.5 References...27

2. DIRECTED SELF-ASSEMBLY OF BLOCK COPOLYMER THIN FILMS
    USING MINIMAL TOPOGRAPHIC PATTERNS 38
    2.1 Introduction..38
    2.2 Experimental Methods...40

2.2.1 Fabrication of Minimal Single Trench Patterns 40
2.2.2 Fabrication of Minimally Patterned Trench Surfaces 41
2.2.3 DSA of BCP Thin Films Under Thermal Annealing 42
2.2.4 DSA of BCP Thin Films Under Solvent Vapor Annealing 42
2.2.5 Characterization 43
2.3 Results and Discussion 44
2.3.1 DSA of BCP Thin films on Minimal Single Trench Patterns 44
2.3.2 DSA of BCP Thin films on Minimally Patterned Trench Surfaces 59
2.4 Conclusions 73
2.5 References 74

3. GISAXS STUDY OF MACROSCOPICALLY ORDERED HEXAGONAL ARRAYS PRODUCED BY DIRECTED SELF-ASSEMBLY OF BLOCK COPOLYMERS WITH MINIMAL TOPOGRAPHIC PATTERNS 80
3.1 Introduction 80
3.2 Experimental Methods 83
3.2.1 Materials 83
3.2.2 Fabrication of Minimal Trench Patterns 84
3.2.3 DSA of BCP Thin Films 84
3.2.4 Characterization 85
3.3 Results and Discussion 86
3.3.1 DSA of BCP Thin Films on Unpatterned Flat Substrates and Minimal Trench Patterns 86
3.3.2 GISAXS Study of Hexagonal Arrays on Minimal Trench Patterns 96
3.3.3 GISAXS Study of Hexagonal Arrays on Unpatterned Flat Substrates 104
3.4 Conclusions 106
3.5 References 107

4. ORTHGONALLY ALIGNED BLOCK COPOLYMER LINE PATTERNS ON MINIMAL TOPOGRAPHIC PATTERNS 112
4.1 Introduction..112
4.2 Experimental Methods 116
4.2.1 Materials 116
4.2.2 Fabrication of Minimal Trench Patterns 116
4.2.3 DSA of PS-*b*-PEO Thin Films..117
4.2.4 DSA of PS-*b*-PDMS Thin Films...118
4.2.5 Characterization 118
4.3 Results and Discussion 120
4.3.1 Orthogonal Alignment of PS-*b*-PEO Line Patterns 120
4.3.2 Orthogonal Alignment of PS-*b*-PDMS Line Patterns.....................133
4.4 Conclusions...137
4.5 References...137

5. 3D NANOSTRUCTURES DERIVED FROM THE DIRECTED SELF-ASSEMBLY OF BLOCK COPOLYMERS WITHIN WOODPILES 142
5.1 Introduction...142
5.2 Experimental Methods 143
5.2.1 Materials 143
5.2.2 Fabrication of Woodpile Structures 143
5.2.3 DSA of PS-*b*-PMMA with Woodpile Structures............................145
5.2.4 DSA of PS-*b*-P2VP with Woodpile Structures...............................146
5.2.5 Deposition of Metal Salts in BCPs within Woodpiles....................146
5.3 Results and Discussion 147
5.3.1 3D Woodpile Structures for Guiding the Self-Assembly of BCPs 147
5.3.2 Incorporation of BCPs in Woodpile Structures 148
5.3.3 PS-*b*-PMMA Morphologies on Top Layers of Woodpile Structures 149
5.3.4 PS-*b*-PMMA Morphologies Inside of Woodpile Structures...........152

5.3.5 3D PS-*b*-P2VP Morphologies in Woodpile Structures....154
5.3.6 3D Metallic Nanostructures in Woodpile Structures....157
5.4 Conclusions....159
5.5 References....159
6. CONCLUSIONS AND OUTLOOK....162
BIBLIOGRAPHY....165

LIST OF TABLES

Table Page

2.1 Orientation of cylindrical microdomains in the single trench region for 16 different trench dimensions....49

2.2 Characteristics of minimal single trench patterns, with gradual increases in *W* and *D*, with $D < L_0$ in all cases. We note that the *W* was measured near the top of the trench. To analyze line edge roughness (LER) using SFM images, SuMMIT software was used. 51

2.3 Characteristics of minimally patterned trench surfaces used to direct the self-assembly of PS-*b*-PEO thin films. We note that *W* was measured near the top of the trench. To analyze LER using SFM images, SuMMIT software was used. 58

3.1 Summary of the results of the pattern dimension reduction after thermal annealing. 94

3.2 Measured principal domain spacing of lattice planes of the hexagonal arrays on the minimal trench pattern at a different Ψ, as determined from the GISAXS patterns. 104

4.1 Solubility parameters of the polymers and solvents and vapor pressures of the solvents used in the PS-*b*-PDMS experiments....134

LIST OF FIGURES

Figure Page

1.1 Calculated phase diagram of an AB diblock copolymer. Schematic illustration at the bottom is representative of equilibrium morphologies of body-centered cubic (BCC), hexagonally-packed cylinder (HEX), gyroid phase (GYR), and lamellar phase (LAM). Reprinted from Hoheisel *et al.*, Block Copolymer-Nanoparticle Hybrid Self-Assembly, *40*, *Prog. Polym. Sci*, 3-32, Copyright (2015), with permission from Elsevier (Ref. 7). 3

1.2 (a) Interfacial energies γSf and γMf and (b) $\Delta\gamma f = \gamma Mf - \gamma Sf$ for PS (circles) and PMMA (triangles) on a PS-*r*-PMMA brush as a function of f. From Mansky *et al.*, *Science* **1997**, *275*, 1458-1460. Reprinted with permission from AAAS (Ref. 14). 5

1.3 Two types of trench patterns. (a) Deep trench pattern. (b) Minimal Trench Pattern. 11

1.4 PS-*b*-PFS in parallel-sided grooves. (a) Plan-view electron micrograph of ordered arrays of PFS domains with *N* = 2 to 12 rows. (b) The number of rows in the groove, *N*, plotted against confinement width, *W*, showing the widths at which arrays with *N* rows are stable. The confinement width is expressed in terms of *d*, the equilibrium row spacing, which is 24.8 nm in this polymer. (c) Energy against confinement width of BCP system. The free energy of the confined BCP (F_c) is presented relative to the free energy of the bulk BCP (F_0). Reprinted by permission from Macmillan Publishers Ltd: *Nature Materials*, Cheng *et al.* (2004), copyright 2004 (Ref. 72). 13

1.5 Schematic illustration of the strategy used for generating BCP cylindrical microdomains on highly oriented crystalline facets on a single-crystal surface. From Park *et al.*, *Science* **2009**, *323*, 1030-1033. Reprinted with permission from AAAS (Ref. 136). 25

2.1 SAXS profile of PS-*b*-PEO. The scattering from PS-*b*-PEO showed a first-order reflection at $q^* = 0.2346$ nm^{-1}, corresponding to the domain spacing ($L_0 = 2\pi/q^*$) of 26.8 nm. It is noted that the SAXS intensity showed the absence of higher-order peaks. 45

2.2 Schematic illustration of the DSA of BCP thin films on minimal single trench patterns. (a) Minimal single trench patterns were fabricated on the silicon substrate with a native oxide layer. The blue dashed square indicates the defined *W* and *D* of the trench. (b) PS-*b*-PEO thin films were prepared by spin-coating and then, thermally annealed at 150 °C under vacuum for 1 day. (c) Thermally annealed PS-*b*-PEO thin films showed two distinct regions of cylindrical microdomains across the single trench patterns. (d) Schematic cross-sectional illustration of the two distinct regions from the red square in (c)...............................46

2.3 Directed BCP thin films on minimal single trench patterns. (a–c) First row shows representative SFM phase images of thermally annealed PS-b-PEO thin films on minimal single trench patterns with different *W* and *D*. Each inset shows a magnified image of cylindrical microdomains in the single trench (blue region), exhibiting perpendicular (a), a mixture of perpendicular and parallel (b), and parallel (c) orientation. The second row presents respective SFM height images of the first row. Scale bars, 200 nm. The third row corresponds to respective height profiles of the second row..48

2.4 Demonstration of minimal single trench patterns. (a) A total of 16 single trench patterns were fabricated on the same silicon substrate having a native oxide layer and designated as No. 1 to 16. The length of each pattern was 100 μm. The separation distance between the patterns was 300 μm. (b) SFM height images and height profiles of the single trench patterns. W and D of each pattern were measured by SFM and listed in Table 2.2. Scale bars, 300 nm. 50

2.5 SFM phase images of thermally annealed PS-*b*-PEO thin films on minimal single trench patterns with different *W* and *D*. Samples of No. 2, 8, and 16 are shown in Figure 2.3a–c (phase images), respectively. In the single trench region, cylindrical microdomains showed perpendicular (No. 1), a mixture of perpendicular and parallel (No. 3 to 7), or parallel (No. 9 to 15) orientation. Scale bars, 300 nm. 52

2.6 (a–m) SFM height images of thermally annealed PS-*b*-PEO thin films on minimal single trench patterns with different *W* and *D*. Samples of No. 2, 8, and 16 are shown in Figure 2.3a–c (height images), respectively. Scale bars, 300 nm. (n) Data scale of SFM height images in (a–m)..53

2.7 Measurement of the propagation distance of cylindrical microdomains oriented normal to the film surface away from the edges of a single trench pattern. (a) Original SFM phase image. (b) Colorized SFM phase image. Blue and green indicate the single trench region and propagation region, respectively. The boundary, where the perpendicular orientation of cylindrical microdomains changes to the parallel orientation after a given distance from the edge of a single trench, is defined as the end of the propagation region. The standard deviation of the measured propagation distance was large, as shown in Figure 2.8a, in particular No. 3 to 16, due to the variation in the propagation distance along the single trench pattern. 54

2.8 Directed BCP thin films on minimal single trench patterns. (a) Propagation surface distance of hexagonal arrays of cylindrical microdomains oriented normal to the film surface away from the edges of a single trench. (b) Measured variation in height between the middle of the single trench region and flat surface. The *x*-axis in (a) and (b) shows the designated single trench patterns from Nos. 1 to 16. 55

2.9 SFM height images and height profiles of minimally patterned trench surfaces. *P*, *W* and *D* of each pattern were measured by SFM and listed in Table 2.3. Scale bars, 300 nm. 57

2.10 Cross-sectional (45° tilted) SEM images of minimally patterned trench surfaces with (a) $P = 5.75L_0$, $W = 1.26L_0$, $D = 0.30L_0$ and (b) $P = 18.84L_0$, $W = 2.16L_0$, $D = 0.30L_0$. Scale bars, 100 nm. 58

2.11 Directed BCP thin films on minimally patterned trench surfaces. (a–c) First row shows SFM phase images of thermally annealed PS-*b*-PEO thin films on minimally patterned trench surfaces with different dimensions. The arrows of each image indicate the underlying trenches, where a single row of PEO cylinders oriented normal to the film surface exists. The inset of each image shows the corresponding 2-D FFT. The second row presents respective SFM height images of the first row. Scale bars, 200 nm. 59

2.12 RMS roughness of PS-*b*-PEO thin films on the minimally patterned trench surfaces (height images in Figure 2.11a−c, respectively) was measured by SFM. Each measured area was 3 µm by 3 µm. 60

2.13 Schematic illustration of the proposed mechanism for the generation of laterally ordered hexagonal arrays by using the minimally patterned trench surface. 62

2.14 (a–c) Orientational correlation function, G_6(r), was calculated from thermally annealed PS-*b*-PEO thin films (phase images in Figure 2.11a–c), where *r* is the distance and *a* is the average domain spacing. 62

2.15 Translational correlation function, G_T(r), was calculated from the thermally annealed PS-*b*-PEO thin film (phase image in Figure 2.11a). A real 2D crystal will have quasi-long-range translational order that can be described by $G_T(r) \propto \left(\frac{r}{a}\right)^{-\eta_T}$, where *r* is the distance, *a* is the average domain spacing, and η_T is the fitting parameter. In the case of the ordered crystal phase, the value of η_T will be in the range of 0.25 to 0.33. For the hexagonal arrays on the patterned surface with $P = 5.75L_0$, $W = 1.26L_0$, $D = 0.30L_0$, G_T(r) could be described by a power law with η_T of 0.31, indicating the presence of quasi-long-range translational order over the average domain spacing of 30. 63

2.16 Transition in the orientation of cylindrical microdomains between the minimally patterned trench surface and unpatterned surface. (a) Schematic illustration of four different edges (left, right, top, and bottom) on the patterned surface. (b–d) SFM phase images of thermally annealed PS-*b*-PEO thin films at different areas. (b) Cylindrical microdomains far away from the patterned surface. (c) Cylindrical microdomains at four different edges on the patterned surface with P = 18.84L_0, W = 2.16L_0, and D = 0.30L_0. (d) Cylindrical microdomains at the right edge and middle area on the patterned surface with P = 25.11L_0, W = 1.81L_0, and D = 0.23L_0. Scale bars, 300 nm......................................65

2.17 Swelling behavior, where the swollen thickness (t) is divided by the initial film thickness (t_0), of the PS-*b*-PEO thin film on the flat silicon substrate exposed to THF and water vapors after pre-swelling in water vapor for 10 min…. 66

2.18 Time evolution of SFM phase images of PS-*b*-PEO thin films exposed to THF and water vapors on the minimally patterned trench surface with P = 5.75L_0, W = 1.26L_0, and D = 0.30L_0. SFM images of 40, 60, and 70 min annealed samples were overlaid with the colorized grain maps. The arrow in each image indicates the underlying trench direction. The color wheel in the 70 min sample shows the orientation of line patterns of cylindrical microdomains. Scale bars, 200 nm… 67

2.19 Demonstration of the image processing to colorize the orientation of line patterns of cylindrical microdomains oriented parallel to the film surface on the minimally patterned trench surface. (a) Original SFM phase image. (b) SFM image was converted to 8-bit gray scale image. (c) High-Pass filtering was applied to 8-bit gray scale image. (d) Filtered image was processed using MATLAB. (e) Low-Pass filtering was used for blurring the image. (f) Original SFM image was overlaid with the blurred image. 69

2.20 SFM phase image of the solvent-vapor annealed PS-*b*-PEO thin film on the minimally patterned trench surface with P = 5.75L_0, W = 1.26L_0, D = 0.30L_0. The film thickness prior to SVA was ~46 nm (1.72L_0). Scale bar, 300 nm. 70

2.21 (a–c) SFM phase images of solvent-vapor annealed PS-*b*-PEO thin films on minimally patterned trench surfaces with different dimensions. Scale bars, 200 nm. (d) Average defect density of line patterns of cylindrical microdomains on the patterned surfaces...72

3.1 SAXS profile of a PS-*b*-PEO. The first-order reflection was observed at q^* = 0.1757 nm^{-1} corresponding to the natural period ($L_0 = 2\pi/q^*$) of 35.8 nm. It is noted that the higher-order peaks of the first-order reflection were not observed… 87

3.2 Swelling behavior of PS-*b*-PEO thin films on a flat silicon substrate, where the swollen film thickness (t) is divided by the initial film thickness (t_0). The films were initially pre-swollen in water vapor for 10 min to avoid dewetting, followed by exposing to THF and water vapors for 60 min 88

3.3 (a) SFM phase image of a solvent-vapor-annealed PS-*b*-PEO thin film on a flat silicon substrate. The inset shows the corresponding 2-D FFT. (b) Schematic diagram of the DSA process. (c) SFM phase image of a solvent-vapor-annealed PS-*b*-PEO thin film on a minimal trench pattern. The inset shows the corresponding 2-D FFT. (d) Schematic illustration of GISAXS experiments. Ψ is the rotation angle of the sample stage. a_i is the incident angle of the X-ray beam. (e) Schematic representation of 2-D hexagonal lattice planes with a different Ψ on the minimal trench pattern. Two basis vectors, a_1 and a_2, are indicated by the magenta arrows..91

3.4 To fabricate a minimal trench pattern, we used size reduction lithography, which is based on nanoimprint lithography (NIL) and thermal annealing. (a) In the first step, a silsesquioxane (SSQ)-based film was prepared by spin-coating onto a flat silicon substrate. (b) Next, a h-PDMS mold consisting of grating lines with the pitch of 132 nm, the line width of 70 nm, and the height of 50 nm was used to nanoimprint the SSQ-based film. Then, the nanoimprinted trench pattern with the pitch of 132 nm, the mesa width of 64 nm, and the trench depth of 50 nm was annealed at 500 °C in air for 2 h to reduce the pattern dimensions, in particular the trench depth. It is noted that this thermal annealing process changes the surface property from hydrophobic (nanoimprinted trench pattern) to hydrophilic (minimal trench pattern) due to the formation of silicon oxide structure. (c) As a result, we obtained the minimal trench pattern with the pitch of 132 nm, the mesa width of 26 nm, the trench width of 106 nm, and the trench depth of 11 nm. Table 3.1 summarizes the results of the pattern dimension reduction. The reduction in pattern dimensions after thermal annealing is related to the elimination of organic molecules in the SSQ-based film and densification of the SSQ material. The reduction in the trench depth (78.0%) was larger than the mesa width reduction (59.4%), which can be attributed to the lateral confinement of the mesas to the substrate. 92

3.5 Cross-sectional (80° tilted) SEM images of patterned trench surfaces. (a) Nanoimprinted trench pattern with the pitch of 132 nm, the mesa width of 64 nm, the trench width of 68 nm, and the trench depth of 50 nm. The inset shows the water contact angle of 113°. Since the nanoimprinted trench pattern is mainly composed of the SSQ material, the surface is hydrophobic. (b) Minimal trench pattern with the pitch of 132 nm, the mesa width of 26 nm, the trench width of 106 nm, and the trench depth of 11 nm. The inset shows the water contact angle of 8°, indicating a hydrophilic surface. Through thermal annealing, the surface property was changed from hydrophilic (113°) to hydrophilic (8°). Since the SSQ-based material (nanoimprinted trench pattern) was converted to silicon oxide structures (minimal trench pattern) by eliminating organic molecules, the surface of the minimal trench pattern became hydrophilic. (c) The magnified image of the minimal trench pattern shows that the surface at the base of the trench is rough, but this roughness could not be measured by SFM due to artifacts arising from the shape of the tip. Since the mesa width of the nanoimprinted trench pattern cannot be readily reduced due to the lateral confinement during thermal annealing, any internal stresses in this pattern are relieved by roughening the bottom surface of the trench. 93

3.6 SFM height images and height profiles of patterned trench surfaces. (a) Nanoimprinted trench pattern. (b) Minimal trench pattern. 95

3.7 (a–f) 2-D GISAXS patterns of a PS-*b*-PEO thin film on a minimal trench pattern taken at a fixed $\Psi = 0°$ while varying α_i: (a) $\alpha_i = 0.18°$, (b) $\alpha_i = 0.10°$, (c) $\alpha_i = 0.08°$, (d) $\alpha_i = 0.06°$, (e) $\alpha_i = 0.04°$, and (f) $\alpha_i = 0.02°$. The white arrows in (b) indicate the first-order reflections arising from the hexagonal arrays of cylindrical microdomains in the PS-*b*-PEO film on the minimal trench pattern. (g) In-plane scattering profiles corresponding to a horizontal cut of (a–f) at $q_z = 0.305$ nm^{-1} ($\alpha_i = 0.18°$), 0.236 nm^{-1} ($\alpha_i = 0.10°$), 0.212 nm^{-1} ($\alpha_i = 0.08°$), 0.196 nm^{-1} ($\alpha_i = 0.06°$), 0.189 nm^{-1} ($\alpha_i = 0.04°$), and 0.183 nm^{-1} ($\alpha_i = 0.02°$), respectively. The dashed line indicates the first-order peak corresponding to the (10) reflection of the hexagonal arrays of PS-*b*-PEO microdomains. 97

3.8 (a–f) 2-D GISAXS patterns of a PS-*b*-PEO thin film on a minimal trench pattern at $\Psi = 60°$. To compare the internal structure and surface morphology, α_i was varied: (a) $\alpha_i = 0.20°$, (b) $\alpha_i = 0.18°$, (c) $\alpha_i = 0.16°$, (d) $\alpha_i = 0.14°$, (e) $\alpha_i = 0.12°$, and (f) $\alpha_i = 0.10°$. (g) In-plane scattering profiles corresponding to a horizontal cut of (a–f) at $q_z = 0.316$ nm^{-1} ($\alpha_i = 0.20°$), 0.303 nm^{-1} ($\alpha_i = 0.18°$), 0.287 nm^{-1} ($\alpha_i = 0.16°$), 0.261 nm^{-1} ($\alpha_i = 0.14°$), 0.247 nm^{-1} ($\alpha_i = 0.12°$), and 0.223 nm^{-1} ($\alpha_i = 0.10°$), respectively. The arrows indicate a scattering shoulder at the (01) reflection. 99

3.9 (a,b) 2-D GISAXS patterns of a PS-*b*-PEO thin film on a minimal trench pattern at Ψ = 30° with α_i = 0.18° (a) and 0.12° (b). (c) In-plane scattering profiles corresponding to a horizontal cut of (a,b) at q_z = 0.294 nm^{-1} (α_i = 0.18°) and 0.243 nm^{-1} (α_i = 0.12°), respectively. (d,e) 2-D GISAXS patterns of a PS-*b*-PEO thin film on a minimal trench pattern at Ψ = 90° with α_i = 0.18° (d) and 0.12° (e). (f) In-plane scattering profiles corresponding to a horizontal cut of (d,e) at q_z = 0.307 nm^{-1} (α_i = 0.18°) and 0.252 nm^{-1} (α_i = 0.12°), respectively. The arrows indicate a scattering shoulder at the 12 reflection. 101

3.10 (a) Schematic illustration of hexagonal arrays of cylindrical microdomains guided by the minimal trench pattern. The X- and Y-axes indicate the confined and unconfined directions, respectively. (b) Schematic representation of the domain spacing of hexagonal planes with a different Ψ on XY directions defined in (a). XY directions are not related to the magnitude of the confinement effect. For a perfect hexagonal array, $d10,\Psi=0° = d01,\Psi=60°$ and $d11,\Psi=30° = d12,\Psi=90°$. 103

3.11 (a) 2-D GISAXS patterns of a PS-*b*-PEO thin film on a flat silicon substrate. The sample was first measured at an arbitrary sample rotation, which is defined as Ψ = 0°. From this point, the sample stage was rotated 30°, 60°, and 90°. At all Ψ, α_i was set at 0.18°. (b) In-plane scattering profiles corresponding to a horizontal cut of (a) at q_z = 0.293 nm^{-1}. The domain spacing of the (10) plane was calculated to be 42.9 nm from the (10) reflection. 105

4.1 Schematic illustration of the DSA process. (a) SSQ-based film spin-coated onto a silicon substrate having a native oxide layer. (b) With a *h*-PDMS mold, SSQ-based film was nanoimprinted using a NIL system. (c) To reduce trench dimensions, in particularly the trench depth, the nanoimprinted trench pattern was annealed at 500 °C in air, finally generating a minimal trench pattern (trench depth < L_0). (d) PS-*b*-PEO thin films were spin-coated onto the minimal trench patterns (e) After SVA with THF and water vapors, PS-*b*-PEO film showed line patterns of cylindrical microdomains oriented orthogonal to the underlying trench direction. 120

4.2 SAXS profile of a PS-b-PEO. The first-order reflection was observed at q^* = 0.2863 nm^{-1} corresponding to the natural period ($L_0 = 2\pi/q^*$) of 21.9 nm. It is noted that the higher-order peaks of the first-order reflection were not observed… 122

4.3 SFM phase images of solvent-vapor annealed PS-*b*-PEO thin films on minimal trench patterns under the same SVA conditions at different film thicknesses: (a) 22.6 nm (1.03L_0), (b) 24.7 nm (1.13L_0), (c) 26.9 nm (1.23L_0), (d) 31.8 nm (1.45L_0), (e) 35.0 nm (1.60L_0), (f) 37.3 nm (1.70L_0), and (g) 41.0 nm (1.87L_0). The arrow of each image indicates the underlying trench direction. All scale bars are 200 nm. 124

4.4 Fourier transformed SFM phase image of the solvent-vapor annealed PS-*b*-PEO thin film with the thickness of 22.6 nm (1.03L_0) on the minimal trench pattern. At this film thickness, there is no orientation of PS-*b*-PEO line patterns of cylindrical microdomains in terms of the direction of the trench pattern. Due to the loops with large radii of curvature, the line patterns of cylindrical microdomains seem to be partially oriented to the trench direction. 125

4.5 Orientation angle distribution from image analysis of PS-*b*-PEO line patterns on minimal trench patterns. (a) Schematic illustration of defined orientation angles of line patterns with respect to the underlying trench direction. (b–f) Orientation angle distribution at different film thicknesses: (b) 24.7 nm (1.13L_0), (c) 26.9 nm (1.23L_0), (d) 31.8 nm (1.45L_0), (e) 35.0 nm (1.60L_0), and (f) 37.3 nm (1.70L_0). The inset in (e) shows the probability between −30° and 30°. 128

4.6 GISAXS measurements of solvent-vapor annealed PS-*b*-PEO thin films on minimal trench patterns. (a) Schematic illustration of GISAXS experiments, where Ψ is the rotation angle of the sample stage. We define $\Psi = 0°$ when the direction of the X-ray beam is parallel to the underlying trench direction. (b–h) 2-D GISAXS patterns taken at different Ψ: (b) $\Psi = 90°$, (c) $\Psi = 0°$, (d) $\Psi = 2°$, (e) $\Psi = 4°$, (f) $\Psi = 6°$, (g) $\Psi = 8°$, and (h) $\Psi = 10°$. 130

4.7 In-plane scattering profiles corresponding to a horizontal cut of (Figure 4.6b–h) at $q_z = 0.320$ nm^{-1}. 132

4.8 Normalized scattering intensity of the first-order reflection from GISAXS patterns as a function of Ψ. Using this data, *f* was calculated to be 0.997, which is characteristic of exceptionally aligned BCP line patterns oriented orthogonal to the trench direction. 133

4.9 SFM phase images of PS-*b*-PDMS thin films on minimal trench patterns annealed using different solvent vapors: (a) acetone, (b) THF, and (c) toluene. The inset of each image shows the corresponding 2-D FFT. The white arrow of each image exhibits the underlying trench direction. The yellow arrow in (c) indicates the direction of PS-*b*-PDMS line patterns. All scale bars are 200 nm. 136

5.1 (a, b) Experimental set-up for 2PP. (c) Chemical structure of photo-curable (organic-inorganic hybrid) material. (Image courtesy of Sangmo Koo, University of California, Berkeley) 145

5.2 (a) Structure of unit block of woodpile structure, where a_z is the distance between four adjacent layers, *a* is the separation distance between parallel rods within each layer. Between every other layer, rods are shifted relative to each other by *a*/2. Face-centered-tetragonal unit cell structure with $a_z = 2a$ was used in this project. (b) SEM images of woodpile structure. (Image courtesy of Sangmo Koo, University of California, Berkeley) 147

5.3 SEM images of woodpile structures fabricated by different laser power while maintaining the scanning speed at 20 μm s^{-1}. (Image courtesy of Sangmo Koo, University of California, Berkeley) 148

5.4 Procedure for incorporation of BCPs in woodpile structures. Red arrow in (c–f) indicates the direction of solvent evaporation. 149

5.5 SEM images of PS-*b*-PMMA patterns on top layers of woodpile structures with pitch of 650 nm and height of 5 μm. The inset shows a high-magnification image of the concentric ring structures. 150

5.6 SEM images of PS-*b*-PMMA patterns on top layers of woodpile structures with the pitch of (a,b) 650 nm and (c,d) 1 μm. (a) Concentric ring patterns. (b) Ellipsoidal patterns. (c) Trapezoidal patterns. (d) Square patterns. All scale bars are 500 nm. 151

5.7 (a) SEM cross section images of PS-*b*-PMMA incorporated woodpile structures. Scale bar is 1 μm. (b) Magnified SEM image from the red dashed rectangle in (a). Scale bar is 300 nm. 153

5.8 SEM cross section image of PS-*b*-P2VP embedded woodpile structures. Scale bar is 1 μm. 154

5.9 SEM images of ethanol reconstructed PS-*b*-P2VP microdomains in woodpile structures. (a) After thermal annealing, PS-*b*-P2VP incorporated woodpile structure was cleaved, and then reconstructed by immersion in ethanol. (b) and (c) are show magnified SEM images from the black and red dashed rectangles in (a), respectively. All scale bars are 1 μm. 155

5.10 Direction of infiltration of PS-*b*-P2VP in woodpile structures. 156

5.11 (a) SEM cross section (80° tilted) of Pt nanostructures in woodpile structure with the pitch of 1 μm and the height of 10 μm. (b) High magnification of 3D Pt nanostructures inside of the woodpile structure from the red dashed rectangle in (a). (c) Pt line patterns on top layer of woodpile structure. Dark featureless regions correspond to non-etched remaining PS layer. All scale bars are 1 μm. 158

CHAPTER 1

INTRODUCTION

1.1 Overview

In the semiconductor industry, device performance and cost are strongly correlated to feature sizes,[1] where top-down lithographic approaches are commonly used to fabricate nanoscale feature sizes. However, further decreasing the feature sizes below the 22 nm half pitch by the lithographic processes is becoming extremely expensive and more challenging.[1] To overcome these limitations, the combination of a top-down approach with a bottom-up self-assembly has been investigated over the past decade.[2, 3]

Among many bottom-up self-assembly methods, the self-assembly of block copolymers (BCPs) has attracted significant research interest, since their microphase separation into periodic lamellar, spherical, cylindrical, or gyroid microdomains, with dimensions ranging from 5 to 100 nm, can be used for the fabrication of bit-patterned media (BPM) and lithographic masks. However, typically, BCP microdomains in thin films on an unpatterned substrate meet intrinsic obstacles, including undesirable domain orientation and short-range lateral order, which limit their capabilities in nanofabrication. To overcome these issues, deep topographic patterns have been widely used to guide the self-assembly of BCP thin films, but relatively little attention has been given to the use of minimal topographic patterns.

---

[*]This chapter has been adapted from J. Choi, K. R. Carter, and T. P. Russell, "5. Directed self-oriented self-assembly of block copolymers using topographical surfaces" in the book entitled "Directed Self-Assembly of Block Co-Polymers for Nano-Manufacturing", *A Volume in Woodhead Publishing Series in Electronic and Optical Materials: No. 83*, pp 99-127, Copyright (**2015**), with permission from Elsevier.

In this dissertation, we will address the question of how minimal topographic patterns have an effect on guiding the self-assembly of BCPs in 2D and 3D. In Chapter 1, we will first introduce the background of BCPs, control of interfacial interactions, and graphoepitaxy. In Chapter 2, we will focus on understanding the directed self-assembly (DSA) of a cylinder-forming BCP with minimal topographic patterning. In Chapter 3, we will study the macroscopically ordered hexagonal arrays of BCP microdomains in thin films guided by minimal topographic patterns using the grazing incidence small angle X-ray scattering (GISAXS) technique. In Chapter 4, we will investigate the orthogonally aligned BCP line patterns on minimal topographic patterns. In Chapter 5, we will demonstrate the fabrication of 3D BCP patterns with tailored functionality using 3D woodpile structures. Finally, in Chapter 6, we will conclude this dissertation and propose an outlook.

1.2 Introduction to Block Copolymers

Block copolymers (BCPs) are composed of two or more chemically distinct polymeric chains (blocks), which are covalently bound together at one or more points.[4] The most extensively investigated type of BCPs is the linear AB diblock copolymer, which consists of a long chain of A monomers covalently bonded to a long chain of B monomers.[5,6] In general, these blocks are thermodynamically incompatible, so that AB diblock copolymers can microphase-separate into well-defined nanostructures, such as lamellae, spheres, gyroids, or cylinders. In the bulk, the phase behavior of AB diblock copolymers is dictated by three parameters: the volume fraction of the blocks, f, the Flory-Huggins

interaction parameter, χ, and the degree of polymerization, N, as shown in Figure 1.1.[7] However, in the thin films, additional parameters, such as the interfacial interactions at substrate/BCP and BCP/air interfaces and the commensurability between the natural period of BCP (L_0) and the film thickness can, also, influence the morphology.

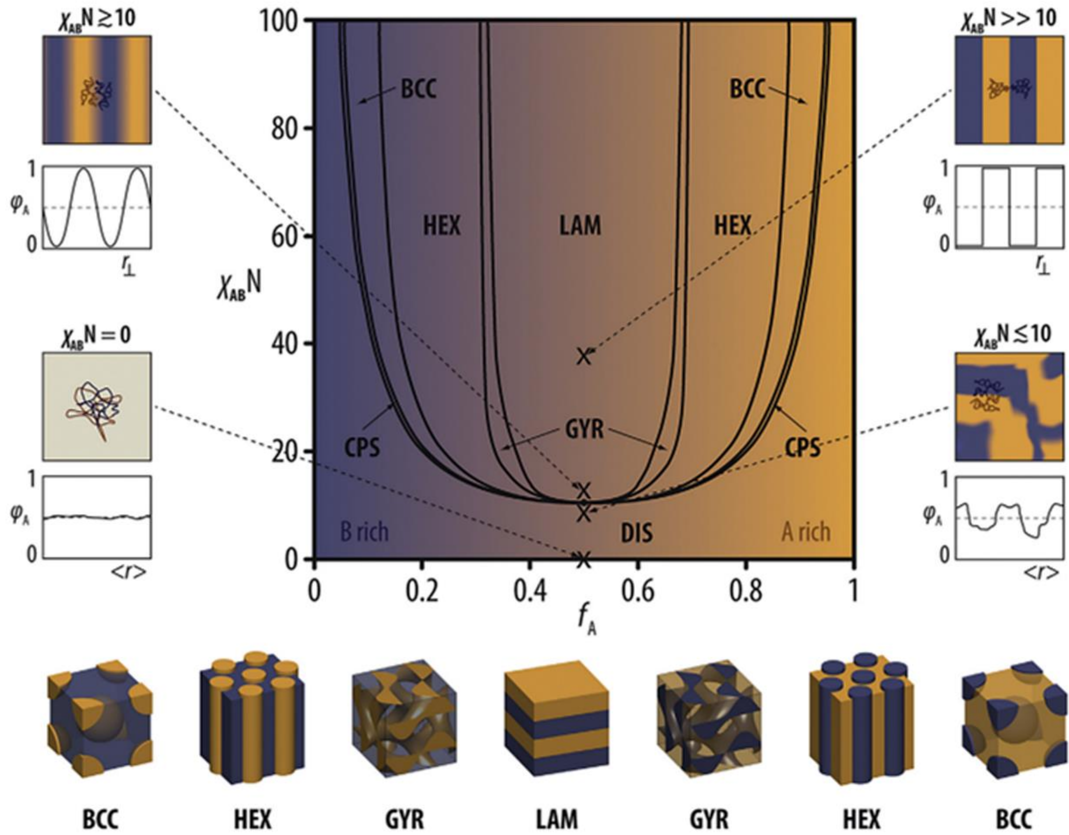

Figure 1.1 Calculated phase diagram of an AB diblock copolymer. Schematic illustration at the bottom is representative of equilibrium morphologies of body-centered cubic (BCC), hexagonally-packed cylinder (HEX), gyroid phase (GYR), and lamellar phase (LAM). Reprinted from Hoheisel *et al.*, Block Copolymer-Nanoparticle Hybrid Self-Assembly, *40*, *Prog. Polym. Sci*, 3-32, Copyright (2015), with permission from Elsevier (Ref. 7).

1.3 Control of Interfacial Interactions

Depending on the specific application, such as membranes, BPM or lithographic masks, different orientations (in-plane or out-of-plane) of BCP microdomains are required, so that controlling the orientation is crucial. In BCP thin films, interfacial interactions at the substrate/BCP and BCP/air interfaces and the commensurability between the film thickness and L_0 are important factors for dictating the orientation and morphology of BCPs.[8-20] Generally, strong preferential interactions of one component of BCPs with the substrate and/or a lower surface energy of one of blocks lead to an orientation of the BCP microdomains parallel to the substrate in the thin films because of the connectivity of the blocks. Russell and co-workers investigated this behavior using a symmetric poly(styrene-*b*-methyl methacrylate) (PS-*b*-PMMA) and characterized it using neutron reflectivity, secondary ion mass spectrometry (SIMS), and interference microscopy.[21-24] In these studies, after thermal annealing, lamellar microdomains of PS-*b*-PMMA diblock copolymer in thin films were oriented parallel to the substrate due to the strong affinity of PMMA block to the oxide layer on the silicon substrate and the lower surface energy of PS block. However, this parallel orientation of BCP microdomains can be overcome by controlling the interfacial energies precisely. If the substrate is neutral, that is, the interfacial interactions of both blocks are balanced, BCP microdomains can orient normal to the substrate. Under this condition, the incommensurability between the film thickness and L_0 also affects the orientation of BCP microdomains.

The most common strategy to control the interfacial interaction is modification of the substrate using random copolymer brushes.[10, 11, 14-16] Russell and co-workers were first to demonstrate the grafting of hydroxyl-terminated PS-*r*-PMMA random copolymers,

where the fraction, *f*, of styrene was varied from 0 to 1 on the oxide layer of the silicon substrate.[14] As shown in Figure 1.2, it was found that the interfacial energies of both PS and PMMA blocks of PS-*r*-PMMA random copolymer brushes were equal when $f \cong 0.57$, which means that the substrate has non-preferential interactions (neutral condition) with both the PS and PMMA blocks. Although, anchoring of PS-*r*-PMMA random copolymer brushes is a simple and effective method to control surface affinities, this approach has disadvantages, such as requiring specific surface chemistries, and the anchoring process is time consuming.

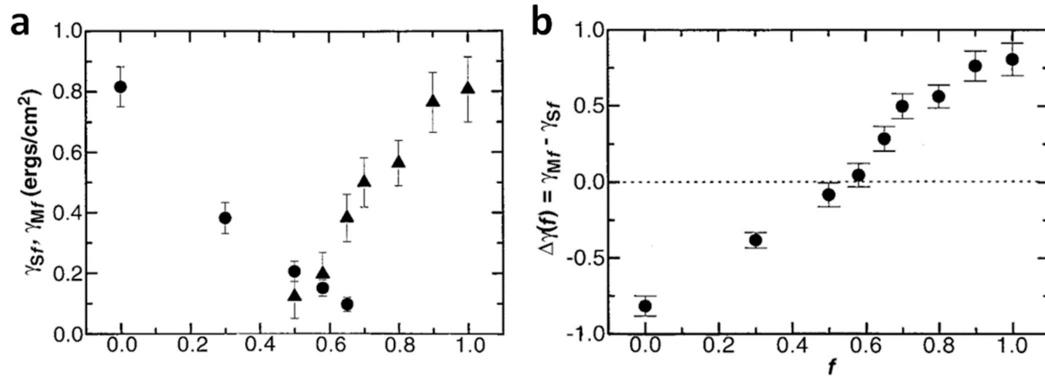

Figure 1.2 (a) Interfacial energies γ_{Sf} and γ_{Mf} and (b) $\Delta\gamma(f) = \gamma_{Mf} - \gamma_{Sf}$ for PS (circles) and PMMA (triangles) on a PS-*r*-PMMA brush as a function of f. From Mansky *et al.*, *Science* **1997**, *275*, 1458-1460. Reprinted with permission from AAAS (Ref. 14).

To circumvent these hurdles, several groups further developed a generalized approach to surface modification using crosslinking reaction.[19, 25-27] This approach was demonstrated using the thin films of benzocyclobutene (BCB) functionalized PS-*r*-PMMA (PS-*r*-PBCB-*r*-PMMA) random copolymers.[19] In this work, it was found that thermally

crosslinked PS-*r*-PBCB-*r*-PMMA ultrathin films can be produced on various solid surfaces, such as Al, Si_3N_4, Kapton, and PET substrates, with controlled surface energies in a simple, rapid, and robust manner. It is noted that interfacial interactions can also be mediated by solvents during solvent vapor annealing (SVA).[28-32]

The coupling of the interfacial interactions and the confinement of BCPs was investigated experimentally and theoretically by confining BCPs between two parallel substrates.[12, 33-39] When BCP films are confined between parallel flat substrates, the formation of the surface topography, such as holes and islands, is suppressed and, depending on the wetting conditions at the interfaces of the confining planes and the separation distance between the confining substrates relative to L_0, the BCPs can be forced into a condition of frustration. As an example, Turner theoretically studied a free energy model, which includes the elastic stretching energy of the polymer, the interactions at the AB interfaces, and the interactions between the polymer and the confining plates, for the confined lamellar microdomains with parallel orientation of the AB diblock copolymer in the strong segregation limit.[38] It was found that the number of layers between two parallel plates was changed from n to $n + 1/2$ as a function of the plate spacing. Walton *et al.* extended Turner's model by considering the case of lamellar microdomains with perpendicular orientation between two parallel walls.[39] In this work, they developed a free energy of the lamellar microdomains with perpendicular orientation to the walls and compared to the symmetric and the antisymmetric parallel lamellar microdomains as a function of the wall spacing. The perpendicular lamellar microdomains were favored over the parallel lamellar microdomains when $F_v < F_h$. However, it was found that the perpendicular lamellar microdomains were favored over in a limited range of the wall

spacing. Lambooy *et al.* used neutron reflectivity to investigate the self-assembly behavior of symmetric PS-*b*-PMMA diblock copolymers in two parallel solid substrates, where the PMMA block preferentially segregated to both substrates.[37] In this work, the lamellar microdomains showed parallel orientation to the solid substrate regardless of the confined film thickness. Also, the BCP chains were either compressed or expanded to accommodate the imposed frustration. In contrast, Kellogg *et al.* found that when the symmetric PS-*b*-PMMA diblock copolymer was confined between parallel substrates, which were modified by PS-*r*-PMMA random copolymer brushes, the lamellar microdomains with incommensurate conditions were oriented normal to the substrates to accommodate the frustrated condition.[34]

1.4 Graphoepitaxy

We have demonstrated so far strategies to control the orientation of BCP microdomains in thin films by tuning interfacial interactions. However, these oriented microdomains on unpatterned flat substrates show generally short-range lateral order, which limits their usefulness for applications in the nanofabrication. The use of graphoepitaxy, which uses artificial surface relief structures to guide the self-assembly of BCP thin films, can enhance the lateral order of BCP microdomains.[40-42] In general, the length scale of the confinement depth of topographic patterns for graphoepitaxy is greater than L_0, where an annealed BCP material will fill the regions confining the BCP. One advantage of using graphoepitaxy is density multiplication. For example, if electron beam lithography (EBL) generates sparse line or post guiding patterns based on L_0, the remaining

unpatterned areas will be filled with the BCP having a much smaller period, thereby reducing the effective pitch of the patterning, so that the writing time of EBL can be significantly reduced. Consequently, this graphoepitaxy approach, which is the combination of a top-down lithographic approach with a bottom-up self-assembly of BCPs, provides an opportunity for multilevel controlling of BCP patterns with the nanometer scale on diverse topographic patterns.

1.4.1 Fabrication of Topographic Patterns

Various methods can be used for the fabrication of topographic patterns that can guide the self-assembly of BCP thin films. Photolithography is the major technique, which includes serial and parallel processes.[43] In this technique, the feature size is generally limited by the wavelength of light and the numerical aperture of the lens. For example, by using 193 nm wavelength, photolithography can fabricate patterns with 37 nm feature sizes.[43] Many topographic patterns for guiding the self-assembly of BCPs were produced using photolithography technique.[41, 44-47]

Interference lithography is a good technique for producing periodic patterns, such as 1D line patterns or 2D dot/hole arrays, over large areas without using the photomask.[48, 49] Different laser sources, such as a Lloyd's mirror system with a 325 nm wavelength He-Cd laser or a 193 nm ArF laser, can be used depending on the required feature size. By using shorter wavelengths, interference lithography can extend resolution capability of photolithography. For example, extreme ultraviolet (EUV) light source with a wavelength of 13.5 nm can achieve a spatial resolution below 10 nm on various photoresists in a single

exposure.[50, 51] Many research groups have used interference lithography to fabricate chemically patterns as well as topographic patterns in the directed self-assembly (DSA) process.[52-61]

EBL is a standard technique for writing patterns that does not require a photomask, but this technique has relatively low throughput compared to photolithography.[62] The resolution of EBL can be below 10 nm, which is determined by several parameters, including the applied voltage, the spot size of the beam, the photoresist, and the effect of electron scattering, i.e. the proximity effect. Poly(methyl methacrylate) (PMMA) is one of the first resists for EBL and functions as an organic positive-tone resist for high-resolution patterning.[63, 64] The negative-tone resist, hydrogen silsesquioxane (HSQ), and the positive-tone resist, ZEP (Nippon Zeon ZEP-520), have also been developed as high resolution e-beam resists.[65-68] A great deal of research on the DSA of BCP thin films has been done using EBL.[69-82]

Alternative approaches such as soft lithography, which uses elastomeric molds, thermal nanoimprint lithography, which transfers a surface relief structure from a master mold to a thermoplastic polymer film by heating above glass transition temperature of the polymer, or UV-assisted imprint lithography, which uses a low viscosity photocurable monomer with UV transparent mold, can be employed to produce topographic patterns.[83-86] Jung and co-workers used poly(dimethylsiloxane) (PDMS) mold as the topographical pattern and then, by combining the DSA of BCPs with nanotransfer printing, they obtained ordered sub-10 nm BCP patterns on various substrates such as indium tin oxide (ITO), silver, and aluminum beverage can.[87] Russell and co-workers fabricated nanoimprinted polymer replica with high fidelity such as polyimide, PDMS, poly(butylene terephthalate)

(PBT), and fluorinated ethylene propylene (FEP) from a faceted sapphire surface.[88, 89] These replica substrates were used for the DSA of poly(styrene-*b*-ethylene oxide) (PS-*b*-PEO) diblock copolymer thin films.

1.4.2 Topographic Patterns with Deep Patterning

To date, in the DSA of BCP thin films with topographic patterns, most studies have focused on the use of topographic patterns with the deep geometry, where the vertical length scale of the confinement areas is greater than L_0. As shown in Figure 1.3a, one representative example of deep geometries is a deep trench pattern. In the deep trench patterns, the confinement depth of the trench is comparable to or larger than L_0, so that it can control the lateral ordering and placement accuracy of BCP microdomains with thickness comparable to L_0 in the confinement areas with relative ease. However, in this case, the grain size of BCP microdomains is limited by the width of the trench. A reversed case is a minimal trench pattern, as shown in Figure 1.3b, i.e. the minimal geometry. In this case, the confinement depth of the trench is much less than L_0, allowing BCP microdomains to span across the patterned substrate. Here, we will first discuss topographic patterns with deep geometries.

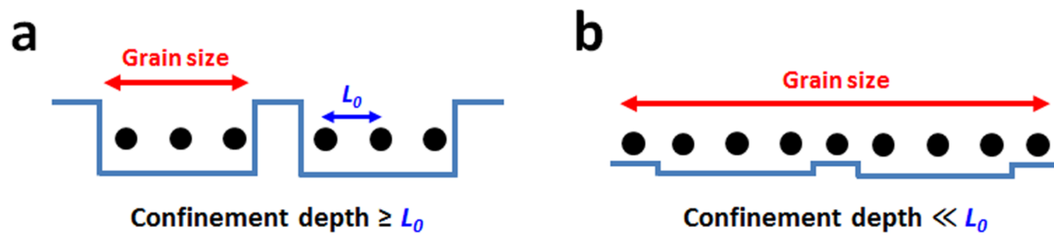

Figure 1.3 Two types of trench patterns. (a) Deep trench pattern. (b) Minimal Trench Pattern.

1.4.2.1 Deep Trench Patterns

Kramer and co-workers first demonstrated the generation of single crystal films of BCPs over large areas on a trench pattern.[41] After thermal annealing of the monolayer of spherical microdomains of poly(styrene-*b*-2-vinylpyridine) (PS-*b*-P2VP) diblock copolymer on the trench pattern, they produced at least 4.5 μm single grain hexagonal arrays of spherical microdomains on the mesa. In this study, the length scales of mesas and trenches played a crucial role in inducing long-range lateral order of spherical microdomains. When the depth of the trench was equal to or greater than L_0 and the width of the mesa was less than 5 μm, they could obtain the single grain of PS-*b*-P2VP microdomains. The same group also investigated the ordering and melting behavior of spherical microdomains of PS-*b*-P2VP on the trench patterns through a continuous defect generation process.[90] By varying temperatures that correspond to χN, where χ is the temperature dependent Flory-Huggins parameter and N is the number of mers in the BCP, they generated a 2D single crystalline layer of PS-*b*-P2VP spherical microdomains with quasi-long-range order with few defects when the temperature of thermal annealing was close to but below the temperature of 2D crystal to hexatic transition ($7.4 < \chi N < 9$). In

addition, the same group found that the topographic confining edge provided the spherical microdomains of PS-*b*-P2VP with the orientational and translational order while the influence of the confining edge decayed as the distance increases from the edge.[91, 92] Similarly, the self-assembly behavior of cylindrical microdomains in thin films on the trench patterns was studied in terms of the orientational order, translational order, and defects by varying temperature.[45, 93] Furthermore, Kramer and co-workers characterized the grain orientation and the single crystal diffraction of PS-*b*-P2VP microdomains on the 2D hexagonal trench patterns using moiré patterns from scanning force microscopy (SFM) or grazing incidence small angle X-ray diffraction.[46, 94]

Ross and co-workers studied the DSA of a sphere-forming BCP on trench patterns.[54, 72, 95-97] They used poly(styrene-*b*-ferrocenyldimethylsilane) (PS-*b*-PFS) diblock copolymer because of its high etching selectivity, which is useful for the pattern transfer into an underlying layer or a substrate. To understand confinement effects of the trench pattern on the self-assembly of BCP thin films, they fabricated the trench pattern of 80 nm depth with various widths using EBL technique, so that the number of rows of PS-*b*-PFS microdomains was controlled (Figure 1.4a).[72] As shown in Figure 1.4b, N rows of spherical microdomains were maintained when $(N - 0.5)L_0 < W < (N + 0.5)L_0$, where L_0 is the natural period of PS-*b*-PFS and W is the width of the trench. It was found that when there was incommensurability between W and L_0, PS-*b*-PFS microdomains were extended or compressed to comply with the confinement condition arising from the trench patterns. To demonstrate this behavior, they developed the free energy model, as shown in Figure 1.4c. The free energy shows its local minimum when $W = NL_0$, so that in this case, spherical microdomains will ideally choose an integer value of N row. When $W \approx (N + 0.5)L_0$,

however, there will be a transition in the number of rows from N to $N + 1$ due to the change in the free energy. Also, Ross and co-workers fabricated 2D topographical patterns with a sharp corner of 60° to investigate high positional accuracy of spherical microdomains.[97] Compared with 1D trench patterns, this 2D pattern could reduce the placement error of hexagonal arrays of PS-*b*-PFS microdomains due to another confinement in a direction of 60°, so that they could achieve the pattern registration with an error of 3 nm, which was comparable to the error by other lithographic techniques.

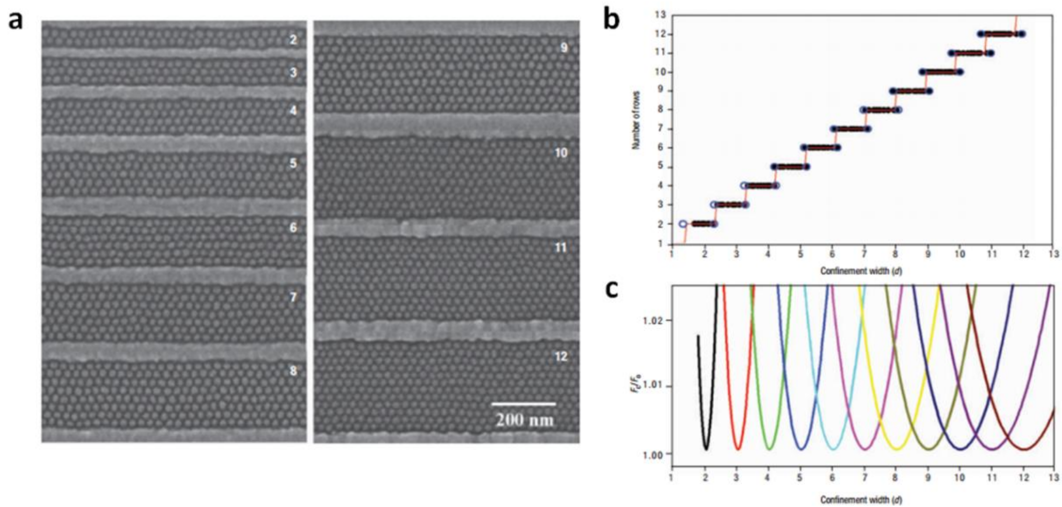

Figure 1.4 PS-*b*-PFS in parallel-sided grooves. (a) Plan-view electron micrograph of ordered arrays of PFS domains with $N = 2$ to 12 rows. (b) The number of rows in the groove, N, plotted against confinement width, W, showing the widths at which arrays with N rows are stable. The confinement width is expressed in terms of d, the equilibrium row spacing, which is 24.8 nm in this polymer. (c) Energy against confinement width of BCP system. The free energy of the confined BCP (F_c) is presented relative to the free energy of the bulk BCP (F_0). Reprinted by permission from Macmillan Publishers Ltd: *Nature Materials*, Cheng *et al.* (2004), copyright 2004 (Ref. 72).

Ross and co-worker also developed graphoepitaxy with poly(styrene-*b*-dimethylsiloxane) (PS-*b*-PDMS) diblock copolymers.[56, 58, 98] Since PS-*b*-PDMS has a relatively high Flory-Huggins interaction parameter ($\chi \approx 0.26$ at room temperature), which is related to scalability of BCP microdomains, smaller L_0 can be achieved in comparison to other BCPs, such as PS-*b*-PMMA ($\chi \approx 0.04$) and PS-*b*-P2VP ($\chi \approx 0.18$). Also, the PDMS block exhibits a high etching contrast to O_2 plasma in comparison to the PS block, due to the presence of Si in the backbone of PDMS, so that it can be used for lithographic masks. However, due to the large difference in the surface tensions between PS ($\gamma = 40.7$ mN/m) and PDMS ($\gamma = 19.9$ mN/m), there is preferential segregation of the PDMS block to the air/BCP interface, causing difficulty in achieving perpendicular orientation of the microdomains. They fabricated trench patterns using Lloyd's Mirror interference lithography, followed by modification of the surface of the trench using PDMS brush layers to facilitate the self-assembly of a cylinder-forming PS-*b*-PDMS diblock copolymer.[58] In this work, they systematically controlled the width ratio (mesa/trench) from 0.18 to 1 with maintaining the trench pitch of 1 μm, toluene vapor pressure, and annealing time. Under a high vapor pressure of toluene for 15 h with the narrow mesa ($W_{\text{mesa}} = 125$ nm and $W_{\text{trench}} = 875$ nm), they obtained in-plain cylindrical microdomains oriented parallel to the trench walls. In contrast, at a lower vapor pressure of toluene for 15 h with the wide mesa ($W_{\text{mesa}} = 270$ nm and $W_{\text{trench}} = 730$ nm), in-plain cylindrical microdomains were aligned perpendicular to the trench walls. In addition, Ross and co-workers produced the concentric ring patterns of PS-*b*-PDMS.[98] In this study, they fabricated circular trench guiding patterns of 40 nm depth with the diameter, *D*, from 60 to 350 nm using Lloyd's Mirror interference lithography. They observed only a PDMS sphere when $D = 60$ or 77 nm, a single PDMS

ring without an inner sphere when 86 nm < D < 94 nm, reappearance of the inner sphere when 102 nm < D < 134 nm. These periodic changes in the presence and the absence of the inner sphere were maintained in the whole range of the trench D. Besides the DSA of diblock copolymers, Ross, Manners, and co-workers investigated the DSA of triblock terpolymers with trench patterns.[99] In this case, they used the blend of poly(isoprene-*b*-styrene-*b*-ferrocenylsilane) (PI-*b*-PS-*b*-PFS) triblock terpolymer with PS homopolymer to induce square symmetry arrays of BCP microdomains. By tuning the surface properties of the trench patterns with various widths, they demonstrated the self-assembly of square-packed triblock terpolymer microdomains.

Sibener and co-workers studied the DSA of BCPs using trench patterns with various widths and depths.[78, 100, 101] In their study, the trench depths greater than 35 nm induced the alignment of poly(styrene-*b*-(ethylene-*alt*-propylene)) (PS-*b*-PEP) microdomains on the mesas as well as in the trenches by overcoming the confined volumes of the trenches, when overfilled.[78] Also, it was found that if the width of the trench was wider, a longer annealing time was required to obtain in-plane cylindrical microdomains of the PS-*b*-PEP. Buriak and co-workers demonstrated the alignment of metallic patterns using rectangular, triangular, and circular trenches of 35 nm depth.[70, 102] In this work, PS-*b*-P2VP diblock copolymers were chosen to load various metal ions into the P2VP blocks. Recently, the same group investigated the compatibility of microwave annealing with graphoepitaxy.[103] By using PS-*b*-P2VP and PS-*b*-PMMA diblock copolymers with microwave annealing in the presence of tetrahydrofuran (THF), they achieved the highly ordered parallel cylindrical microdomains in the trenches with SiO_2 walls.

Trench patterns with chemically homogeneous surfaces, i.e. non-preferential trench bottoms and sidewalls, are useful for guiding the self-assembly of sphere- and cylinder-forming BCPs. In contrast, to guide the self-assembly of lamellar-forming BCPs, in particular controlling the alignment of the microdomains, trench patterns with chemically heterogeneous surfaces, which have non-preferential trench bottoms and preferential sidewalls, are required. For example, Nealey and co-workers controlled the interactions of the blocks of the PS-*b*-PMMA with the bottoms and the sidewalls of the trench patterns to achieve desired orientation of lamellar microdomains.[75] In this case, when the bottom of the trench is neutral to both PS and PMMA blocks while the sidewall of the trench selectively interacts with PS blocks, lamellar microdomains oriented normal to the film surface were aligned parallel with the sidewall of the trench. In contrast, when both the bottom and the sidewall of the trench were SiO_2, which preferentially interacts with the PMMA blocks, lamellar microdomains oriented parallel to the film surface were produced in the trench pattern. Also, when the surface of the trenches was uniformly modified by neutral brush layers (PS-*r*-PMMA), the trench pattern induced perpendicular lamellar microdomains to both the bottom and the sidewall. In this approach, the optimization of experimental parameters, such as the film thickness of BCPs, molecular weight of BCPs, and commensurability between the width of the trench and L_0, was important to obtain high degree of alignment of lamellar microdomains. Similarly, Yamaguchi and co-workers produced PS-*b*-PMMA lamellar microdomains oriented normal to the film surface in the line, rectangular, and hexagonal trench patterns, where these topographic patterns have heterogeneous surface.[104, 105] Recently, Gopalan and co-workers examined not only

symmetric BCPs, but also asymmetric BCPs in the trench patterns by simultaneously controlling the surface chemical composition and the BCP film thickness. [106, 107]

Kim and co-workers studied the DSA of BCPs using various trench patterns.[108-111] Using the hybrid mixture of PS-*b*-PEO and polymethylsiloxane (PMS) resin, they produced wave-like structure of lamellar microdomains oriented perpendicular to the trench direction.[109] This orthogonal alignment of lamellar microdomains was explained by the large difference in the bending properties of aligned lamellar microdomains along two axes. However, in this study, they could not induce wave-like structure when the same trench patterns were applied to PS-*b*-PMMA lamellar microdomains. Recently, the same group extended a previous approach to induce wave-like structures of PS-*b*-PMMA lamellar microdomains by using broader range of length scales of the trench patterns.[110] It was found that the wave-like alignment of PS-*b*-PMMA lamellar microdomains on trench patterns was dependent on not only the film thickness of BCPs, but also the trench pattern dimension, such as the depth and the pitch.

Black and Bezencenet systematically demonstrated the pattern registration and alignment of PS-*b*-PMMA diblock copolymers using square, circular, and general trench patterns.[44] It was found that the initial variation of the film thickness within the trench pattern after spin-coating was critical for obtaining well-ordered cylindrical microdomains oriented parallel to the film surface in the trenches. Specifically, when the film thickness was thicker near a step edge than that of a middle of the trench, the microdomains was first nucleated along the step edges and then, propagated to the middle of the trench. However, the thickness variations within the trench pattern were dependent on the pattern dimensions, such as a narrow width and a wide width, so that the length scales of the pattern should be

optimized to achieve registration of BCP microdomains. Ruiz *et al.* investigated the local defectivity of parallel lamellar microdomains of the PS-*b*-PMMA confined in a tapered trench geometry.[112] In this geometry, the narrow region imposes a higher free energy penalty for defect formation than that of the wider areas. By using this approach, they produced defect-free microdomains in the narrow trench regions up to the width of 0.64 μm ($20L_0$) and the length of 5 μm ($150L_0$).

The influence of the line edge roughness (LER) of the trench pattern on the DSA of BCP films was studied.[113, 114] Yang *et al.* reported that the ordering of PS-*b*-PMMA cylindrical microdomains oriented normal to the film surface was strongly affected by the LER of the trench pattern.[114] Similarly, Nealey and co-workers investigated the influence of the trench width roughness (TWR) on defectivity of cylindrical microdomains of the PS-*b*-PMMA.[113] In this case, the defect formation was strongly dependent on commensurability between the width of the trench and L_0 while TWR did not strongly impact on defectivity.

Kim and co-workers demonstrated the DSA of BCP thin films using photoresist patterns.[47, 115, 116] One of the advantages using the photoresist pattern is that this pattern can be completely removed by a simple cleaning method after pattern transfer, so that further overlay processes can be facilitated. By using symmetric and asymmetric PS-*b*-PMMA diblock copolymers with SU8 photoresist trench patterns, they produced highly ordered BCP microdomains.[47] In this case, since the sidewall of the photoresist trench pattern preferentially interacted with the PS blocks, the perpendicular orientation of BCP microdomains was produced when interactions between the blocks of the BCP and the bottom of the trench were balanced. Moreover, they demonstrated that lateral order of

lamellar microdomains oriented normal to the film surface could be achieved over large areas (17.5 μm by 12.5 μm) by combining graphoepitaxy with epitaxial self-assembly.[115]

1.4.2.2 Deep Post Patterns

To guide the self-assembly of a sphere-forming PS-*b*-PDMS, Berggren, Thomas, Ross, and co-workers fabricated 2D arrays of HSQ posts using EBL.[69] In contrast to previous 1D trench patterns, here, the sparse HSQ posts were fabricated over the substrate, interacting both locally and globally with spherical microdomains of the BCP. They functionalized the HSQ posts on the silicon substrate with a short PDMS brush layer, so that these posts can be used as surrogates for minor PDMS spheres in the close-packed array. These HSQ posts also can be modified by a PS brush layer. When there were no guiding posts on the substrate, spherical microdomains in PS-*b*-PDMS thin film showed short-range lateral order. In contrast, when brush-coated HSQ post were used to guide the self-assembly of PS-*b*-PDMS thin films, a single grain of spherical microdomains was produced. Also, they found that the orientation and domain spacing of the spherical microdomains on post patterns were dictated by the commensurability between the equilibrium spacing of the BCP on a flat surface (L_0) and the period of HSQ post (L_{post}), which is supported by a free-energy model. When they plotted this free energy curve as a function of L_{post}/L_0, the free energy showed a minimum at L_{post}/L_0 values, where the HSQ post lattice was commensurate with a lattice of unstrained BCP microdomain. This theoretical prediction was closely accorded with the obtained experimental results, so that they could observe all predicted BCP microdomains lattice types, such as <11>, <20>,

<21>, <30>, <22>, <31>, <40>, <32>, and <41>, by varying L_{post}. Also, a single BCP lattice orientation or two or more different BCP lattice orientations were observed depending on a value of L_{post}/L_0 due to changing width and number of the potential wells in the free energy curve. Furthermore, Berggren, Ross and co-workers reported more complex self-assembled BCP patterns guided by HSQ post patterns.[117] By changing the post lattice parameters of L_x and L_y, where L_x and L_y are the periodicities in the x and y directions, respectively, the lattice orientation angles of BCP microdomains were controlled. When they varied the geometry of the HSQ posts and their motif, more complex BCP patterns including bends, junctions, and zig-zag patterns could be produced.

Berggren and co-workers reported the DSA of a cylinder-forming PS-*b*-PDMS with a sub-10 nm period using rectangular arrays of post patterns.[118] In this study, every possible commensurate case to have the orientations of PDMS cylinders from 0° to 90° with respect to the x-axis was investigated by varying parameters of L_x and L_y. Also, the effect of length scales of HSQ posts on the self-assembly of BCPs was demonstrated. It was found that the larger diameter and greater height of the HSQ posts enhanced the y-axis orientation similar to 1D trench patterns while the smaller diameter and shorter height of the posts resulted in poor ordering. Recently, Berggren, Ross, and co-workers fabricated 3D multilevel structures of BCPs using a bilayer of in-plane PDMS cylinders in a PS matrix with chemically functionalized HSQ posts.[79] By varying the periodicity of the post arrays in the x and y directions, the orientation and morphology of BCP microdomains in each layer were controlled, so that various structures, such as perpendicular and angled mesh-shaped structures, different periodic superstructures, cylinders on top of spheres, cylinders on top of square symmetry perforated lamellae, and cylinders on top of ellipsoids, could be

achieved, which are described by self-consistent field theory (SCFT) simulations. They demonstrated that this strategy for 3D routing of dense BCP microdomains could be a new route to fabricate nanoscale device manufacturing. Further, Hannon *et al.* studied the optimization of post patterns for the target BCP patterns with complex features by using inverse design simulations.[119] In this work, they first performed simulations to predict the patterns of HSQ posts necessary that can guide the self-assembly of PS-*b*-PDMS diblock copolymers. By using these simulated posts, they produced the target BCP patterns, such as junctions, lines, and terminations.

1.4.2.3 Other Patterns

Kim and co-workers investigated the self-assembly of symmetric PS-*b*-PMMA diblock copolymers on wrinkled surfaces with balanced interfacial interactions.[120] They fabricated a wrinkled pattern using Norland Optical Adhesive (NOA71) UV-curable epoxy thin film, which was biaxially strained using oxygen plasma. After curing with UV irradiation, they obtained randomly oriented wrinkled patterns with a pitch of 4 μm and an amplitude of 800 nm due to the uniform equi-biaxial stress on NOA71 surface. After the DSA of a lamellar-forming PS-*b*-PMMA on this wrinkled surface, it was found that lamellar microdomains in the center of the wrinkle were aligned normal to the wrinkle direction, due to the thickness gradient by geometric anchoring. They also studied the DSA of BCPs on various straight and periodic wrinkled patterns and on graphene-wrinkled surfaces.

On 1D or 2D planar patterned substrates, such as trench and post patterns, the commensurability between the pattern dimension and L_0 and the preferential interaction between the one block of BCPs and the substrate play a key role in dictating morphology of BCP thin films. However, BCP morphologies on non-planar surfaces, such as cylindrical or spherical templates, can be affected by both the commensurability and curvature of the template.[121-128] Russell and co-workers studied poly(styrene-*b*-butadiene) (PS-*b*-PBD) diblock copolymers confined in cylindrical nanoporous alumina membranes.[124] In the bulk, the PS-*b*-PBD diblock copolymer showed lamellar morphology while when the PS-*b*-PBD was confined in cylindrical pore with diameter, *d*, of 45 nm ($d/L_0 \sim 2.6$), it showed a stacked-disc or toroidal-type structures, which deviated from the bulk morphology because of the imposed high degree of the curvature and incommensurability.

1.4.3 Topographic Patterns with Minimal Patterning

As mentioned before, although topographic patterns with the deep geometry can control the orientation and/or position of BCP microdomains with lateral order, there is limitation in the final grain size of BCP microdomains owing to the confinement width. Minimal topographic patterning can be a route to overcome this limitation. Generally, the vertical length scale of the confinement area of the minimal topographic patterns is much smaller than L_0 so that, on substrates with minimal topographical patterning, the grain sizes of BCPs several orders of magnitude greater than that of BCPs on deep topographic patterns can be achieved by overcoming the width of the confinement.

1.4.3.1 Faceted Substrates

Perhaps the simplest means of minimal patterning a surface is to reconstruct the surface of a single crystalline material, like Si or sapphire, that is miscut, namely, cut along a crystal plane that is stable at room temperature but unstable at elevated temperatures.[129-132] The facets have a depth of several nanometers with a pitch of tens of nanometers, so that they can be used to guide the self-assembly of BCPs. Fasolka *et al.* studied symmetric diblock copolymer thin films with thickness below L_0 on the faceted Si substrate.[133] They found that BCP microdomains were decorated along the facet ridges due to the variation in film thickness on the faceted substrate. Rockford *et al.* investigated a lamellar-forming PS-*b*-PMMA on the faceted substrate.[134] In this case, they prepared periodic heterogeneous surfaces of polar (silicon oxide) and nonpolar (gold) using the glancing angle evaporation of metals on the miscut Si wafer having a sawtooth-type pattern with an amplitude of several nanometers. In this case, the silicon oxide preferentially interacts with PMMA block while the gold interacts with PS block. It was found that the orientation and the ordering of lamellar microdomains of PS-*b*-PMMA thin films on the faceted substrate were strongly affected by the commensurability between L_0 and the period of the faceted substrate. Also, they reported a surface-directed morphology of lamellar microdomains in thick PS-*b*-PMMA films on the Si faceted substrate with alternating stripes of silicon oxide and gold.[135]

Recently, Russell and co-workers demonstrated the fabrication of an ultradense single grain array of cylindrical microdomains of BCPs on the sapphire faceted substrate.[136] To produce the faceted surface, the miscut single crystal sapphire surface (Figure 1.5a) was thermally annealed in air from 1300 °C to 1500 °C, which produced patterns with pitches

from 24 to 160 nm and amplitudes from 3 to 20 nm (Figure 1.5b). These sawtooth patterns were used to guide the self-assembly of cylinder-forming PS-*b*-PEO diblock copolymers with different molecular weights. After producing PS-*b*-PEO thin films (Figure 1.5c), followed by SVA, they produced a single hexagonal array of cylindrical microdomains oriented normal to the film surface with areal densities of 0.74 to 10.5 terabit/inch^2 on a 1.5 cm × 1.5 cm faceted pattern (Figure 1.5d). Grazing incidence small angle X-ray scattering (GISAXS) was used to characterize the single grain of PS-*b*-PEO thin films on the sapphire sawtooth pattern by rotating the sample stage from 0° to 90°. Even though there were defects in the underlying faceted pattern and variations in the pitches and the amplitudes of the facets, the generated single grain of BCP microdomains showed a perfect orientational order and a quasi-long-range crystalline order. Furthermore, Russell and co-workers produced hexagonal arrays of cylindrical microdomains oriented normal to the film surface over large areas on various flexible faceted substrates, which were replicated from the faceted sapphire surface.[89]

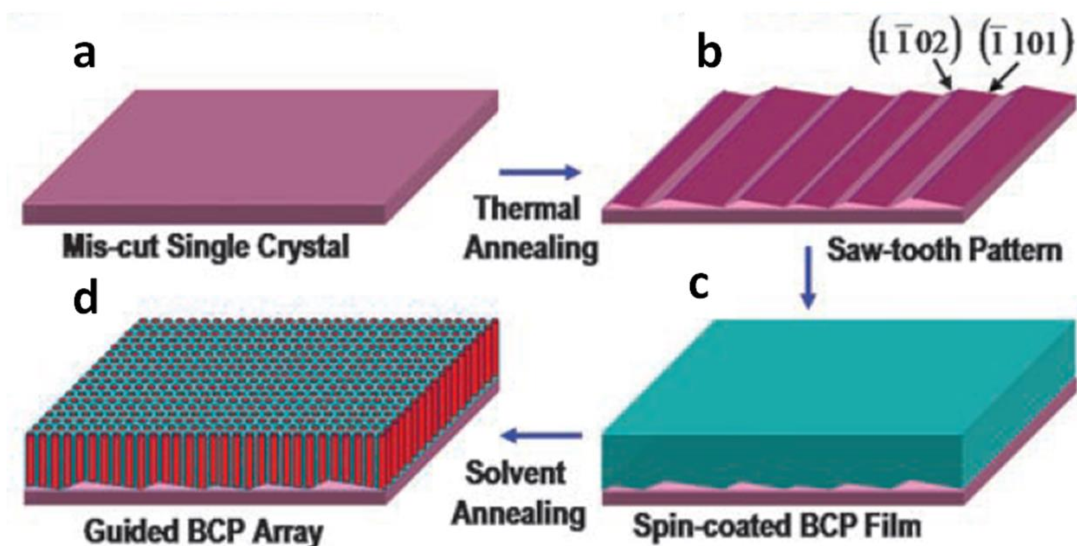

Figure 1.5 Schematic illustration of the strategy used for generating BCP cylindrical microdomains on highly oriented crystalline facets on a single-crystal surface. From Park *et al.*, *Science* **2009**, *323*, 1030-1033. Reprinted with permission from AAAS (Ref. 136).

Line patterns of cylindrical microdomains in BCP thin films on imprinted polymer replicas as well as faceted sapphire substrates were investigated by Russell and co-workers.[88] They produced a single grain line pattern of the PS-*b*-PEO diblock copolymer on the sapphire sawtooth substrate with SVA, which was driven by entropic penalties of chain packing of the BCP at the facet geometry. These line patterns were studied using GISAXS with a rotating sample stage. With increasing the rotation angle of the sample from 0°, where the X-ray beam was parallel to the (10) lattice line, to 4°, the (10) reflection was broadened and its intensity was significantly decreased. Based on these GISAXS data, the orientation parameter, f, where $f = 1.0$ for perfect orientation of the microdomains, and $f = 0$ for random orientation, was calculated. In this study, f was more than 0.97, which is characteristic of the unidirectionally aligned line patterns of cylindrical microdomains. Furthermore, the same group demonstrated the line pattern of cylindrical microdomains in

PS-*b*-PEO thin films on the faceted Si pattern, which shows more asymmetric geometry than that of the faceted sapphire substrate.[137] In this case, by rotating the sample stage during GISAXS experiments, the orientation and the lateral ordering of PS-*b*-PEO microdomains were characterized.

1.4.3.2 Minimal Trench Patterns

Russell and co-worker studied the DSA of poly(styrene-*b*-4-vinylpyridine) (PS-*b*-P4VP) diblock copolymers with SVA on the minimal trench patterns with two different depths.[138] For the minimal trench pattern with the depth of 14 nm, they varied the widths of the mesa from 50 to 120 nm. In this case, all obtained hexagonal arrays of PS-*b*-P4VP microdomains in the trenches showed long-range lateral order, where the final grain size was determined by the width of the trench. In contrast, when they used the trench pattern with the depth of 5 nm, they produced a single grain with at least 5 μm × 5 μm of hexagonal arrays of PS-*b*-P4VP microdomains over the trench pattern with a high degree of lateral order.

Russell and co-workers also produced circular PS-*b*-PEO line patterns using circular shallow trench patterns with the depth of 8 nm.[73] In this study, they fabricated three different pattern dimensions, such as $I_{29,80}$ (trench width = 29 nm and trench pitch = 80 nm), $M_{31,99}$ (trench width = 31 nm and trench pitch = 99 nm), and $O_{34,121}$ (trench width = 34 nm and trench width = 121 nm) using EBL. Among these three patterns, only $M_{31,99}$ pattern could guide the self-assembly of PS-*b*-PEO thin films, generating circular line patterns of cylindrical microdomains due to commensurability between the dimension of the $M_{31,99}$

pattern and domain spacing of the PS-*b*-PEO. They also used the same circular trench patterns to guide the self-assembly of a cylinder-forming PS-*b*-P2VP diblock copolymer. In this case, highly ordered circular line patterns of PS-*b*-P2VP microdomains were achieved only on the $I_{29,80}$ pattern because of the commensurability between the dimension of the $I_{29,80}$ pattern and domain spacing of the PS-*b*-P2VP.

1.5 References

1. ITRS. International Technology Roadmap for Semiconductors (ITRS) 2013 Edition. *http://http://www.itrs2.net/2013-itrs.html* **2013**.

2. Hawker, C. J.; Russell, T. P. Block Copolymer Lithography: Merging “Bottom-up” with “Top-Down” Processes. *MRS Bull.* **2005**, *30*, 952-966.

3. Li, W.; Müller, M. Directed Self-Assembly of Block Copolymers by Chemical or Topographical Guiding Patterns: Optimizing Molecular Architecture, Thin-Film Properties, and Kinetics. *Prog. Polym. Sci.* **2016**, *54–55*, 47-75.

4. Bates, F. S.; Fredrickson, G. H. Block Copolymer Thermodynamics: Theory and Experiment. *Annu. Rev. Phys. Chem.* **1990**, *41*, 525-557.

5. Bates, F. S.; Fredrickson, G. H. Block Copolymers-Designer Soft Materials. *Phys. Today* **1999**, *52*, 32-38.

6. Bates, F. S. Polymer-Polymer Phase Behavior. *Science* **1991**, *251*, 898-905.

7. Hoheisel, T. N.; Hur, K.; Wiesner, U. B. Block Copolymer-Nanoparticle Hybrid Self-Assembly. *Prog. Polym. Sci.* **2015**, *40*, 3-32.

8. Cai, Z. h.; Huang, K.; Montano, P. A.; Russell, T. P.; Bai, J. M.; Zajac, G. W. Experimental Study of the Surface Structure of Diblock Copolymer Films Using Microscopy and X-Ray Scattering. *J. Chem. Phys.* **1993**, *98*, 2376-2386.

9. Hawker, C. J.; Elce, E.; Dao, J.; Volksen, W.; Russell, T. P.; Barclay, G. G. Well-Defined Random Copolymers by a “Living” Free-Radical Polymerization Process. *Macromolecules* **1996**, *29*, 2686-2688.

10. Huang, E.; Mansky, P.; Russell, T. P.; Harrison, C.; Chaikin, P. M.; Register, R. A.; Hawker, C. J.; Mays, J. Mixed Lamellar Films: Evolution, Commensurability Effects, and Preferential Defect Formation. *Macromolecules* **2000**, *33*, 80-88.

11. Huang, E.; Pruzinsky, S.; Russell, T. P.; Mays, J.; Hawker, C. J. Neutrality Conditions for Block Copolymer Systems on Random Copolymer Brush Surfaces. *Macromolecules* **1999**, *32*, 5299-5303.

12. Huang, E.; Russell, T. P.; Harrison, C.; Chaikin, P. M.; Register, R. A.; Hawker, C. J.; Mays, J. Using Surface Active Random Copolymers to Control the Domain Orientation in Diblock Copolymer Thin Films. *Macromolecules* **1998**, *31*, 7641-7650.

13. Husseman, M.; Malmström, E. E.; McNamara, M.; Mate, M.; Mecerreyes, D.; Benoit, D. G.; Hedrick, J. L.; Mansky, P.; Huang, E.; Russell, T. P.; Hawker, C. J. Controlled Synthesis of Polymer Brushes by "Living" Free Radical Polymerization Techniques. *Macromolecules* **1999**, *32*, 1424-1431.

14. Mansky, P.; Liu, Y.; Huang, E.; Russell, T. P.; Hawker, C. Controlling Polymer-Surface Interactions with Random Copolymer Brushes. *Science* **1997**, *275*, 1458-1460.

15. Mansky, P.; Russell, T. P.; Hawker, C. J.; Mays, J.; Cook, D. C.; Satija, S. K. Interfacial Segregation in Disordered Block Copolymers: Effect of Tunable Surface Potentials. *Phys. Rev. Lett.* **1997**, *79*, 237-240.

16. Mansky, P.; Russell, T. P.; Hawker, C. J.; Pitsikalis, M.; Mays, J. Ordered Diblock Copolymer Films on Random Copolymer Brushes. *Macromolecules* **1997**, *30*, 6810-6813.

17. Mansky, P.; Tsui, O. K. C.; Russell, T. P.; Gallot, Y. Phase Coherence and Microphase Separation Transitions in Diblock Copolymer Thin Films. *Macromolecules* **1999**, *32*, 4832-4837.

18. Russell, T. P.; Thurn-Albrecht, T.; Tuominen, M.; Huang, E.; Hawker, C. J. Block Copolymers as Nanoscopic Templates. *Macromol. Symp.* **2000**, *159*, 77-88.

19. Ryu, D. Y.; Shin, K.; Drockenmuller, E.; Hawker, C. J.; Russell, T. P. A Generalized Approach to the Modification of Solid Surfaces. *Science* **2005**, *308*, 236-239.

20. Xu, T.; Hawker, C. J.; Russell, T. P. Interfacial Interaction Dependence of Microdomain Orientation in Diblock Copolymer Thin Films. *Macromolecules* **2005**, *38*, 2802-2805.

21. Anastasiadis, S. H.; Russell, T. P.; Satija, S. K.; Majkrzak, C. F. Neutron Reflectivity Studies of the Surface-Induced Ordering of Diblock Copolymer Films. *Phys. Rev. Lett.* **1989**, *62*, 1852-1855.

22. Coulon, G.; Russell, T. P.; Deline, V. R.; Green, P. F. Surface-Induced Orientation of Symmetric, Diblock Copolymers: A Secondary Ion Mass-Spectrometry Study. *Macromolecules* **1989**, *22*, 2581-2589.

23. Menelle, A.; Russell, T. P.; Anastasiadis, S. H.; Satija, S. K.; Majkrzak, C. F. Ordering of Thin Diblock Copolymer Films. *Phys. Rev. Lett.* **1992**, *68*, 67-70.

24. Russell, T. P.; Coulon, G.; Deline, V. R.; Miller, D. C. Characteristics of the Surface-Induced Orientation for Symmetric Diblock PS/PMMA Copolymers. *Macromolecules* **1989**, *22*, 4600-4606.

25. Bang, J.; Bae, J.; Löwenhielm, P.; Spiessberger, C.; Given-Beck, S. A.; Russell, T. P.; Hawker, C. J. Facile Routes to Patterned Surface Neutralization Layers for Block Copolymer Lithography. *Adv. Mater.* **2007**, *19*, 4552-4557.

26. Han, E.; In, I.; Park, S. M.; La, Y. H.; Wang, Y.; Nealey, P. F.; Gopalan, P. Photopatternable Imaging Layers for Controlling Block Copolymer Microdomain Orientation. *Adv. Mater.* **2007**, *19*, 4448-4452.

27. Ryu, D. Y.; Wang, J.-Y.; Lavery, K. A.; Drockenmuller, E.; Satija, S. K.; Hawker, C. J.; Russell, T. P. Surface Modification with Cross-Linked Random Copolymers: Minimum Effective Thickness. *Macromolecules* **2007**, *40*, 4296-4300.

28. Kim, G.; Libera, M. Morphological Development in Solvent-Cast Polystyrene−Polybutadiene−Polystyrene (SBS) Triblock Copolymer Thin Films. *Macromolecules* **1998**, *31*, 2569-2577.

29. Kim, G.; Libera, M. Kinetic Constraints on the Development of Surface Microstructure in SBS Thin Films. *Macromolecules* **1998**, *31*, 2670-2672.

30. Kim, S. H.; Misner, M. J.; Russell, T. P. Solvent-Induced Ordering in Thin Film Diblock Copolymer/Homopolymer Mixtures. *Adv. Mater.* **2004**, *16*, 2119-2123.

31. Kim, S. H.; Misner, M. J.; Xu, T.; Kimura, M.; Russell, T. P. Highly Oriented and Ordered Arrays from Block Copolymers Via Solvent Evaporation. *Adv. Mater.* **2004**, *16*, 226-231.

32. Lin, Z. Q.; Kim, D. H.; Wu, X. D.; Boosahda, L.; Stone, D.; LaRose, L.; Russell, T. P. A Rapid Route to Arrays of Nanostructures in Thin Films. *Adv. Mater.* **2002**, *14*, 1373-1376.

33. Brown, G.; Chakrabarti, A. Ordering of Block Copolymer Melts in Confined Geometry. *J. Chem. Phys.* **1995**, *102*, 1440-1448.

34. Kellogg, G. J.; Walton, D. G.; Mayes, A. M.; Lambooy, P.; Russell, T. P.; Gallagher, P. D.; Satija, S. K. Observed Surface Energy Effects in Confined Diblock Copolymers. *Phys. Rev. Lett.* **1996**, *76*, 2503-2506.

35. Kikuchi, M.; Binder, K. Monte Carlo Study of Thin Films of the Symmetric Diblock-Copolymer Melt. *Europhys. Lett.* **1993**, *21*, 427.

36. Koneripalli, N.; Singh, N.; Levicky, R.; Bates, F. S.; Gallagher, P. D.; Satija, S. K. Confined Block Copolymer Thin Films. *Macromolecules* **1995**, *28*, 2897-2904.

37. Lambooy, P.; Russell, T. P.; Kellogg, G. J.; Mayes, A. M.; Gallagher, P. D.; Satija, S. K. Observed Frustration in Confined Block Copolymers. *Phys. Rev. Lett.* **1994**, *72*, 2899-2902.

38. Turner, M. S. Equilibrium Properties of a Diblock Copolymer Lamellar Phase Confined between Flat Plates. *Phys. Rev. Lett.* **1992**, *69*, 1788-1791.

39. Walton, D. G.; Kellogg, G. J.; Mayes, A. M.; Lambooy, P.; Russell, T. P. A Free Energy Model for Confined Diblock Copolymers. *Macromolecules* **1994**, *27*, 6225-6228.

40. Geis, M. W.; Flanders, D. C.; Smith, H. I. Crystallographic Orientation of Silicon on an Amorphous Substrate Using an Artificial Surface-Relief Grating and Laser Crystallization. *Appl. Phys. Lett.* **1979**, *35*, 71-74.

41. Segalman, R. A.; Yokoyama, H.; Kramer, E. J. Graphoepitaxy of Spherical Domain Block Copolymer Films. *Adv. Mater.* **2001**, *13*, 1152-1155.

42. Smith, H. I.; Flanders, D. C. Oriented Crystal Growth on Amorphous Substrates Using Artificial Surface-Relief Gratings. *Appl. Phys. Lett.* **1978**, *32*, 349-350.

43. Gates, B. D.; Xu, Q.; Stewart, M.; Ryan, D.; Willson, C. G.; Whitesides, G. M. New Approaches to Nanofabrication: Molding, Printing, and Other Techniques. *Chem. Rev.* **2005**, *105*, 1171-1196.

44. Black, C. T.; Bezencenet, O. Nanometer-Scale Pattern Registration and Alignment by Directed Diblock Copolymer Self-Assembly. *IEEE Trans. Nanotechnol.* **2004**, *3*, 412-415.

45. Hammond, M. R.; Cochran, E.; Fredrickson, G. H.; Kramer, E. J. Temperature Dependence of Order, Disorder, and Defects in Laterally Confined Diblock Copolymer Cylinder Monolayers. *Macromolecules* **2005**, *38*, 6575-6585.

46. Hexemer, A.; Stein, G. E.; Kramer, E. J.; Magonov, S. Block Copolymer Monolayer Structure Measured with Scanning Force Microscopy Moiré Patterns. *Macromolecules* **2005**, *38*, 7083-7089.

47. Jeong, S.-J.; Kim, J. E.; Moon, H.-S.; Kim, B. H.; Kim, S. M.; Kim, J. B.; Kim, S. O. Soft Graphoepitaxy of Block Copolymer Assembly with Disposable Photoresist Confinement. *Nano Lett.* **2009**, *9*, 2300-2305.

48. Farhoud, M.; Ferrera, J.; Lochtefeld, A. J.; Murphy, T. E.; Schattenburg, M. L.; Carter, J.; Ross, C. A.; Smith, H. I. Fabrication of 200 nm Period Nanomagnet Arrays Using Interference Lithography and a Negative Resist. *J. Vac. Sci. Technol. B* **1999**, *17*, 3182-3185.

49. Savas, T. A.; Schattenburg, M. L.; Carter, J. M.; Smith, H. I. Large-Area Achromatic Interferometric Lithography for 100 nm Period Gratings and Grids. *J. Vac. Sci. Technol. B* **1996**, *14*, 4167-4170.

50. Auzelyte, V.; Dais, C.; Farquet, P.; Grützmacher, D.; Heyderman, L. J.; Luo, F.; Olliges, S.; Padeste, C.; Sahoo, P. K.; Thomson, T.; Turchanin, A.; David, C.; Solak, H. H. Extreme Ultraviolet Interference Lithography at the Paul Scherrer Institut. *J. Micro/Nanolith., MEMS MOEMS* **2009**, *8*, 021204-10.

51. Wagner, C.; Harned, N. Euv Lithography: Lithography Gets Extreme. *Nat. Photonics* **2010**, *4*, 24-26.

52. Chang, S.-W.; Chuang, V. P.; Boles, S. T.; Ross, C. A.; Thompson, C. V. Densely Packed Arrays of Ultra-High-Aspect-Ratio Silicon Nanowires Fabricated Using Block-Copolymer Lithography and Metal-Assisted Etching. *Adv. Funct. Mater.* **2009**, *19*, 2495-2500.

53. Cheng, J. Y.; Ross, C. A.; Thomas, E. L.; Smith, H. I.; Vancso, G. J. Fabrication of Nanostructures with Long-Range Order Using Block Copolymer Lithography. *Appl. Phys. Lett.* **2002**, *81*, 3657-3659.

54. Chuang, V. P.; Cheng, J. Y.; Savas, T. A.; Ross, C. A. Three-Dimensional Self-Assembly of Spherical Block Copolymer Domains into V-Shaped Grooves. *Nano Lett.* **2006**, *6*, 2332-2337.

55. Edwards, E. W.; Stoykovich, M. P.; Solak, H. H.; Nealey, P. F. Long-Range Order and Orientation of Cylinder-Forming Block Copolymers on Chemically Nanopatterned Striped Surfaces. *Macromolecules* **2006**, *39*, 3598-3607.

56. Jung, Y. S.; Chang, J. B.; Verploegen, E.; Berggren, K. K.; Ross, C. A. A Path to Ultranarrow Patterns Using Self-Assembled Lithography. *Nano Lett.* **2010**, *10*, 1000-1005.

57. Jung, Y. S.; Jung, W.; Tuller, H. L.; Ross, C. A. Nanowire Conductive Polymer Gas Sensor Patterned Using Self-Assembled Block Copolymer Lithography. *Nano Lett.* **2008**, *8*, 3776-3780.

58. Jung, Y. S.; Ross, C. A. Orientation-Controlled Self-Assembled Nanolithography Using a Polystyrene−Polydimethylsiloxane Block Copolymer. *Nano Lett.* **2007**, *7*, 2046-2050.

59. La, Y.-H.; Edwards, E. W.; Park, S.-M.; Nealey, P. F. Directed Assembly of Cylinder-Forming Block Copolymer Films and Thermochemically Induced Cylinder to Sphere Transition: A Hierarchical Route to Linear Arrays of Nanodots. *Nano Lett.* **2005**, *5*, 1379-1384.

60. Liu, C.-C.; Nealey, P. F.; Raub, A. K.; Hakeem, P. J.; Brueck, S. R. J.; Han, E.; Gopalan, P. Integration of Block Copolymer Directed Assembly with 193 Immersion Lithography. *J. Vac. Sci. Technol. B* **2010**, *28*, C6B30-C6B34.

61. Stoykovich, M. P.; Müller, M.; Kim, S. O.; Solak, H. H.; Edwards, E. W.; de Pablo, J. J.; Nealey, P. F. Directed Assembly of Block Copolymer Blends into Nonregular Device-Oriented Structures. *Science* **2005**, *308*, 1442-1446.

62. Geissler, M.; Xia, Y. Patterning: Principles and Some New Developments. *Adv. Mater.* **2004**, *16*, 1249-1269.

63. Hatzakis, M. Electron Resists for Microcircuit and Mask Production. *J. Electrochem. Soc.* **1969**, *116*, 1033-1037.

64. McCord, M. A.; Rooks, M. J. *Handbook of Microlithography, Micromachining, and Microfabrication. Volume 1: Microlithography*. SPIE: Bellingham, 1997; Vol. 1.

65. Grigorescu, A. E.; Hagen, C. W. Resists for Sub-20-nm Electron Beam Lithography with a Focus on HSQ: State of the Art. *Nanotechnology* **2009**, *20*, 292001.

66. Kurihara, K.; Iwadate, K.; Namatsu, H.; Nagase, M.; Takenaka, H.; Murase, K. An Electron Beam Nanolithography System and its Application to Si Nanofabrication. *Jpn. J. Appl. Phys.* **1995**, *34*, 6940.

67. Namatsu, H.; Takahashi, Y.; Yamazaki, K.; Yamaguchi, T.; Nagase, M.; Kurihara, K. Three-Dimensional Siloxane Resist for the Formation of Nanopatterns with Minimum Linewidth Fluctuations. *J. Vac. Sci. Technol. B* **1998**, *16*, 69-76.

68. Nishida, T.; Notomi, M.; Iga, R.; Tamamura, T. Quantum Wire Fabrication by E-Beam Elithography Using High-Resolution and High-Sensitivity E-Beam Resist ZEP-520. *Jpn. J. Appl. Phys.* **1992**, *31*, 4508-4514.

69. Bita, I.; Yang, J. K. W.; Jung, Y. S.; Ross, C. A.; Thomas, E. L.; Berggren, K. K. Graphoepitaxy of Self-Assembled Block Copolymers on Two-Dimensional Periodic Patterned Templates. *Science* **2008**, *321*, 939-943.

70. Chai, J.; Wang, D.; Fan, X.; Buriak, J. M. Assembly of Aligned Linear Metallic Patterns on Silicon. *Nat. Nanotechnol.* **2007**, *2*, 500-506.

71. Chang, J.-B.; Choi, H. K.; Hannon, A. F.; Alexander-Katz, A.; Ross, C. A.; Berggren, K. K. Design Rules for Self-Assembled Block Copolymer Patterns Using Tiled Templates. *Nat. Commun.* **2014**, *5*, Article number: 3305, 1-9.

72. Cheng, J. Y.; Mayes, A. M.; Ross, C. A. Nanostructure Engineering by Templated Self-Assembly of Block Copolymers. *Nat. Mater.* **2004**, *3*, 823-828.

73. Hong, S. W.; Gu, X.; Huh, J.; Xiao, S.; Russell, T. P. Circular Nanopatterns over Large Areas from the Self-Assembly of Block Copolymers Guided by Shallow Trenches. *ACS Nano* **2011**, *5*, 2855-2860.

74. Kim, S. O.; Solak, H. H.; Stoykovich, M. P.; Ferrier, N. J.; de Pablo, J. J.; Nealey, P. F. Epitaxial Self-Assembly of Block Copolymers on Lithographically Defined Nanopatterned Substrates. *Nature* **2003**, *424*, 411-414.

75. Park, S.-M.; Stoykovich, M. P.; Ruiz, R.; Zhang, Y.; Black, C. T.; Nealey, P. F. Directed Assembly of Lamellae-Forming Block Copolymers by Using Chemically and Topographically Patterned Substrates. *Adv. Mater.* **2007**, *19*, 607-611.

76. Ruiz, R.; Kang, H.; Detcheverry, F. A.; Dobisz, E.; Kercher, D. S.; Albrecht, T. R.; de Pablo, J. J.; Nealey, P. F. Density Multiplication and Improved Lithography by Directed Block Copolymer Assembly. *Science* **2008**, *321*, 936-939.

77. Stoykovich, M. P.; Kang, H.; Daoulas, K. C.; Liu, G.; Liu, C.-C.; de Pablo, J. J.; Müller, M.; Nealey, P. F. Directed Self-Assembly of Block Copolymers for Nanolithography: Fabrication of Isolated Features and Essential Integrated Circuit Geometries. *ACS Nano* **2007**, *1*, 168-175.

78. Sundrani, D.; Darling, S. B.; Sibener, S. J. Guiding Polymers to Perfection: Macroscopic Alignment of Nanoscale Domains. *Nano Lett.* **2004**, *4*, 273-276.

79. Tavakkoli K. G., A.; Gotrik, K. W.; Hannon, A. F.; Alexander-Katz, A.; Ross, C. A.; Berggren, K. K. Templating Three-Dimensional Self-Assembled Structures in Bilayer Block Copolymer Films. *Science* **2012**, *336*, 1294-1298.

80. Xiao, S.; Yang, X.; Edwards, E. W.; La, Y.-H.; Nealey, P. F. Graphoepitaxy of Cylinder-Forming Block Copolymers for Use as Templates to Pattern Magnetic Metal Dot Arrays. *Nanotechnology* **2005**, *16*, S324-S329.

81. Xiao, S.; Yang, X.; Park, S.; Weller, D.; Russell, T. P. A Novel Approach to Addressable 4 Teradot/In.^{2} Patterned Media. *Adv. Mater.* **2009**, *21*, 2516-2519.

82. Yang, X.; Wan, L.; Xiao, S.; Xu, Y.; Weller, D. K. Directed Block Copolymer Assembly versus Electron Beam Lithography for Bit-Patterned Media with Areal Density of 1 Terabit/Inch^2 and Beyond. *ACS Nano* **2009**, *3*, 1844-1858.

83. Chou, S. Y.; Krauss, P. R.; Renstrom, P. J. Nanoimprint Lithography. *J. Vac. Sci. Technol. B* **1996**, *14*, 4129-4133.

84. Long, B. K.; Keitz, B. K.; Willson, C. G. Materials for Step and Flash Imprint Lithography (S-Fil®). *J. Mater. Chem.* **2007**, *17*, 3575-3580.

85. Marrian, C. R. K.; Tennant, D. M. Nanofabrication. *J. Vac. Sci. Technol. A* **2003**, *21*, S207-S215.

86. Xia, Y.; Whitesides, G. M. Soft Lithography. *Annu. Rev. Mater. Sci.* **1998**, *28*, 153-184.

87. Jeong, J. W.; Park, W. I.; Do, L.-M.; Park, J.-H.; Kim, T.-H.; Chae, G.; Jung, Y. S. Nanotransfer Printing with Sub-10 nm Resolution Realized Using Directed Self-Assembly. *Adv. Mater.* **2012**, *24*, 3526-3531.

88. Hong, S. W.; Huh, J.; Gu, X.; Lee, D. H.; Jo, W. H.; Park, S.; Xu, T.; Russell, T. P. Unidirectionally Aligned Line Patterns Driven by Entropic Effects on Faceted Surfaces. *Proc. Natl. Acad. Sci.* **2012**, *109*, 1402-1406.

89. Park, S.; Lee, D. H.; Russell, T. P. Self-Assembly of Block Copolymers on Flexible Substrates. *Adv. Mater.* **2010**, *22*, 1882-1884.

90. Segalman, R. A.; Hexemer, A.; Hayward, R. C.; Kramer, E. J. Ordering and Melting of Block Copolymer Spherical Domains in 2 and 3 Dimensions. *Macromolecules* **2003**, *36*, 3272-3288.

91. Segalman, R. A.; Hexemer, A.; Kramer, E. J. Edge Effects on the Order and Freezing of a 2D Array of Block Copolymer Spheres. *Phys. Rev. Lett.* **2003**, *91*, 196101.

92. Segalman, R. A.; Hexemer, A.; Kramer, E. J. Effects of Lateral Confinement on Order in Spherical Domain Block Copolymer Thin Films. *Macromolecules* **2003**, *36*, 6831-6839.

93. Hammond, M. R.; Kramer, E. J. Edge Effects on Thermal Disorder in Laterally Confined Diblock Copolymer Cylinder Monolayers. *Macromolecules* **2006**, *39*, 1538-1544.

94. Stein, G. E.; Kramer, E. J.; Li, X.; Wang, J. Single-Crystal Diffraction from Two-Dimensional Block Copolymer Arrays. *Phys. Rev. Lett.* **2007**, *98*, 086101.

95. Cheng, J. Y.; Ross, C. A.; Thomas, E. L.; Smith, H. I.; Vancso, G. J. Templated Self-Assembly of Block Copolymers: Effect of Substrate Topography. *Adv. Mater.* **2003**, *15*, 1599-1602.

96. Cheng, J. Y.; Zhang, F.; Chuang, V. P.; Mayes, A. M.; Ross, C. A. Self-Assembled One-Dimensional Nanostructure Arrays. *Nano Lett.* **2006**, *6*, 2099-2103.

97. Cheng, J. Y.; Zhang, F.; Smith, H. I.; Vancso, G. J.; Ross, C. A. Pattern Registration between Spherical Block-Copolymer Domains and Topographical Templates. *Adv. Mater.* **2006**, *18*, 597-601.

98. Jung, Y. S.; Jung, W.; Ross, C. A. Nanofabricated Concentric Ring Structures by Templated Self-Assembly of a Diblock Copolymer. *Nano Lett.* **2008**, *8*, 2975-2981.

99. Chuang, V. P.; Gwyther, J.; Mickiewicz, R. A.; Manners, I.; Ross, C. A. Templated Self-Assembly of Square Symmetry Arrays from an ABC Triblock Terpolymer. *Nano Lett.* **2009**, *9*, 4364-4369.

100. Sundrani, D.; Darling, S. B.; Sibener, S. J. Hierarchical Assembly and Compliance of Aligned Nanoscale Polymer Cylinders in Confinement. *Langmuir* **2004**, *20*, 5091-5099.

101. Sundrani, D.; Sibener, S. J. Spontaneous Spatial Alignment of Polymer Cylindrical Nanodomains on Silicon Nitride Gratings. *Macromolecules* **2002**, *35*, 8531-8539.

102. Chai, J.; Buriak, J. M. Using Cylindrical Domains of Block Copolymers to Self-Assemble and Align Metallic Nanowires. *ACS Nano* **2008**, *2*, 489-501.

103. Zhang, X.; Harris, K. D.; Wu, N. L. Y.; Murphy, J. N.; Buriak, J. M. Fast Assembly of Ordered Block Copolymer Nanostructures through Microwave Annealing. *ACS Nano* **2010**, *4*, 7021-7029.

104. Yamaguchi, T.; Yamaguchi, H. Resist-Pattern Guided Self-Assembly of Symmetric Diblock Copolymer. *J. Photopolym. Sci. Technol.* **2006**, *19*, 385-388.

105. Yamaguchi, T.; Yamaguchi, H. Two-Dimensional Patterning of Flexible Designs with High Half-Pitch Resolution by Using Block Copolymer Lithography. *Adv. Mater.* **2008**, *20*, 1684-1689.

106. Han, E.; Kang, H.; Liu, C.-C.; Nealey, P. F.; Gopalan, P. Graphoepitaxial Assembly of Symmetric Block Copolymers on Weakly Preferential Substrates. *Adv. Mater.* **2010**, *22*, 4325-4329.

107. Kim, M.; Han, E.; Sweat, D. P.; Gopalan, P. Interplay of Surface Chemical Composition and Film Thickness on Graphoepitaxial Assembly of Asymmetric Block Copolymers. *Soft Matter* **2013**, *9*, 6135-6141.

108. Cheng, J. Y.; Pitera, J.; Park, O.-H.; Flickner, M.; Ruiz, R.; Black, C. T.; Kim, H.-C. Rapid Directed Self Assembly of Lamellar Microdomains from a Block Copolymer Containing Hybrid. *Appl. Phys. Lett.* **2007**, *91*, 143106-3.

109. Kim, H.-C.; Rettner, C., T.; Sundström, L. Fabrication of 20 nm Half-Pitch Gratings by Corrugation-Directed Self-Assembly. *Nanotechnology* **2008**, *19*, 235301.

110. Park, S.-M.; Berry, B. C.; Dobisz, E.; Kim, H.-C. Observation of Surface Corrugation-Induced Alignment of Lamellar Microdomains in PS-b-PMMA Thin Films. *Soft Matter* **2009**, *5*, 957-961.

111. Park, S.-M.; Rettner, C. T.; Pitera, J. W.; Kim, H.-C. Directed Self-Assembly of Lamellar Microdomains of Block Copolymers Using Topographic Guiding Patterns. *Macromolecules* **2009**, *42*, 5895-5899.

112. Ruiz, R.; Ruiz, N.; Zhang, Y.; Sandstrom, R. L.; Black, C. T. Local Defectivity Control of 2D Self-Assembled Block Copolymer Patterns. *Adv. Mater.* **2007**, *19*, 2157-2162.

113. Welander, A. M.; Nealey, P. F.; Cao, H.; Bristol, R. Impact of Trench Width Roughness on the Graphoepitaxial Assembly of Block Copolymers. *J. Vac. Sci. Technol. B* **2008**, *26*, 2484-2488.

114. Yang, X.; Xiao, S.; Liu, C.; Pelhos, K.; Minor, K. Nanoscopic Templates Using Self-Assembled Cylindrical Diblock Copolymers for Patterned Media. *J. Vac. Sci. Technol. B* **2004**, *22*, 3331-3334.

115. Jeong, S.-J.; Moon, H.-S.; Kim, B. H.; Kim, J. Y.; Yu, J.; Lee, S.; Lee, M. G.; Choi, H.; Kim, S. O. Ultralarge-Area Block Copolymer Lithography Enabled by Disposable Photoresist Prepatterning. *ACS Nano* **2010**, *4*, 5181-5186.

116. Jeong, S.-J.; Moon, H.-S.; Shin, J.; Kim, B. H.; Shin, D. O.; Kim, J. Y.; Lee, Y.-H.; Kim, J. U.; Kim, S. O. One-Dimensional Metal Nanowire Assembly via Block Copolymer Soft Graphoepitaxy. *Nano Lett.* **2010**, *10*, 3500-3505.

117. Yang, J. K. W.; Jung, Y. S.; Chang, J.-B.; Mickiewicz, R. A.; Alexander Katz, A.; Ross, C. A.; Berggren, K. K. Complex Self-Assembled Patterns Using Sparse Commensurate Templates with Locally Varying Motifs. *Nat. Nanotechnol.* **2010**, *5*, 256-260.

118. Chang, J.-B.; Son, J. G.; Hannon, A. F.; Alexander-Katz, A.; Ross, C. A.; Berggren, K. K. Aligned Sub-10-nm Block Copolymer Patterns Templated by Post Arrays. *ACS Nano* **2012**, *6*, 2071-2077.

119. Hannon, A. F.; Ding, Y.; Bai, W.; Ross, C. A.; Alexander-Katz, A. Optimizing Topographical Templates for Directed Self-Assembly of Block Copolymers via Inverse Design Simulations. *Nano Lett.* **2014**, *14*, 318-325.

120. Kim, B. H.; Choi, Y.; Kim, J. Y.; Shin, H.; Kim, S.; Son, S.-W.; Kim, S. O.; Kim, P. Wrinkle-Directed Self-Assembly of Block Copolymers for Aligning of Nanowire Arrays. *Adv. Mater.* **2014**, *26*, 4665-4670.

121. Dobriyal, P.; Xiang, H.; Kazuyuki, M.; Chen, J.-T.; Jinnai, H.; Russell, T. P. Cylindrically Confined Diblock Copolymers. *Macromolecules* **2009**, *42*, 9082-9088.

122. He, X.; Song, M.; Liang, H.; Pan, C. Self-Assembly of the Symmetric Diblock Copolymer in a Confined State: Monte Carlo Simulation. *J. Chem. Phys.* **2001**, *114*, 10510-10513.

123. Sevink, G. J. A.; Zvelindovsky, A. V.; Fraaije, J. G. E. M.; Huinink, H. P. Morphology of Symmetric Block Copolymer in a Cylindrical Pore. *J. Chem. Phys.* **2001**, *115*, 8226-8230.

124. Shin, K.; Xiang, H.; Moon, S. I.; Kim, T.; McCarthy, T. J.; Russell, T. P. Curving and Frustrating Flatland. *Science* **2004**, *306*, 76.

125. Wu, Y.; Cheng, G.; Katsov, K.; Sides, S. W.; Wang, J.; Tang, J.; Fredrickson, G. H.; Moskovits, M.; Stucky, G. D. Composite Mesostructures by Nano-Confinement. *Nat. Mater.* **2004**, *3*, 816-822.

126. Xiang, H.; Shin, K.; Kim, T.; Moon, S.; McCarthy, T. J.; Russell, T. P. The Influence of Confinement and Curvature on the Morphology of Block Copolymers. *J. Polym. Sci., Part B: Polym. Phys.* **2005**, *43*, 3377-3383.

127. Xiang, H.; Shin, K.; Kim, T.; Moon, S. I.; McCarthy, T. J.; Russell, T. P. Block Copolymers under Cylindrical Confinement. *Macromolecules* **2004**, *37*, 5660-5664.

128. Xiang, H.; Shin, K.; Kim, T.; Moon, S. I.; McCarthy, T. J.; Russell, T. P. From Cylinders to Helices Upon Confinement. *Macromolecules* **2005**, *38*, 1055-1056.

129. Gabai, R.; Ismach, A.; Joselevich, E. Nanofacet Lithography: A New Bottom-up Approach to Nanopatterning and Nanofabrication by Soft Replication of Spontaneously Faceted Crystal Surfaces. *Adv. Mater.* **2007**, *19*, 1325-1330.

130. Huth, M.; Ritley, K. A.; Oster, J.; Dosch, H.; Adrian, H. Highly Ordered Fe and Nb Stripe Arrays on Facetted A-Al_2o_3 (1010). *Adv. Funct. Mater.* **2002**, *12*, 333-338.

131. Song, S.; Mochrie, S. G. J. Attractive Step-Step Interactions, Tricriticality, and Faceting in the Orientational Phase Diagram of Silicon Surfaces between [113] and [114]. *Phys. Rev. B* **1995**, *51*, 10068-10084.

132. Song, S.; Mochrie, S. G. J.; Stephenson, G. B. Faceting Kinetics of Stepped Si(113) Surfaces: A Time-Resolved X-Ray Scattering Study. *Phys. Rev. Lett.* **1995**, *74*, 5240-5243.

133. Fasolka, M. J.; Harris, D. J.; Mayes, A. M.; Yoon, M.; Mochrie, S. G. J. Observed Substrate Topography-Mediated Lateral Patterning of Diblock Copolymer Films. *Phys. Rev. Lett.* **1997**, *79*, 3018-3021.

134. Rockford, L.; Liu, Y.; Mansky, P.; Russell, T. P.; Yoon, M.; Mochrie, S. G. J. Polymers on Nanoperiodic, Heterogeneous Surfaces. *Phys. Rev. Lett.* **1999**, *82*, 2602-2605.

135. Rockford, L.; Mochrie, S. G. J.; Russell, T. P. Propagation of Nanopatterned Substrate Templated Ordering of Block Copolymers in Thick Films. *Macromolecules* **2001**, *34*, 1487-1492.

136. Park, S.; Lee, D. H.; Xu, J.; Kim, B.; Hong, S. W.; Jeong, U.; Xu, T.; Russell, T. P. Macroscopic 10-Terabit–Per–Square-Inch Arrays from Block Copolymers with Lateral Order. *Science* **2009**, *323*, 1030-1033.

137. Hong, S. W.; Voronov, D. L.; Lee, D. H.; Hexemer, A.; Padmore, H. A.; Xu, T.; Russell, T. P. Controlled Orientation of Block Copolymers on Defect-Free Faceted Surfaces. *Adv. Mater.* **2012**, *24*, 4278-4283.

138. Park, S.; Kim, B.; Yavuzcetin, O.; Tuominen, M. T.; Russell, T. P. Ordering of PS-*b*-P4VP on Patterned Silicon Surfaces. *ACS Nano* **2008**, *2*, 1363-1370.

CHAPTER 2

DIRECTED SELF-ASSEMBLY OF BLOCK COPOLYMER THIN FILMS USING MINIMAL TOPOGRAPHIC PATTERNS

2.1 Introduction

The self-assembly of block copolymers (BCPs) in thin films has received considerable attention for many applications, including bit-patterned media[1] and the generation of lithographic masks,[2] due to the formation of highly ordered arrays of nanoscopic microdomains, like lamellae, cylinders, or spheres.[3] However, without the use of an external field to bias the assembly, long-range lateral order is lacking with grains of ordered BCP nanostructures typically only several microns in size, which limits many practical applications.[4] To overcome this issue, a number of strategies to direct the self-assembly, so-called directed self-assembly (DSA) methods, have been developed.[5-8] Among them, graphoepitaxy, i.e. the use of topographically patterned substrates, is one of the most widely used techniques.[9-21] In this approach, the topographic patterns typically have a confinement depth (*D*) that is comparable to or larger than the domain spacing of BCPs (L_0), so that the microdomains in films with thicknesses of one period or less can be trapped within confinement regions and lateral order can be controlled with relative ease. In this case, previous studies have shown that one of the key factors in controlling the lateral ordering is the confining edge.[22-24] For example, Kramer and coworkers observed

[†]This chapter has been adapted with permission from J. Choi, J. Huh, K.R. Carter, and T.P. Russell, "Directed Self-Assembly of Block Copolymer Thin Films Using Minimal Topographic Patterns", *ACS Nano*, **2016**, *10*, 7915-7925. Copyright (2016) American Chemical Society.

that the confining edge, that is, the sidewall of the trench, imparted both orientational and translational order to hexagonal arrays of sphere microdomains, but the influence of the confining edge on lateral ordering decayed with increasing distance from the edge, resulting in poor ordering near the middle of the confinement.[22, 23] As a result, the final grain size of BCP microdomains is limited by the confinement width (W). To overcome this limitation, chemically patterned substrates[25-29] or a combination of topographic patterning with the epitaxial self-assembly[30] have been developed, so that the grain size can be increased to 100 μm by 100 μm.[26, 29] In an alternative approach, several types of minimal topographic patterns, such as shallow trenches,[31, 32] dot patterns with low-topography,[33, 34] or sinusoidal patterns[35] have been used in the DSA process. Compared to using the typical topographic patterns, the use of minimal topographic patterns can increase the final grain size of the microdomains by several orders of magnitude because the confinement D is much less than L_0, allowing BCP microdomains to span across the patterned surface. More recently, some research groups have reported the combination of minimal topographic patterns (shallow trenches) with chemoepitaxy to overcome the patterning resolution challenges.[36, 37] However, the unanswered questions still remain in the field of the DSA process using minimal topographic patterns. Previously, we have shown that the sapphire faceted substrates can direct the self-assembly of cylinder-forming BCP thin films, producing highly ordered hexagonal arrays[38] or unidirectionally aligned line patterns[39] over macroscopic length scales. This sapphire faceted substrate is one type of the minimal topographic patterns because the amplitudes of the facets, that is, the confinement D, are much less than L_0. However, the major drawback of using this substrate is the difficulty of understanding the underlying guiding mechanism, in terms of the

commensurability between the pattern dimensions and L_0 due to the distribution of the amplitudes and the pitches of the facets.

Here, we present a novel approach to study the minimum amount of topographic patterning necessary to successfully guide the self-assembly of cylinder-forming BCP thin films. Minimal single trench patterns with different *W* and *D* were used to investigate the propagation of order of BCP microdomains away from the confining edge. Upon thermal annealing, the important observation was the propagation of hexagonal arrays of cylindrical microdomains oriented normal to the film surface away from the edges of a single trench. This propagation of the hexagonal arrays can be attributed to the gradient in the film thickness from the edges of the minimal single trench. Based on these results, we fabricated the minimally patterned trench surfaces by integration of the minimal single trench patterns with varying the pitch (*P*) of the trench that can be used to generate highly ordered hexagonal arrays over large areas. Moreover, we produced line patterns of cylindrical microdomains oriented parallel to the film surface by using solvent vapor annealing (SVA) on the minimally patterned trench surfaces for comparison.

2.2 Experimental Methods

2.2.1 Fabrication of Minimal Single Trench Patterns

Si (100) wafers (International Wafer Service, Inc.) with a 2 nm native oxide layer were cleaned in acetone under sonication, followed by rinsing with isopropyl alcohol (IPA) and then, blown dry with nitrogen. Poly(methyl methacrylate) (PMMA) photoresist (950 kg mol^{-1}, Microchem Corp.) films with the thickness of 150 nm were prepared by spin-

coating onto the silicon substrate and then, baked at 180 °C for 3 min. A total of 16 single trench patterns were exposed on the PMMA photoresist using EBL (JEOL JSM-7001F FESEM with JC Nabity nanometer pattern generation system) with an accelerating voltage of 30 kV, a beam current of 28 pA – 35 pA, and an area dose of 110 $\mu C\ cm^{-2}$ – 220 $\mu C\ cm^{-2}$. All exposed patterns were developed in a 2:1 (v/v) mixture of IPA and methyl isobutyl ketone for 1 min, rinsed in IPA for 1 min, followed by thoroughly rinsing in running deionized water for 30 s and then, blown dry with nitrogen. After development, ICP-RIE (Trion Phantom III) with O_2 plasma (21 W ICP, 26 W RIE, 100 mTorr, 35 sccm O_2) was used to remove resist residues and then, CF_4 plasma treatment (27 W ICP, 39 W RIE, 12 mTorr, 40 sccm CF_4) was performed to transfer the single trench patterns to the underlying silicon substrate. After pattern transfer, the residual PMMA photoresist was removed in acetone under sonication, followed by O_2 plasma treatment (320 W ICP, 107 W RIE, 250 mTorr, 49 sccm O_2).

2.2.2 Fabrication of Minimally Patterned Trench Surfaces

The minimally patterned trench surfaces were also fabricated in the same fashion as the single trench patterns with an adjustment to the EBL operating conditions: an accelerating voltage of 30 kV, a beam current of 25 pA – 88 pA, and an area dose of 145 $\mu C\ cm^{-2}$ – 435 $\mu C\ cm^{-2}$ were used. The size of each patterned surface was 100 μm by 100 μm.

2.2.3 DSA of BCP Thin Films Under Thermal Annealing

Both the minimal single trench patterns and minimally patterned trench surfaces were cleaned with the carbon dioxide snow jet, followed by UV-Ozone cleaning (UVO Cleaner Model 342, Jelight Company Inc.). PS-*b*-PEO (M_n = 20.0 kg mol^{-1} for PS block and M_n = 6.5 kg mol^{-1} for PEO block, PDI = 1.06) was purchased from Polymer Source, Inc. and used as received. PS-*b*-PEO thin films were prepared by spin-coating from 0.8 % (wt/v) PS-*b*-PEO solution in benzene onto the minimal single trench patterns or minimally patterned trench surfaces. Subsequently, the samples were annealed at 150 °C under vacuum for 1 day. Prior to thermal annealing, the thicknesses of PS-*b*-PEO films on the flat silicon substrate were ~39 nm, as measured by the ellipsometer (Model LSE, Gaertner Scientific Corp.).

2.2.4 DSA of BCP Thin Films Under Solvent Vapor Annealing

PS-*b*-PEO thin films were prepared by spin-coating from 0.8 % (wt/v) PS-*b*-PEO solution in benzene onto the minimally patterned trench surfaces. Before SVA, the film thicknesses on the flat silicon substrate were ~39 nm, as measured by the ellipsometer. SVA was performed in the sealed jar (volume of the jar = 46.5 cm^3, surface area of THF = 12.6 cm^2, and surface area of water = 1.3 cm^2) at room temperature. The PS-*b*-PEO thin films were pre-swollen in water vapor for 10 min to avoid dewetting, followed by SVA with THF and water vapor environment for 60 min. The in-situ thickness of the PS-*b*-PEO film on the flat silicon substrate during solvent vapor annealing (SVA) was monitored using the reflectometer (F20-UV, FILMETRICS Inc.).

2.2.5 Characterization

The morphologies of PS-*b*-PEO thin films on the minimal topographic patterns were investigated by scanning force microscopy (SFM, Dimension 3100, Digital Instruments) operated in the tapping mode. The SFM tip has a pyramidal shape with a nominal radius of curvature of ~6 nm at the tip apex. Scanning electron microscopy (SEM) images of the minimally patterned trench surfaces were obtained using JEOL JSM-7001F FESEM operated with an acceleration voltage of 5 kV and 10 kV.

To measure L_0 of the PS-*b*-PEO in the bulk, small angle X-ray scattering (SAXS) measurements were done at the University of Massachusetts, Amherst using an in-house setup from Molecular Metrology Inc. It uses a 30 W microsource (Bede) with a 30 μm by 30 μm spot size matched to a Maxflux optical system (Osmic) leading to a low-divergence beam of monochromatic CuKα radiation (wavelength λ = 0.1542 nm). For the preparation of SAXS samples, 10 wt % of PS-*b*-PEO solution in benzene was immersed in liquid nitrogen for 10 s and then, moved to a vacuum oven quickly. After drying at room temperature for 20 h, the sample was annealed at 150 °C under vacuum for 1 day and then, slowly cooled to room temperature. This bulk sample of the PS-*b*-PEO was collected onto a Kapton film.

To investigate the propagation surface distances of hexagonal arrays and height variation across the single trenches, two SFM images, 3 μm by 3 μm in size, were randomly taken from each sample (single trench patterns from No. 1 to 16). These images were analyzed using Image-Pro Plus (Media Cybernetics) and NanoScope Analysis (Bruker Corp.) software. The defect density of line patterns on the minimally patterned trench surfaces was measured using ImageJ software. To do this, six SFM images, 5 μm by 5 μm

in size, were randomly selected from each sample. For the colorized grain maps of line patterns, SFM images were processed using MATLAB (MathWorks) and Image-Pro Plus (Media Cybernetics). The line edge roughness (LER) of the minimal single trench patterns and minimally patterned trench surfaces was analyzed using SuMMIT software (EUV Technology).

2.3 Results and Discussion

2.3.1 DSA of BCP Thin films on Minimal Single Trench Patterns

We first examined the self-assembly behavior of cylinder-forming poly(styrene-*b*-ethylene oxide) PS-*b*-PEO (M_n = 20.0 kg mol^{-1} for PS block and M_n = 6.5 kg mol^{-1} for PEO block) thin films on minimal single trench patterns. In the bulk, the observed L_0 of PS-*b*-PEO was 26.8 nm (Figure 2.1). Figure 2.2 shows the schematic illustration of the procedure for the DSA of PS-*b*-PEO thin films. Using electron-beam lithography (EBL) and inductively coupled plasma reactive ion etching (ICP-RIE), we fabricated minimal single trench patterns, with $D < L_0$ in all cases, on the same silicon substrate having a native oxide layer to maintain the same experimental conditions such as the annealing temperature and the initial film thickness (Figure 2.2a). Next, PS-*b*-PEO thin films were prepared by spin-coating from benzene solutions onto single trench patterns and subsequently annealed at 150 °C under vacuum for 1 day (Figure 2.2b). The thicknesses of the films were ~39 nm ($1.46L_0$), as measured on a flat silicon substrate prior to thermal annealing. After thermal annealing, the films showed two distinct regions of cylindrical microdomains associated

with the underlying single trench pattern. This is shown in Figure 2.2d, an enlargement of the dashed red square in Figure 2.2c: (1) a single trench region and (2) a propagation region.

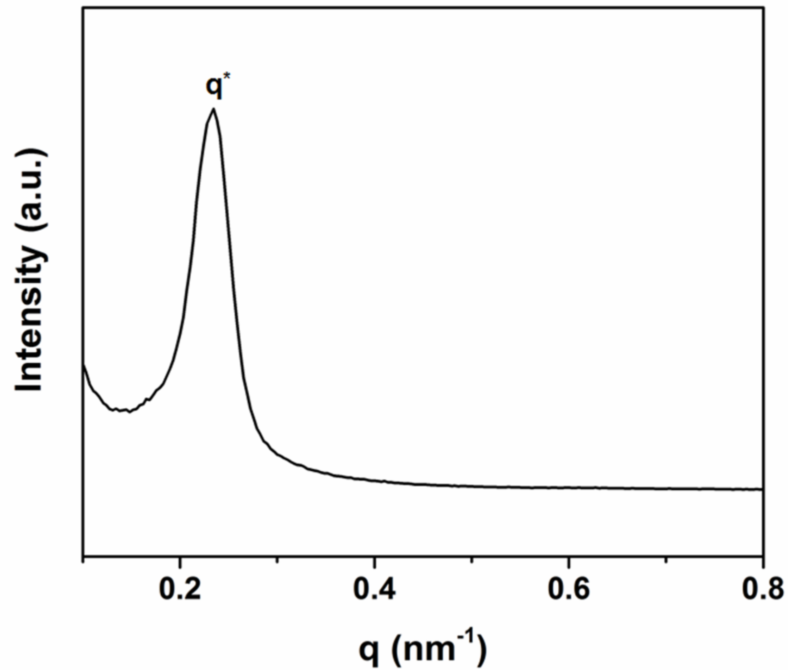

Figure 2.1 SAXS profile of PS-*b*-PEO. The scattering from PS-*b*-PEO showed a first-order reflection at $q^* = 0.2346$ nm^{-1}, corresponding to the domain spacing ($L_0 = 2\pi/q^*$) of 26.8 nm. It is noted that the SAXS intensity showed the absence of higher-order peaks.

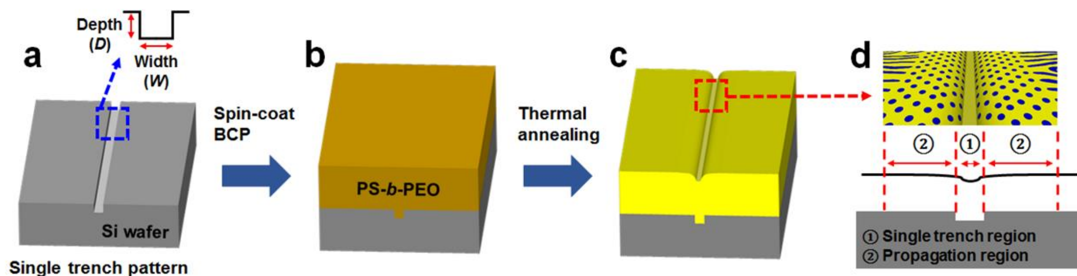

Figure 2.2 Schematic illustration of the DSA of BCP thin films on minimal single trench patterns. (a) Minimal single trench patterns were fabricated on the silicon substrate with a native oxide layer. The blue dashed square indicates the defined *W* and *D* of the trench. (b) PS-*b*-PEO thin films were prepared by spin-coating and then, thermally annealed at 150 °C under vacuum for 1 day. (c) Thermally annealed PS-*b*-PEO thin films showed two distinct regions of cylindrical microdomains across the single trench patterns. (d) Schematic cross-sectional illustration of the two distinct regions from the red square in (c).

Figure 2.3a–c show representative scanning force microscopy (SFM) phase (first row) and height (second row) images, and height profiles (third row) of thermally annealed PS-*b*-PEO thin films under the same annealing conditions on the single trench patterns with different *W* and *D*. As shown in the phase images (first row in Figure 2.3a–c), the PS-*b*-PEO thin films produced two distinct regions of cylindrical microdomains over each single trench, as shown in the schematic illustration in Figure 2.2d. The first was in the single trench, where cylindrical microdomains showed different orientations: perpendicular (Figure 2.3a, $W = 2.69L_0$, $D = 0.31L_0$), a mixture of perpendicular and parallel (Figure 2.3b, $W = 3.90L_0$, $D = 0.56L_0$), and parallel (Figure 2.3c, $W = 10.10L_0$, D = $0.55L_0$), depending on *W* and *D*. In the SFM phase images, the brighter and darker areas correspond to PS and PEO microdomains, respectively. Each inset shows a magnified image of the cylindrical microdomains in the single trench (blue region). The observed different orientations as a function of *W* and *D* are summarized in Table 2.1. It is noted that the fabricated single

trenches were designated as No. 1 to 16 (Figure 2.4 and Table 2.2), where our attempts to vary *D* with fixing *W* were unsuccessful due to our lithographic limitations. As seen in Table 2.1, for No. 1 and 2, cylindrical microdomains in the trench showed perpendicular orientation. Interestingly, for No. 3 to 8, cylindrical microdomains in the trench had a mixture of orientations, but, for No. 9 to 16, cylindrical microdomains with parallel orientation were observed in the trench. Indeed, in the case of cylindrical microdomains confined within trenches, a number of factors, such as the time of thermal annealing with the trench dimensions,[40] the interplay of the film thickness and surface wetting characteristics,[41] and the film thickness variations caused by the different trench dimensions,[42, 43] can influence the orientation of cylindrical microdomains. In particular, as thermal annealing proceeds, there is continuous decrease in the thickness of BCP films across the trench pattern, namely, at the center of the trench, near the sidewall, and on the mesa due to the simultaneous process of the polymer flowing from the mesas into the trench and evaporation of the trapped solvent.[42] On the basis of these factors, in our study, the change in the orientation of cylindrical microdomains can be thought of as a consequence of variation in thickness of the films in the single trench regions. Since both *W* and *D* were varied at the same time for 16 single trenches, the film thicknesses within the single trenches could be allowed to approach the critical film thickness that favors perpendicular (No. 1 and 2), a mixed of perpendicular and parallel (No. 3 to 8), or parallel (No. 9 to 16) orientation. All SFM images of thermally annealed PS-*b*-PEO thin films on minimal single trench patterns are shown in Figure 2.5 and 2.6.

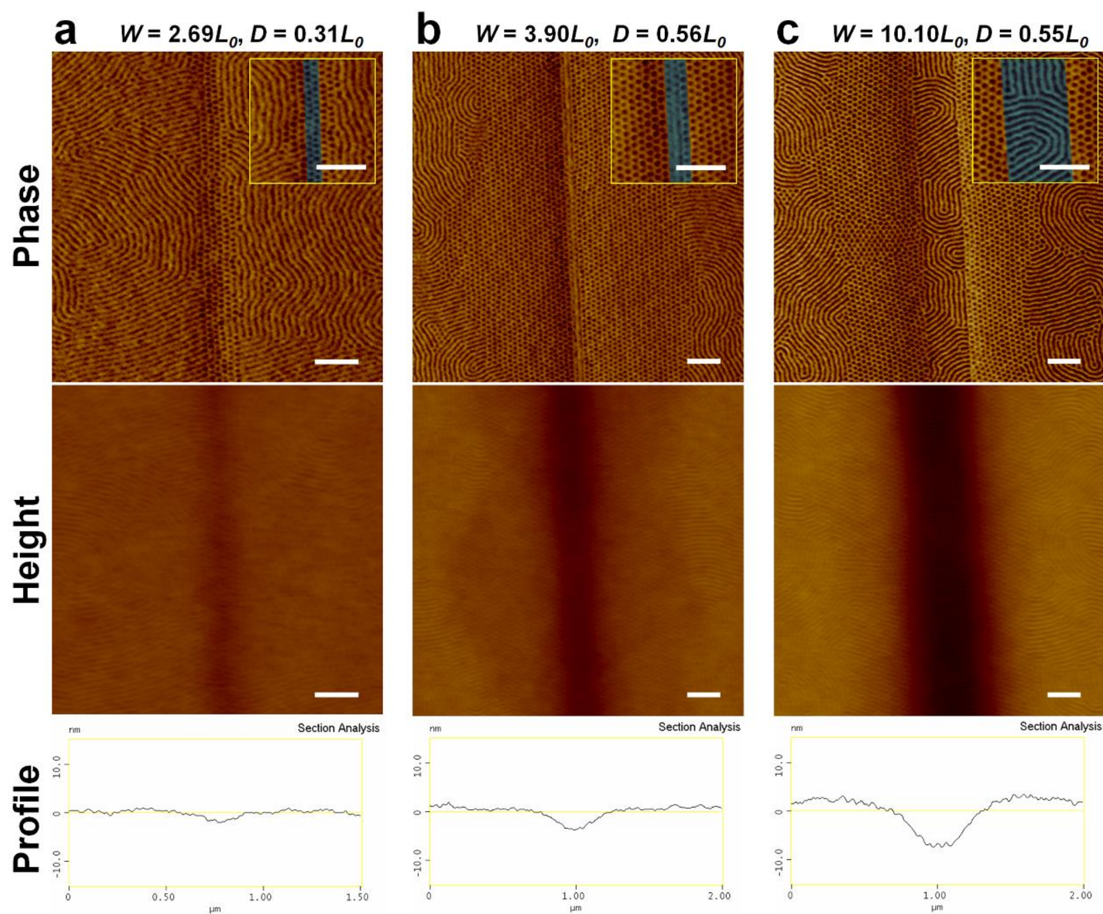

Figure 2.3 Directed BCP thin films on minimal single trench patterns. (a–c) First row shows representative SFM phase images of thermally annealed PS-b-PEO thin films on minimal single trench patterns with different *W* and *D*. Each inset shows a magnified image of cylindrical microdomains in the single trench (blue region), exhibiting perpendicular (a), a mixture of perpendicular and parallel (b), and parallel (c) orientation. The second row presents respective SFM height images of the first row. Scale bars, 200 nm. The third row corresponds to respective height profiles of the second row.

Table 2.1 Orientation of cylindrical microdomains in the single trench region for 16 different trench dimensions.

No.	W (nm)	D (nm)	Orientation
1	$2.52L_0$	$0.20L_0$	perpendicular
2	$2.69L_0$	$0.31L_0$	
3	$3.32L_0$	$0.35L_0$	a mixed of perpendicular and parallel
4	$3.62L_0$	$0.50L_0$	
5	$3.75L_0$	$0.54L_0$	
6	$3.77L_0$	$0.47L_0$	
7	$3.80L_0$	$0.52L_0$	
8	$3.90L_0$	$0.56L_0$	
9	$4.04L_0$	$0.45L_0$	parallel
10	$4.41L_0$	$0.47L_0$	
11	$6.57L_0$	$0.55L_0$	
12	$7.47L_0$	$0.56L_0$	
13	$8.27L_0$	$0.56L_0$	
14	$8.85L_0$	$0.54L_0$	
15	$9.52L_0$	$0.55L_0$	
16	$10.10L_0$	$0.55L_0$	

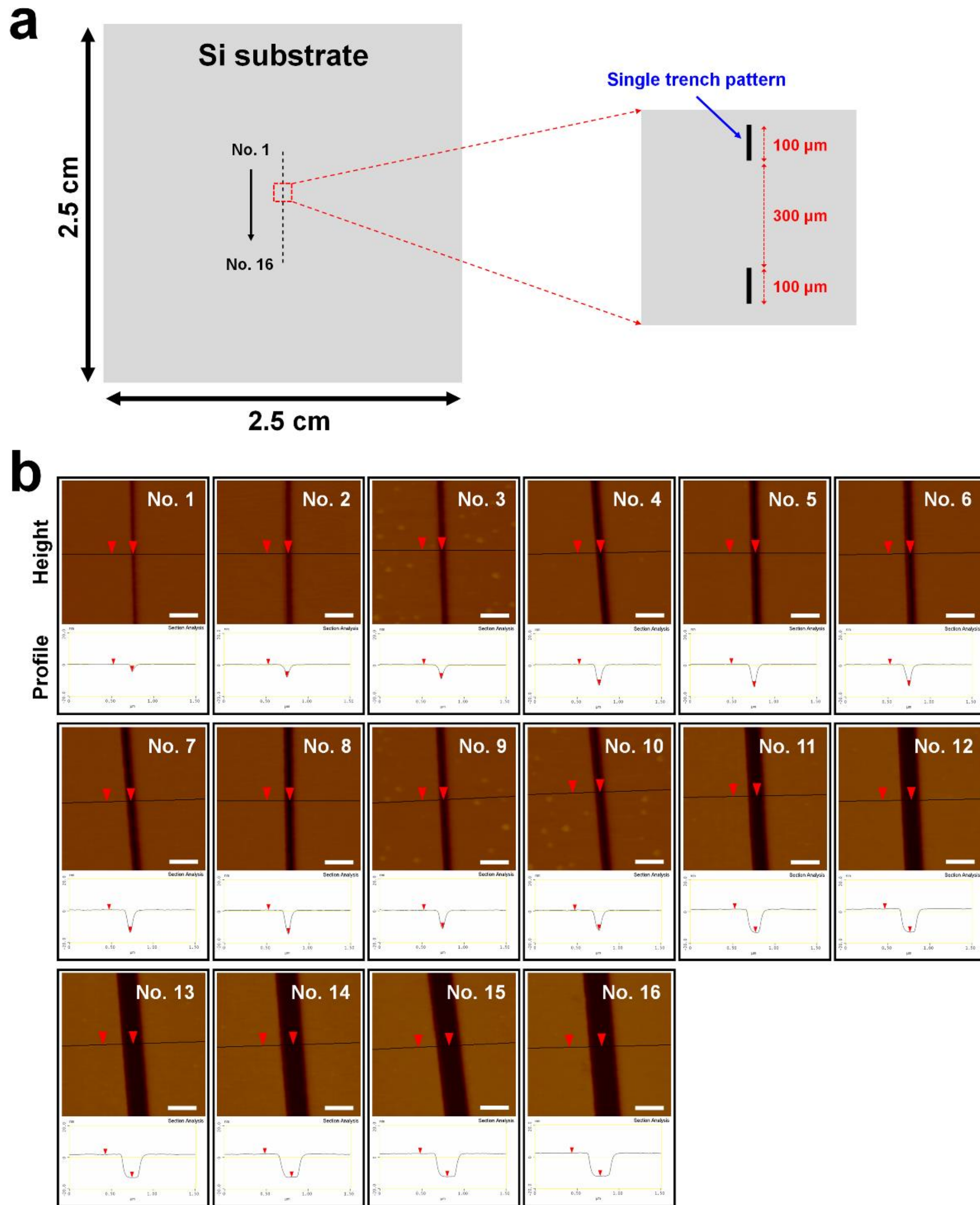

Figure 2.4 Demonstration of minimal single trench patterns. (a) A total of 16 single trench patterns were fabricated on the same silicon substrate having a native oxide layer and designated as No. 1 to 16. The length of each pattern was 100 μm. The separation distance between the patterns was 300 μm. (b) SFM height images and height profiles of the single trench patterns. W and D of each pattern were measured by SFM and listed in Table 2.2. Scale bars, 300 nm.

Table 2.2 Characteristics of minimal single trench patterns, with gradual increases in W and D, with $D < L_0$ in all cases. We note that the W was measured near the top of the trench. To analyze line edge roughness (LER) using SFM images, SuMMIT software was used.

No.	***W* (nm)**	***D* (nm)**	**LER (nm) of single trench**
1	67.6 (2.52L_0)	5.4 (0.20L_0)	6.40
2	72.0 (2.69L_0)	8.3 (0.31L_0)	6.08
3	88.9 (3.32L_0)	9.5 (0.35L_0)	5.01
4	97.1 (3.62L_0)	13.5 (0.50L_0)	3.81
5	100.6 (3.75L_0)	14.6 (0.54L_0)	3.68
6	101.0 (3.77L_0)	12.6 (0.47L_0)	4.68
7	101.8 (3.80L_0)	14.0 (0.52L_0)	4.48
8	104.4 (3.90L_0)	14.9 (0.56L_0)	4.39
9	108.2 (4.04L_0)	12.1 (0.45L_0)	3.78
10	118.1 (4.41L_0)	12.6 (0.47L_0)	3.32
11	176.1 (6.57L_0)	14.7 (0.55L_0)	3.71
12	200.1 (7.47L_0)	14.9 (0.56L_0)	2.81
13	221.6 (8.27L_0)	15.0 (0.56L_0)	3.26
14	237.2 (8.85L_0)	14.6 (0.54L_0)	3.93
15	255.1 (9.52L_0)	14.7 (0.55L_0)	4.81
16	270.7 (10.10L_0)	14.8 (0.55L_0)	4.30

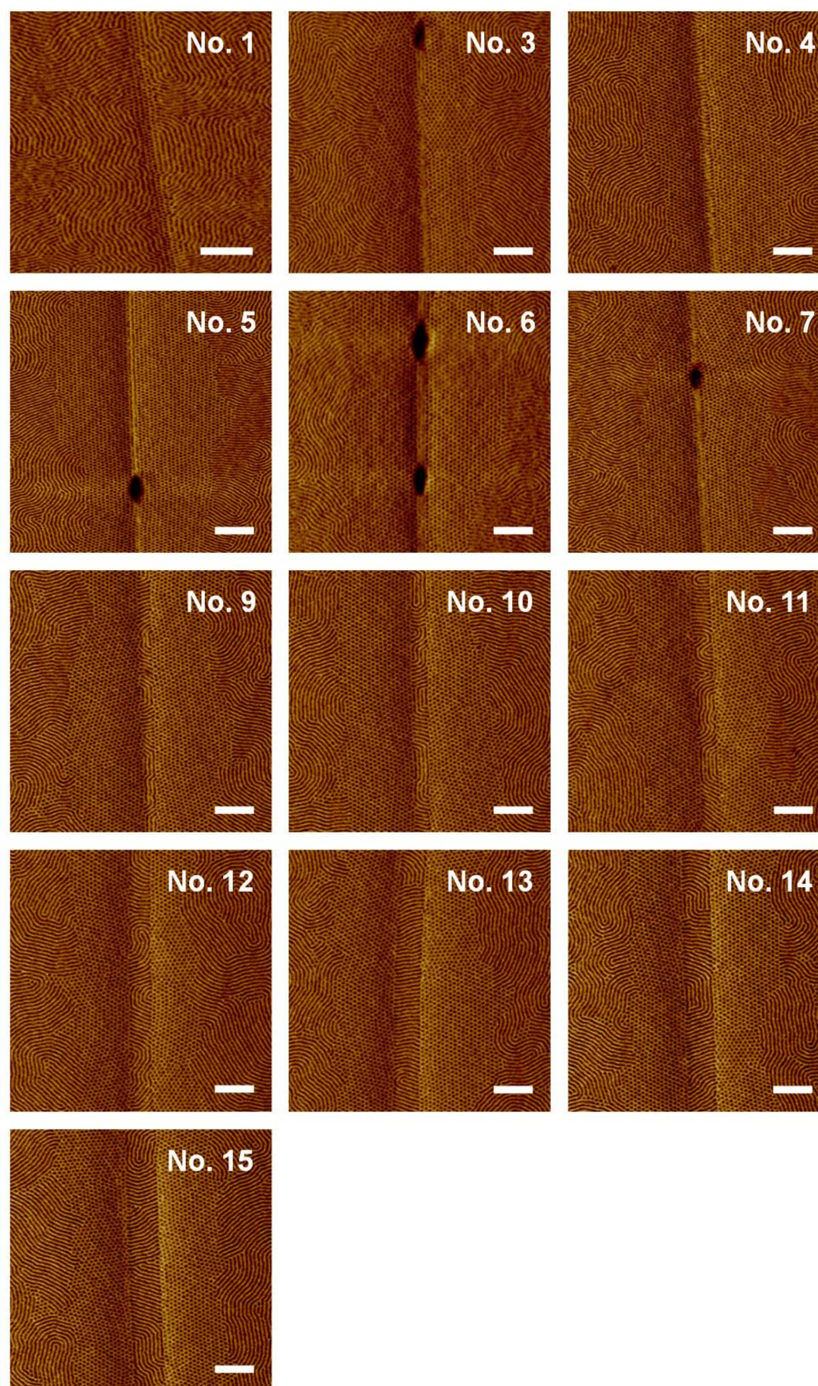

Figure 2.5 SFM phase images of thermally annealed PS-*b*-PEO thin films on minimal single trench patterns with different *W* and *D*. Samples of No. 2, 8, and 16 are shown in Figure 2.3a–c (phase images), respectively. In the single trench region, cylindrical microdomains showed perpendicular (No. 1), a mixture of perpendicular and parallel (No. 3 to 7), or parallel (No. 9 to 15) orientation. Scale bars, 300 nm.

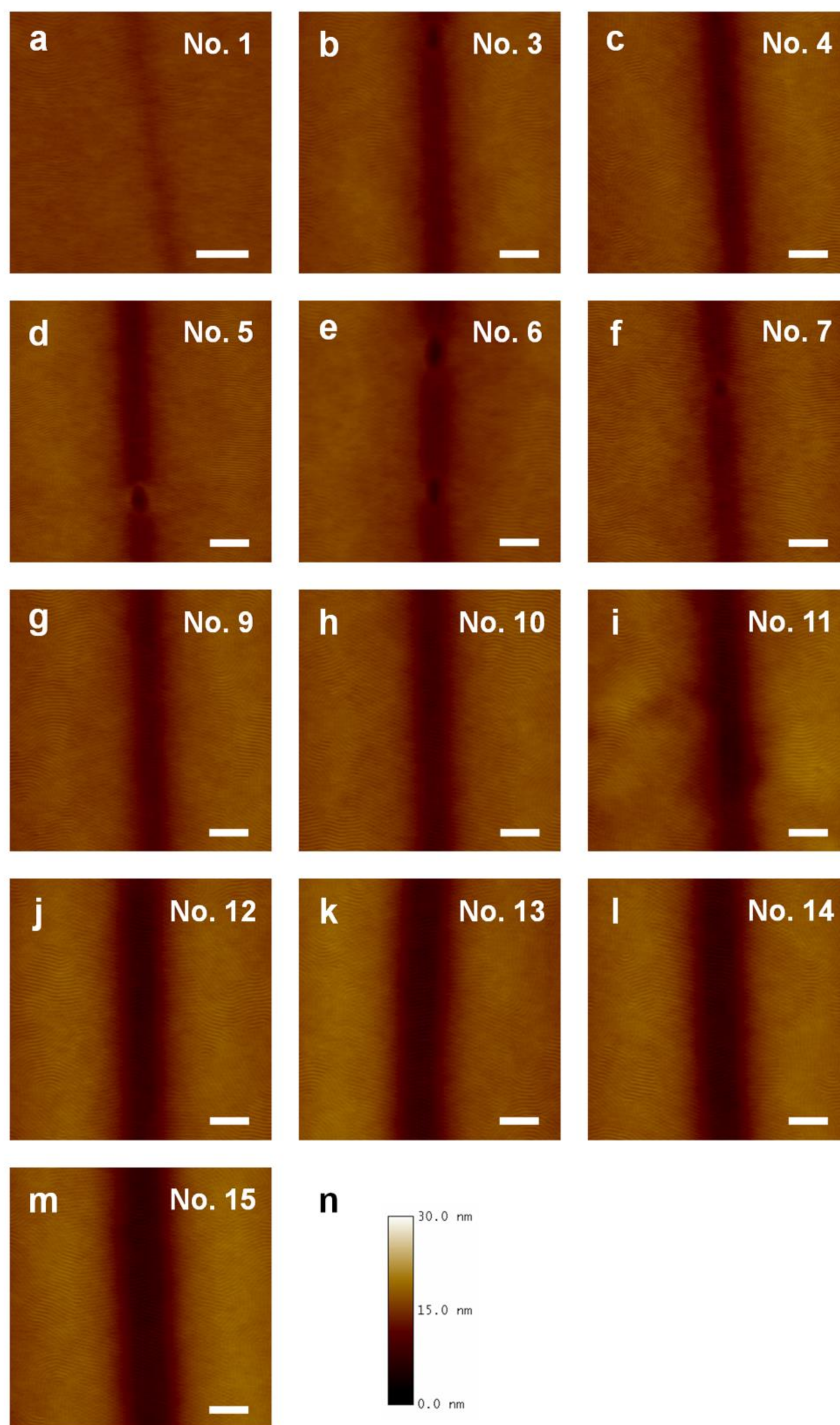

Figure 2.6 (a–m) SFM height images of thermally annealed PS-*b*-PEO thin films on minimal single trench patterns with different *W* and *D*. Samples of No. 2, 8, and 16 are shown in Figure 2.3a–c (height images), respectively. Scale bars, 300 nm. (n) Data scale of SFM height images in (a–m).

As seen in the phase images of Figure 2.3a–c, another distinct feature was the propagation of the cylindrical microdomains oriented normal to the film surface away from the edges of a single trench to the outside of the trench. Here, the (10) planes of hexagonal arrays were oriented parallel to the direction of the trench. To determine the distance over which this orientation propagates away from the edges of the single trench, two SFM images, 3 μm by 3 μm in size, were randomly selected from each sample (Figure 2.7).

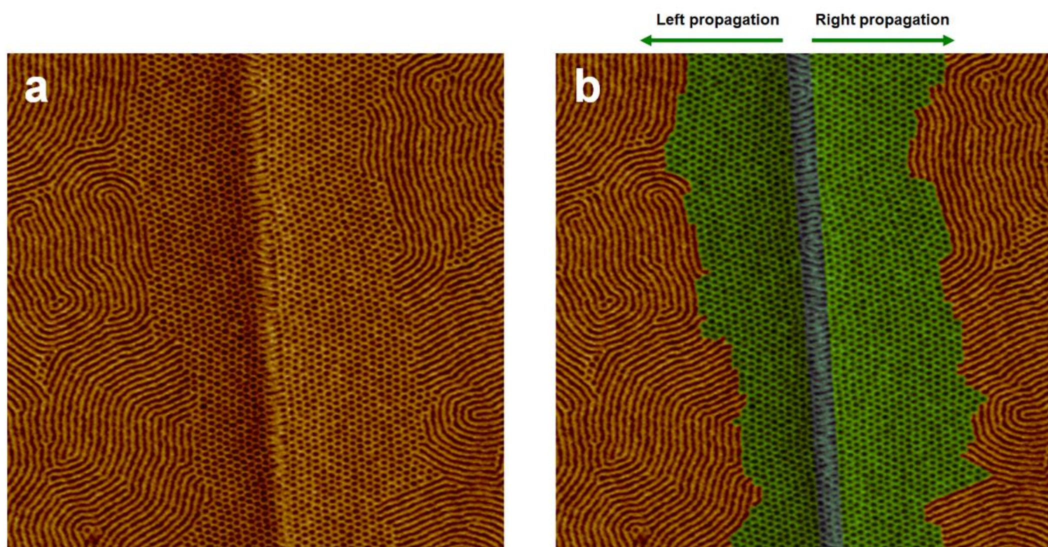

Figure 2.7 Measurement of the propagation distance of cylindrical microdomains oriented normal to the film surface away from the edges of a single trench pattern. (a) Original SFM phase image. (b) Colorized SFM phase image. Blue and green indicate the single trench region and propagation region, respectively. The boundary, where the perpendicular orientation of cylindrical microdomains changes to the parallel orientation after a given distance from the edge of a single trench, is defined as the end of the propagation region. The standard deviation of the measured propagation distance was large, as shown in Figure 2.8a, in particular No. 3 to 16, due to the variation in the propagation distance along the single trench pattern.

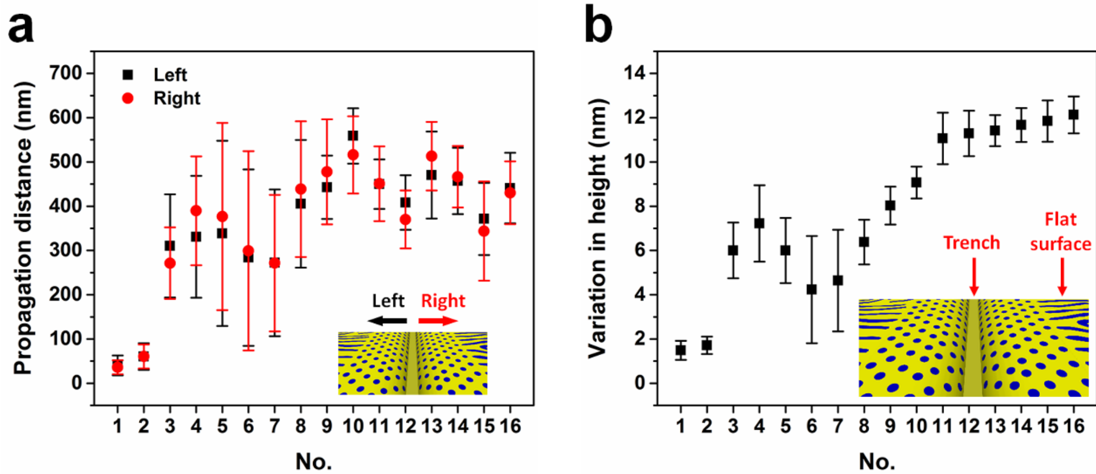

Figure 2.8 Directed BCP thin films on minimal single trench patterns. (a) Propagation surface distance of hexagonal arrays of cylindrical microdomains oriented normal to the film surface away from the edges of a single trench. (b) Measured variation in height between the middle of the single trench region and flat surface. The *x*-axis in (a) and (b) shows the designated single trench patterns from Nos. 1 to 16.

As shown in Figure 2.8a, in the case of No. 1 and 2, they showed nearly the same propagation distance (left (black square) and right (red circle)), but, in the case of No. 3 through 16, the propagation distance was markedly increased with showing large deviations. From the height images and profiles (second and third row in Figure 2.3a–c), it is seen that the underlying single trench patterns led to variation in the thickness of PS-*b*-PEO films across the trenches without a breakage in the films, due to the minimal geometry of the trench ($D < L_0$), so that the surfaces of the films were not flat. To measure the variation in height between the middle of the single trench region and the flat surface, two SFM images, 3μm by 3 μm in size, were taken from each sample. As shown in Figure 2.8b, for No. 1 and 2 (relatively small trench dimensions), the variation between the two regions was less than ~2 nm. Interestingly, the variation abruptly increased to ~6 nm for No. 3 and showed fluctuations between No. 3 to 8, whereas, between No. 9 to 16, the variation

gradually increased. In all cases, these variations can be attributed to the polymer flowing from the outside of the trench into the single trench region due to the increased mobility of the polymer and capillary action during thermal annealing.[44-46] It should be noted that the orientation of the cylindrical microdomains in BCP thin films is very sensitive to the film thickness.[47, 48] Therefore, the observed propagation of cylindrical microdomains oriented normal to the film surface away from the edges of the single trench is related to the gradient in the film thickness from the edges of the trench (height profiles in Figure 2.3a–c). In other words, with decreasing the film thickness from the outside of the trench to near the edges of the single trench, the orientation of cylindrical microdomains changes from parallel to perpendicular due to frustration arising from the incommensurability between the film thickness and L_0. This observation agrees well with the thickness-induced transition in the orientation of cylindrical microdomains in poly(styrene-*b*-methyl methacrylate) (PS-*b*-PMMA) thin films at the edge of island structures.[49] Also, similar effects of the film thickness on the abrupt transition in the orientation of cylindrical microdomains were reported on PS-*b*-PMMA films confined within the deep trench patterns[43, 44, 50] and near the nanoparticles embedded in PS-*b*-PMMA thin films.[51] However, we note that the relationship between the propagation distance of hexagonal arrays and the gradient in the film thickness remains unclear.

Based on observations in the minimal single trench experiments, the propagated hexagonal arrays of cylindrical microdomains away from the edges of the single trenches were predicted to overlap at a minimum separation distance between two parallel single trenches, generating hexagonal arrays over large areas without producing cylindrical microdomains oriented parallel to the film surface. To do this, cylindrical microdomains

in the single trench regions must be oriented normal to the film surface. The minimal change in height between the single trench region and the flat surface is necessary, since a large change in height near the edge of the trench can produce a grain boundary.[22] As a result, the conditions of pattern No. 1 and 2 can be regarded as a target to design minimally patterned trench surfaces by varying *P* of the trench. The minimum *P* was determined to be ~150 nm by considering the propagation distances (left and right) of pattern No. 1 and 2 in Figure 2.8a. Consequently, we fabricated minimally patterned trench surfaces with four different dimensions (Figure 2.9 and 2.10 and Table 2.3) to validate the predictions. We note that our attempts to vary *P* with fixing both *W* and *D* were unsuccessful due to our lithographic limitation, such as the proximity effect in EBL process.

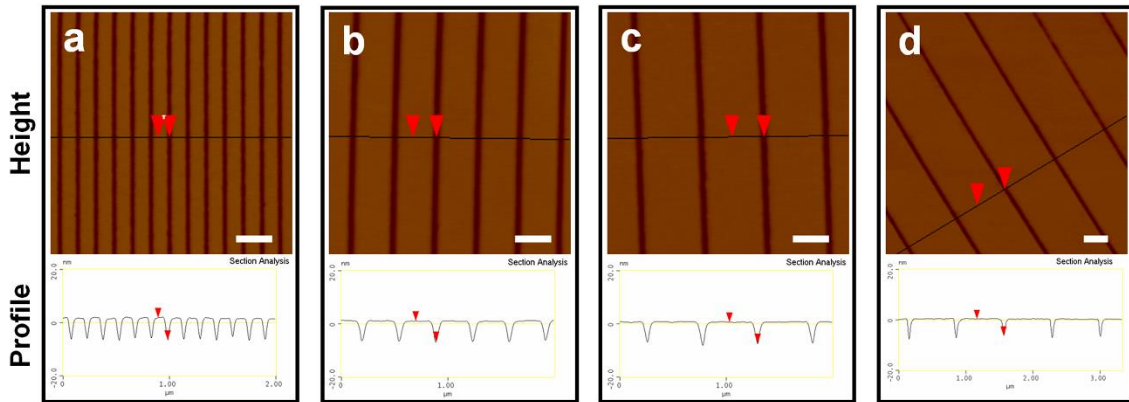

Figure 2.9 SFM height images and height profiles of minimally patterned trench surfaces. *P*, *W* and *D* of each pattern were measured by SFM and listed in Table 2.3. Scale bars, 300 nm.

Table 2.3 Characteristics of minimally patterned trench surfaces used to direct the self-assembly of PS-*b*-PEO thin films. We note that W was measured near the top of the trench. To analyze LER using SFM images, SuMMIT software was used.

	P (nm)	**W (nm)**	**D (nm)**	**LER (nm) of trench**
Figure 2.9a	154 ($5.75L_0$)	33.8 ($1.26L_0$)	8.0 ($0.30L_0$)	4.08
Figure 2.9b	340 ($12.69L_0$)	52.7 ($1.97L_0$)	8.0 ($0.30L_0$)	3.46
Figure 2.9c	505 ($18.84L_0$)	57.8 ($2.16L_0$)	8.0 ($0.30L_0$)	4.52
Figure 2.9d	673 ($25.11L_0$)	48.5 ($1.81L_0$)	6.1 ($0.23L_0$)	8.60

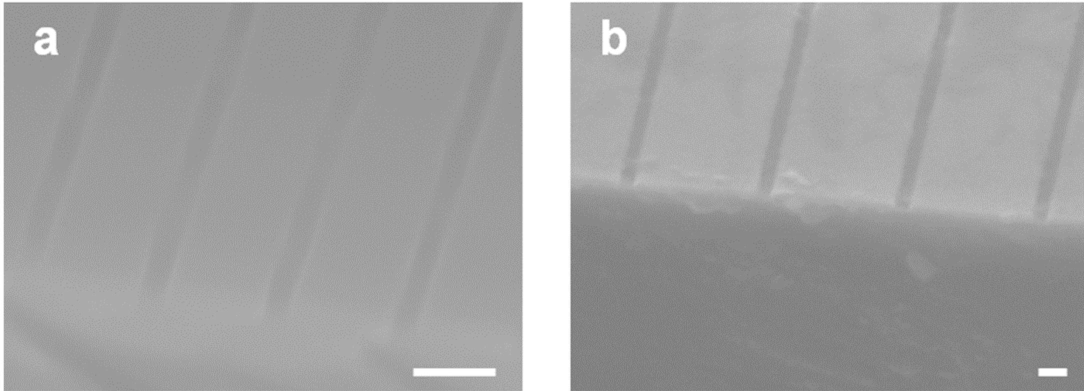

Figure 2.10 Cross-sectional (45° tilted) SEM images of minimally patterned trench surfaces with (a) $P = 5.75L_0$, $W = 1.26L_0$, $D = 0.30L_0$ and (b) $P = 18.84L_0$, $W = 2.16L_0$, $D = 0.30L_0$. Scale bars, 100 nm.

2.3.2 DSA of BCP Thin films on Minimally Patterned Trench Surfaces

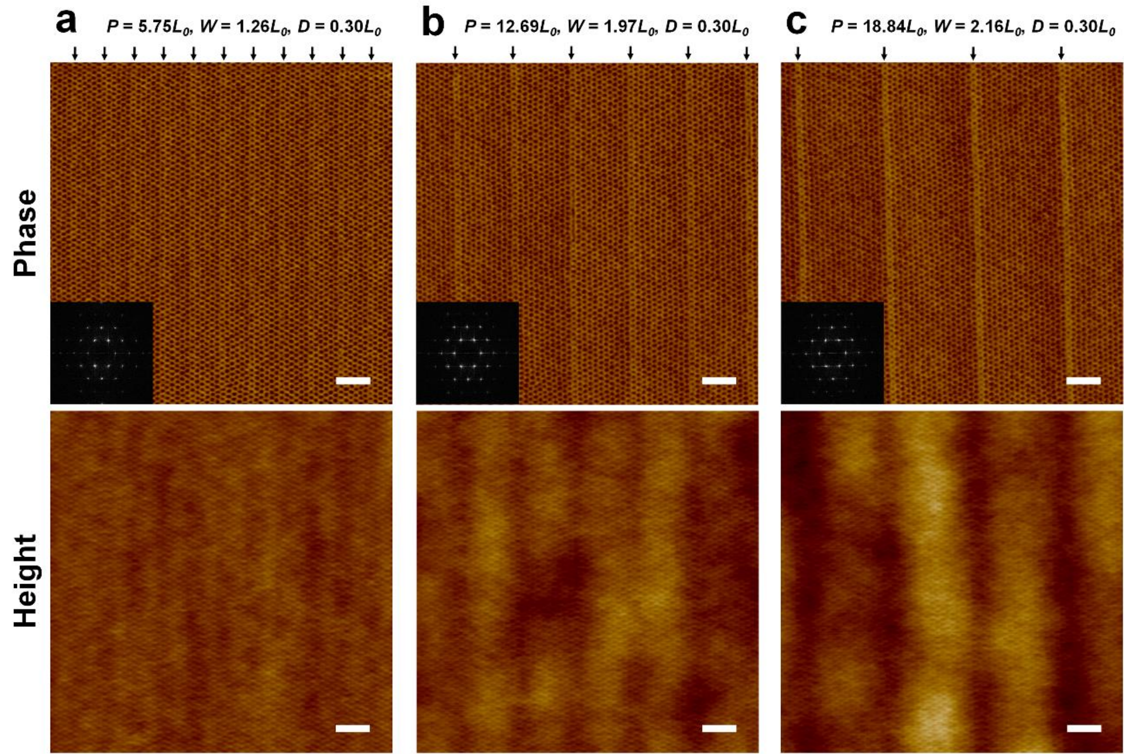

Figure 2.11 Directed BCP thin films on minimally patterned trench surfaces. (a–c) First row shows SFM phase images of thermally annealed PS-*b*-PEO thin films on minimally patterned trench surfaces with different dimensions. The arrows of each image indicate the underlying trenches, where a single row of PEO cylinders oriented normal to the film surface exists. The inset of each image shows the corresponding 2-D FFT. The second row presents respective SFM height images of the first row. Scale bars, 200 nm.

Figure 2.11a–c show SFM phase (first row) and height (second row) images of thermally annealed PS-*b*-PEO thin films on the minimally patterned trench surfaces with $P = 5.75L_0$, $W = 1.26L_0$ (Figure 2.11a), $P = 12.69L_0$, $W = 1.97L_0$ (Figure 2.11b), and $P = 18.84L_0$, $W = 2.16L_0$ (Figure 2.11c), while D was fixed at $0.30L_0$. It is noted that thermal annealing was performed in the same manner as the single trench experiments. As shown in the phase images of Figure 2.11a–c, when P was increased from $5.75L_0$ to $18.84L_0$, the

distance over which the orientation of the cylindrical microdomains normal to the film surface propagated away from the edges of the trench overlapped on the mesas, eventually producing laterally ordered hexagonal arrays with few defects within the entire surfaces of ~100 μm by 100 μm for each sample. This behavior is identical to our prediction and can be related to pattern amplification, where the self-assembly of PS-*b*-PEO amplifies, *i.e*. effectively reduces, the minimum dimension to the repeat period of PEO cylinders, *i.e*. by a factor of 6 (Figure 2.11a), 11 (Figure 2.11b), and 17 (Figure 2.11c), respectively. It was also found that the surfaces of the films (height images in Figure 2.11a–c) were nearly flat, where the root mean square (RMS) roughness was less than 1.0 nm, as shown in Figure 2.12.

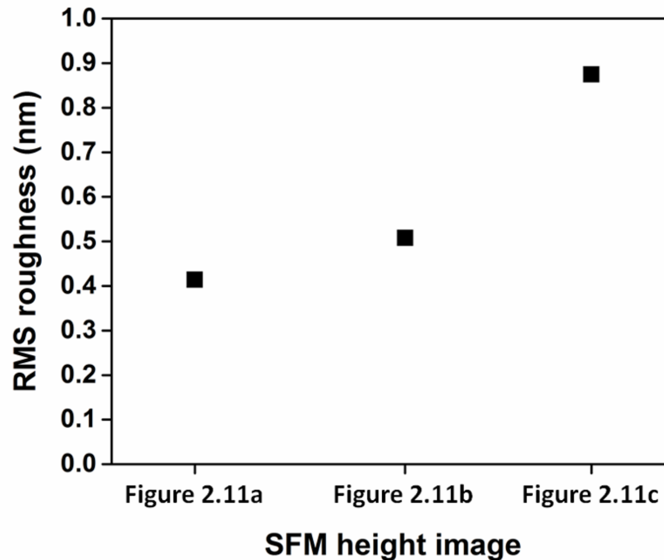

Figure 2.12 RMS roughness of PS-*b*-PEO thin films on the minimally patterned trench surfaces (height images in Figure 2.11a–c, respectively) was measured by SFM. Each measured area was 3 μm by 3 μm.

The 2-D fast Fourier transform (FFT) in the inset of each phase image in Figure 2.11a–c shows not only six sharp first-order peaks, but also multiple higher-order peaks, indicating characteristic of very highly ordered hexagonal arrays of the microdomains. As indicated by arrows in Figure 2.11a–c, it is noteworthy that a single row of PEO cylinders oriented normal to the film surface was formed in the trench regions, while the size of PEO cylinders appeared smaller with increasing W. This smaller size could be attributed to frustration arising from the incommensurability between the W and L_0. The values of W of $1.97L_0$ (Figure 2.11b) and $2.16L_0$ (Figure 2.11c), which are closer to $2L_0$, more favor two rows of PEO cylinders in the trench, but there is only a single row of cylinders, imposing a large chain stretching on the polymer. Therefore, cylindrical microdomains relieve the imposed frustration of chain packing at a given W by decreasing the size of PEO cylinders. Figure 2.13 shows the schematic illustration of the proposed mechanism for the generation of hexagonal arrays of PS-*b*-PEO microdomains over large areas by using the minimally patterned trench surfaces, where P of the minimal single trench is varied.

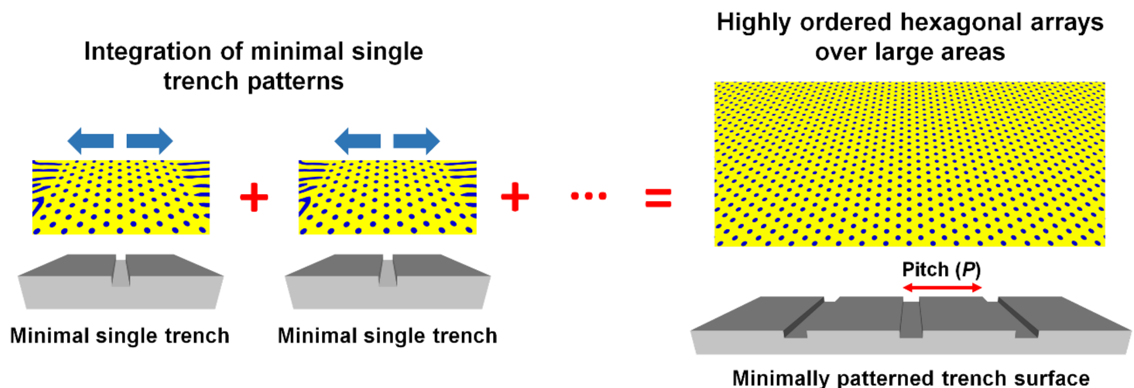

Figure 2.13 Schematic illustration of the proposed mechanism for the generation of laterally ordered hexagonal arrays by using the minimally patterned trench surface.

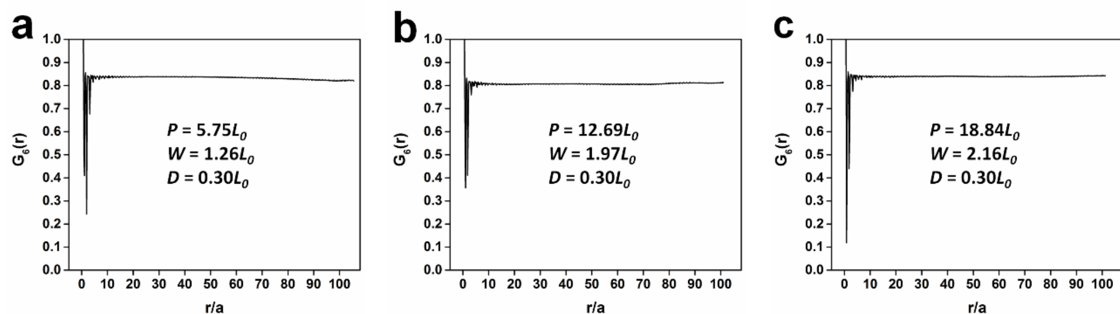

Figure 2.14 (a–c) Orientational correlation function, G_6(r), was calculated from thermally annealed PS-*b*-PEO thin films (phase images in Figure 2.11a–c), where *r* is the distance and *a* is the average domain spacing.

Figure 2.14 show the orientational order of the hexagonal arrays, which was calculated from the SFM phase images in Figure 2.11a–c using the orientational correlation function, G_6(r).[52] The values of G_6(r) are 0.83 (Figure 2.14a), 0.81 (Figure 2.14b), and 0.84 (Figure 2.14c), respectively, where the value of G_6(r) for a perfect hexagonal lattice is 1. Each G_6(r) decays very little (Figure 2.14a) or does not decay (Figure 2.14b and 2.14c) over the average domain spacing of 100, indicating the presence of long-range orientational

order in this range. We also used the translational correlation function, G_T(r),[52] to calculate the translational order of the hexagonal arrays, as shown in Figure 2.15. For the patterned surface with $P = 5.75L_0$, $W = 1.26L_0$, $D = 0.30L_0$ (phase image in Figure 2.11a), the hexagonal arrays showed quasi-long-range translational order over the average domain spacing of 30. It should be noted that thermal drift distortions in SFM images can influence the calculation of translational order.[53]

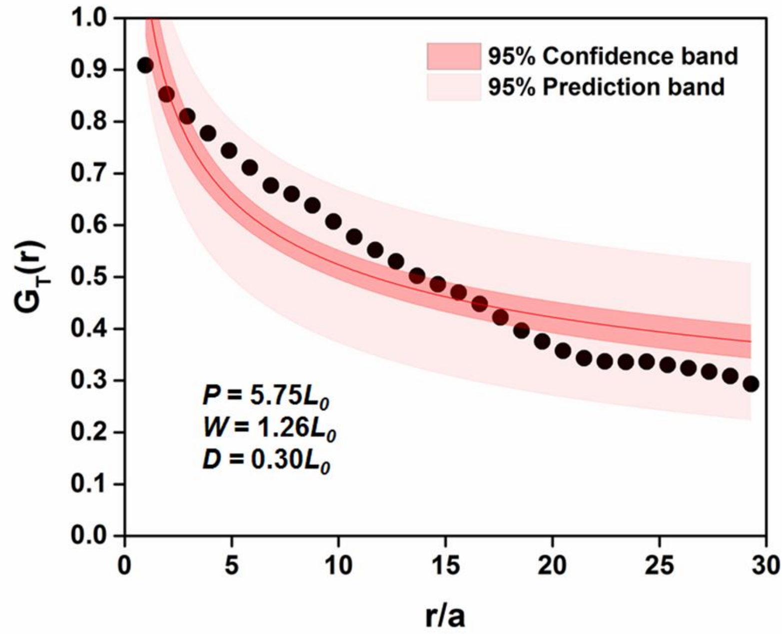

Figure 2.15 Translational correlation function, G_T(r), was calculated from the thermally annealed PS-*b*-PEO thin film (phase image in Figure 2.11a). A real 2D crystal will have quasi-long-range translational order that can be described by $G_T(r) \propto \left(\frac{r}{a}\right)^{-\eta_T}$, where r is the distance, a is the average domain spacing, and η_T is the fitting parameter. In the case of the ordered crystal phase, the value of η_T will be in the range of 0.25 to 0.33. For the hexagonal arrays on the patterned surface with $P = 5.75L_0$, $W = 1.26L_0$, $D = 0.30L_0$, G_T(r) could be described by a power law with η_T of 0.31, indicating the presence of quasi-long-range translational order over the average domain spacing of 30.

The transition in the orientation of cylindrical microdomains between the minimally patterned trench surface and unpatterned surface at four different edges (left, right, top, and bottom) was examined, as shown in Figure 2.16a. It should be noted that the cylindrical microdomains far away from the patterned surface were oriented predominantly parallel to the film surface because of the preferential interaction between the PEO block and the oxide layer on the silicon substrate (Figure 2.16b). Figure 2.16c shows SFM phase images of the cylindrical microdomains at four different edges of the minimally patterned trench surface with $P = 18.84L_0$, $W = 2.16L_0$, $D = 0.30L_0$. It was evident that the orientation of the cylindrical microdomains changed after a given distance (left and right image in Figure 2.16c). This behavior was observed in the propagation region in the minimal single trench experiments. Also, without the direct influence of the edge of the trench, the same propagation phenomenon was observed at both the top and bottom edges. These results show the effect of the minimally patterned trench surfaces on the orientation of cylindrical microdomains and demonstrate how highly ordered hexagonal arrays can be achieved over large areas. However, in our study, when $P = 25.11L_0$, $W = 1.81L_0$, $D = 0.23L_0$, mixed orientations (perpendicular and parallel) were observed (Figure 2.16d).

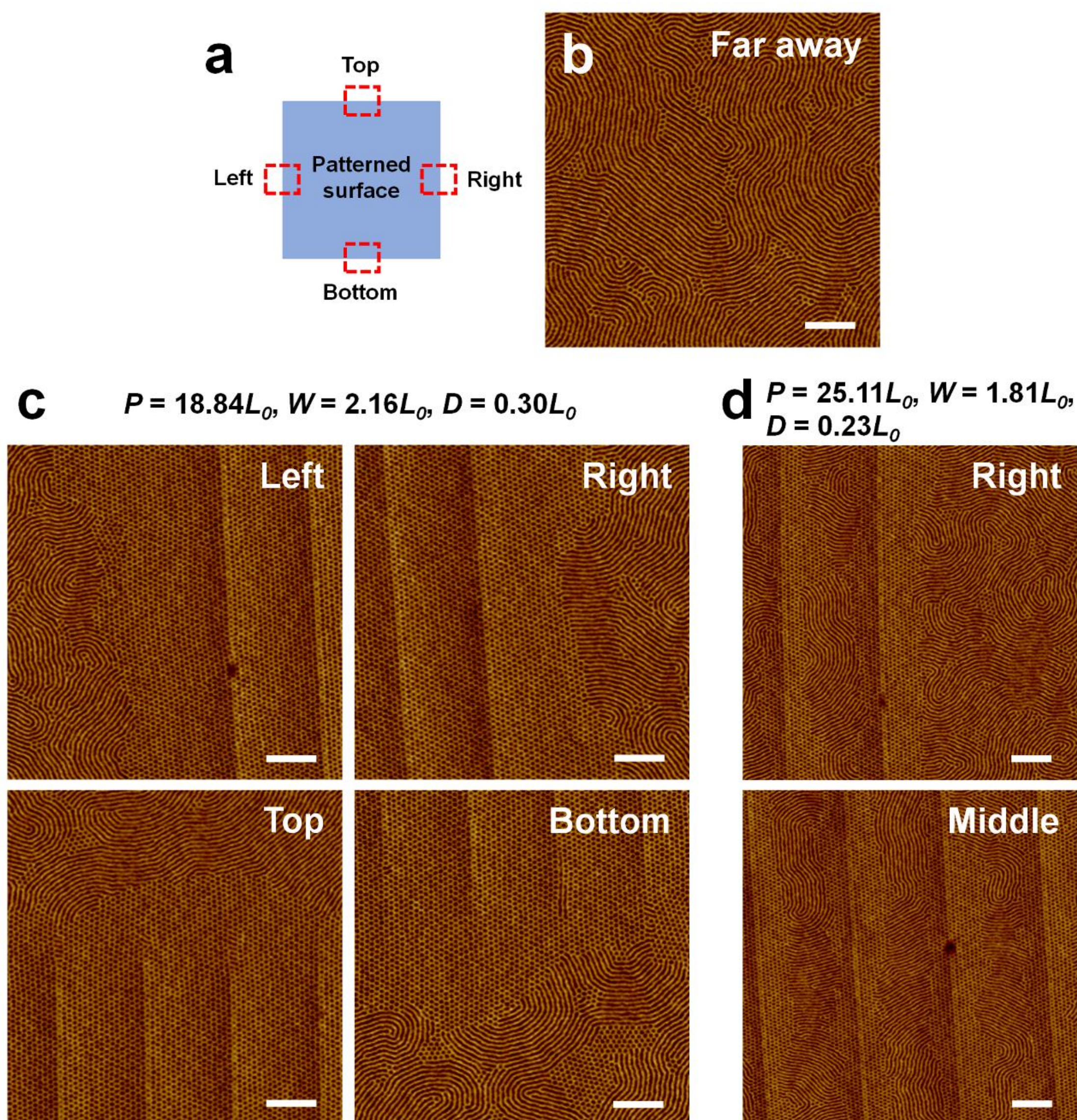

Figure 2.16 Transition in the orientation of cylindrical microdomains between the minimally patterned trench surface and unpatterned surface. (a) Schematic illustration of four different edges (left, right, top, and bottom) on the patterned surface. (b–d) SFM phase images of thermally annealed PS-*b*-PEO thin films at different areas. (b) Cylindrical microdomains far away from the patterned surface. (c) Cylindrical microdomains at four different edges on the patterned surface with $P = 18.84L_0$, $W = 2.16L_0$, and $D = 0.30L_0$. (d) Cylindrical microdomains at the right edge and middle area on the patterned surface with $P = 25.11L_0$, $W = 1.81L_0$, and $D = 0.23L_0$. Scale bars, 300 nm.

We further studied the influence of the minimally patterned trench surface on the lateral ordering of line pattern of cylindrical microdomains oriented parallel to the film surface. In the first step, PS-*b*-PEO thin films were prepared onto the minimally patterned trench surfaces. Then, SVA was performed using tetrahydrofuran (THF), a good solvent for both blocks, and water, a selective solvent for PEO block. The initial film thicknesses were 1.46L_0, which are identical to the film thicknesses in thermal annealing experiments. To prevent the films from dewetting during SVA, the PS-*b*-PEO thin films were pre-swollen in water vapor for 10 min (Figure 2.17).

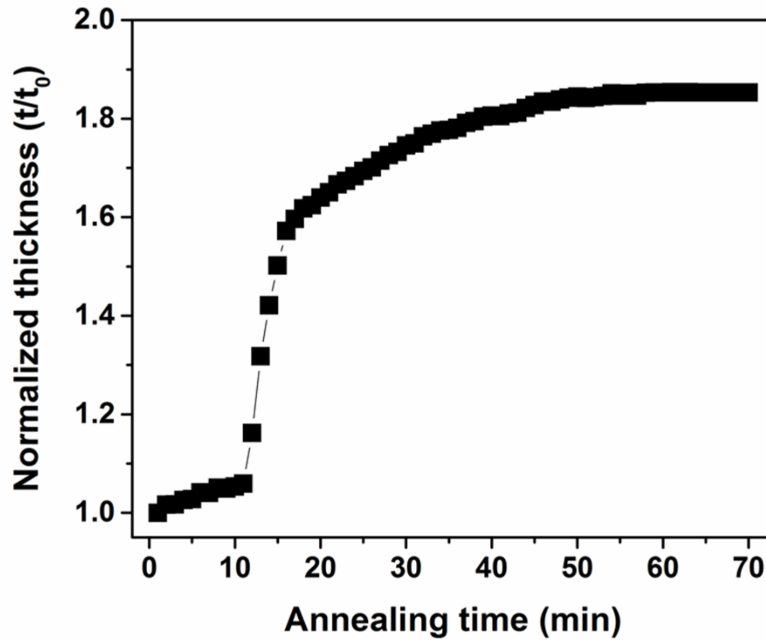

Figure 2.17 Swelling behavior, where the swollen thickness (t) is divided by the initial film thickness (t_0), of the PS-*b*-PEO thin film on the flat silicon substrate exposed to THF and water vapors after pre-swelling in water vapor for 10 min.

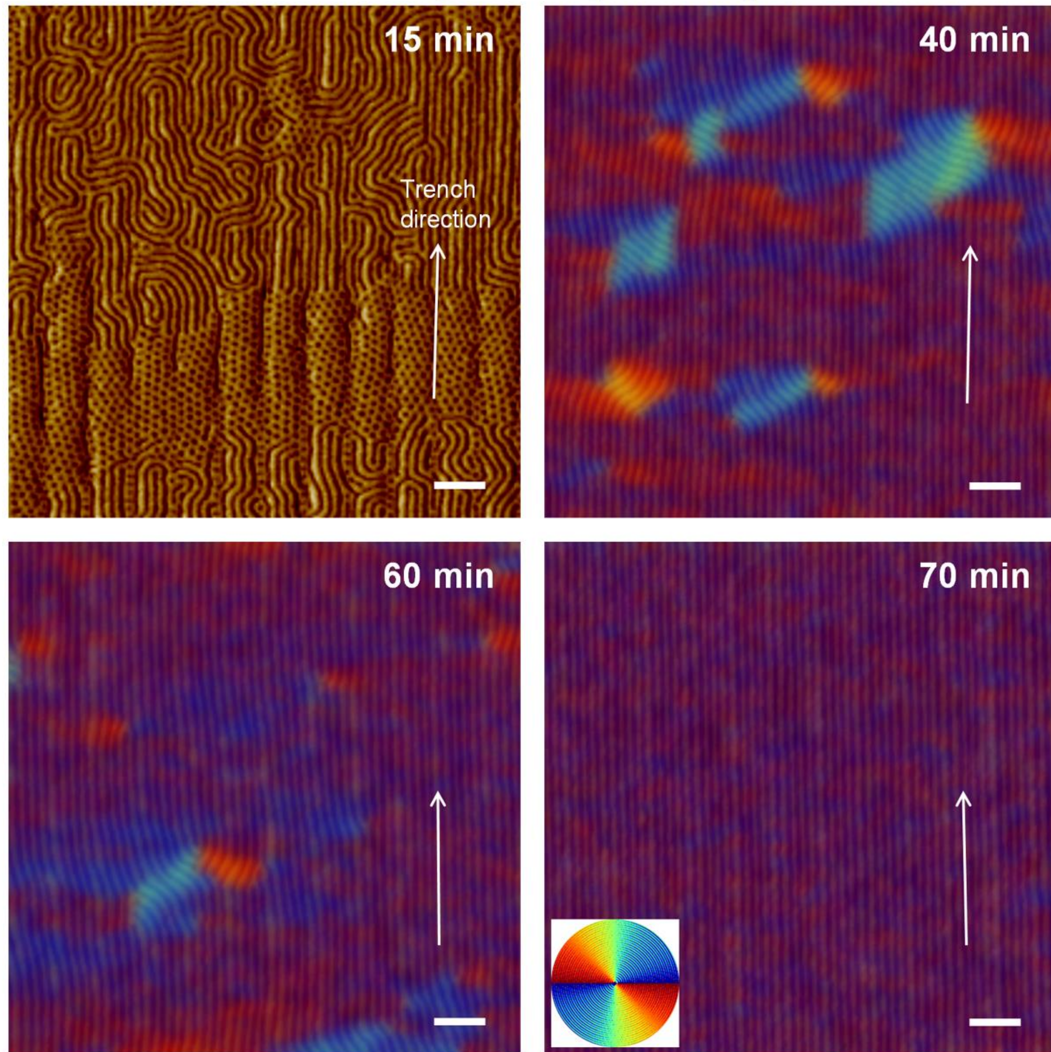

Figure 2.18 Time evolution of SFM phase images of PS-*b*-PEO thin films exposed to THF and water vapors on the minimally patterned trench surface with $P = 5.75L_0$, $W = 1.26L_0$, and $D = 0.30L_0$. SFM images of 40, 60, and 70 min annealed samples were overlaid with the colorized grain maps. The arrow in each image indicates the underlying trench direction. The color wheel in the 70 min sample shows the orientation of line patterns of cylindrical microdomains. Scale bars, 200 nm.

Figure 2.18 shows SFM phase images of solvent vapor annealed PS-*b*-PEO thin films on the minimally patterned trench surface with $P = 5.75L_0$, $W = 1.26L_0$, $D = 0.30L_0$ at different annealing times. An interesting feature was that initial hexagonal arrays of cylindrical microdomains oriented normal to the film surface began to change into line patterns of cylindrical microdomains oriented parallel to the film surface by connecting with adjacent PEO microdomains at the early stage of SVA (15 min). This observation is consistent with our previous results.[31, 39, 54] Recently, Mokarian-Tabari *et al.* has demonstrated that the transition in the orientation of cylindrical microdomains in PS-*b*-PEO thin films from perpendicular to parallel is related to the swelling during SVA process, reaching a critical thickness which favors parallel orientation.[55] For the 40 min annealed sample, the orientation of cylindrical microdomains were completely changed to being parallel to the surface, where SFM image were overlaid with the colorized grain map (Figure 2.19). In addition, the grain coarsening of the microdomains with annihilation of defects such as disclinations and dislocations was observed with increased SVA time, finally producing highly aligned line patterns of cylindrical microdomains (70 min), which are parallel to the underlying trench direction. However, when the initial film thickness was increased from $1.46L_0$ to $1.72L_0$, the minimally patterned trench surface with $P = 5.75L_0$, $W = 1.26L_0$, $D = 0.30L_0$ generated fingerprint patterns of cylindrical microdomains, as shown in Figure 2.20. This result indicates that the film thickness is also important parameter to direct the self-assembly process. Similar effects of the film thickness were reported for hexagonal arrays of PS-*b*-PEO microdomains on the sinusoidal patterns[35] and the sapphire faceted substrates.[38]

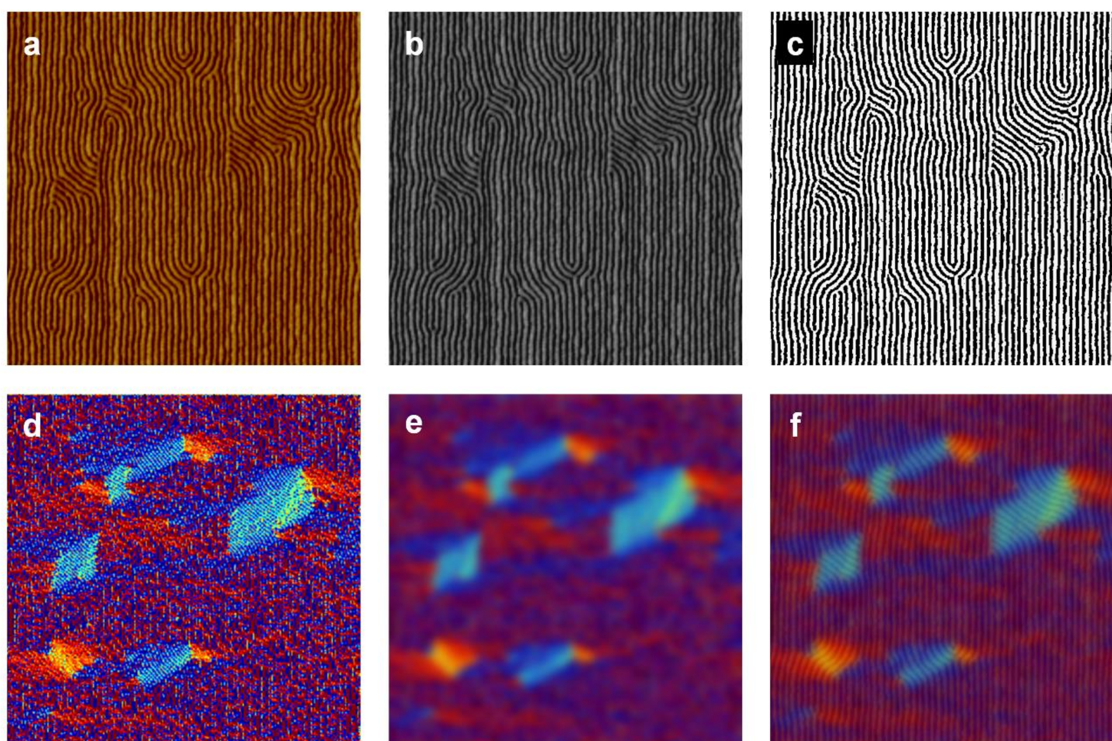

Figure 2.19 Demonstration of the image processing to colorize the orientation of line patterns of cylindrical microdomains oriented parallel to the film surface on the minimally patterned trench surface. (a) Original SFM phase image. (b) SFM image was converted to 8-bit gray scale image. (c) High-Pass filtering was applied to 8-bit gray scale image. (d) Filtered image was processed using MATLAB. (e) Low-Pass filtering was used for blurring the image. (f) Original SFM image was overlaid with the blurred image.

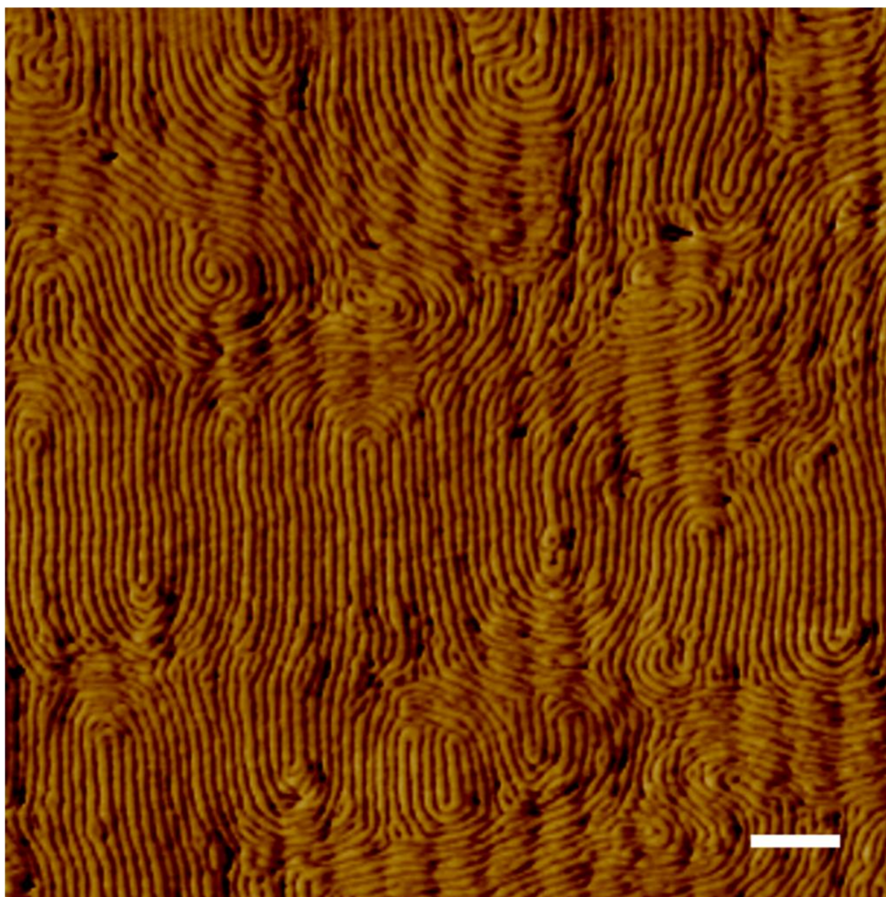

Figure 2.20 SFM phase image of the solvent-vapor annealed PS-*b*-PEO thin film on the minimally patterned trench surface with P = 5.75L_0, W = 1.26L_0, D = 0.30L_0. The film thickness prior to SVA was ~46 nm (1.72L_0). Scale bar, 300 nm.

Figure 2.21a–c show SFM phase images of solvent vapor annealed PS-*b*-PEO thin films under the same annealing conditions on the minimally patterned trench surfaces with different dimensions. In contrast to guiding the hexagonal arrays of cylindrical microdomains oriented normal to the film surface, the influence of the minimally patterned trench surface on directing the self-assembly of line patterns of cylindrical microdomains oriented parallel to the film surface diminished as the P and W increase at the fixed D of 0.30L_0. As seen in Figure 2.21a, the highly aligned line patterns with very few defects were

achieved on the patterned surface with $P = 5.75L_0$, $W = 1.26L_0$, $D = 0.30L_0$. However, discernible defects began to increase on the patterned surface with $P = 12.69L_0$, $W = 1.97L_0$, $D = 0.30L_0$ (Figure 2.21b). As a result, the line patterns of cylindrical microdomain were partially aligned with the underlying patterned surface with $P = 18.84L_0$, $W = 2.16L_0$, $D = 0.30L_0$, showing many defects, such as dislocations and disclinations (Figure 2.21c). To measure defect density of line patterns of cylindrical microdomains, six SFM images were randomly selected from each sample. The size of each image was 5 μm by 5 μm. As shown in Figure 2.21d, the line patterns exhibited very few defects less than 0.1 μm^{-2} on the patterned surface with $P = 5.75L_0$, $W = 1.26L_0$, $D = 0.30L_0$. The defect density of line pattern increased slightly to ~0.1 μm^{-2} on the patterned surface with $P = 12.69L_0$, $W = 1.97L_0$, $D = 0.30L_0$. However, the defect density increased rapidly to ~17 μm^{-2} on the patterned surface with $P = 18.84L_0$, $W = 2.16L_0$, $D = 0.30L_0$. Since both P and W are varied at the same time at the fixed D of $0.30L_0$, it is unclear to determine which dimension has a strong influence on increase in the defect density of line pattern. However, from these results, the minimally patterned trench surface appears more effective in guiding hexagonal arrays of cylindrical microdomains oriented normal to the film surface than line patterns of cylindrical microdomains oriented parallel to the film surface although these BCP microdomains were produced by the different annealing methods (thermal annealing and SVA).

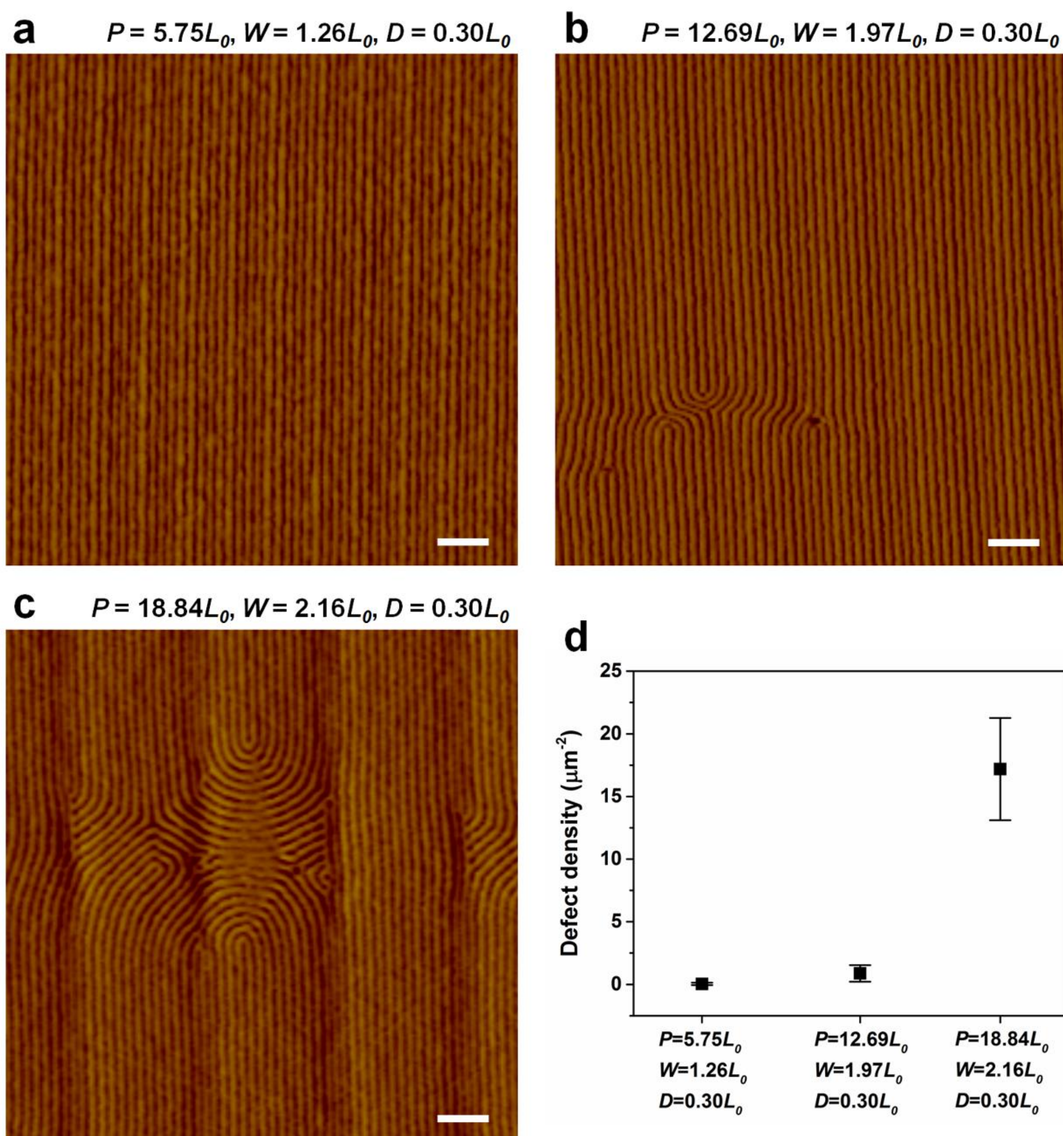

Figure 2.21 (a–c) SFM phase images of solvent-vapor annealed PS-*b*-PEO thin films on minimally patterned trench surfaces with different dimensions. Scale bars, 200 nm. (d) Average defect density of line patterns of cylindrical microdomains on the patterned surfaces.

2.4 Conclusions

In summary, we have demonstrated the effect of the minimally patterned trench surfaces on the lateral ordering of cylindrical microdomains in PS-*b*-PEO thin films under thermal annealing or SVA. For thermal annealing experiments, the minimal single trench patterns with different W and D (with $D < L_0$) were used to explore the propagation of order of PS-*b*-PEO microdomains away from the edges of the trench that can determine the minimum P of the trench necessary to direct the self-assembly process. For PS-*b*-PEO thin films on the flat silicon substrate, cylindrical microdomains were oriented parallel to the film surface due to the preferential interaction of the PEO block with the oxide layer on the silicon substrate. However, for this film thickness on the minimal single trench patterns, the underlying trench resulted in the film thickness variation over the trench, leading to two distinct regions (single trench and propagation) of cylindrical microdomains. Within the single trench region, the different dimensions of each single trench pattern play an important role for approaching the critical thickness of BCP films that can favor perpendicular, a mixed of perpendicular and parallel, or parallel orientation of cylindrical microdomains. As a result, the perpendicular orientation could be achieved in the single trench region when $W = 2.52L_0$ with $D = 0.20L_0$ or $W = 2.69L_0$ with $D = 0.31L_0$. However, in the propagation region, we found that hexagonal arrays of cylindrical microdomains oriented normal to the film surface propagated away from the edges of the single trench. This can be attributed to the gradient in the film thickness from the edges of the single trench, imposing frustration on BCP microdomains arising from the incommensurability between the film thickness and L_0. Based on these observations, the key to success in overlapping the propagated hexagonal arrays of cylindrical microdomains was integration

of minimal single trench patterns by varying P of the trench. Our results show that the dimensions of minimally patterned trench surfaces required to generate laterally ordered hexagonal arrays were the D of $0.30L_0$ with the W in the range of $1.26L_0$ to $2.16L_0$ and the P as long as $18.84L_0$. Moreover, we produced line patterns of cylindrical microdomains by using SVA on the minimally patterned trench. However, unlike guiding the hexagonal arrays, the guiding effect of the minimally patterned trench surface on the line patterns decreased as the P and W increase at the fixed D of $0.30L_0$. We achieved highly ordered line patterns of cylindrical microdomains only on the patterned surface with $P = 5.75L_0$, $W = 1.26L_0$, $D = 0.30L_0$. Thus, it is likely that the minimally patterned trench surface is more effective in directing the self-assembly of hexagonal arrays than that of line patterns in BCP thin films.

2.5 References

1. Rhys Alun, G.; Aled, W.; Chloe, O.; Jonathan, R.; Aravind, V.; Thomas, T. Directed Self-Assembly of Block Copolymers for Use in Bit Patterned Media Fabrication. *J. Phys. D: Appl. Phys.* **2013**, *46*, 503001.

2. Park, M.; Harrison, C.; Chaikin, P. M.; Register, R. A.; Adamson, D. H. Block Copolymer Lithography: Periodic Arrays of ~10^{11} Holes in 1 Square Centimeter. *Science* **1997**, *276*, 1401-1404.

3. Segalman, R. A. Patterning with Block Copolymer Thin Films. *Mater. Sci. Eng. R* **2005**, *48*, 191-226.

4. Cheng, J. Y.; Ross, C. A.; Thomas, E. L.; Smith, H. I.; Vancso, G. J. Fabrication of Nanostructures with Long-Range Order Using Block Copolymer Lithography. *Appl. Phys. Lett.* **2002**, *81*, 3657-3659.

5. Cheng, J. Y.; Ross, C. A.; Smith, H. I.; Thomas, E. L. Templated Self-Assembly of Block Copolymers: Top-Down Helps Bottom-Up. *Adv. Mater.* **2006**, *18*, 2505-2521.

6. Luo, M.; Epps, T. H. Directed Block Copolymer Thin Film Self-Assembly: Emerging Trends in Nanopattern Fabrication. *Macromolecules* **2013**, *46*, 7567-7579.

7. Hu, H.; Gopinadhan, M.; Osuji, C. O. Directed Self-Assembly of Block Copolymers: A Tutorial Review of Strategies for Enabling Nanotechnology with Soft Matter. *Soft Matter* **2014**, *10*, 3867-3889.

8. Koo, K.; Ahn, H.; Kim, S.-W.; Ryu, D. Y.; Russell, T. P. Directed Self-Assembly of Block Copolymers in the Extreme: Guiding Microdomains from the Small to the Large. *Soft Matter* **2013**, *9*, 9059-9071.

9. Segalman, R. A.; Yokoyama, H.; Kramer, E. J. Graphoepitaxy of Spherical Domain Block Copolymer Films. *Adv. Mater.* **2001**, *13*, 1152-1155.

10. Cheng, J. Y.; Mayes, A. M.; Ross, C. A. Nanostructure Engineering by Templated Self-Assembly of Block Copolymers. *Nat. Mater.* **2004**, *3*, 823-828.

11. Sundrani, D.; Darling, S. B.; Sibener, S. J. Guiding Polymers to Perfection: Macroscopic Alignment of Nanoscale Domains. *Nano Lett.* **2004**, *4*, 273-276.

12. Xiao, S.; Yang, X.; Edwards, E. W.; La, Y.-H.; Nealey, P. F. Graphoepitaxy of Cylinder-Forming Block Copolymers for Use as Templates to Pattern Magnetic Metal Dot Arrays. *Nanotechnology* **2005**, *16*, S324-S329.

13. Chai, J.; Wang, D.; Fan, X.; Buriak, J. M. Assembly of Aligned Linear Metallic Patterns on Silicon. *Nat. Nanotechnol.* **2007**, *2*, 500-506.

14. Jung, Y. S.; Ross, C. A. Orientation-Controlled Self-Assembled Nanolithography Using a Polystyrene−Polydimethylsiloxane Block Copolymer. *Nano Lett.* **2007**, *7*, 2046-2050.

15. Park, S.-M.; Stoykovich, M. P.; Ruiz, R.; Zhang, Y.; Black, C. T.; Nealey, P. F. Directed Assembly of Lamellae-Forming Block Copolymers by Using Chemically and Topographically Patterned Substrates. *Adv. Mater.* **2007**, *19*, 607-611.

16. Ruiz, R.; Ruiz, N.; Zhang, Y.; Sandstrom, R. L.; Black, C. T. Local Defectivity Control of 2D Self-Assembled Block Copolymer Patterns. *Adv. Mater.* **2007**, *19*, 2157-2162.

17. Tavakkoli K. G., A.; Gotrik, K. W.; Hannon, A. F.; Alexander-Katz, A.; Ross, C. A.; Berggren, K. K. Templating Three-Dimensional Self-Assembled Structures in Bilayer Block Copolymer Films. *Science* **2012**, *336*, 1294-1298.

18. Kim, E.; Ahn, H.; Park, S.; Lee, H.; Lee, M.; Lee, S.; Kim, T.; Kwak, E.-A.; Lee, J. H.; Lei, X.; Huh, J.; Bang, J.; Lee, B.; Ryu, D. Y. Directed Assembly of High Molecular Weight Block Copolymers: Highly Ordered Line Patterns of Perpendicularly Oriented Lamellae with Large Periods. *ACS Nano* **2013**, *7*, 1952-1960.

19. Borah, D.; Shaw, M. T.; Holmes, J. D.; Morris, M. A. Sub-10 nm Feature Size PS-*b*-PDMS Block Copolymer Structures Fabricated by a Microwave-Assisted Solvothermal Process. *ACS Appl. Mater. Interfaces* **2013**, *5*, 2004-2012.

20. Berry, B. C.; Singh, G.; Kim, H.-C.; Karim, A. Highly Aligned Block Copolymer Thin Films by Synergistic Coupling of Static Graphoepitaxy and Dynamic Thermal Annealing Fields. *ACS Macro Lett.* **2013**, *2*, 346-350.

21. Perego, M.; Andreozzi, A.; Vellei, A.; Lupi, F. F.; Seguini, G. Collective Behavior of Block Copolymer Thin Films within Periodic Topographical Structures. *Nanotechnology* **2013**, *24*, 245301.

22. Segalman, R. A.; Hexemer, A.; Kramer, E. J. Effects of Lateral Confinement on Order in Spherical Domain Block Copolymer Thin Films. *Macromolecules* **2003**, *36*, 6831-6839.

23. Segalman, R. A.; Hexemer, A.; Kramer, E. J. Edge Effects on the Order and Freezing of a 2D Array of Block Copolymer Spheres. *Phys. Rev. Lett.* **2003**, *91*, 196101.

24. Hammond, M. R.; Kramer, E. J. Edge Effects on Thermal Disorder in Laterally Confined Diblock Copolymer Cylinder Monolayers. *Macromolecules* **2006**, *39*, 1538-1544.

25. Kim, S. O.; Solak, H. H.; Stoykovich, M. P.; Ferrier, N. J.; de Pablo, J. J.; Nealey, P. F. Epitaxial Self-Assembly of Block Copolymers on Lithographically Defined Nanopatterned Substrates. *Nature* **2003**, *424*, 411-414.

26. Ruiz, R.; Kang, H.; Detcheverry, F. A.; Dobisz, E.; Kercher, D. S.; Albrecht, T. R.; de Pablo, J. J.; Nealey, P. F. Density Multiplication and Improved Lithography by Directed Block Copolymer Assembly. *Science* **2008**, *321*, 936-939.

27. Yang, X.; Wan, L.; Xiao, S.; Xu, Y.; Weller, D. K. Directed Block Copolymer Assembly versus Electron Beam Lithography for Bit-Patterned Media with Areal Density of 1 Terabit/Inch^2 and Beyond. *ACS Nano* **2009**, *3*, 1844-1858.

28. Liu, C.-C.; Ramírez-Hernández, A.; Han, E.; Craig, G. S. W.; Tada, Y.; Yoshida, H.; Kang, H.; Ji, S.; Gopalan, P.; de Pablo, J. J.; Nealey, P. F. Chemical Patterns for Directed Self-Assembly of Lamellae-Forming Block Copolymers with Density Multiplication of Features. *Macromolecules* **2013**, *46*, 1415-1424.

29. Tada, Y.; Akasaka, S.; Yoshida, H.; Hasegawa, H.; Dobisz, E.; Kercher, D.; Takenaka, M. Directed Self-Assembly of Diblock Copolymer Thin Films on Chemically-Patterned Substrates for Defect-Free Nano-Patterning. *Macromolecules* **2008**, *41*, 9267-9276.

30. Jeong, S.-J.; Moon, H.-S.; Kim, B. H.; Kim, J. Y.; Yu, J.; Lee, S.; Lee, M. G.; Choi, H.; Kim, S. O. Ultralarge-Area Block Copolymer Lithography Enabled by Disposable Photoresist Prepatterning. *ACS Nano* **2010**, *4*, 5181-5186.

31. Hong, S. W.; Gu, X.; Huh, J.; Xiao, S.; Russell, T. P. Circular Nanopatterns over Large Areas from the Self-Assembly of Block Copolymers Guided by Shallow Trenches. *ACS Nano* **2011**, *5*, 2855-2860.

32. Sun, Z.; Chen, Z.; Zhang, W.; Choi, J.; Huang, C.; Jeong, G.; Coughlin, E. B.; Hsu, Y.; Yang, X.; Lee, K. Y.; Kuo, D. S.; Xiao, S.; Russell, T. P. Directed Self-Assembly of Poly(2-Vinylpyridine)-*b*-Polystyrene-*b*-Poly(2-Vinylpyridine) Triblock Copolymer with Sub-15 nm Spacing Line Patterns Using a Nanoimprinted Photoresist Template. *Adv. Mater.* **2015**, *27*, 4364-4370.

33. Xiao, S.; Yang, X.; Steiner, P.; Hsu, Y.; Lee, K.; Wago, K.; Kuo, D. Servo-Integrated Patterned Media by Hybrid Directed Self-Assembly. *ACS Nano* **2014**, *8*, 11854-11859.

34. Xiao, S.; Yang, X.; Hwu, J. J.; Lee, K. Y.; Kuo, D. A Facile Route to Regular and Nonregular Dot Arrays by Integrating Nanoimprint Lithography with Sphere-Forming Block Copolymer Directed Self-Assembly. *J. Polym. Sci., Part B: Polym. Phys.* **2014**, *52*, 361-367.

35. Aissou, K.; Shaver, J.; Fleury, G.; Pécastaings, G.; Brochon, C.; Navarro, C.; Grauby, S.; Rampnoux, J.-M.; Dilhaire, S.; Hadziioannou, G. Nanoscale Block Copolymer Ordering Induced by Visible Interferometric Micropatterning: A Route Towards Large Scale Block Copolymer 2D Crystals. *Adv. Mater.* **2013**, *25*, 213-217.

36. Cushen, J.; Wan, L.; Blachut, G.; Maher, M. J.; Albrecht, T. R.; Ellison, C. J.; Willson, C. G.; Ruiz, R. Double-Patterned Sidewall Directed Self-Assembly and Pattern Transfer of Sub-10 nm PTMSS-*b*-PMOST. *ACS Appl. Mater. Interfaces* **2015**, *7*, 13476-13483.

37. Pandav, G.; Durand, W. J.; Ellison, C. J.; Willson, C. G.; Ganesan, V. Directed Self Assembly of Block Copolymers Using Chemical Patterns with Sidewall Guiding Lines, Backfilled with Random Copolymer Brushes. *Soft Matter* **2015**, *11*, 9107-9114.

38. Park, S.; Lee, D. H.; Xu, J.; Kim, B.; Hong, S. W.; Jeong, U.; Xu, T.; Russell, T. P. Macroscopic 10-Terabit-Per-Square-Inch Arrays from Block Copolymers with Lateral Order. *Science* **2009**, *323*, 1030-1033.

39. Hong, S. W.; Huh, J.; Gu, X.; Lee, D. H.; Jo, W. H.; Park, S.; Xu, T.; Russell, T. P. Unidirectionally Aligned Line Patterns Driven by Entropic Effects on Faceted Surfaces. *Proc. Natl. Acad. Sci.* **2012**, *109*, 1402-1406.

40. Ferrarese Lupi, F.; Giammaria, T. J.; Seguini, G.; Laus, M.; Enrico, E.; De Leo, N.; Boarino, L.; Ober, C. K.; Perego, M. Thermally Induced Orientational Flipping of Cylindrical Phase Diblock Copolymers. *Journal of Materials Chemistry C* **2014**, *2*, 2175-2182.

41. Kim, M.; Han, E.; Sweat, D. P.; Gopalan, P. Interplay of Surface Chemical Composition and Film Thickness on Graphoepitaxial Assembly of Asymmetric Block Copolymers. *Soft Matter* **2013**, *9*, 6135-6141.

42. Fitzgerald, T. G.; Farrell, R. A.; Petkov, N.; Bolger, C. T.; Shaw, M. T.; Charpin, J. P. F.; Gleeson, J. P.; Holmes, J. D.; Morris, M. A. Study on the Combined Effects of Solvent Evaporation and Polymer Flow Upon Block Copolymer Self-Assembly and Alignment on Topographic Patterns. *Langmuir* **2009**, *25*, 13551-13560.

43. Ferrarese Lupi, F.; Aprile, G.; Giammaria, T. J.; Seguini, G.; Zuccheri, G.; De Leo, N.; Boarino, L.; Laus, M.; Perego, M. Thickness and Microdomain Orientation of Asymmetric PS-*b*-PMMA Block Copolymer Films inside Periodic Gratings. *ACS Appl. Mater. Interfaces* **2015**, *7*, 23615-23622.

44. Sundrani, D.; Sibener, S. J. Spontaneous Spatial Alignment of Polymer Cylindrical Nanodomains on Silicon Nitride Gratings. *Macromolecules* **2002**, *35*, 8531-8539.

45. Black, C. T.; Bezencenet, O. Nanometer-Scale Pattern Registration and Alignment by Directed Diblock Copolymer Self-Assembly. *IEEE Trans. Nanotechnol.* **2004**, *3*, 412-415.

46. Park, S.-M.; Berry, B. C.; Dobisz, E.; Kim, H.-C. Observation of Surface Corrugation-Induced Alignment of Lamellar Microdomains in PS-*b*-PMMA Thin Films. *Soft Matter* **2009**, *5*, 957-961.

47. Knoll, A.; Horvat, A.; Lyakhova, K. S.; Krausch, G.; Sevink, G. J. A.; Zvelindovsky, A. V.; Magerle, R. Phase Behavior in Thin Films of Cylinder-Forming Block Copolymers. *Phys. Rev. Lett.* **2002**, *89*, 035501.

48. Park, C.; Cheng, J. Y.; Fasolka, M. J.; Mayes, A. M.; Ross, C. A.; Thomas, E. L.; De Rosa, C. Double Textured Cylindrical Block Copolymer Domains via Directional Solidification on a Topographically Patterned Substrate. *Appl. Phys. Lett.* **2001**, *79*, 848-850.

49. Kim, H.-C.; Russell, T. P. Ordering in Thin Films of Asymmetric Diblock Copolymers. *J. Polym. Sci., Part B: Polym. Phys.* **2001**, *39*, 663-668.

50. Kim, S.; Shin, D. O.; Choi, D.-G.; Jeong, J.-R.; Mun, J. H.; Yang, Y.-B.; Kim, J. U.; Kim, S. O.; Jeong, J.-H. Graphoepitaxy of Block-Copolymer Self-Assembly Integrated with Single-Step Zno Nanoimprinting. *Small* **2012**, *8*, 1563-1569.

51. Zhang, X.; De Paoli Lacerda, S. H.; Yager, K. G.; Berry, B. C.; Douglas, J. F.; Jones, R. L.; Karim, A. Target Patterns Induced by Fixed Nanoparticles in Block Copolymer Films. *ACS Nano* **2009**, *3*, 2115-2120.

52. Segalman, R. A.; Hexemer, A.; Hayward, R. C.; Kramer, E. J. Ordering and Melting of Block Copolymer Spherical Domains in 2 and 3 Dimensions. *Macromolecules* **2003**, *36*, 3272-3288.

53. Angelescu, D. E.; Harrison, C. K.; Trawick, M. L.; Register, R. A.; Chaikin, P. M. Two-Dimensional Melting Transition Observed in a Block Copolymer. *Phys. Rev. Lett.* **2005**, *95*, 025702.

54. Hong, S. W.; Voronov, D. L.; Lee, D. H.; Hexemer, A.; Padmore, H. A.; Xu, T.; Russell, T. P. Controlled Orientation of Block Copolymers on Defect-Free Faceted Surfaces. *Adv. Mater.* **2012**, *24*, 4278-4283.

55. Mokarian-Tabari, P.; Collins, T. W.; Holmes, J. D.; Morris, M. A. Cyclical "Flipping" of Morphology in Block Copolymer Thin Films. *ACS Nano* **2011**, *5*, 4617-4623.

CHAPTER 3

GISAXS STUDY OF MACROSCOPICALLY ORDERED HEXAGONAL ARRAYS PRODUCED BY DIRECTED SELF-ASSEMBLY OF BLOCK COPOLYMERS WITH MINIMAL TOPOGRAPHIC PATTERNS

3.1 Introduction

The directed self-assembly (DSA) of block copolymers (BCPs) has attracted widespread interest, since it has enabled the generation of highly ordered arrays of the nanoscopic microdomains, such as lamellae, cylinders, or spheres, with feature sizes of 10 to 50 nm over large areas.[1, 2] There has been extensive research in this area due to the promise of achieving 2-D patterns that may be used for the fabrication of magnetic bit-patterned media (BPM) and semiconductor devices.[3-9] For these applications, it is important to control the lateral ordering, as well as the orientation and placement of BCP microdomains.[1, 10] The lateral ordering of BCP microdomains in thin films can be controlled by external fields, such as graphoepitaxy,[11] chemical patterning of surfaces,[12] shearing,[13] and zone annealing.[14] Among these methods, graphoepitaxy, where surface topography is used to guide the self-assembly process, can be further divided into the use of deep[15-24] or minimal[25-33] topographic patterns depending on the vertical length scale of the confinement depth. More specifically, deep topographic patterns have a confinement depth that is comparable to or larger than the natural period of the BCP (L_0). When BCP thin films with thicknesses of a single period or less are prepared on deep topographic

---

[‡]This chapter has been adapted from J. Choi, I. Gunkel, Y. Li, Z. Sun, F. Liu, H. Kim, K. R. Carter, and T. P. Russell, "Macroscopically Ordered Hexagonal Arrays by Directed Self-Assembly of Block Copolymers with Minimal Topographic Patterns" *The manuscript to be submitted for publication*, **2017**.

patterns, followed by solvent vapor annealing (SVA) or thermal annealing, the self-assembled BCP microdomains can be trapped in the confinement regions, allowing lateral control over the spatial arrangement of the microdomains. In this case, depending on the type of BCPs, surface chemistry is required to control the interfacial interaction between the BCP and surface of the confinement region that allows the desired orientation and alignment of the microdomains to be achieved.[34] However, the effect of deep topographic patterns on the lateral ordering of BCP microdomains generally decreases as the confinement width increases.[35] Consequently, the final grain size of highly ordered or aligned BCP microdomains is restricted by the optimized confinement width. In contrast, the use of minimal topographic patterns enables BCP microdomains to significantly increase their final grain size because the confinement depth is much less than L_0, allowing the microdomains to exist both inside and outside of the confinement regions over the patterned surface while maintaining good placement accuracy and lateral ordering.[33] Surface chemistry may also be required on the minimal topographic patterns to promote the lateral ordering depending on the type of BCPs.[27]

Laterally ordered BCP microdomains in thin films guided by deep or minimal topographic patterns can be examined by scanning electron microscopy (SEM) or scanning force microscopy (SFM). However, both techniques are limited to investigating the local ordering within an area of several square microns. Alternatively, one can use grazing incidence small angle X-ray scattering (GISAXS) which provides statistically averaged information on the internal structure and lateral ordering of BCP microdomains in thin films over macroscopic length scales.[36-41] The use of GISAXS to study BCP microdomains guided by topographic patterns was performed by Kramer and co-workers.[42, 43] However,

despite the advantages of GISAXS, relatively little attention has been given to its use for studying BCP microdomains guided by topographic patterns. For deep topographic patterns, one of the main reasons for this is the size of the patterned surfaces. Many substrates patterned by electron beam lithography (EBL) have been used to direct the self-assembly of BCP thin films, but the sizes of the patterned surfaces are generally smaller than that of the footprint of the X-ray beam, causing difficulties in GISAXS measurements. However, Maret and co-workers recently reported using GISAXS to investigate hexagonal arrays of cylindrical microdomains in poly(styrene-*b*-methyl methacrylate) (PS-*b*-PMMA) thin films guided by a deep trench pattern.[44] In this case, the patterned surface (10×1 mm^2 in size, with a stitching error of ~6 nm at every 33 μm) allowed the X-ray beam to align with the hexagonal arrays on the deep trench pattern, showing that the (10) planes of hexagonal arrays were oriented parallel to the trench direction. However, they did not rotate a sample stage to study hexagonal arrays further. Berggren and co-workers also used GISAXS to confirm the lateral ordering of bilayer stacks of orthogonal line patterns of poly(styrene-*b*-dimethylsiloxane) (PS-*b*-PDMS) microdomains guided by a deep trench pattern (sized of 12×12 mm^2).[45] In this case, depending on the X-ray beam alignment direction, different scattering peaks were observed due to the mesh-shaped PDMS line patterns. For minimal topographic patterns, Russell and co-workers studied the lateral ordering of cylindrical microdomains of poly(styrene-*b*-ethylene oxide) (PS-*b*-PEO) thin films on faceted sapphire[30, 46] and silicon[47] substrates using GISAXS. Since the area of both surfaces was sufficiently large (several square centimeters) to perform GISAXS, well-defined hexagonal arrays[30] and line patterns[46, 47] over macroscopic length scales could be investigated. Nevertheless, there has been little research on the investigation of BCP

microdomains on topographic patterns using GISAXS and, in particular, no systematic investigation of how hexagonal arrays of cylindrical microdomains exist on topographic patterns.

In this work, we report a strategy for producing macroscopically ordered hexagonal arrays of cylindrical microdomains in PS-*b*-PEO thin films using a minimal trench pattern with SVA, where the trench depth of 11 nm ($0.3L_0$) was found to be effective to guide the self-assembly of PS-*b*-PEO thin films. The hexagonal arrays of cylindrical microdomains on minimal trench patterns were systematically investigated through the use of GISAXS with a rotation of the sample stage, providing insights into the morphological characteristic and lateral ordering of hexagonal arrays of cylindrical microdomains guided by 1-D topographic patterns, such as the minimal trench pattern discussed here. We also investigated the GISAXS patterns of hexagonal arrays of cylindrical microdomains in PS-*b*-PEO thin films on an unpatterned flat substrate for comparison.

3.2 Experimental Methods

3.2.1 Materials

Poly(styrene-*b*-ethylene oxide) (PS-*b*-PEO) (M_n = 32.0 kg mol^{-1} and M_n = 11.0 kg mol^{-1} for PS and PEO blocks, respectively, PDI = 1.06) was purchased from Polymer Source, Inc. and used as received. Benzene (anhydrous, 99.8%) and tetrahydrofuran (THF) (anhydrous, ≥99.9%, inhibitor-free) were purchased from Sigma-Aldrich. Each material was used without further purification. Epoxy permanent resist version 142, samples A-Z

was supplied from Microchem Corp. for the fabrication of silsesquioxane (SSQ)-based films.

3.2.2 Fabrication of Minimal Trench Patterns

Nanoimprint molds consisting of "hardened" crosslinked PDMS elastomer (*h*-PDMS) were replicated from a silicon master mold having the pitch of 140 nm, the line width of 70 nm, and the height of 50 nm using the previously demonstrated method.[48] SSQ-based films were prepared by spin-coating from propylene glycol monomethyl ether acetate (20 wt%) at 2000 rpm for 60 s onto silicon substrates (orientation of (100), University Wafer, Inc.). The thicknesses of the as-spun SSQ-based films were 274 ± 4 nm. These SSQ-based films were imprinted and UV cured with the *h*-PDMS mold by using the nanoimprinter (NX-2000, Nanonex) operating at 80 psi for 5 min. To reduce pattern dimensions, the patterned SSQ-based films, i.e. the nanoimprinted trench patterns, were annealed at 500 °C in air for 2 h, finally producing the minimal trench patterns.

3.2.3 DSA of BCP Thin Films

The minimal trench patterns were cleaned with carbon dioxide snow jet, followed by UV-Ozone cleaning (UVO cleaner model 342, Jelight Company Inc.). PS-*b*-PEO thin films were prepared by spin-coating from 0.8% (w/v) PS-*b*-PEO solution in benzene onto the minimal trench patterns. Prior to SVA, the thicknesses of PS-*b*-PEO films on the flat silicon substrate were ~36 nm, as measured by the ellipsometer (model LSE, Gaertner

Scientific Corp.). SVA was performed at room temperature in a sealed glass jar (volume of the jar = 46.5 cm^3, surface area of THF = 12.6 cm^2, and surface area of water = 1.3 cm^2). The PS-*b*-PEO thin films were pre-swollen in water vapor for 10 min to avoid dewetting, followed by SVA in THF and water vapors for 60 min. The swelling of PS-*b*-PEO films was characterized by measuring the swollen thickness of a film on a flat silicon substrate during SVA in real time using the reflectometer (F20-UV, FILMETRICS Inc.).

3.2.4 Characterization

Scanning force microscopy (SFM) images of solvent-vapor-annealed PS-*b*-PEO thin films were obtained using a SFM (Dimension 3100, Digital Instruments) operated in the tapping mode. The SFM tip has a pyramidal shape with a nominal radius of curvature of ~6 nm at the tip apex. Scanning electron microscopy (SEM) images of the nanoimprinted trench patterns and minimal trench patterns were obtained using a JEOL JSM-7001F FESEM operated with an acceleration voltage of 10 and 15 kV. Water contact angles were measured using a VCA Optima surface analysis/goniometry system with a droplet volume of 1.0 μL.

To determine L_0 of PS-*b*-PEO in the bulk, small angle X-ray scattering (SAXS) measurements were performed at the University of Massachusetts, Amherst using an in-house setup from Molecular Metrology Inc. It uses a 30 W microsource (Bede) with a 30 μm by 30 μm spot size matched to a Maxflux optical system (Osmic), leading to a low-divergence beam of monochromatic Cu Kα radiation (wavelength λ = 0.1542 nm).

Grazing incidence small angle X-ray scattering (GISAXS) measurements were performed at Beamline 7.3.3 at the Advanced Light Source, Lawrence Berkeley National Laboratory, at a constant X-ray energy of 10 keV.[49] The sample-to-detector distance was calibrated using a silver behenate standard. Scattering images were collected on a Pilatus 2M 2-D pixel detector (Dectris). During GISAXS measurements on the solvent-vapor-annealed PS-*b*-PEO thin films on the minimal trench patterns, the sample stage was rotated about the surface normal, where the rotation angle of $\Psi = 0°$ is defined when the X-ray beam is aligned with the underlying trench direction, which coincides with the (10) planes of hexagonal arrays. Then, the sample stage was rotated 30°, 60°, and 90° to collect scattering images at different sample rotations. The incident angle (α_i) was varied between 0.02° and 0.20°. For the solvent-vapor-annealed PS-*b*-PEO thin films on the flat silicon substrates, the X-ray beam was first aligned with an arbitrary direction on the substrate. From this point, the sample stage was rotated 30°, 60°, and 90°. At all Ψ, α_i was set at 0.18°.

3.3 Results and Discussion

3.3.1 DSA of BCP Thin Films on Unpatterned Flat Substrates and Minimal Trench Patterns

We first prepared PS-*b*-PEO (L_0 = 35.8 nm in the bulk, Figure 3.1) thin films with a thickness of ~36 nm (~L_0) by spin-coating from benzene solutions onto the flat silicon substrates. The films were then solvent-vapor annealed using tetrahydrofuran (THF), a good solvent for both blocks, and water, a selective solvent for the PEO block, to generate well-developed cylindrical microdomains oriented normal to the film surface. The PS-*b*-

PEO thin films were initially pre-swollen in water vapor to avoid film dewetting during SVA (Figure 3.2).

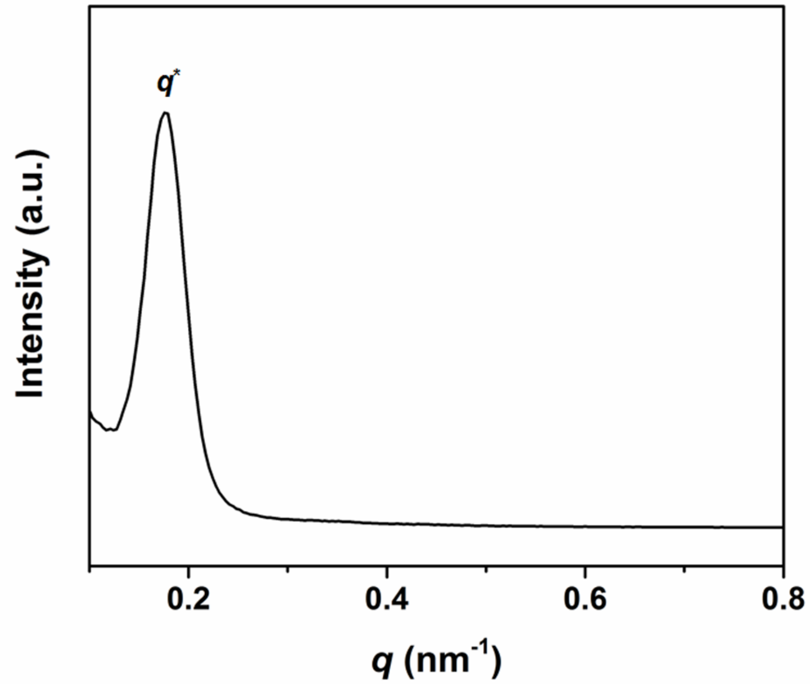

Figure 3.1 SAXS profile of a PS-*b*-PEO. The first-order reflection was observed at $q^* = 0.1757$ nm^{-1} corresponding to the natural period ($L_0 = 2\pi/q^*$) of 35.8 nm. It is noted that the higher-order peaks of the first-order reflection were not observed.

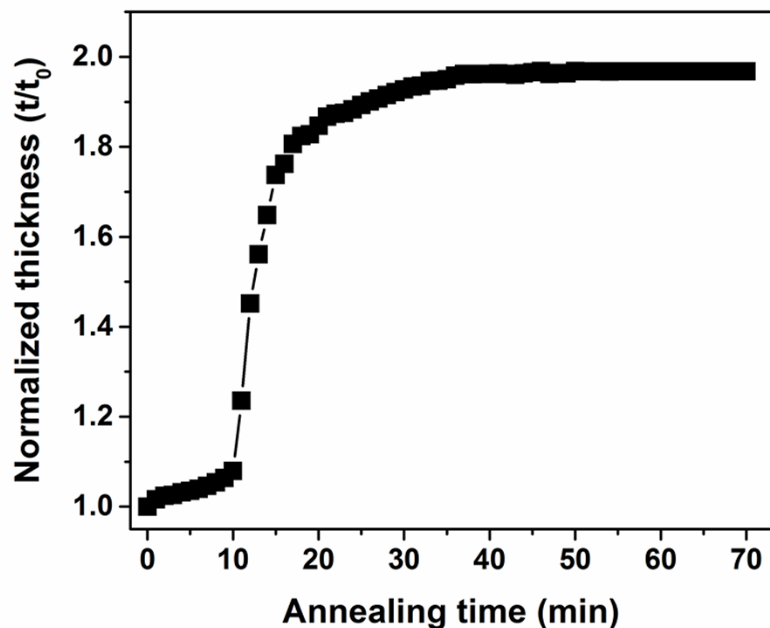

Figure 3.2 Swelling behavior of PS-*b*-PEO thin films on a flat silicon substrate, where the swollen film thickness (t) is divided by the initial film thickness (t_0). The films were initially pre-swollen in water vapor for 10 min to avoid dewetting, followed by exposing to THF and water vapors for 60 min

As seen in the SFM phase image (Figure 3.3a), when the films were annealed on flat silicon substrates, hexagonal arrays of cylindrical microdomains oriented normal to the film surface were produced. However, in this case, multiple grains were obtained, as evidenced by the 2-D fast Fourier transform (FFT) (inset of Figure 3.3a), which shows isotropic halos with several spots, indicating randomly oriented hexagonal arrays. To guide the self-assembly of these PS-*b*-PEO microdomains, we fabricated a minimal trench pattern with the depth of 11 nm ($0.3L_0$), width of 106 nm ($3.0L_0$), and pitch of 132 nm ($3.7L_0$) using size reduction lithography.[50] It is noted that the surface of the minimal trench pattern is hydrophilic (Figure 3.4–6 and Table 3.1). Figure 3.3b shows the schematic

illustration of the DSA process. After fabrication of minimal trench patterns, PS-*b*-PEO thin films with the thickness of ~L_0, as measured on a flat silicon substrate before SVA, were spin-coated from benzene solutions onto the patterned surfaces. Then, SVA was performed as described above to induce lateral ordering of hexagonal arrays of cylindrical microdomains. Figure 3.3c shows the SFM phase image of the solvent-vapor-annealed PS-*b*-PEO thin film on the minimal trench pattern. In contrast to the hexagonal arrays on flat silicon substrates, the (10) planes of hexagonal arrays were aligned with the underlying trench direction, generating a single grain of microdomains with few defects. The 2-D FFT (inset of Figure 3.3c) shows six sharp first-order peaks with higher-order reflections, indicating a well-defined single hexagonal grain. This result shows that the minimal trench pattern with a confinement depth of $0.3L_0$ effectively directs the self-assembly of hexagonal arrays of cylindrical microdomains, despite the incommensurability between the trench pitch and L_0 (Table 3.1). We obtained identical SFM images to those in Figure 3.3c with respect to the degree of ordering of the hexagonal arrays when many different areas were randomly scanned on the patterned surface of ~1×1 cm^2. To quantitatively analyze the morphological characteristics and lateral ordering of the hexagonal arrays, we performed GISAXS measurements, as shown in Figure 3.3d. During the measurements, the sample stage was rotated about the surface normal to investigate the hexagonal arrays in more detail. Also, the incident angle (α_i) was varied to compare the internal structure and surface morphology in PS-*b*-PEO thin films. As shown in Figure 3.3e, the rotation angle of $\Psi = 0°$ is defined when the X-ray beam is aligned with the underlying trench direction, which coincides with the (10) planes of hexagonal arrays. Based on $\Psi = 0°$, the sample stage was rotated 30°, 60°, and 90°. Hexagonal symmetry dictates that the incoming

X-ray beam follows the (10) planes at $\Psi = 0°$, the (11) planes at $\Psi = 30°$, the (01) planes at $\Psi = 60°$, and the $(\bar{1}2)$ planes at $\Psi = 90°$.

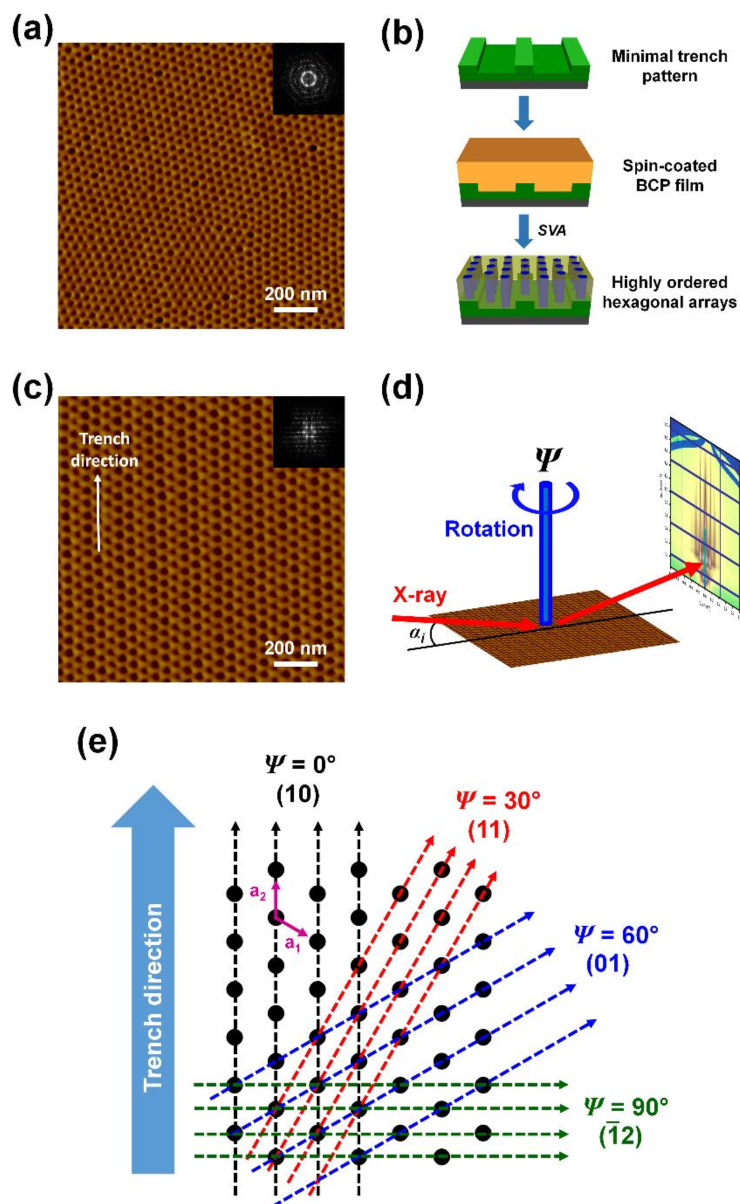

Figure 3.3 (a) SFM phase image of a solvent-vapor-annealed PS-*b*-PEO thin film on a flat silicon substrate. The inset shows the corresponding 2-D FFT. (b) Schematic diagram of the DSA process. (c) SFM phase image of a solvent-vapor-annealed PS-*b*-PEO thin film on a minimal trench pattern. The inset shows the corresponding 2-D FFT. (d) Schematic illustration of GISAXS experiments. Ψ is the rotation angle of the sample stage. a_i is the incident angle of the X-ray beam. (e) Schematic representation of 2-D hexagonal lattice planes with a different Ψ on the minimal trench pattern. Two basis vectors, a_1 and a_2, are indicated by the magenta arrows.

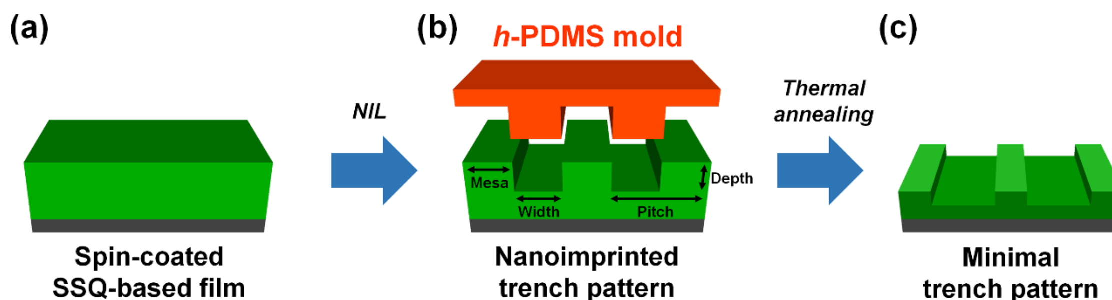

Figure 3.4 To fabricate a minimal trench pattern, we used size reduction lithography, which is based on nanoimprint lithography (NIL) and thermal annealing. (a) In the first step, a silsesquioxane (SSQ)-based film was prepared by spin-coating onto a flat silicon substrate. (b) Next, a h-PDMS mold consisting of grating lines with the pitch of 132 nm, the line width of 70 nm, and the height of 50 nm was used to nanoimprint the SSQ-based film. Then, the nanoimprinted trench pattern with the pitch of 132 nm, the mesa width of 64 nm, and the trench depth of 50 nm was annealed at 500 °C in air for 2 h to reduce the pattern dimensions, in particular the trench depth. It is noted that this thermal annealing process changes the surface property from hydrophobic (nanoimprinted trench pattern) to hydrophilic (minimal trench pattern) due to the formation of silicon oxide structure. (c) As a result, we obtained the minimal trench pattern with the pitch of 132 nm, the mesa width of 26 nm, the trench width of 106 nm, and the trench depth of 11 nm. Table 3.1 summarizes the results of the pattern dimension reduction. The reduction in pattern dimensions after thermal annealing is related to the elimination of organic molecules in the SSQ-based film and densification of the SSQ material. The reduction in the trench depth (78.0%) was larger than the mesa width reduction (59.4%), which can be attributed to the lateral confinement of the mesas to the substrate.

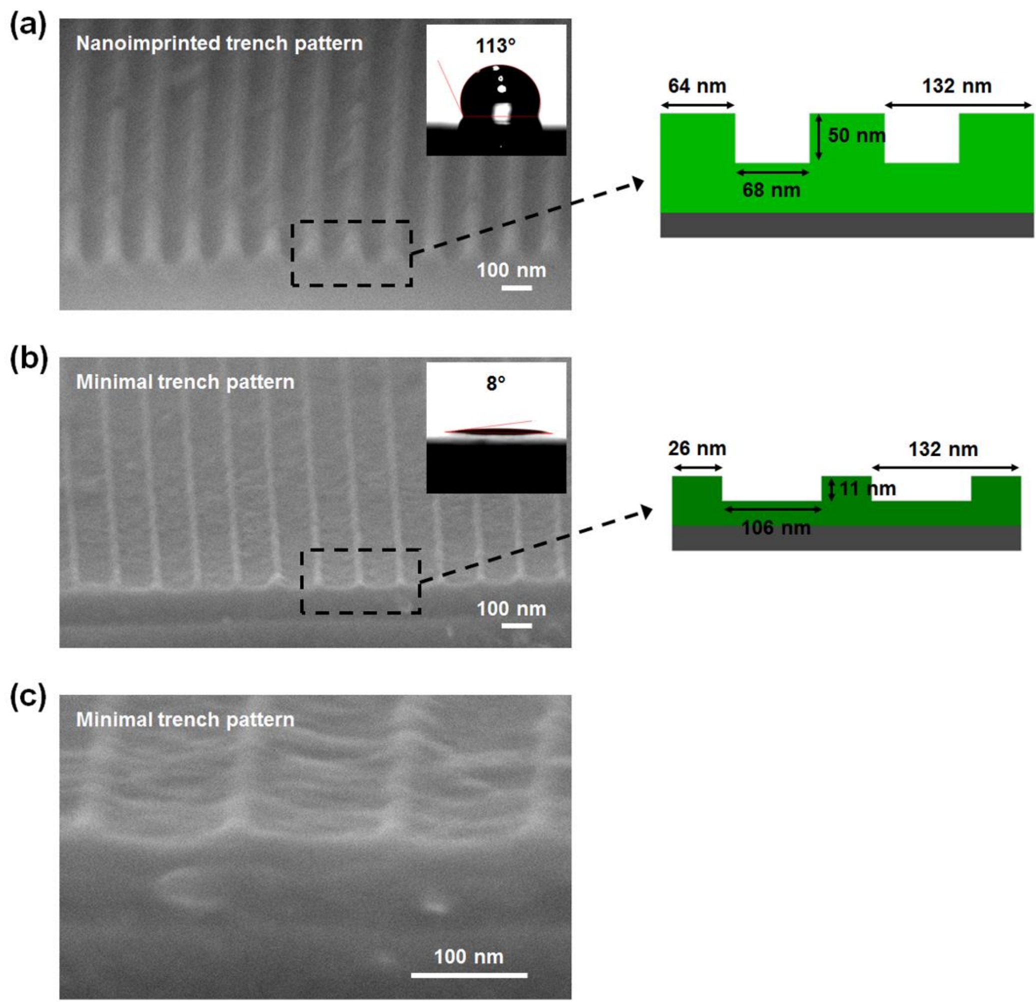

Figure 3.5 Cross-sectional (80° tilted) SEM images of patterned trench surfaces. (a) Nanoimprinted trench pattern with the pitch of 132 nm, the mesa width of 64 nm, the trench width of 68 nm, and the trench depth of 50 nm. The inset shows the water contact angle of 113°. Since the nanoimprinted trench pattern is mainly composed of the SSQ material, the surface is hydrophobic. (b) Minimal trench pattern with the pitch of 132 nm, the mesa width of 26 nm, the trench width of 106 nm, and the trench depth of 11 nm. The inset shows the water contact angle of 8°, indicating a hydrophilic surface. Through thermal annealing, the surface property was changed from hydrophilic (113°) to hydrophilic (8°). Since the SSQ-based material (nanoimprinted trench pattern) was converted to silicon oxide structures (minimal trench pattern) by eliminating organic molecules, the surface of the minimal trench pattern became hydrophilic. (c) The magnified image of the minimal trench pattern shows that the surface at the base of the trench is rough, but this roughness could not be measured by SFM due to artifacts arising from the shape of the tip. Since the mesa width of the nanoimprinted trench pattern cannot be readily reduced due to the lateral confinement during thermal annealing, any internal stresses in this pattern are relieved by roughening the bottom surface of the trench.

Table 3.1 Summary of the results of the pattern dimension reduction after thermal annealing.

Dimension	Nanoimprinted trench pattern (before thermal annealing)	Minimal trench pattern (after thermal annealing)
Trench pitch (nm)	132	132 (3.7[a])
Mesa width (nm)	64	26
Trench width (nm)	68	106 (3.0[b])
Trench depth (nm)	50	11 (0.3[c])

[a]Commensurability between the trench pitch and L_0.

[b]Commensurability between the trench width and L_0.

[c]Commensurability between the trench depth and L_0.

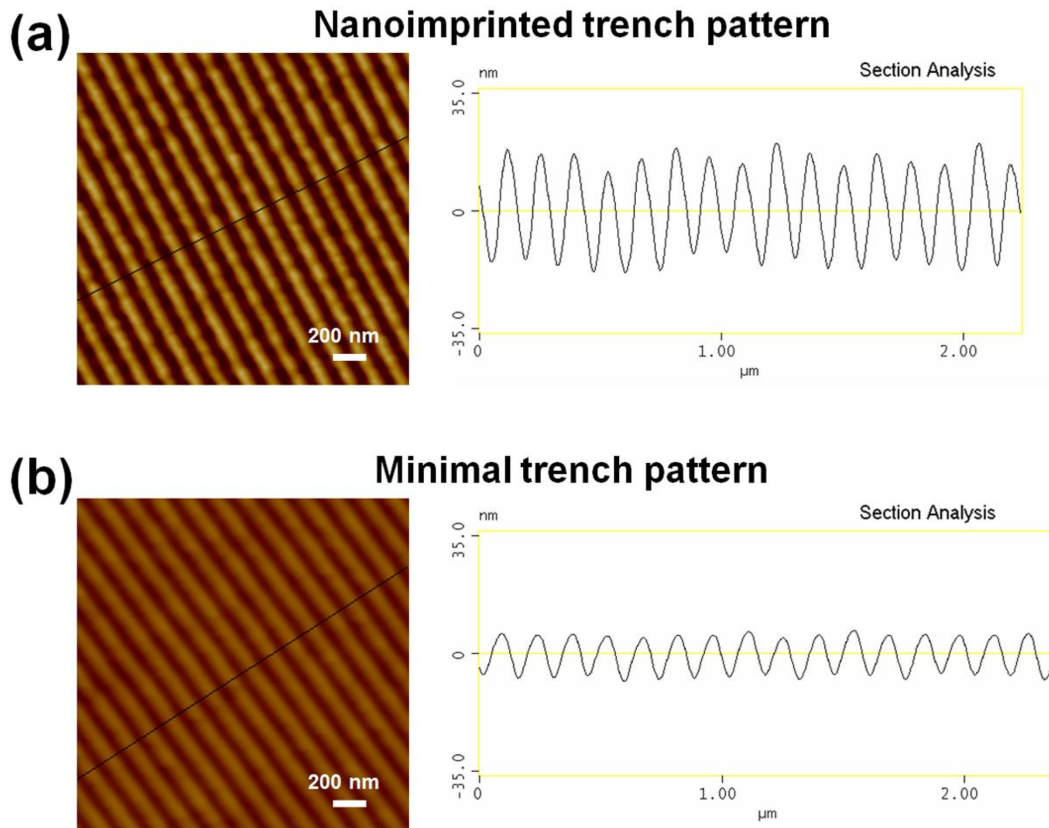

Figure 3.6 SFM height images and height profiles of patterned trench surfaces. (a) Nanoimprinted trench pattern. (b) Minimal trench pattern.

3.3.2 GISAXS Study of Hexagonal Arrays on Minimal Trench Patterns

Figure 3.7a–f shows the 2-D GISAXS patterns of the PS-*b*-PEO thin film on the minimal trench pattern at $\Psi = 0°$, where q_y is the in-plane scattering vector (parallel to the film surface) and q_z is the out-of-plane scattering vector (normal to the film surface). Initially, α_i was set at 0.18° (Figure 3.7a), which is above the critical angle of the polymer film ($\alpha_c = 0.16°$),[47] but below that of the silicon substrate (0.22°), to achieve full penetration of the X-ray beam into the film. In this case, the strong vertical streaks arising from the minimal trench pattern were observed. These streaks were also accompanied by an arc-shaped pattern due to the intersection of the truncation rods with the Ewald sphere, which is characteristic of 2-D GISAXS patterns when the X-ray beam is aligned with the grating line direction.[51, 52] It should be noted that the arc shape is very sensitive to the alignment of the X-ray beam with respect to the trench direction.[51, 53, 54] To mitigate the scattering from the minimal trench pattern, α_i was gradually decreased from 0.18° to 0.02°, so that Bragg rods (reflections extended in the vertical direction), as indicated by the arrows in Figure 3.7b, from the PS-*b*-PEO microdomains appeared at $\alpha_i = 0.10°$. The corresponding in-plane profiles from the 2-D GISAXS patterns (Figure 3.7a–f) are shown in Figure 3.7g. At $\alpha_i = 0.18°$, the reflections from hexagonal arrays of cylindrical microdomains in the PS-*b*-PEO thin film were hidden by the strong reflections arising from the minimal trench pattern, as mentioned above. However, when α_i was lowered to 0.10°, the very weak first-order peak corresponding to the (10) reflection of hexagonal arrays of cylindrical microdomains appeared at $q_y = 0.162$ nm^{-1} (dashed line in Figure 3.7g), eventually showing the highest relative intensity at $\alpha_i = 0.02°$. The domain spacing of the (10) plane at $\Psi = 0°$, $d_{(10),\Psi=0°} = 2\pi/q_y$, was calculated to be 38.8 nm from the position of the (10) reflection. The

higher-order peaks of the (10) reflection were not observed at $\Psi = 0°$, but they could be detected at $\Psi = 60°$, as discussed below.

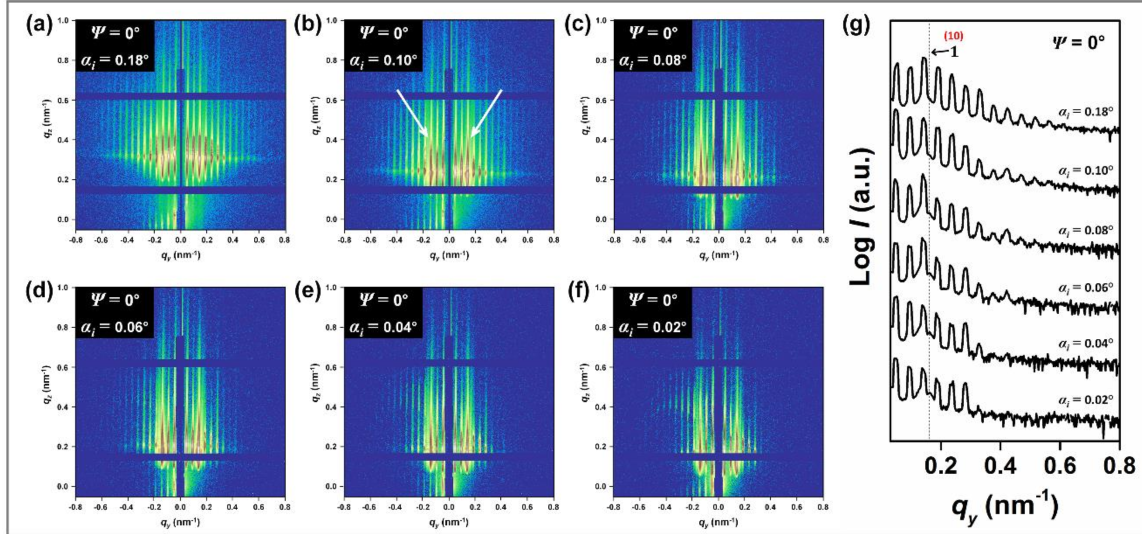

Figure 3.7 (a–f) 2-D GISAXS patterns of a PS-*b*-PEO thin film on a minimal trench pattern taken at a fixed $\Psi = 0°$ while varying α_i: (a) $\alpha_i = 0.18°$, (b) $\alpha_i = 0.10°$, (c) $\alpha_i = 0.08°$, (d) $\alpha_i = 0.06°$, (e) $\alpha_i = 0.04°$, and (f) $\alpha_i = 0.02°$. The white arrows in (b) indicate the first-order reflections arising from the hexagonal arrays of cylindrical microdomains in the PS-*b*-PEO film on the minimal trench pattern. (g) In-plane scattering profiles corresponding to a horizontal cut of (a–f) at $q_z = 0.305$ nm^{-1} ($\alpha_i = 0.18°$), 0.236 nm^{-1} ($\alpha_i = 0.10°$), 0.212 nm^{-1} ($\alpha_i = 0.08°$), 0.196 nm^{-1} ($\alpha_i = 0.06°$), 0.189 nm^{-1} ($\alpha_i = 0.04°$), and 0.183 nm^{-1} ($\alpha_i = 0.02°$), respectively. The dashed line indicates the first-order peak corresponding to the (10) reflection of the hexagonal arrays of PS-*b*-PEO microdomains.

Figure 3.8a–f shows the 2-D GISAXS patterns of the PS-*b*-PEO thin film on the minimal trench pattern at $\Psi = 60°$. In this case, the X-ray beam was parallel to the (01) planes of the hexagonal arrays. However, strong scattering arising from the minimal trench pattern was not observed because the direction of the X-ray beam and direction of the trench pattern were not the same. To compare the internal structure and surface morphology, α_i was varied from 0.20° to 0.10°, i.e. above and below α_c. As seen in Figure 3.8a–f, Bragg rods corresponding to the PS-*b*-PEO microdomains were clearly observed at

all α_i. Figure 3.8g shows the corresponding in-plane profiles. At $\alpha_i = 0.20°$, which is above α_c, four peaks with scattering vector ratios of 1:2:3:4 relative to the first-order peak were observed and were assigned to the (01), (02), (03), and (04) reflections, respectively. This result indicates that the well-defined (01) plane of hexagonal arrays of cylindrical microdomains oriented normal to the film surface persists throughout the film over the entire area investigated at $\Psi = 60°$. The domain spacing of the (01) plane at $\Psi = 60°$, $d_{(01),\Psi=60°}$, was calculated to be 45.9 nm from the (01) reflection. This $d_{(01),\Psi=60°}$ of 45.9 nm is larger than $d_{(10),\Psi=0°}$ of 38.8 nm and will be discussed in more detail later. When α_i was gradually decreased from 0.20° to 0.10°, all reflections were maintained at the identical positions of q_y, indicating that there is no difference between the internal structure and surface morphology. However, the (01) reflection showed a scattering shoulder (indicated by the arrows in Figure 3.8g) with increasing relative intensity, as α_i increased. This observation can be attributed to frustration of BCP microdomains. Although the trench width of the minimal trench pattern is commensurate with L_0, the value of 3.0, the trench pitch is not commensurate with L_0, the value of 3.7 (Table 3.1). This incommensurate condition imposes frustration on the hexagonal arrays of PS-*b*-PEO microdomains that must stretch or compress to accommodate the topographic constraints at the base of the trench. The PS-*b*-PEO microdomains at the top of the trench (near the air/polymer interface), on the other hand, can order with minimal constraints. We note that the scattering shoulders at the (02) and (03) reflections are also related to the shoulder at the (01) reflection. A complete understanding of the scattering profiles in Figure 3.8g would require simulations or fitting of the 2-D scattering images in Figure 3.8a-f, which lies outside of the scope of this study.

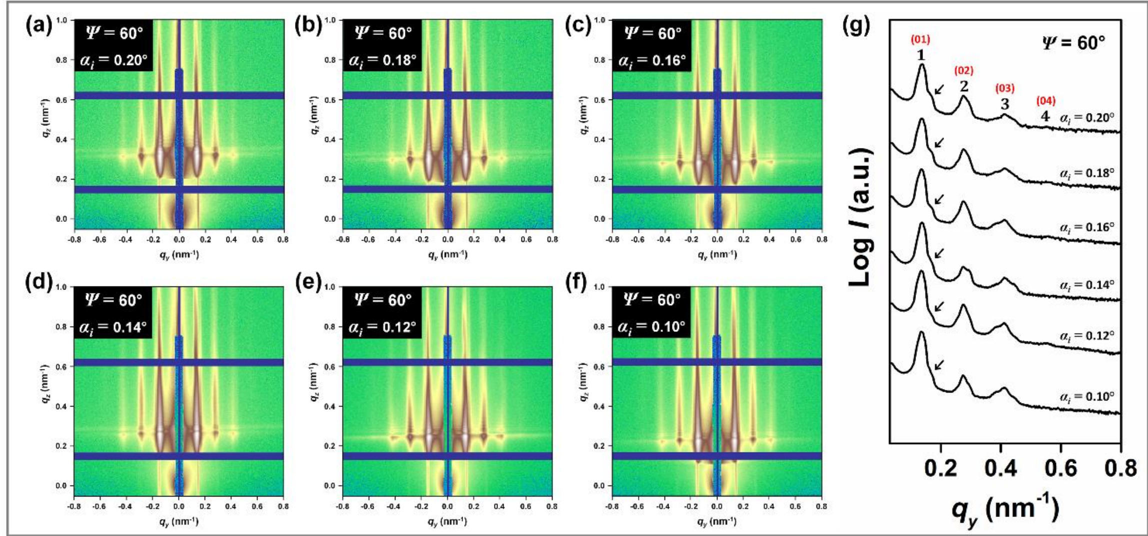

Figure 3.8 (a–f) 2-D GISAXS patterns of a PS-*b*-PEO thin film on a minimal trench pattern at $\Psi = 60°$. To compare the internal structure and surface morphology, α_i was varied: (a) $\alpha_i = 0.20°$, (b) $\alpha_i = 0.18°$, (c) $\alpha_i = 0.16°$, (d) $\alpha_i = 0.14°$, (e) $\alpha_i = 0.12°$, and (f) $\alpha_i = 0.10°$. (g) In-plane scattering profiles corresponding to a horizontal cut of (a–f) at $q_z = 0.316$ nm^{-1} ($\alpha_i = 0.20°$), 0.303 nm^{-1} ($\alpha_i = 0.18°$), 0.287 nm^{-1} ($\alpha_i = 0.16°$), 0.261 nm^{-1} ($\alpha_i = 0.14°$), 0.247 nm^{-1} ($\alpha_i = 0.12°$), and 0.223 nm^{-1} ($\alpha_i = 0.10°$), respectively. The arrows indicate a scattering shoulder at the (01) reflection.

Figure 3.9 shows the 2-D GISAXS patterns of the PS-*b*-PEO thin films on the minimal trench pattern and the corresponding in-plane profiles at $\Psi = 30°$ (Figure 3.9a–c) and 90° (Figure 3.9d–f), respectively. In both cases, the films were measured at $\alpha_i = 0.18°$ ($> \alpha_c$) and 0.12° ($< \alpha_c$) to compare the internal structure and surface morphology. Compared with the 2-D GISAXS patterns at $\Psi = 60°$, there is a marked change in the scattering profiles at $\Psi = 30°$ and 90°, with strong (11) and $(\bar{1}2)$ reflections, respectively. The reflections were analyzed based on the corresponding in-plane scattering profiles, as shown in Figure 3.9c. At $\alpha_i = 0.18°$, the observed peaks were found to have scattering vector ratios of $1:\sqrt{3}:\sqrt{7}:\sqrt{12}:\sqrt{27}$ relative to the first-order peak and were assigned to the (10), (11), (21), (22), and (33) reflections, respectively. For a perfect single hexagonal array on the

minimal trench pattern (Figure 3.3e), only the (11) reflection and the corresponding higher order peaks ((22), (33), …) should be present in a scattering profile at $\Psi = 30°$, since, in this case, the direction of the X-ray beam is parallel to the (11) plane. Indeed, the strong (11) reflection with its higher scattering orders, such as the (22) and (33) reflections, was observed in the scattering profiles at $\Psi = 30°$ (Figure 3.9c). However, the vestiges of broad (10) and (21) reflections suggest that the volume of the film sampled does not consist of a single grain of hexagonal arrays of cylindrical microdomains oriented normal to the film surface with the (10) plane aligned parallel to the trench direction; grains of other orientations of hexagonal arrays with short-range ordering must be present. Nonetheless, it is evident that the intensity of the (11) reflection significantly outweighs the intensity of the (10) reflection at $\Psi = 30°$. This result indicates that the well-defined (11) plane of hexagonal arrays of cylindrical microdomains oriented normal to the film surface is dominant over the area examined at $\Psi = 30°$. The domain spacing of the (11) plane at $\Psi = 30°$, $d_{(11),\Psi=30°}$, was calculated to be 26.0 nm from the (11) reflection. At $\alpha_i = 0.12°$, the peak positions were found to remain unchanged compared to those at $\alpha_i = 0.18°$, showing that the surface morphology is identical to the internal structure. The 2-D GISAXS patterns at $\Psi = 90°$ (Figure 3.9d,e) were similar to those at $\Psi = 30°$ (Figure 3.9a,b), but the peaks were found to be broader at $\Psi = 90°$. The corresponding in-plane profiles are shown in Figure 3.9f. At both $\alpha_i = 0.18°$ and 0.12°, the five peaks were observed with scattering vector ratios of 1:$\sqrt{3}$:$\sqrt{7}$:$\sqrt{12}$:$\sqrt{27}$ relative to the first-order peak and were assigned to the (01), $(\bar{1}2)$, $(\bar{1}3)$, $(\bar{2}4)$, and $(\bar{3}6)$ reflections, respectively. Similar to the in-plane scattering profiles at $\Psi = 30°$, the $(\bar{1}2)$ reflection is stronger than the (01) reflection at $\Psi = 90°$. However, the vestiges of broad (01) and $(\bar{1}3)$ reflections were also observed at $\Psi =$

90°, confirming that, while a few smaller grains with different orientations of hexagonal arrays exist, the well-defined $(\bar{1}2)$ plane of hexagonal arrays of cylindrical microdomains oriented normal to the film surface predominates over the area examined at $\Psi = 90°$. The domain spacing of the $(\bar{1}2)$ plane at $\Psi = 90°$, $d_{(\bar{1}2),\Psi=90°}$, was calculated to be 26.4 nm from the $(\bar{1}2)$ reflection. Interestingly, scattering shoulders (indicated by the arrows in Figure 3.9f) were observed on the left of the $(\bar{1}2)$ reflections, i.e. at smaller scattering vectors, at both $\alpha_i = 0.18°$ and 0.12°, suggesting a larger or stretched domain spacing at $\Psi = 90°$. This is likely due to the absence of topographic restraints for the $(\bar{1}2)$ planes being perpendicular to the trench direction, as will be discussed in more detail below.

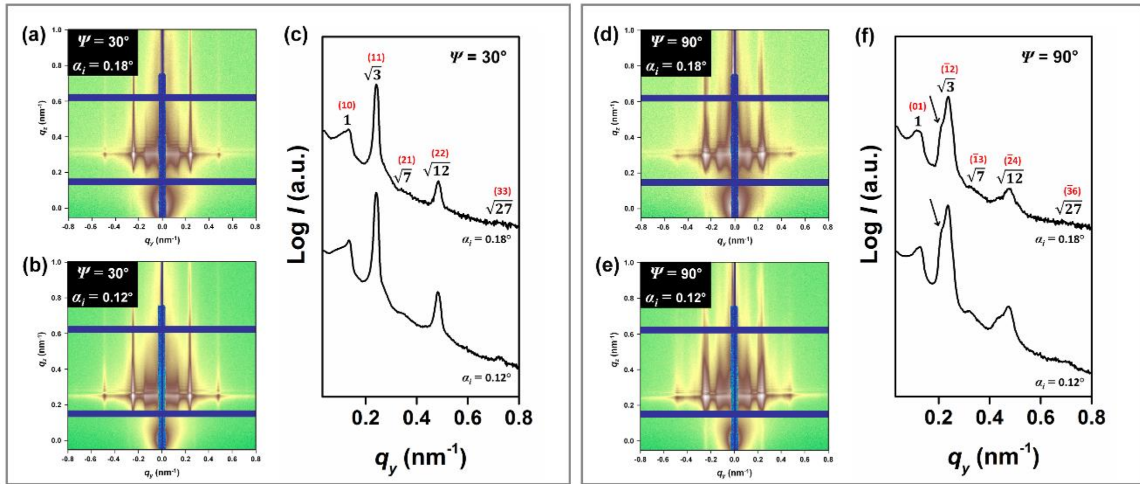

Figure 3.9 (a,b) 2-D GISAXS patterns of a PS-*b*-PEO thin film on a minimal trench pattern at $\Psi = 30°$ with $\alpha_i = 0.18°$ (a) and 0.12° (b). (c) In-plane scattering profiles corresponding to a horizontal cut of (a,b) at $q_z = 0.294$ nm^{-1} ($\alpha_i = 0.18°$) and 0.243 nm^{-1} ($\alpha_i = 0.12°$), respectively. (d,e) 2-D GISAXS patterns of a PS-*b*-PEO thin film on a minimal trench pattern at $\Psi = 90°$ with $\alpha_i = 0.18°$ (d) and 0.12° (e). (f) In-plane scattering profiles corresponding to a horizontal cut of (d,e) at $q_z = 0.307$ nm^{-1} ($\alpha_i = 0.18°$) and 0.252 nm^{-1} ($\alpha_i = 0.12°$), respectively. The arrows indicate a scattering shoulder at the $(\bar{1}2)$ reflection.

Figure 3.10a shows a schematic illustration of hexagonal arrays of PS-*b*-PEO microdomains guided by the minimal trench pattern, where the confined and unconfined directions are defined as the X- and Y-axes, respectively. It should be noted that each direction is not related to the magnitude of the confinement effect. When the BCP microdomains are guided by a 1-D template, like the minimal trench pattern discussed here, the microdomains can be more easily distorted in the unconfined direction than in the confined direction, due to the absence of topographic constraints, allowing the domain spacing to change so as to relax the frustration imposed which also allows for wider positional variations in the unconfined direction.[55] This, more than likely, affects the domain spacing of the (10), (11), (01), and $(\bar{1}2)$ planes, as shown in Figure 3.10b, so that $d_{(10),\Psi=0^\circ} = d_{(01),\Psi=60^\circ}$ and $d_{(11),\Psi=30^\circ} = d_{(\bar{1}2),\Psi=90^\circ}$, which holds for a perfect hexagonal array, are no longer valid for the hexagonal arrays of cylindrical microdomains on the minimal trench pattern. To investigate distortions of hexagonal arrays of cylindrical microdomains on the minimal trench pattern, the measured principal domain spacing of the different lattice planes, as determined from the GISAXS patterns, were compared in Table 3.2. For the (10) and (01) planes, $d_{(01),\Psi=60^\circ}$ of 45.9 nm was larger than $d_{(10),\Psi=0^\circ}$ of 38.8 nm, indicating a distorted hexagonal array. It is noted that the (10) planes are oriented parallel to the trench direction and, thus, $d_{(10),\Psi=0^\circ}$ is expected to reflect the confinement effect by the trench width and trench pitch. However, the confinement effects should be significantly weaker for the (01) planes, since the (01) planes have an angle of 60 degrees with respect to the trench direction, which likely caused an increased domain spacing in comparison to that of the (10) planes. In contrast, the (11) and $(\bar{1}2)$ planes showed a similar difference in the confinement effect. While the difference between $d_{(11),\Psi=30^\circ}$ of 26.0 nm and $d_{(\bar{1}2),\Psi=90^\circ}$

of 26.4 nm was negligible (Table 3.2), an additional shoulder was observed on the left of the $(\bar{1}2)$ reflections at Ψ = 90° at both α_i = 0.18° and 0.12° (indicated by the arrows in Figure 3.9f), whereas only a single (11) reflection was found at Ψ = 30° (Figure 3.9c). This shoulder corresponds to a domain spacing of ~29 nm and likely reflects the stretched domain spacing of the $(\bar{1}2)$ plane in the unconfined direction on the minimal trench pattern, as shown in Figure 3.10b.

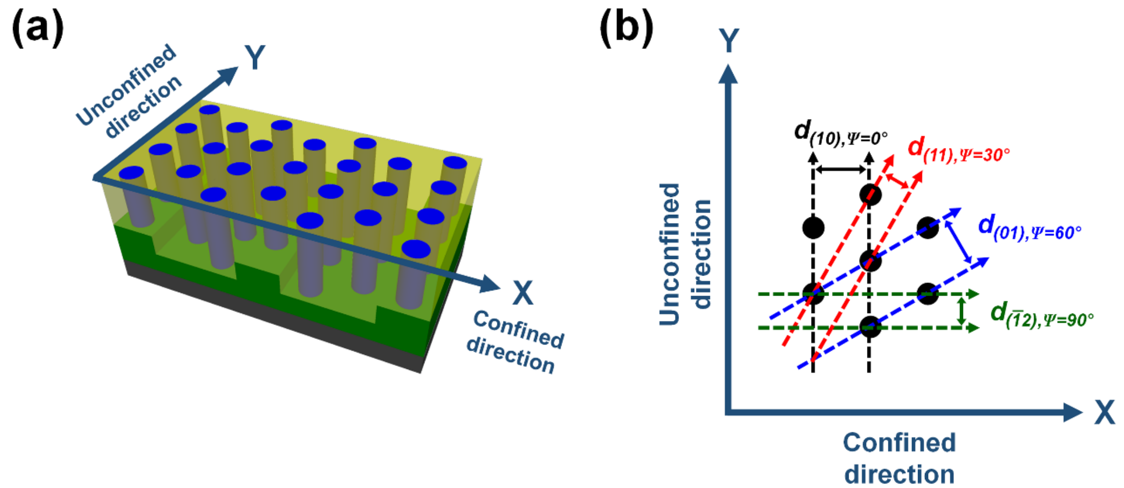

Figure 3.10 (a) Schematic illustration of hexagonal arrays of cylindrical microdomains guided by the minimal trench pattern. The X- and Y-axes indicate the confined and unconfined directions, respectively. (b) Schematic representation of the domain spacing of hexagonal planes with a different Ψ on XY directions defined in (a). XY directions are not related to the magnitude of the confinement effect. For a perfect hexagonal array, $d_{(10),\Psi=0°} = d_{(01),\Psi=60°}$ and $d_{(11),\Psi=30°} = d_{(\bar{1}2),\Psi=90°}$.

Table 3.2 Measured principal domain spacing of lattice planes of the hexagonal arrays on the minimal trench pattern at a different Ψ, as determined from the GISAXS patterns.

lattice plane	Ψ (deg.)	domain spacing (nm)
(10)	0	$d_{(10),\Psi=0°} = 38.8$
(11)	30	$d_{(11),\Psi=30°} = 26.0$
(01)	60	$d_{(01),\Psi=60°} = 45.9$
$(\bar{1}2)$	90	$d_{(\bar{1}2),\Psi=90°} = 26.4$

3.3.3 GISAXS Study of Hexagonal Arrays on Unpatterned Flat Substrates

GISAXS measurements were also performed on hexagonal arrays of cylindrical microdomains in PS-*b*-PEO thin films on a flat silicon substrate (the sample in Figure 3.3a). For a comparison to the GISAXS measurements of the films on the minimal trench pattern, the films on the flat silicon substrate were also rotated about the surface normal. Since well-defined specific planes of hexagonal arrays over macroscopic length scales were absent, the selection of $\Psi = 0°$ was arbitrary. From this point, the sample stage was rotated 30°, 60°, and 90°. At all Ψ, α_i was fixed at 0.18°, which is above α_c, so that the X-ray beam penetrated the entire film. As seen in Figure 3.11a, all 2-D GISAXS patterns showed identical Bragg rods arising from the PS-*b*-PEO microdomains. The corresponding in-plane profiles are shown in Figure 3.11b. At all Ψ, four peaks were observed with scattering vector ratios of $1{:}\sqrt{3}{:}\sqrt{4}{:}\sqrt{7}$ relative to the first-order peak and were assigned to the (10), (11), (20), and (21) reflections, respectively. This result clearly indicates that the hexagonal

arrays of cylindrical microdomains oriented normal to the film surface on the flat silicon substrate are randomly oriented in the PS-*b*-PEO film, although the microdomains are laterally ordered.

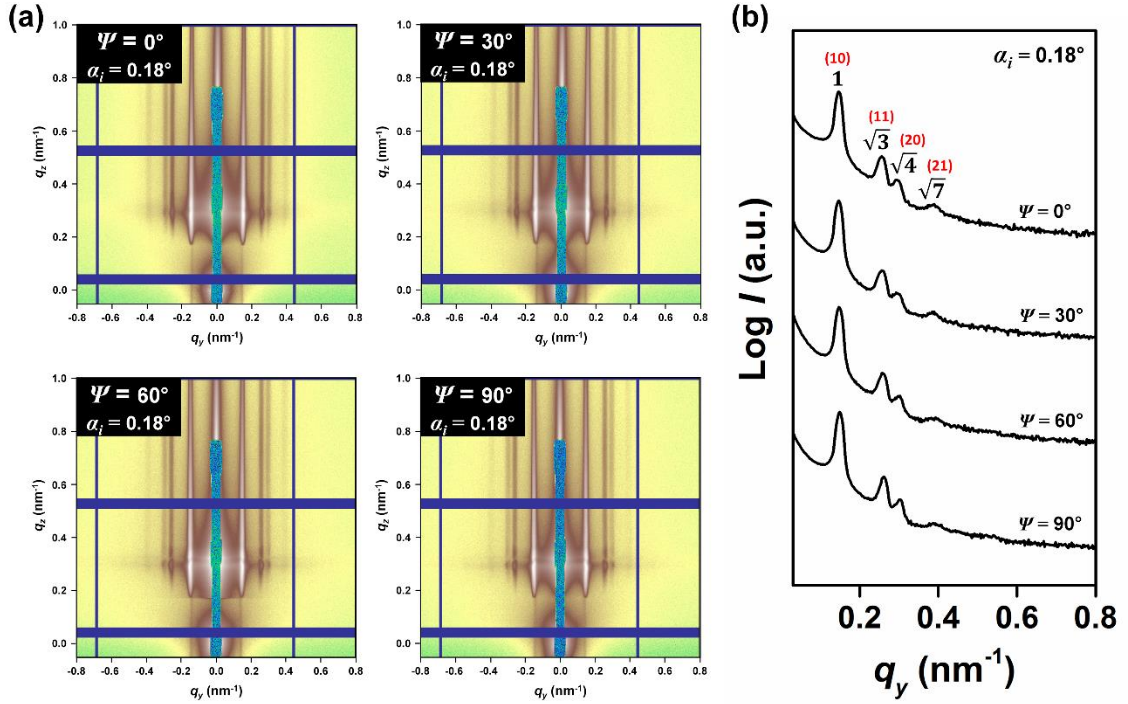

Figure 3.11 (a) 2-D GISAXS patterns of a PS-*b*-PEO thin film on a flat silicon substrate. The sample was first measured at an arbitrary sample rotation, which is defined as $\Psi = 0°$. From this point, the sample stage was rotated 30°, 60°, and 90°. At all Ψ, α_i was set at 0.18°. (b) In-plane scattering profiles corresponding to a horizontal cut of (a) at $q_z = 0.293$ nm^{-1}. The domain spacing of the (10) plane was calculated to be 42.9 nm from the (10) reflection.

3.4 Conclusions

In summary, the minimal trench patterns with the depth of 11 nm ($0.3L_0$), width of 106 nm ($3.0L_0$), and pitch of 132 nm ($3.7L_0$) have been successfully used to guide the self-assembly of PS-*b*-PEO thin films under SVA, achieving well-defined hexagonal arrays of cylindrical microdomains oriented normal to the film surface over macroscopic length scales (~1×1 cm^2), where the (10) planes of hexagonal arrays are predominantly oriented parallel to the underlying trench direction. Since the minimal trench pattern was buried under self-assembled BCP microdomains, it allowed us to elucidate the internal structure and lateral ordering of hexagonal arrays using GISAXS with the rotation of the sample stage, by avoiding strong scattering arising from the underlying patterned surface. The hexagonal arrays of cylindrical microdomains on the minimal trench pattern were found to be distorted. A combination of the absence of topographic constraints in the unconfined direction on the minimal trench pattern with the frustration of PS-*b*-PEO microdomains, arising from the incommensurability between the trench pitch and L_0 near the base of the trench, can explain this distortion. The quantitative analysis in this work provides an in-depth understanding of the morphological characteristic and lateral ordering of self-assembled BCP microdomains guided by 1-D topographic patterns and may provide a platform for the characterization of BCP morphologies directed by 2-D or 3-D topographic patterns using GISAXS.

3.5 References

1. Bang, J.; Jeong, U.; Ryu, D. Y.; Russell, T. P.; Hawker, C. J. Block Copolymer Nanolithography: Translation of Molecular Level Control to Nanoscale Patterns. *Adv. Mater.* **2009**, *21*, 4769-4792.

2. Hu, H.; Gopinadhan, M.; Osuji, C. O. Directed Self-Assembly of Block Copolymers: A Tutorial Review of Strategies for Enabling Nanotechnology with Soft Matter. *Soft Matter* **2014**, *10*, 3867-3889.

3. Ruiz, R.; Dobisz, E.; Albrecht, T. R. Rectangular Patterns Using Block Copolymer Directed Assembly for High Bit Aspect Ratio Patterned Media. *ACS Nano* **2011**, *5*, 79-84.

4. Ross, C. A.; Cheng, J. Y. Patterned Magnetic Media Made by Self-Assembled Block-Copolymer Lithography. *MRS Bull.* **2008**, *33*, 838-845.

5. Tsai, H.; Pitera, J. W.; Miyazoe, H.; Bangsaruntip, S.; Engelmann, S. U.; Liu, C.-C.; Cheng, J. Y.; Bucchignano, J. J.; Klaus, D. P.; Joseph, E. A.; Sanders, D. P.; Colburn, M. E.; Guillorn, M. A. Two-Dimensional Pattern Formation Using Graphoepitaxy of PS-*b*-PMMA Block Copolymers for Advanced FinFET Device and Circuit Fabrication. *ACS Nano* **2014**, *8*, 5227-5232.

6. Yang, X.; Wan, L.; Xiao, S.; Xu, Y.; Weller, D. K. Directed Block Copolymer Assembly versus Electron Beam Lithography for Bit-Patterned Media with Areal Density of 1 Terabit/Inch^2 and Beyond. *ACS Nano* **2009**, *3*, 1844-1858.

7. Kim, H.-C.; Rettner, C., T.; Sundström, L. Fabrication of 20 nm Half-Pitch Gratings by Corrugation-Directed Self-Assembly. *Nanotechnology* **2008**, *19*, 235301.

8. Ji, S.; Wan, L.; Liu, C.-C.; Nealey, P. F. Directed Self-Assembly of Block Copolymers on Chemical Patterns: A Platform for Nanofabrication. *Prog. Polym. Sci.* **2016**, *54–55*, 76-127.

9. Segalman, R. A. Patterning with Block Copolymer Thin Films. *Mater. Sci. Eng. R* **2005**, *48*, 191-226.

10. Stoykovich, M. P.; Nealey, P. F. Block Copolymers and Conventional Lithography. *Mater. Today* **2006**, *9*, 20-29.

11. Segalman, R. A.; Yokoyama, H.; Kramer, E. J. Graphoepitaxy of Spherical Domain Block Copolymer Films. *Adv. Mater.* **2001**, *13*, 1152-1155.

12. Ruiz, R.; Kang, H.; Detcheverry, F. A.; Dobisz, E.; Kercher, D. S.; Albrecht, T. R.; de Pablo, J. J.; Nealey, P. F. Density Multiplication and Improved Lithography by Directed Block Copolymer Assembly. *Science* **2008**, *321*, 936-939.

13. Angelescu, D. E.; Waller, J. H.; Adamson, D. H.; Deshpande, P.; Chou, S. Y.; Register, R. A.; Chaikin, P. M. Macroscopic Orientation of Block Copolymer Cylinders in Single-Layer Films by Shearing. *Adv. Mater.* **2004**, *16*, 1736-1740.

14. Berry, B. C.; Bosse, A. W.; Douglas, J. F.; Jones, R. L.; Karim, A. Orientational Order in Block Copolymer Films Zone Annealed Below the Order−Disorder Transition Temperature. *Nano Lett.* **2007**, *7*, 2789-2794.

15. Sundrani, D.; Darling, S. B.; Sibener, S. J. Hierarchical Assembly and Compliance of Aligned Nanoscale Polymer Cylinders in Confinement. *Langmuir* **2004**, *20*, 5091-5099.

16. Jung, Y. S.; Ross, C. A. Orientation-Controlled Self-Assembled Nanolithography Using a Polystyrene−Polydimethylsiloxane Block Copolymer. *Nano Lett.* **2007**, *7*, 2046-2050.

17. Chai, J.; Buriak, J. M. Using Cylindrical Domains of Block Copolymers to Self-Assemble and Align Metallic Nanowires. *ACS Nano* **2008**, *2*, 489-501.

18. Cheng, J. Y.; Mayes, A. M.; Ross, C. A. Nanostructure Engineering by Templated Self-Assembly of Block Copolymers. *Nat. Mater.* **2004**, *3*, 823-828.

19. Salaun, M.; Zelsmann, M.; Archambault, S.; Borah, D.; Kehagias, N.; Simao, C.; Lorret, O.; Shaw, M. T.; Sotomayor Torres, C. M.; Morris, M. A. Fabrication of Highly Ordered Sub-20 nm Silicon Nanopillars by Block Copolymer Lithography Combined with Resist Design. *J. Mater. Chem. C* **2013**, *1*, 3544-3550.

20. Choi, E.; Park, S.; Ahn, H.; Lee, M.; Bang, J.; Lee, B.; Ryu, D. Y. Substrate-Independent Lamellar Orientation in High-Molecular-Weight Polystyrene-*b*-Poly(Methyl Methacrylate) Films: Neutral Solvent Vapor and Thermal Annealing Effect. *Macromolecules* **2014**, *47*, 3969-3977.

21. Kim, S.; Shin, D. O.; Choi, D.-G.; Jeong, J.-R.; Mun, J. H.; Yang, Y.-B.; Kim, J. U.; Kim, S. O.; Jeong, J.-H. Graphoepitaxy of Block-Copolymer Self-Assembly Integrated with Single-Step Zno Nanoimprinting. *Small* **2012**, *8*, 1563-1569.

22. Xiao, S.; Yang, X.; Edwards, E. W.; La, Y.-H.; Nealey, P. F. Graphoepitaxy of Cylinder-Forming Block Copolymers for Use as Templates to Pattern Magnetic Metal Dot Arrays. *Nanotechnology* **2005**, *16*, S324-S329.

23. Tavakkoli K. G., A.; Gotrik, K. W.; Hannon, A. F.; Alexander-Katz, A.; Ross, C. A.; Berggren, K. K. Templating Three-Dimensional Self-Assembled Structures in Bilayer Block Copolymer Films. *Science* **2012**, *336*, 1294-1298.

24. Rho, Y.; Aissou, K.; Mumtaz, M.; Kwon, W.; Pécastaings, G.; Mocuta, C.; Stanecu, S.; Cloutet, E.; Brochon, C.; Fleury, G.; Hadziioannou, G. Laterally Ordered Sub-10 nm Features Obtained from Directed Self-Assembly of Si-Containing Block Copolymer Thin Films. *Small* **2015**, *11*, 6377-6383.

25. Cushen, J.; Wan, L.; Blachut, G.; Maher, M. J.; Albrecht, T. R.; Ellison, C. J.; Willson, C. G.; Ruiz, R. Double-Patterned Sidewall Directed Self-Assembly and Pattern Transfer of Sub-10 nm PTMSS-*b*-PMOST. *ACS Appl. Mater. Interfaces* **2015**, *7*, 13476-13483.

26. Hong, S. W.; Gu, X.; Huh, J.; Xiao, S.; Russell, T. P. Circular Nanopatterns over Large Areas from the Self-Assembly of Block Copolymers Guided by Shallow Trenches. *ACS Nano* **2011**, *5*, 2855-2860.

27. Xiao, S.; Yang, X.; Steiner, P.; Hsu, Y.; Lee, K.; Wago, K.; Kuo, D. Servo-Integrated Patterned Media by Hybrid Directed Self-Assembly. *ACS Nano* **2014**, *8*, 11854-11859.

28. Sun, Z.; Chen, Z.; Zhang, W.; Choi, J.; Huang, C.; Jeong, G.; Coughlin, E. B.; Hsu, Y.; Yang, X.; Lee, K. Y.; Kuo, D. S.; Xiao, S.; Russell, T. P. Directed Self-Assembly of Poly(2-Vinylpyridine)-*b*-Polystyrene-*b*-Poly(2-Vinylpyridine) Triblock Copolymer with Sub-15 nm Spacing Line Patterns Using a Nanoimprinted Photoresist Template. *Adv. Mater.* **2015**, *27*, 4364-4370.

29. Fasolka, M. J.; Harris, D. J.; Mayes, A. M.; Yoon, M.; Mochrie, S. G. J. Observed Substrate Topography-Mediated Lateral Patterning of Diblock Copolymer Films. *Phys. Rev. Lett.* **1997**, *79*, 3018-3021.

30. Park, S.; Lee, D. H.; Xu, J.; Kim, B.; Hong, S. W.; Jeong, U.; Xu, T.; Russell, T. P. Macroscopic 10-Terabit-Per-Square-Inch Arrays from Block Copolymers with Lateral Order. *Science* **2009**, *323*, 1030-1033.

31. Pandav, G.; Durand, W. J.; Ellison, C. J.; Willson, C. G.; Ganesan, V. Directed Self Assembly of Block Copolymers Using Chemical Patterns with Sidewall Guiding Lines, Backfilled with Random Copolymer Brushes. *Soft Matter* **2015**, *11*, 9107-9114.

32. Peng, M.; Ma, S.; Hu, J.; Wang, R. Hierarchical Nanostructures of Diblock Copolymer Thin Films Directed by a Saw-Toothed Substrate. *Soft Matter* **2015**, *11*, 6642-6651.

33. Choi, J.; Huh, J.; Carter, K. R.; Russell, T. P. Directed Self-Assembly of Block Copolymer Thin Films Using Minimal Topographic Patterns. *ACS Nano* **2016**, *10*, 7915-7925.

34. Park, S.-M.; Stoykovich, M. P.; Ruiz, R.; Zhang, Y.; Black, C. T.; Nealey, P. F. Directed Assembly of Lamellae-Forming Block Copolymers by Using Chemically and Topographically Patterned Substrates. *Adv. Mater.* **2007**, *19*, 607-611.

35. Segalman, R. A.; Hexemer, A.; Kramer, E. J. Edge Effects on the Order and Freezing of a 2D Array of Block Copolymer Spheres. *Phys. Rev. Lett.* **2003**, *91*, 196101.

36. Kim, S. H.; Misner, M. J.; Xu, T.; Kimura, M.; Russell, T. P. Highly Oriented and Ordered Arrays from Block Copolymers via Solvent Evaporation. *Adv. Mater.* **2004**, *16*, 226-231.

37. Lee, B.; Park, I.; Yoon, J.; Park, S.; Kim, J.; Kim, K.-W.; Chang, T.; Ree, M. Structural Analysis of Block Copolymer Thin Films with Grazing Incidence Small-Angle X-Ray Scattering. *Macromolecules* **2005**, *38*, 4311-4323.

38. Paik, M. Y.; Bosworth, J. K.; Smilges, D.-M.; Schwartz, E. L.; Andre, X.; Ober, C. K. Reversible Morphology Control in Block Copolymer Films via Solvent Vapor Processing: An in Situ GISAXS Study. *Macromolecules* **2010**, *43*, 4253-4260.

39. Gu, X.; Gunkel, I.; Hexemer, A.; Gu, W.; Russell, T. P. An in Situ Grazing Incidence X-Ray Scattering Study of Block Copolymer Thin Films During Solvent Vapor Annealing. *Adv. Mater.* **2014**, *26*, 273-281.

40. Majewski, P. W.; Yager, K. G. Latent Alignment in Pathway-Dependent Ordering of Block Copolymer Thin Films. *Nano Lett.* **2015**.

41. Qiang, Z.; Zhang, L.; Stein, G. E.; Cavicchi, K. A.; Vogt, B. D. Unidirectional Alignment of Block Copolymer Films Induced by Expansion of a Permeable Elastomer During Solvent Vapor Annealing. *Macromolecules* **2014**, *47*, 1109-1116.

42. Stein, G. E.; Kramer, E. J.; Li, X.; Wang, J. Single-Crystal Diffraction from Two-Dimensional Block Copolymer Arrays. *Phys. Rev. Lett.* **2007**, *98*, 086101.

43. Stein, G. E.; Lee, W. B.; Fredrickson, G. H.; Kramer, E. J.; Li, X.; Wang, J. Thickness Dependent Ordering in Laterally Confined Monolayers of Spherical-Domain Block Copolymers. *Macromolecules* **2007**, *40*, 5791-5800.

44. Maret, M.; Tiron, R.; Chevalier, X.; Gergaud, P.; Gharbi, A.; Lapeyre, C.; Pradelles, J.; Jousseaume, V.; Fleury, G.; Hadziioannou, G.; Boudet, N.; Navarro, C. Probing Self-Assembly of Cylindrical Morphology Block Copolymer Using in Situ and ex Situ Grazing Incidence Small-Angle X-Ray Scattering: The Attractive Case of Graphoepitaxy. *Macromolecules* **2014**, *47*, 7221-7229.

45. Tavakkoli K. G, A.; Nicaise, S. M.; Gadelrab, K. R.; Alexander-Katz, A.; Ross, C. A.; Berggren, K. K. Multilayer Block Copolymer Meshes by Orthogonal Self-Assembly. *Nat Commun* **2016**, *7*, 10518.

46. Hong, S. W.; Huh, J.; Gu, X.; Lee, D. H.; Jo, W. H.; Park, S.; Xu, T.; Russell, T. P. Unidirectionally Aligned Line Patterns Driven by Entropic Effects on Faceted Surfaces. *Proc. Natl. Acad. Sci.* **2012**, *109*, 1402-1406.

47. Hong, S. W.; Voronov, D. L.; Lee, D. H.; Hexemer, A.; Padmore, H. A.; Xu, T.; Russell, T. P. Controlled Orientation of Block Copolymers on Defect-Free Faceted Surfaces. *Adv. Mater.* **2012**, *24*, 4278-4283.

48. Li, Y.; Peterson, J. J.; Jhaveri, S. B.; Carter, K. R. Patterned Polymer Films via Reactive Silane Infusion-Induced Wrinkling. *Langmuir* **2013**, *29*, 4632-4639.

49. Hexemer, A.; Bras, W.; Glossinger, J.; Schaible, E.; Gann, E.; Kirian, R.; MacDowell, A.; Church, M.; Rude, B.; Padmore, H. A SAXS/WAXS/GISAXS Beamline with Multilayer Monochromator. *J. Phys. Conf. Ser.* **2010**, *247*, 012007.

50. Park, H.-H.; Law, W. L.; Zhang, X.; Hwang, S.-Y.; Jung, S. H.; Shin, H.-B.; Kang, H. K.; Park, H.-H.; Hill, R. H.; Ko, C. K. Facile Size-Tunable Fabrication of Functional Tin Dioxide Nanostructures by Multiple Size Reduction Lithography. *ACS Appl. Mater. Interfaces* **2012**, *4*, 2507-2514.

51. Yan, M.; Gibaud, A. On the Intersection of Grating Truncation Rods with the Ewald Sphere Studied by Grazing-Incidence Small-Angle X-Ray Scattering. *J. Appl. Crystallogr.* **2007**, *40*, 1050-1055.

52. Rueda, D. R.; Martín-Fabiani, I.; Soccio, M.; Alayo, N.; Pérez-Murano, F.; Rebollar, E.; García-Gutiérrez, M. C.; Castillejo, M.; Ezquerra, T. A. Grazing-Incidence Small-Angle X-Ray Scattering of Soft and Hard Nanofabricated Gratings. *J. Appl. Crystallogr.* **2012**, *45*, 1038-1045.

53. Mikulík, P.; Jergel, M.; Baumbach, T.; Majková, E.; Pincík, E.; Luby, S.; Ortega, L.; Tucoulou, R.; Hudek, P.; Kostic, I. Coplanar and Non-Coplanar X-Ray Reflectivity Characterization of Lateral W/Si Multilayer Gratings. *J. Phys. D: Appl. Phys.* **2001**, *34*, A188.

54. Mishra, V.; Fredrickson, G. H.; Kramer, E. J. Effect of Film Thickness and Domain Spacing on Defect Densities in Directed Self-Assembly of Cylindrical Morphology Block Copolymers. *ACS Nano* **2012**, *6*, 2629-2641.

55. Cheng, J. Y.; Zhang, F.; Smith, H. I.; Vancso, G. J.; Ross, C. A. Pattern Registration between Spherical Block-Copolymer Domains and Topographical Templates. *Adv. Mater.* **2006**, *18*, 597-601.

CHAPTER 4

ORTHGONALLY ALIGNED BLOCK COPOLYMER LINE PATTERNS ON MINIMAL TOPOGRAPHIC PATTERNS

4.1 Introduction

Directed self-assembly (DSA) of block copolymers (BCPs) has gained widespread interest as one of the most promising solutions for overcoming resolution limitations in the current lithographic process in the semiconductor industry. This method provides opportunities to fabricate dense periodic/aperiodic nanostructures with sizes below 10 nm.[1-11] In the DSA process, BCP microdomains, such as lamellae, cylinders, or spheres, are typically guided by chemical[12-15] or topographic[16-19] patterns. Previous studies have shown that one of the key parameters to achieve high-quality BCP patterns on either chemical patterns or topographic patterns is the film thickness. For cylindrical microdomains on chemical patterns, Nealey and co-workers reported that the thickness of poly(styrene-*b*-methyl methacrylate) (PS-*b*-PMMA) films should be within 2 nm of the preferred quantized film thickness on striped chemical patterns to produce a single layer of defect-free line patterns of cylindrical microdomains.[20] The same group also studied the DSA of PS-*b*-PMMA thin films on spotted chemical patterns.[21] In this case, hexagonal arrays of cylindrical microdomains with a high degree of registration and perfection were achieved at the film thickness of 54 nm, when the pattern period was approximately commensurate with center-to-center distance between cylinders of the BCP in the bulk (L_l). However, the 30 nm and 70 nm thick films showed some defects and bridged cylinders at the surface of the films, respectively. Recently, Nealey and co-workers reported the

effect of film thickness on the DSA of a lamellar-forming PS-*b*-PMMA on stripe chemical patterns.[22]

As mentioned above, the film thickness plays an important role in producing uniformly ordered BCP patterns on topographic patterns. For deep topographic patterns, where the confinement depth is comparable to or larger than the natural period of the BCP in the bulk (L_0), Jeong and co-workers demonstrated that the thickness variations of PS-*b*-PMMA films within the trench patterns resulted in complex morphologies consisting of hexagonal arrays and line patterns of cylindrical microdomains.[23] Gopalan and co-workers demonstrated that the film thickness is critical for achieving laterally ordered hexagonal arrays of cylindrical microdomains in the trench patterns with the surfaces weakly preferential to one of the BCP blocks.[24] For minimal topographic patterns, where the confinement depth is much less than L_0, Russell and co-workers demonstrated that lateral ordering of hexagonal arrays of cylindrical microdomains on sapphire faceted substrates was lost when the film thickness of poly(styrene-*b*-ethylene oxide) (PS-*b*-PEO) was increased from 37 nm to 46 nm.[3] Recently, the same group reported that highly aligned PS-*b*-PEO line patterns of cylindrical microdomains on minimal trench patterns were collapsed when the film thickness was increased from 39 nm to 46 nm, resulting in typical fingerprint patterns.[25]

Particularly with the DSA of cylinder-forming BCPs on faceted substrates, another interesting phenomenon is that BCP line patterns can be aligned orthogonally to the underlying ridge direction by increasing the thickness of the BCP films.[26, 27] For faceted sapphire substrates, Russell and co-workers have shown that unidirectionally aligned line

patterns of cylindrical microdomains oriented orthogonally to the ridge direction can be generated over macroscopic length scales with increasing BCP film thickness from 38.0 nm to 47.5 nm.[26] In this system, the line patterns of cylindrical microdomains were truncated at the crests of the facets at the film thickness of 38.0 nm, while these microdomains were orthogonally aligned with respect to the ridge direction. However, the truncated microdomains could be connected across the facets with an increase in film thickness to 47.5 nm, so that macroscopically aligned line patterns oriented orthogonally to the ridge direction were achieved. This orthogonal alignment of BCP line patterns is attributed to the entropic penalties related to chain packing and the incommensurability between the pitch of the facets and L_0. In addition, the same group reported the effect of BCP film thickness on the orthogonal alignment of line patterns of cylindrical microdomains on faceted silicon substrates, where the geometry of the faceted silicon substrates is more asymmetric than that of the faceted sapphire substrates.[27] In this case, the BCP line patterns were oriented parallel to the ridge direction when the film thickness was 35.0 nm, but showed a tendency for being oriented almost orthogonal to the ridge direction at the thickness of 47.6 nm. However, in terms of lithography applications, a major challenge for the use of faceted substrates is pattern transfer of BCP templates to the underlying substrate due to the triangular groove structures of the facet.

For deep trench patterns, methods to produce orthogonally aligned BCP line patterns within the trenches have been studied.[28, 29] For example, Gopalan and co-workers demonstrated the generation of lamellar line patterns oriented orthogonally to the trench direction in deep trench patterns through the modification of interfacial interactions between BCPs and surfaces of the sidewall of the trenches.[29] In contrast, using corrugated

substrates with non-selective surfaces for both blocks, Kim and co-workers showed the orthogonal alignment of line patterns of lamellar microdomains in PS-*b*-PMMA thin films, where the line patterns span across the corrugated substrates.[30] They found that this orthogonal alignment was strongly sensitive to the relative BCP film thickness, to the depth of the corrugation, as well as to the pitch of the corrugated substrates. Recently, based on experimental and simulated studies, Berggren and co-workers demonstrated the orthogonal self-assembly of a cylinder-forming poly(styrene-*b*-dimethylsiloxane) (PS-*b*-PDMS) over line, concentric circle, and Y-junction patterned substrates.[31] In this case, the depth and surface property of the topographic patterns were critical to induce the orthogonal self-assembly process. These orthogonally aligned line patterns of BCP microdomains have potential to be used for the fabrication of integrated circuit interconnects,[4, 17] nanowire arrays,[29, 32] or bit-patterned media (BPM).[33] However, there are still many unanswered questions that may limit this promising approach to generate orthogonally aligned BCP line patterns on topographic patterns.

Here, we present the orthogonal alignment of PS-*b*-PEO line patterns of cylindrical microdomains with respect to trench direction on minimal trench patterns. We discovered that the thickness of PS-*b*-PEO films was found to be a critical parameter for inducing the orthogonal alignment. A single grain of line patterns of cylindrical microdomains with an orientation parameter of 0.997, as determined from grazing incidence small angle X-ray scattering (GISAXS) data, was produced in PS-*b*-PEO thin films at the thickness of 37.3 nm ($1.70L_0$) on minimal trench patterns with the depth of 15 nm ($0.68L_0$). Interestingly, this orthogonal alignment occurred for line patterns of cylindrical microdomains in PS-*b*-PDMS thin films on minimal trench patterns without varying the film thickness when the

films were annealed using a solvent vapor with a relatively low vapor pressure. This study demonstrates that there are likely different key parameters that are critical for promoting orthogonal alignment of BCP line patterns on minimal trench patterns depending on the type of BCPs.

4.2 Experimental Methods

4.2.1 Materials

Poly(styrene-*b*-ethylene oxide) (PS-*b*-PEO) (M_n = 20.5 kg mol^{-1} and M_n = 7.0 kg mol^{-1} for PS and PEO blocks, respectively, PDI = 1.05) and poly(styrene-*b*-dimethylsiloxane) PS-*b*-PDMS (M_n = 31.0 kg mol^{-1} and M_n = 14.5 kg mol^{-1} for PS and PDMS blocks, respectively, PDI = 1.15) were purchased from Polymer Source, Inc. and used as received. Benzene (anhydrous, 99.8%), toluene (anhydrous, 99.8%), and tetrahydrofuran (THF) (anhydrous, ≥99.9%, inhibitor-free) were purchased from Sigma-Aldrich. Acetone (≥99.5%) was purchased from Fisher Chemical. Each material was used without further purification. Epoxy permanent resist version 142, samples A-Z was supplied from Microchem Corp. for the fabrication of silsesquioxane (SSQ)-based films.

4.2.2 Fabrication of Minimal Trench Patterns

Nanoimprint molds composed of "hardened", crosslinked PDMS elastomer (*h*-PDMS) were replicated from a silicon master mold having a 140 nm pitch, 70 nm line width, and 50 nm height according to the previously described method.[34] Silsesquioxane

(SSQ)-based films were spin-coated at 2000 rpm for 60 s from propylene glycol monomethyl ether acetate (20 wt%) onto a silicon substrate with a native oxide layer (orientation of (100), University Wafer, Inc.). The thickness of the as-spun SSQ films was 274 ± 4 nm. Then, the SSQ films were nanoimprinted and UV cured with the *h*-PDMS mold with grating lines that have a pitch of 139 nm, width of 70 nm, and height of 50 nm using the nanoimprinter (NX-2000, Nanonex) operating at 80 psi for 5 min. To decrease the trench dimensions, the patterned SSQ films, i.e. nanoimprinted trench patterns, were annealed at 500 °C in air for 2 h, resulting in minimal trench patterns with the pitch = 139 nm, width = 99 nm, and depth = 15 nm.

4.2.3 DSA of PS-*b*-PEO Thin Films

The minimal trench patterns were cleaned with carbon dioxide snow jet, followed by UV-Ozone cleaning (UVO cleaner model 342, Jelight Company Inc.). PS-*b*-PEO thin films were prepared onto the minimal trench patterns by spin-coating from PS-*b*-PEO solution in benzene. Before SVA, the thicknesses of the films were measured on a flat silicon substrate by the ellipsometer (model LSE, Gaertner Scientific Corp.), where the thicknesses were varied by controlling the concentration of the PS-*b*-PEO solution (0.6% − 1.0% (wt/v)) and the speed (1700 rpm − 3000 rpm) of spin-coating. SVA was performed in a sealed glass jar (volume of the jar = 46.5 cm^3, surface area of THF = 12.6 cm^2, and surface area of water = 1.3 cm^2) at room temperature. To avoid dewetting, PS-*b*-PEO thin films were pre-swollen using water vapor for 10 min, followed by SVA with THF and water vapors for 60 min.

4.2.4 DSA of PS-*b*-PDMS Thin Films

PS-*b*-PDMS thin films were spin-coated onto minimal trench patterns from 1.6% (wt/v) PS-*b*-PDMS solution in toluene. Prior to SVA, the thicknesses of the films were 38.8 nm, as measured by the ellipsometer (model LSE, Gaertner Scientific Corp.). PS-*b*-PDMS films were solvent-vapor annealed using acetone, THF, or toluene vapor in three individually sealed glass jars at room temperature for 60 min: (1) SVA with acetone vapor (volume of the jar = 46.5 cm^3 and surface area of acetone = 12.6 cm^2), (2) SVA with THF vapor (volume of the jar = 46.5 cm^3 and surface area of THF = 12.6 cm^2), and (3) SVA with toluene vapor (volume of the jar = 46.5 cm^3 and surface area of toluene = 12.6 cm^2).

4.2.5 Characterization

Scanning force microscopy (SFM) images of solvent-vapor-annealed PS-*b*-PEO and PS-*b*-PDMS thin films were obtained using a SFM (Dimension 3100, Digital Instruments) operated in the tapping mode. SFM images were processed using MATLAB with a procedure developed by Murphy *et al.*[35] Image processing began with enhancing the contrast between two BCP domains by multiplying pixel values with themselves. Each pixel was then replaced with median value of adjacent eight pixels to reduce noise (i.e. median filter), and the filtered frame was transformed into a binary image by thresholding; black (0) and white (1) represent PS and PEO respectively. After being skeletonized into single-pixel width, each domain was trimmed to remove unwanted short branches formed by domain thickness undulation. To smooth out pixelated skeletons, the coordinates of each pixel were repeatedly adjusted to an average location of adjacent two pixels, but within ±

0.5 pixel from the initial coordinates. Finally, the orientations of each domain were calculated by dot product of two unit vectors: (1) unit vector between every two connected pixels in skeletons and (2) unit vector parallel to the trench line pattern.

Small Angle X-ray Scattering (SAXS) measurements were performed at the University of Massachusetts, Amherst using an in-house setup from Molecular Metrology Inc. to measure L_0 of the PS-*b*-PEO in the bulk. It uses a 30 W microsource (Bede) with a 30 μm by 30 μm spot size matched to a Maxflux optical system (Osmic), leading to a low-divergence beam of monochromatic Cu Kα radiation (wavelength $\lambda = 0.1542$ nm). Grazing incidence small angle X-ray scattering (GISAXS) measurements were performed at Beamline 7.3.3 at the Advanced Light Source, Lawrence Berkeley National Laboratory, at a constant X-ray energy of 10 keV.[36] The sample-to-detector distance was calibrated using a silver behenate standard. Scattering images were collected on a Pilatus 2M 2-D pixel detector (Dectris). During GISAXS measurements on the solvent-vapor-annealed PS-*b*-PEO thin films on the minimal trench patterns, the sample stage was rotated about the surface normal, where the rotation angle of $\Psi = 90°$ is defined when the X-ray beam is parallel to the trench direction. Then, the sample stage was rotated 90° to find PS-*b*-PEO line patterns (oriented orthogonal to the trench direction), which is defined as $\Psi = 0°$. From this point, the sample stage was rotated. The incident angle was fixed at 0.18°, which is above the critical angle of the polymer film (0.16°).

4.3 Results and Discussion

4.3.1 Orthogonal Alignment of PS-*b*-PEO Line Patterns

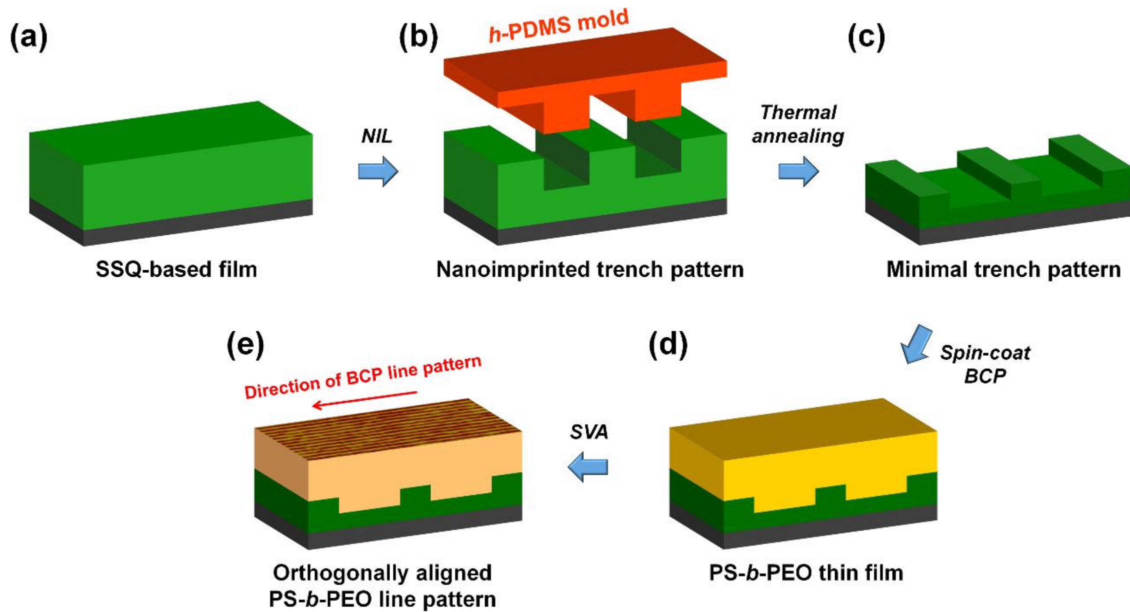

Figure 4.1 Schematic illustration of the DSA process. (a) SSQ-based film spin-coated onto a silicon substrate having a native oxide layer. (b) With a *h*-PDMS mold, SSQ-based film was nanoimprinted using a NIL system. (c) To reduce trench dimensions, in particularly the trench depth, the nanoimprinted trench pattern was annealed at 500 °C in air, finally generating a minimal trench pattern (trench depth < L_0). (d) PS-*b*-PEO thin films were spin-coated onto the minimal trench patterns (e) After SVA with THF and water vapors, PS-*b*-PEO film showed line patterns of cylindrical microdomains oriented orthogonal to the underlying trench direction.

Figure 4.1 shows the schematic illustration of the DSA process to produce orthogonally aligned BCP line patterns. First, a silsesquioxane (SSQ)-based film was spin-coated onto a flat silicon substrate with a native oxide layer (Figure 4.1a). Then, the SSQ-based film was nanoimprinted via nanoimprint lithography (NIL) using a *h*-PDMS mold with grating lines that have a pitch of 139 nm, width of 70 nm, and height of 50 nm (Figure 4.1b). To decrease the pattern dimensions, especially the trench depth, the nanoimprinted

trench pattern was annealed at 500 °C in air for 2 h, finally producing the minimal trench pattern with the pitch of 139 nm, width of 99 nm, and depth of 15 nm (Figure 4.1c). It is noted that the surface of the minimal trench pattern is hydrophilic. The details of the procedure for the fabrication of minimal trench patterns can be found in Chapter 3. After the fabrication of minimal trench patterns, a thin film of a cylinder-forming PS-*b*-PEO (L_0 = 21.9 nm in the bulk, as measured by small angle X-ray scattering (SAXS), Figure 4.2) was spin-coated onto the minimal trench pattern (Figure 4.1d), and subsequently solvent-vapor annealed using tetrahydrofuran (THF) and water vapors, where THF is a good solvent for both blocks and water is a selective solvent for the PEO block. It should be noted that the thickness of the PS-*b*-PEO films was varied to achieve well-defined line patterns of cylindrical microdomains oriented orthogonal to the underlying trench direction (Figure 4.1e). The film thickness was measured on the flat silicon substrate before solvent vapor annealing (SVA).

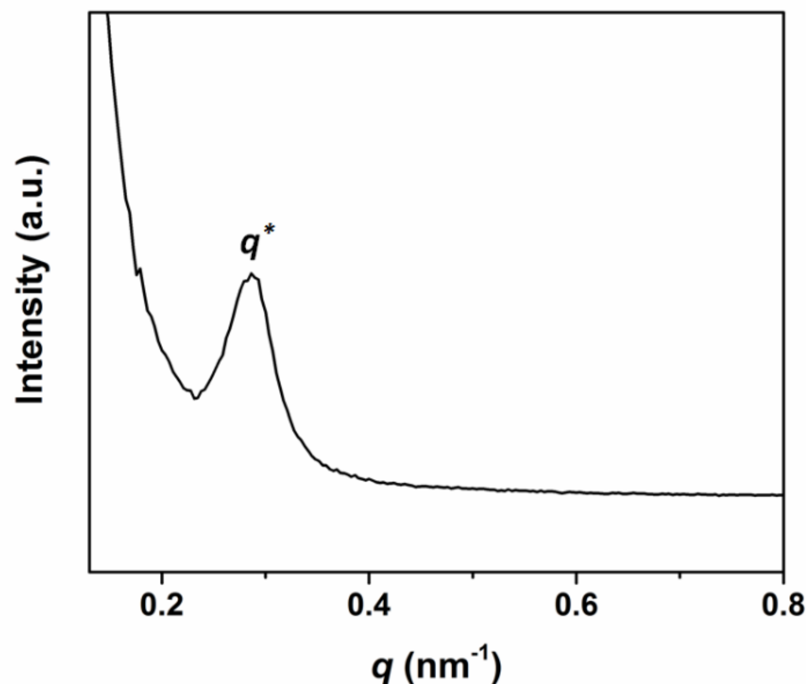

Figure 4.2 SAXS profile of a PS-b-PEO. The first-order reflection was observed at $q^* = 0.2863\ \mathrm{nm}^{-1}$ corresponding to the natural period ($L_0 = 2\pi/q^*$) of 21.9 nm. It is noted that the higher-order peaks of the first-order reflection were not observed.

Figure 4.3 shows scanning force microscopy (SFM) phase images of solvent-vapor annealed PS-*b*-PEO thin films on minimal trench patterns at different film thicknesses under identical annealing conditions. As shown in Figure 4.3a, when the film thickness was 22.6 nm ($1.03L_0$), the line patterns of the cylindrical microdomains oriented parallel to the film surface were obtained without breakage in the film. It would appear that the line patterns are partially oriented parallel or orthogonal to the trench direction. However, such an observation is due to the loops with large radii of curvature (Figure 4.4).[31] Interestingly, when the film thickness was increased to 24.7 nm ($1.13L_0$) (Figure 4.3b), two major orientations were observed, where the line patterns of cylindrical microdomains are

oriented nearly (1) parallel or (2) orthogonal to the trench direction. As seen in Figure 4.3c and d, further increasing the film thickness resulted in a rise of the orthogonal alignment of the line patterns with respect to the trench direction. As a result, the line patterns of cylindrical microdomains were practically oriented orthogonal to the trench direction with no trace of the underlying minimal trench pattern at the film thickness of 35.0 nm (1.60L_0) (Figure 4.3e). A few defects, such as dislocations and disclinations, existed in the films. However, the annihilation of these defects was observed with increasing the film thickness more, so that highly aligned line patterns of cylindrical microdomains oriented orthogonal to the underlying trench direction were achieved over the patterned substrate at the film thickness of 37.3 nm (1.70L_0) (Figure 4.3f). Moreover, this orthogonal alignment of PS-*b*-PEO line patterns was maintained even at the film thickness of 41.0 nm (1.87L_0) (Figure 4.3g).

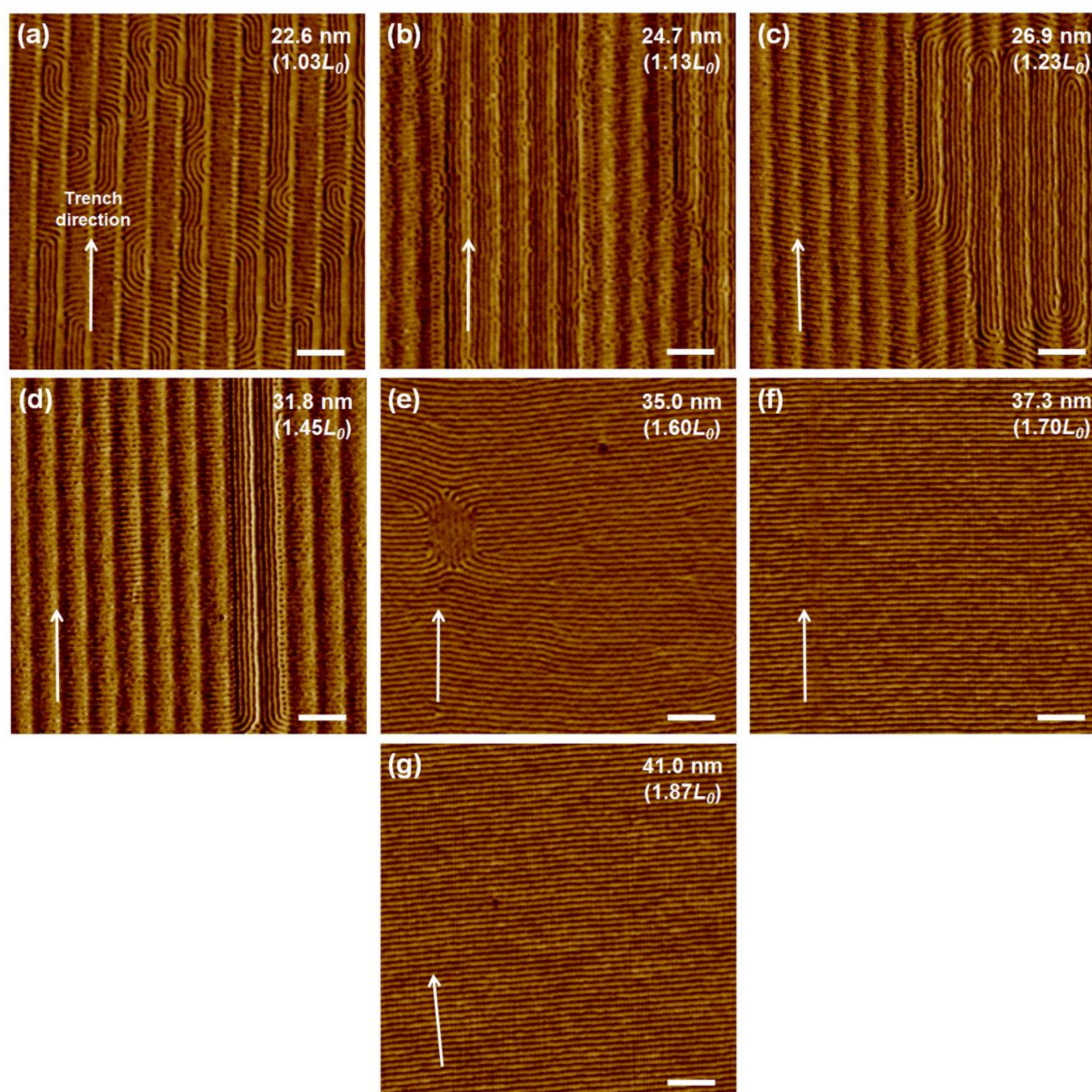

Figure 4.3 SFM phase images of solvent-vapor annealed PS-*b*-PEO thin films on minimal trench patterns under the same SVA conditions at different film thicknesses: (a) 22.6 nm (1.03L_0), (b) 24.7 nm (1.13L_0), (c) 26.9 nm (1.23L_0), (d) 31.8 nm (1.45L_0), (e) 35.0 nm (1.60L_0), (f) 37.3 nm (1.70L_0), and (g) 41.0 nm (1.87L_0). The arrow of each image indicates the underlying trench direction. All scale bars are 200 nm.

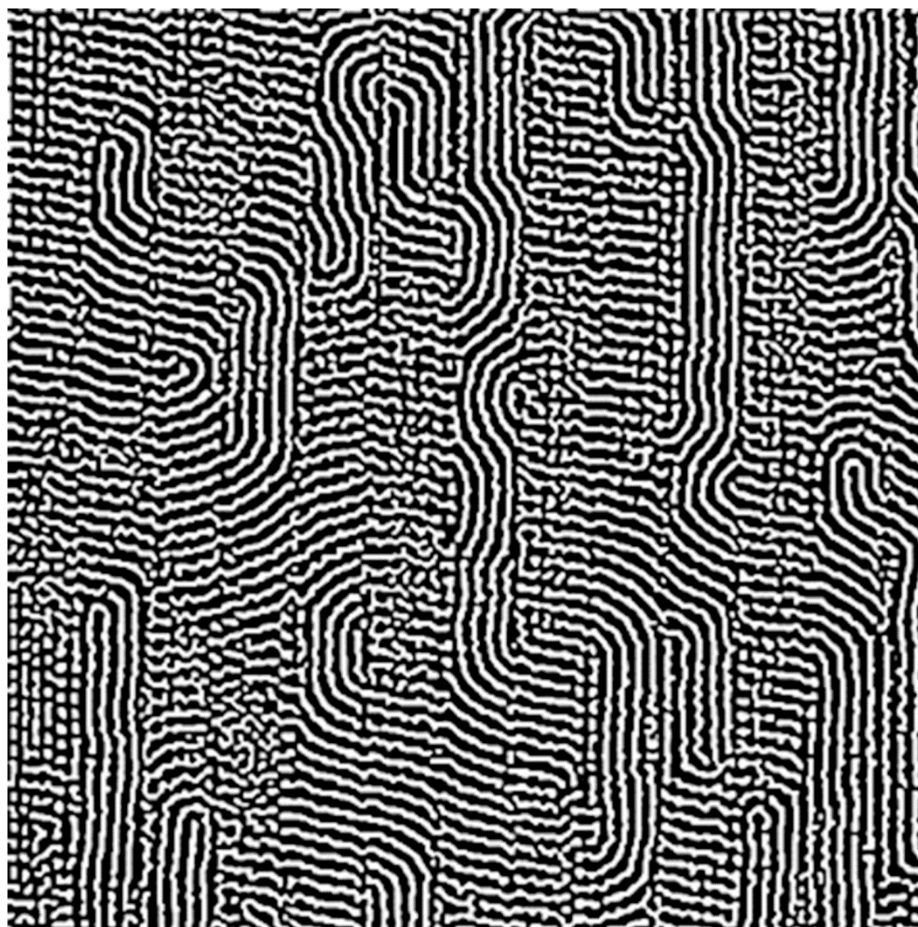

Figure 4.4 Fourier transformed SFM phase image of the solvent-vapor annealed PS-*b*-PEO thin film with the thickness of 22.6 nm (1.03L_0) on the minimal trench pattern. At this film thickness, there is no orientation of PS-*b*-PEO line patterns of cylindrical microdomains in terms of the direction of the trench pattern. Due to the loops with large radii of curvature, the line patterns of cylindrical microdomains seem to be partially oriented to the trench direction.

The orientations of line patterns in Figure 4 were quantitatively analyzed using image processing, as described by Murphy *et al.*,[35] where the distribution of the orientation angle is plotted in histograms with Gaussian curve fitting, as shown in Figure 4.5; the plots depict tendency of domain orientations effectively although the orientation measurements can be affected by SFM imaging artifacts from thermal drift distortions. Figure 4.5a shows the schematic illustration of the orientation angles of line patterns of cylindrical

microdomains with respect to the underlying trench direction, where the orientation angle of 0 degrees is defined when the direction of line patterns is parallel to the trench direction. From this data, we found that the line patterns of cylindrical microdomains on the minimal trench patterns showed the tendency for being oriented 90 degrees as the film thickness was increased. Specifically, in the thickness range of 24.7 nm (1.13L_0) to 31.8 nm (1.45L_0) (Figure 4.5b–d), two obvious orientations are observed: line patterns oriented nearly (1) parallel or (2) orthogonal to the trench direction. The average parallel orientations were −1.4 ± 9.6°, −2.0 ± 8.4°, and −1.2 ± 8.0° for the 24.7 nm (1.13L_0), 26.9 nm (1.23L_0), and 31.8 nm (1.45L_0) thicknesses, respectively, showing a decrease in their probability as the film thickness was increased. In contrast, the average orthogonal orientations were 93.4 ± 23.0°, 79.0 ± 14.0°, and 90.3 ± 17.1° for the 24.7 nm (1.13L_0), 26.9 nm (1.23L_0), and 31.8 nm (1.45L_0) thicknesses, respectively, and their probability gradually increased with increasing the film thickness. At the film thickness of 35.0 nm (1.60L_0) (Figure 4.5e), the orthogonal alignment with an average orientation of 90.6 ± 12.5° was predominant, whereas the parallel orientation was hardly seen (inset of Figure 4.5e). When the thickness was increased to 37.3 nm (1.70L_0) (Figure 4.5f), highly aligned line patterns oriented orthogonal to the underlying trench direction with an average orientation of 90.0 ± 7.3° were observed. Recently, Berggren and co-workers showed the fabrication of the orthogonally aligned PS-*b*-PDMS line patterns with respect to direction of the underlying hydrogen silsesquioxane (HSQ) line templates.[31] Based on self-consistent field theory (SCFT) modeling, they described that the key parameters to induce the orthogonal alignment of PS-*b*-PDMS line patterns were the height and chemical preference of templates. However, in this case, the thickness of BCP films was fixed at L_0, whereas the

film thickness in our study was varied. The origin of the orthogonal alignment for the PS-*b*-PEO system is currently underway.

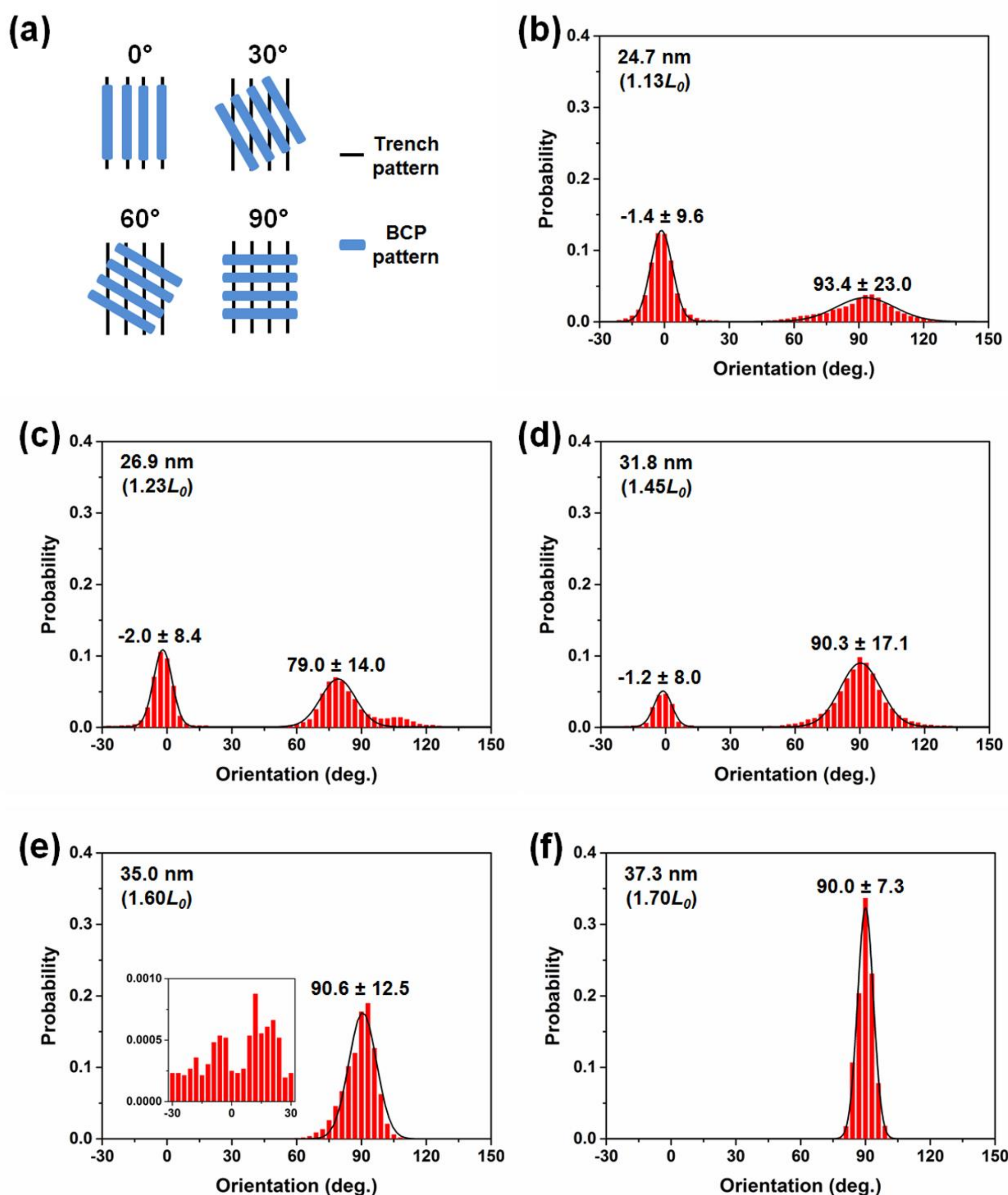

Figure 4.5 Orientation angle distribution from image analysis of PS-*b*-PEO line patterns on minimal trench patterns. (a) Schematic illustration of defined orientation angles of line patterns with respect to the underlying trench direction. (b–f) Orientation angle distribution at different film thicknesses: (b) 24.7 nm ($1.13L_0$), (c) 26.9 nm ($1.23L_0$), (d) 31.8 nm ($1.45L_0$), (e) 35.0 nm ($1.60L_0$), and (f) 37.3 nm ($1.70L_0$). The inset in (e) shows the probability between −30° and 30°.

Since SFM is limited to examining the local ordering of BCP microdomains within the area of several square micrometers, we used GISAXS to elucidate the lateral ordering and orientation of line patterns of cylindrical microdomains over macroscopic distances.[37, 38] Figure 4.6a shows the schematic illustration of GISAXS experiments, where the sample stage is rotated about the surface normal during the measurements. We defined the rotation angle, Ψ, as the angle between the direction of the X-ray beam and the direction of PS-*b*-PEO line patterns on the minimal trench pattern. The X-ray beam was first aligned with the trench direction, which is defined as $\Psi = 90°$. Then, the sample stage was rotated 90°, which is defined as $\Psi = 0°$, because PS-*b*-PEO line patterns were oriented orthogonal to the trench direction. From $\Psi = 0°$, the sample stage was rotated 2° to 10°. The incident angle was set at 0.18°, which is above the critical angle of the polymer film (0.16°), allowing us to characterize the BCP morphology throughout the film. Figure 4.6b–h shows the 2-D GISAXS patterns of the PS-*b*-PEO thin film on the minimal trench pattern at different Ψ, where q_y is the in-plane scattering vector and q_z is the out-of-plane scattering vector. As shown in Figure 4.6b, when the direction of the X-ray beam was parallel to the trench direction ($\Psi = 90°$), strong streaks in the vertical direction arising from the minimal trench pattern were observed. In addition, these streaks were accompanied by a semicircle-like scattering pattern because of the intersection of the Ewald sphere with the grating truncation rods, which is characteristic of GISAXS patterns when the direction of the X-ray beam is parallel to the direction of the grating.[39, 40] It should be noted that the semicircle-like scattering pattern is very sensitive to the azimuthal alignment of the trench direction with respect to the direction of the incoming X-ray beam.[41, 42] When the direction of the X-ray beam was aligned with the direction of the PS-*b*-PEO line patterns ($\Psi = 0°$),

Bragg rods corresponding to the PS-*b*-PEO microdomains were observed (Figure 4.6c). As the sample stage was rotated (Figure 4.6d–h), increasing *Ψ*, a change in the intensity of Bragg rods was observed.

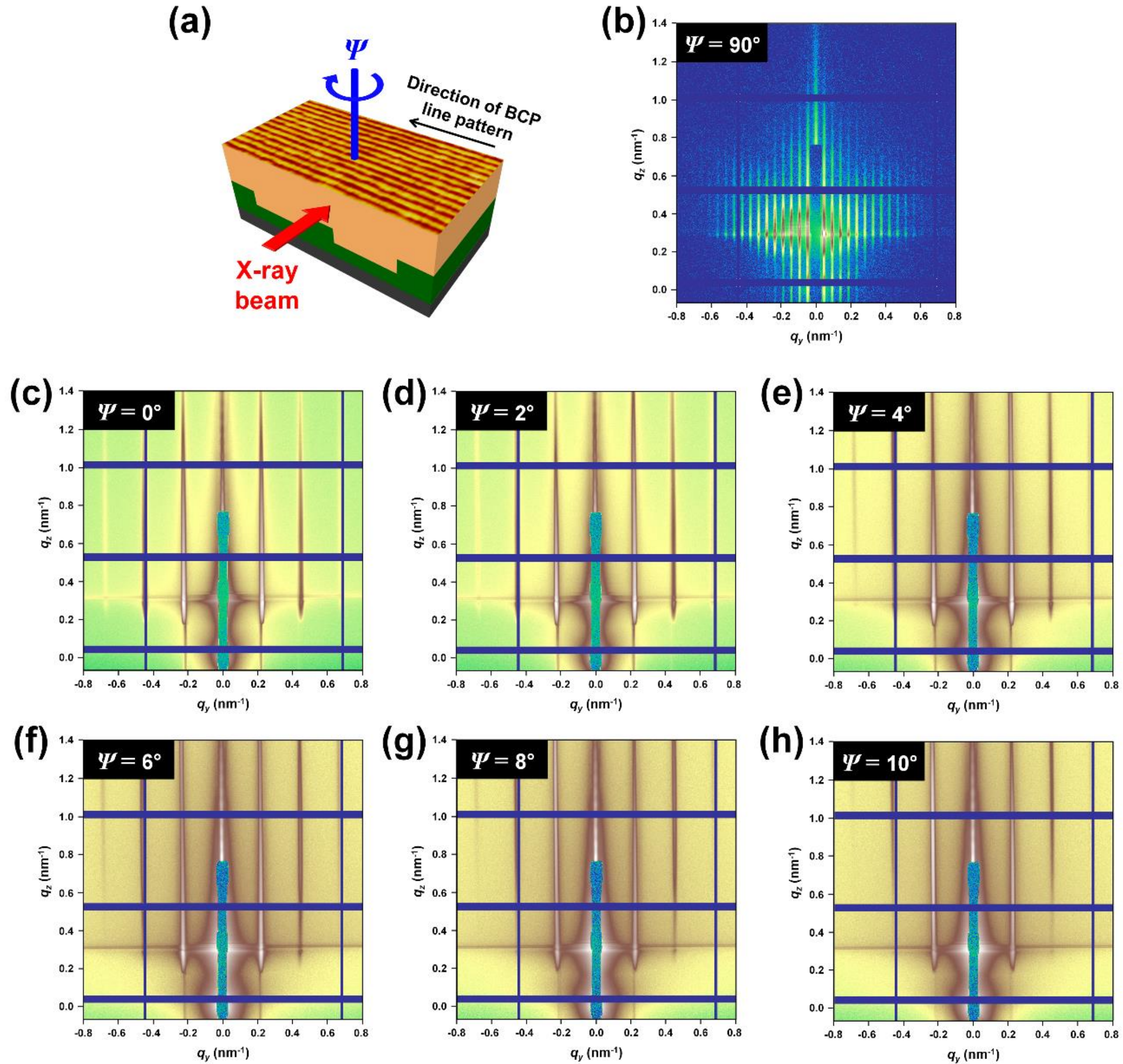

Figure 4.6 GISAXS measurements of solvent-vapor annealed PS-*b*-PEO thin films on minimal trench patterns. (a) Schematic illustration of GISAXS experiments, where *Ψ* is the rotation angle of the sample stage. We define *Ψ* = 0° when the direction of the X-ray beam is parallel to the underlying trench direction. (b–h) 2-D GISAXS patterns taken at different *Ψ*: (b) *Ψ* = 90°, (c) *Ψ* = 0°, (d) *Ψ* = 2°, (e) *Ψ* = 4°, (f) *Ψ* = 6°, (g) *Ψ* = 8°, and (h) *Ψ* = 10°.

The corresponding in-plane profiles from the 2-D GISAXS patterns (Figure 4.6b–h) are shown in Figure 4.7. At $\Psi = 90°$, the strong reflections from the underlying minimal trench pattern were seen. However, at $\Psi = 0°$, three reflections arising from the PS-*b*-PEO line patterns were observed with scattering vector ratios of 1:2:3 relative to the first-order reflection. In this case, strong reflections from the underlying minimal trench pattern were not observed since the direction of the trench pattern and the direction of the X-ray beam were not the same. The domain spacing ($= 2\pi/q_y$) of the PS-*b*-PEO line patterns of cylindrical microdomains was calculated to be 28.3 nm from the first-order reflection. With increasing Ψ from 0° to 10°, there are two distinct changes in the scattering profiles: (1) the first-order reflection becomes weaker and wider and (2) the higher-order reflections vanish. Since the scattering is dependent on Ψ, we can quantify the degree of orientation of BCP line patterns using the orientation parameter, f, for the 2-D system in a film, which is calculated using the following function:[26, 43]

$$f = 2\langle \cos^2\Psi \rangle - 1 \tag{4.1}$$

$$\langle \cos^2\Psi \rangle = \frac{\sum I(\Psi)\cos^2\Psi}{\sum I(\Psi)} \tag{4.2}$$

where, Ψ is the rotation angle and $I(\Psi)$ is the intensity of the first-order reflection at each Ψ from the GISAXS patterns. Figure 4.8 shows the scattering intensity of the first-order reflection as a function of Ψ. Based on the integration of the intensity, f was calculated to be 0.997, indicating the extraordinarily high degree of orientation of the line patterns over macroscopic length scales. It is noted that $f = 1.0$ for perfect orientation of line patterns of cylindrical microdomains and $f = 0$ for random orientation.

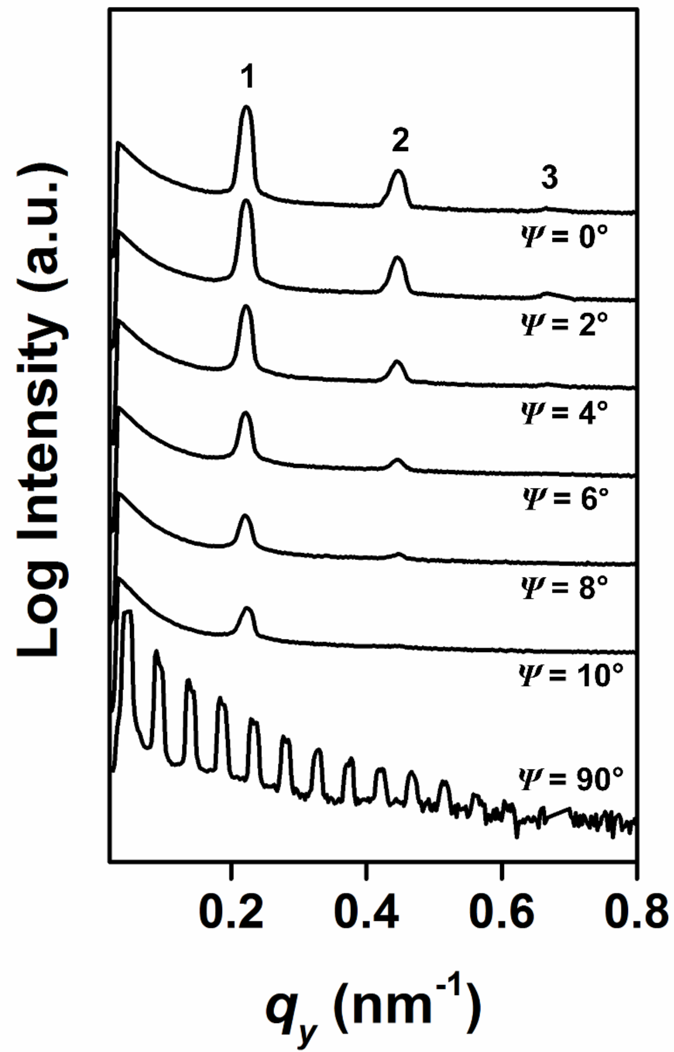

Figure 4.7 In-plane scattering profiles corresponding to a horizontal cut of (Figure 4.6b–h) at $q_z = 0.320$ nm^{-1}.

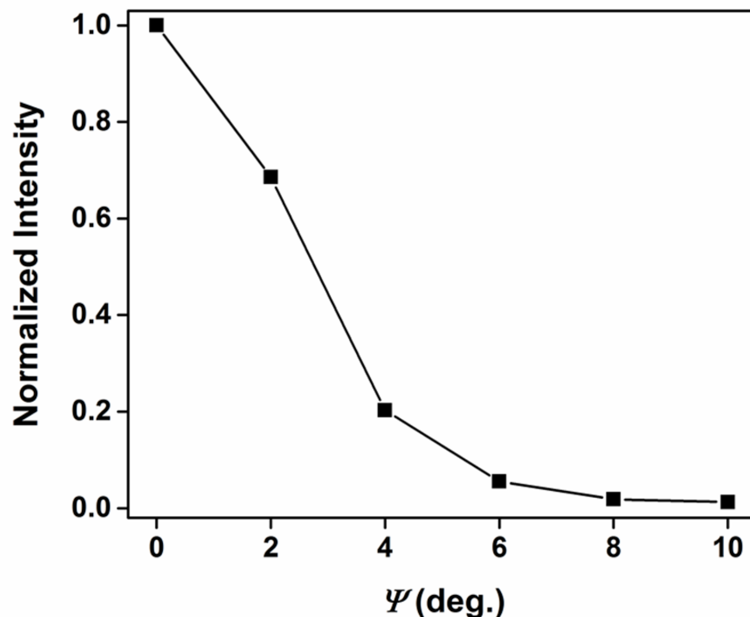

Figure 4.8 Normalized scattering intensity of the first-order reflection from GISAXS patterns as a function of Ψ. Using this data, f was calculated to be 0.997, which is characteristic of exceptionally aligned BCP line patterns oriented orthogonal to the trench direction.

4.3.2 Orthogonal Alignment of PS-*b*-PDMS Line Patterns

We also investigated the self-assembly of a cylinder-forming PS-*b*-PDMS (M_n = 31.0 kg mol^{-1} and M_n = 14.5 kg mol^{-1} for PS and PDMS blocks, respectively; the domain spacing of solvent-vapor annealed cylindrical microdomains oriented parallel to the film surface on a flat silicon substrate is 38 nm) on minimal trench patterns to study whether the different BCP microdomains can also produce orthogonally aligned line patterns on a minimal trench pattern. For this purpose, PS-*b*-PDMS thin films were prepared by spin-coating onto minimal trench patterns, where the film thickness was fixed at 38.8 nm, as measured on the flat silicon substrate prior to SVA. In this film thickness, a single layer of

line patterns of PDMS microdomains in a PS matrix was formed, with a thin layer of PDMS at the air/polymer interface due to the large difference in surface energy, γ, between PS ($\gamma_{PS} \sim 40.7$ mN m^{-1}) and PDMS ($\gamma_{PDMS} \sim 20.4$ mN m^{-1}).[44] Then, SVA was performed using acetone, THF, or toluene vapor for the same annealing time. All solvents are more selective for the PS blocks because of the differences in the solubility parameters between the polymers and solvents ($|\delta_{polymer} - \delta_{solvent}|$) (Table 4.1).[45]

Table 4.1 Solubility parameters of the polymers and solvents and vapor pressures of the solvents used in the PS-*b*-PDMS experiments.

Polymer or Solvent	Solubility parameter (MPa)$^{1/2}$	Vapor pressure at 25 °C (kPa)
PS	18.6	–
PDMS	15.4	–
Acetone	20.1	30.8
THF	19.4	21.6
Toluene	18.2	3.79

As seen in the SFM phase image in Figure 4.9, the solvent-vapor annealed PS-*b*-PDMS thin films on the minimal trench patterns were shown to generate orthogonally aligned line patterns of cylindrical microdomains with respect to the underlying trench direction depending on the type of the annealed solvent vapors, without increasing the film thickness. It is noted that SFM imaging of PS-*b*-PDMS microdomains was affected by the thin surface layer of PDMS at the top surface in the films. As shown in Figure 4.9a, when the PS-*b*-PDMS thin film was annealed using acetone vapor, typical fingerprint patterns of

cylindrical microdomains were produced on the minimal trench pattern. This is confirmed by the 2-D fast Fourier transform (FFT) (inset of Figure 4.9a), which exhibits a halo, indicating randomly oriented microdomains. It should be noted that a chain of spots in the middle of the FFT is arising from the underlying minimal trench pattern. Similarly, in the case of SVA with THF vapor (Figure 4.9b), the fingerprint patterns of cylindrical microdomains with shorter correlation lengths were generated. However, when the film was annealed with toluene vapor (Figure 4.9c), we found that the line patterns of cylindrical microdomain were oriented orthogonal to the underlying trench direction. The FFT (inset of Figure 4.9c) also showed diffuse spots parallel to the axis of a chain of spots in the middle of the FFT, confirming orthogonally aligned PS-*b*-PDMS line patterns with respect to the trench direction. Previously, Ross and Jung observed the orthogonal alignment of PS-*b*-PDMS line patterns within deep trench patterns modified with a PDMS brush layer.[46] In this case, the origin of the orthogonal alignment was attributed to the wide mesas of the deep trenches and SVA with relatively low vapor pressures. However, in our study, orthogonally aligned PS-*b*-PDMS line patterns form over minimal trench patterns. Moreover, both PS and PDMS blocks are not attracted to the surface of the minimal trench pattern due to its hydrophilicity. Despite such differences in the experimental system, we suggest that the relatively low vapor pressure of toluene could be a factor in driving the orthogonal alignment of PS-*b*-PDMS line patterns of cylindrical microdomains on the minimal trench pattern. Among the solvents, the vapor pressure of toluene is noticeably smaller than that of the other solvents (Table 4.1),[47] implying one of the factors related to inducing the orthogonal alignment in the PS-*b*-PDMS system. More investigation is needed to clarify the relationship between the vapor pressure of the solvents and the orthogonal

alignment of PS-*b*-PDMS line patterns of cylindrical microdomains on minimal trench patterns.

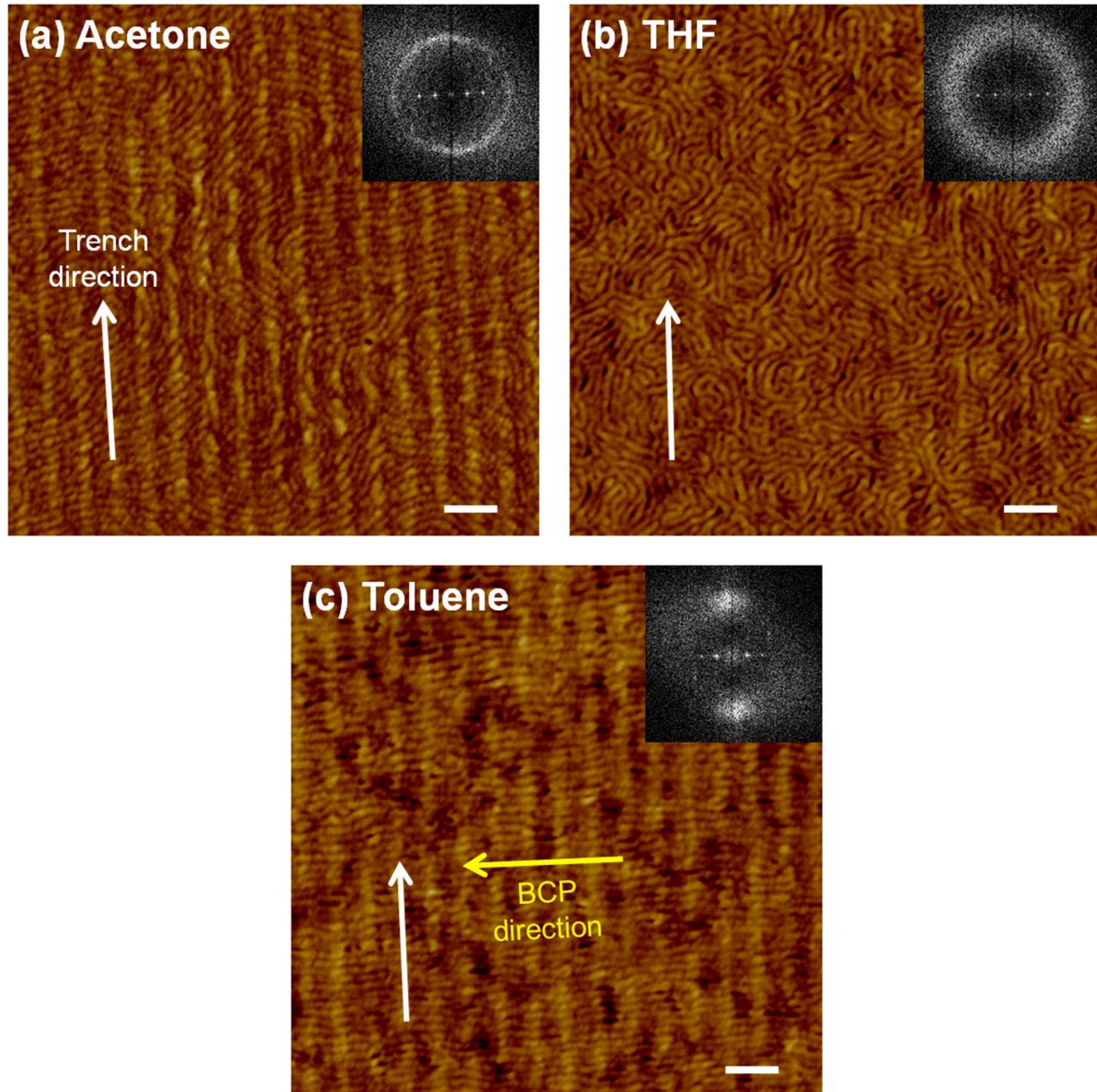

Figure 4.9 SFM phase images of PS-*b*-PDMS thin films on minimal trench patterns annealed using different solvent vapors: (a) acetone, (b) THF, and (c) toluene. The inset of each image shows the corresponding 2-D FFT. The white arrow of each image exhibits the underlying trench direction. The yellow arrow in (c) indicates the direction of PS-*b*-PDMS line patterns. All scale bars are 200 nm.

4.4 Conclusions

In summary, we demonstrated a simple and novel route to produce orthogonally aligned BCP line patterns with respect to the trench direction on minimal trench patterns. For the PS-*b*-PEO microdomains, increasing the film thickness on the minimal trench patterns induced the orthogonal alignment, resulting in the generation of exceptionally aligned line patterns of cylindrical microdomains oriented orthogonal to the trench direction over arbitrary macroscopic areas. In contrast, for the PS-*b*-PDMS microdomains, the orthogonal alignment of line patterns of cylindrical microdomains was achieved through SVA with a low vapor pressure solvent. We believe that the approach presented here could be extended to the fabrication of multilayer mesh-shaped nanostructures or nanowire arrays without the use of a complex lithographic process.

4.5 References

1. Kim, S.; Nealey, P. F.; Bates, F. S. Directed Assembly of Lamellae Forming Block Copolymer Thin Films near the Order–Disorder Transition. *Nano Lett.* **2013**, *14*, 148-152.

2. Aissou, K.; Mumtaz, M.; Fleury, G.; Portale, G.; Navarro, C.; Cloutet, E.; Brochon, C.; Ross, C. A.; Hadziioannou, G. Sub-10 nm Features Obtained from Directed Self-Assembly of Semicrystalline Polycarbosilane-Based Block Copolymer Thin Films. *Adv. Mater.* **2015**, *27*, 261-265.

3. Park, S.; Lee, D. H.; Xu, J.; Kim, B.; Hong, S. W.; Jeong, U.; Xu, T.; Russell, T. P. Macroscopic 10-Terabit-Per-Square-Inch Arrays from Block Copolymers with Lateral Order. *Science* **2009**, *323*, 1030-1033.

4. Stoykovich, M. P.; Kang, H.; Daoulas, K. C.; Liu, G.; Liu, C.-C.; de Pablo, J. J.; Müller, M.; Nealey, P. F. Directed Self-Assembly of Block Copolymers for Nanolithography: Fabrication of Isolated Features and Essential Integrated Circuit Geometries. *ACS Nano* **2007**, *1*, 168-175.

5. Borah, D.; Shaw, M. T.; Holmes, J. D.; Morris, M. A. Sub-10 nm Feature Size PS-*b*-PDMS Block Copolymer Structures Fabricated by a Microwave-Assisted Solvothermal Process. *ACS Appl. Mater. Interfaces* **2013**, *5*, 2004-2012.

6. Ji, S.; Wan, L.; Liu, C.-C.; Nealey, P. F. Directed Self-Assembly of Block Copolymers on Chemical Patterns: A Platform for Nanofabrication. *Prog. Polym. Sci.* **2016**, *54–55*, 76-127.

7. Park, S.-M.; Park, O.-H.; Cheng, J. Y.; Rettner, C. T.; Kim, H.-C. Patterning Sub-10 nm Line Patterns from a Block Copolymer Hybrid. *Nanotechnology* **2008**, *19*, 455304.

8. Stoykovich, M. P.; Müller, M.; Kim, S. O.; Solak, H. H.; Edwards, E. W.; de Pablo, J. J.; Nealey, P. F. Directed Assembly of Block Copolymer Blends into Nonregular Device-Oriented Structures. *Science* **2005**, *308*, 1442-1446.

9. Jeong, J. W.; Park, W. I.; Kim, M.-J.; Ross, C. A.; Jung, Y. S. Highly Tunable Self-Assembled Nanostructures from a Poly(2-Vinylpyridine-*b*-Dimethylsiloxane) Block Copolymer. *Nano Lett.* **2011**, *11*, 4095-4101.

10. Rho, Y.; Aissou, K.; Mumtaz, M.; Kwon, W.; Pécastaings, G.; Mocuta, C.; Stanecu, S.; Cloutet, E.; Brochon, C.; Fleury, G.; Hadziioannou, G. Laterally Ordered Sub-10 nm Features Obtained from Directed Self-Assembly of Si-Containing Block Copolymer Thin Films. *Small* **2015**, *11*, 6377-6383.

11. Blachut, G.; Sirard, S. M.; Maher, M. J.; Asano, Y.; Someya, Y.; Lane, A. P.; Durand, W. J.; Bates, C. M.; Dinhobl, A. M.; Gronheid, R.; Hymes, D.; Ellison, C. J.; Willson, C. G. A Hybrid Chemo-/Grapho-Epitaxial Alignment Strategy for Defect Reduction in Sub-10 nm Directed Self-Assembly of Silicon-Containing Block Copolymers. *Chem. Mater.* **2016**.

12. Ruiz, R.; Kang, H.; Detcheverry, F. A.; Dobisz, E.; Kercher, D. S.; Albrecht, T. R.; de Pablo, J. J.; Nealey, P. F. Density Multiplication and Improved Lithography by Directed Block Copolymer Assembly. *Science* **2008**, *321*, 936-939.

13. Xu, J.; Park, S.; Wang, S.; Russell, T. P.; Ocko, B. M.; Checco, A. Directed Self-Assembly of Block Copolymers on Two-Dimensional Chemical Patterns Fabricated by Electro-Oxidation Nanolithography. *Adv. Mater.* **2010**, *22*, 2268-2272.

14. Cheng, J. Y.; Rettner, C. T.; Sanders, D. P.; Kim, H.-C.; Hinsberg, W. D. Dense Self-Assembly on Sparse Chemical Patterns: Rectifying and Multiplying Lithographic Patterns Using Block Copolymers. *Adv. Mater.* **2008**, *20*, 3155-3158.

15. Yang, G.-W.; Wu, G.-P.; Chen, X.; Xiong, S.; Arges, C. G.; Ji, S.; Nealey, P. F.; Lu, X.-B.; Darensbourg, D. J.; Xu, Z.-K. Directed Self-Assembly of Polystyrene-*b*-Poly(Propylene Carbonate) on Chemical Patterns via Thermal Annealing for Next Generation Lithography. *Nano Lett.* **2017**, *17*, 1233-1239.

16. Segalman, R. A.; Yokoyama, H.; Kramer, E. J. Graphoepitaxy of Spherical Domain Block Copolymer Films. *Adv. Mater.* **2001**, *13*, 1152-1155.

17. Tavakkoli K. G., A.; Gotrik, K. W.; Hannon, A. F.; Alexander-Katz, A.; Ross, C. A.; Berggren, K. K. Templating Three-Dimensional Self-Assembled Structures in Bilayer Block Copolymer Films. *Science* **2012**, *336*, 1294-1298.

18. Sun, Z.; Chen, Z.; Zhang, W.; Choi, J.; Huang, C.; Jeong, G.; Coughlin, E. B.; Hsu, Y.; Yang, X.; Lee, K. Y.; Kuo, D. S.; Xiao, S.; Russell, T. P. Directed Self-Assembly of Poly(2-Vinylpyridine)-*b*-Polystyrene-*b*-Poly(2-Vinylpyridine) Triblock Copolymer with Sub-15 nm Spacing Line Patterns Using a Nanoimprinted Photoresist Template. *Adv. Mater.* **2015**, *27*, 4364-4370.

19. Yang, J. K. W.; Jung, Y. S.; Chang, J.-B.; Mickiewicz, R. A.; Alexander Katz, A.; Ross, C. A.; Berggren, K. K. Complex Self-Assembled Patterns Using Sparse Commensurate Templates with Locally Varying Motifs. *Nat. Nanotechnol.* **2010**, *5*, 256-260.

20. Edwards, E. W.; Stoykovich, M. P.; Solak, H. H.; Nealey, P. F. Long-Range Order and Orientation of Cylinder-Forming Block Copolymers on Chemically Nanopatterned Striped Surfaces. *Macromolecules* **2006**, *39*, 3598-3607.

21. Park, S.-M.; Craig, G. S. W.; Liu, C.-C.; La, Y.-H.; Ferrier, N. J.; Nealey, P. F. Characterization of Cylinder-Forming Block Copolymers Directed to Assemble on Spotted Chemical Patterns. *Macromolecules* **2008**, *41*, 9118-9123.

22. Welander, A. M.; Craig, G. S. W.; Tada, Y.; Yoshida, H.; Nealey, P. F. Directed Assembly of Block Copolymers in Thin to Thick Films. *Macromolecules* **2013**, *46*, 3915-3921.

23. Kim, S.; Shin, D. O.; Choi, D.-G.; Jeong, J.-R.; Mun, J. H.; Yang, Y.-B.; Kim, J. U.; Kim, S. O.; Jeong, J.-H. Graphoepitaxy of Block-Copolymer Self-Assembly Integrated with Single-Step Zno Nanoimprinting. *Small* **2012**, *8*, 1563-1569.

24. Kim, M.; Han, E.; Sweat, D. P.; Gopalan, P. Interplay of Surface Chemical Composition and Film Thickness on Graphoepitaxial Assembly of Asymmetric Block Copolymers. *Soft Matter* **2013**, *9*, 6135-6141.

25. Choi, J.; Huh, J.; Carter, K. R.; Russell, T. P. Directed Self-Assembly of Block Copolymer Thin Films Using Minimal Topographic Patterns. *ACS Nano* **2016**, *10*, 7915-7925.

26. Hong, S. W.; Huh, J.; Gu, X.; Lee, D. H.; Jo, W. H.; Park, S.; Xu, T.; Russell, T. P. Unidirectionally Aligned Line Patterns Driven by Entropic Effects on Faceted Surfaces. *Proc. Natl. Acad. Sci.* **2012**, *109*, 1402-1406.

27. Hong, S. W.; Voronov, D. L.; Lee, D. H.; Hexemer, A.; Padmore, H. A.; Xu, T.; Russell, T. P. Controlled Orientation of Block Copolymers on Defect-Free Faceted Surfaces. *Adv. Mater.* **2012**, *24*, 4278-4283.

28. Park, S.-M.; Stoykovich, M. P.; Ruiz, R.; Zhang, Y.; Black, C. T.; Nealey, P. F. Directed Assembly of Lamellae-Forming Block Copolymers by Using Chemically and Topographically Patterned Substrates. *Adv. Mater.* **2007**, *19*, 607-611.

29. Han, E.; Kang, H.; Liu, C.-C.; Nealey, P. F.; Gopalan, P. Graphoepitaxial Assembly of Symmetric Block Copolymers on Weakly Preferential Substrates. *Adv. Mater.* **2010**, *22*, 4325-4329.

30. Park, S.-M.; Berry, B. C.; Dobisz, E.; Kim, H.-C. Observation of Surface Corrugation-Induced Alignment of Lamellar Microdomains in PS-*b*-PMMA Thin Films. *Soft Matter* **2009**, *5*, 957-961.

31. Tavakkoli K. G, A.; Nicaise, S. M.; Gadelrab, K. R.; Alexander-Katz, A.; Ross, C. A.; Berggren, K. K. Multilayer Block Copolymer Meshes by Orthogonal Self-Assembly. *Nat. Commun.* **2016**, *7*, 10518.

32. Black, C. T. Self-Aligned Self Assembly of Multi-Nanowire Silicon Field Effect Transistors. *Appl. Phys. Lett.* **2005**, *87*, 163116-3.

33. Ruiz, R.; Dobisz, E.; Albrecht, T. R. Rectangular Patterns Using Block Copolymer Directed Assembly for High Bit Aspect Ratio Patterned Media. *ACS Nano* **2011**, *5*, 79-84.

34. Li, Y.; Peterson, J. J.; Jhaveri, S. B.; Carter, K. R. Patterned Polymer Films via Reactive Silane Infusion-Induced Wrinkling. *Langmuir* **2013**, *29*, 4632-4639.

35. Murphy, J. N.; Harris, K. D.; Buriak, J. M. Automated Defect and Correlation Length Analysis of Block Copolymer Thin Film Nanopatterns. *PLoS ONE* **2015**, *10*, e0133088.

36. Hexemer, A.; Bras, W.; Glossinger, J.; Schaible, E.; Gann, E.; Kirian, R.; MacDowell, A.; Church, M.; Rude, B.; Padmore, H. A SAXS/WAXS/GISAXS Beamline with Multilayer Monochromator. *J. Phys. Conf. Ser.* **2010**, *247*, 012007.

37. Ree, M. Probing the Self-Assembled Nanostructures of Functional Polymers with Synchrotron Grazing Incidence X-Ray Scattering. *Macromol. Rapid Commun.* **2014**, *35*, 930-959.

38. Majewski, P. W.; Yager, K. G. Latent Alignment in Pathway-Dependent Ordering of Block Copolymer Thin Films. *Nano Lett.* **2015**, *15*, 5221-5228.

39. Rueda, D. R.; Martín-Fabiani, I.; Soccio, M.; Alayo, N.; Pérez-Murano, F.; Rebollar, E.; García-Gutiérrez, M. C.; Castillejo, M.; Ezquerra, T. A. Grazing-Incidence Small-Angle X-Ray Scattering of Soft and Hard Nanofabricated Gratings. *J. Appl. Crystallogr.* **2012**, *45*, 1038-1045.

40. Yan, M.; Gibaud, A. On the Intersection of Grating Truncation Rods with the Ewald Sphere Studied by Grazing-Incidence Small-Angle X-Ray Scattering. *J. Appl. Crystallogr.* **2007**, *40*, 1050-1055.

41. Mikulík, P.; Jergel, M.; Baumbach, T.; Majková, E.; Pincík, E.; Luby, S.; Ortega, L.; Tucoulou, R.; Hudek, P.; Kostic, I. Coplanar and Non-Coplanar X-Ray Reflectivity Characterization of Lateral W/Si Multilayer Gratings. *J. Phys. D: Appl. Phys.* **2001**, *34*, A188.

42. Mishra, V.; Fredrickson, G. H.; Kramer, E. J. Effect of Film Thickness and Domain Spacing on Defect Densities in Directed Self-Assembly of Cylindrical Morphology Block Copolymers. *ACS Nano* **2012**, *6*, 2629-2641.

43. Kao, J.; Jeong, S.-J.; Jiang, Z.; Lee, D. H.; Aissou, K.; Ross, C. A.; Russell, T. P.; Xu, T. Direct 3-D Nanoparticle Assemblies in Thin Films Via Topographically Patterned Surfaces. *Adv. Mater.* **2014**, *26*, 2777-2781.

44. Son, J. G.; Gotrik, K. W.; Ross, C. A. High-Aspect-Ratio Perpendicular Orientation of PS-*b*-PDMS Thin Films under Solvent Annealing. *ACS Macro Lett.* **2012**, *1*, 1279-1284.

45. Brandrup, J.; Immergut, E. H.; Grulke, E. A. *Polymer Handbook*. John Wiley & Sons: New York, 1999; Vol. 2.

46. Jung, Y. S.; Ross, C. A. Orientation-Controlled Self-Assembled Nanolithography Using a Polystyrene−Polydimethylsiloxane Block Copolymer. *Nano Lett.* **2007**, *7*, 2046-2050.

47. Haynes, W. M. *Crc Handbook of Chemistry and Physics 98rd Edition*. CRC Press: Boca Raton, 2012.

CHAPTER 5

3D NANOSTRUCTURES DERIVED FROM THE DIRECTED SELF-ASSEMBLY OF BLOCK COPOLYMERS WITHIN WOODPILES

5.1 Introduction

Block copolymers (BCPs) have been extensively studied due to their ability to self-assemble into well-ordered nanostructures, such as lamellae, cylinders, gyroids, and spheres.[1, 2] BCP thin films have been of particular interests to both academia and industry for potential lithographic applications in the semiconductor and storage industries.[3-5] Mansky *et al.* first reported the concept of using BCP morphologies in thin films for lithographic applications, in the mid-1990s.[6, 7] This concept was developed by Park *et al.* using well-ordered spherical microdomains in BCP thin films as a lithographic mask for pattern transfer, producing dense periodic arrays of holes and dots in the silicon nitride layer.[8] To date, many advances in the directed self-assembly (DSA) of BCPs have been made in 2D processes that are compatible with the planar processing techniques, such as etching and lift off, which are used in the semiconductor industry.[4, 9-11] However, ventures into the fabrication of 3D nanoscale patterns using the DSA of BCPs remain an essentially unexplored area.

This chapter focuses on the fabrication of 3D BCP nanostructures using woodpile structures as a 3D guiding template. After filling woodpile structures with BCPs by drop casting, thermal annealing was performed, where the preferential interactions of the blocks with the surfaces of woodpile structures direct the self-assembly of BCPs. We also show

the fabrication of 3D metallic patterns in woodpile structures by infiltration of metal salts into one of the blocks in the BCP.

5.2 Experimental Methods

5.2.1 Materials

Poly(styrene-*b*-methyl methacrylate) (PS-*b*-PMMA) (M_n = 38.0 kg mol^{-1} and M_n = 36.8 kg mol^{-1} for PS and PMMA blocks, respectively, PDI = 1.08) and poly(styrene-*b*-2-vinyl pyridine) (PS-*b*-P2VP) (M_n = 55.0 kg mol^{-1} and M_n = 50.0 kg mol^{-1} for PS and P2VP blocks, respectively, PDI = 1.05) were purchased from Polymer Source, Inc. and used as received. Toluene (anhydrous, 99.8%) was purchased from Sigma-Aldrich and used without further purification. Hydrochloric acid (HCl) was purchased from Fisher Scientific and used as received. Sodium tetrachloroplatinate(II) hydrate ($Na_2PtCl_4 \cdot xH_2O$) was purchased from Sigma-Aldrich and used as received.

5.2.2 Fabrication of Woodpile Structures

The 3D woodpile structures were fabricated using a multi-photon polymerization technique. As shown in Figure 5.1a and b, two-photon polymerization (2PP) was initiated in the laser focal zone when the ultrafast laser (Femtosecond laser, TOPTICA, 780 nm, 80 MHz, 100 fs) beam was tightly focused on the photo-curable material using high numerical aperture oil-immersion objective lens (100x, N.A. = 1.4, Zeiss). The arbitrary 3D structures can be achieved through movement of the focused laser beam with a prescribed trajectory.

The combination of the piezoelectric with linear stages (Physik Instrumente) was able to move the photo-curable material during the 2PP process. The piezoelectric stage was used for fine movement, whereas the linear stage was used for large step movement. The beam shot was controlled by a mechanical shutter, and intensity control was achieved using a motorized attenuator. The stages, mechanical shutter and attenuator, were computer-controlled via Labview program. A charge-coupled device (CCD) camera was mounted behind a dichroic mirror for imaging during the whole process.

As shown in Figure 5.1c, the photo-curable material is based on the organic-inorganic hybrid structure. To prepare this material, methacryloxy-propyl trimethoxysilane (MAPTMS), methacrylic acid (MAA), and 2-(dimethylamino)ethyl methacrylate (DMAEMA) were used as the organic photopolymerizable monomers, where zirconium propoxide (ZPO, 70% in propanol) and alkoxysilane groups of MAPTMS serve as the inorganic network forming moieties. 4,4-bis(diethylamino) benzophenone (BIS) was used as a photo-initiator. After 2PP process, the samples were developed in a mixture of 4-methyl-2-pentanone and 2-propanol for 20 min to remove the uncured regions.

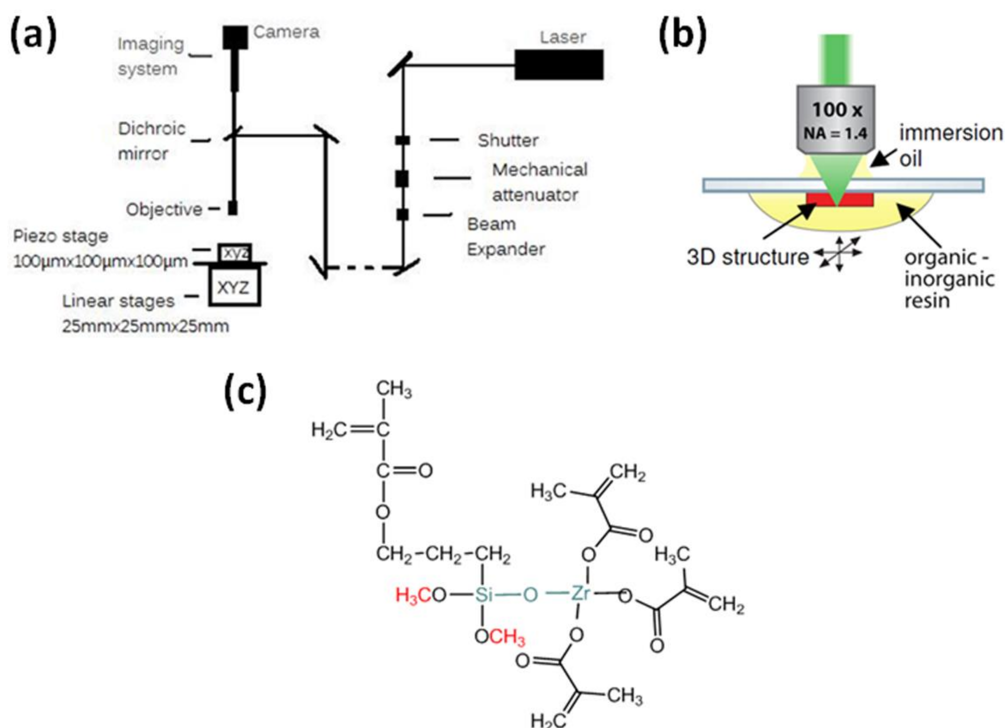

Figure 5.1 (a, b) Experimental set-up for 2PP. (c) Chemical structure of photo-curable (organic-inorganic hybrid) material. (Image courtesy of Sangmo Koo, University of California, Berkeley)

5.2.3 DSA of PS-*b*-PMMA with Woodpile Structures

A single droplet of 1.4% (W/V) PS-*b*-PMMA solution in toluene was dropped onto woodpile structures on a glass substrate. Subsequently, the samples were annealed at 190 °C under vacuum for 4 days. After thermal annealing, reactive ion etching (RIE, STS Vision 320 Mark II RIE System) with O_2/Ar plasma (RF Power: 100 W, Pressure: 10 mTorr, O_2: 15 sccm, Ar: 5 sccm) was performed to enhance the phase contrast between the two blocks.

5.2.4 DSA of PS-*b*-P2VP with Woodpile Structures

A single droplet of 1.6% (W/V) PS-*b*-P2VP solution in toluene was dropped onto woodpile structures on a glass substrate. The samples were then annealed at 190 °C under vacuum for 4 days.

5.2.5 Deposition of Metal Salts in BCPs within Woodpiles

3D metallic patterns were prepared according to the literatures.[12-14] After thermal annealing of PS-*b*-P2VP incorporated woodpile structures, the sample was frozen in liquid nitrogen, and then quickly cleaved. This cleaved sample was immersed in 2.0% (W/V) Na_2PtCl_4 aqueous solution with 0.9 wt% HCl in a Teflon dish for 18 h. Then, the sample was rinsed with water, followed by drying under a nitrogen stream for 2 days. To remove the polymer, RIE (STS Vision 320 Mark II RIE System) with O_2/Ar plasma (RF Power: 100 W, Pressure: 10 mTorr, O_2: 15 sccm, Ar: 5 sccm) was performed. It is noted that metal ions are reduced during RIE process.

5.2.6 Characterization

To examine the BCP morphologies and the metallic patterns in the woodpile structures, field emission scanning electron microscopy (FESEM, JEOL JSM-7001F) was used with an acceleration voltage of 5.0 − 15.0 kV. Before SEM imaging, all samples were sputter-coated with gold.

5.3 Results and Discussion

5.3.1 3D Woodpile Structures for Guiding the Self-Assembly of BCPs

3D multi-layered woodpile structures composed of multiple unit blocks were fabricated using a two-photon polymerization (2PP) technique.[15] As shown in Figure 5.2a, each unit block is repeated four layers in the stacking sequence, where each layer consists of 1D rods.

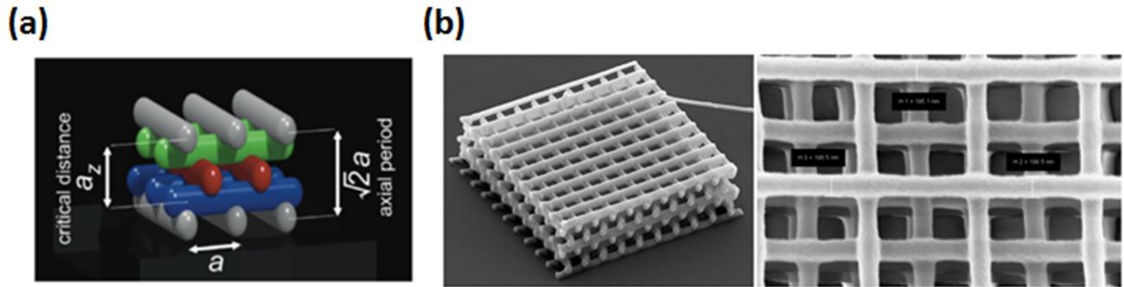

Figure 5.2 (a) Structure of unit block of woodpile structure, where a_z is the distance between four adjacent layers, a is the separation distance between parallel rods within each layer. Between every other layer, rods are shifted relative to each other by $a/2$. Face-centered-tetragonal unit cell structure with $a_z = \sqrt{2}a$ was used in this project. (b) SEM images of woodpile structure. (Image courtesy of Sangmo Koo, University of California, Berkeley)

We can vary a thickness of 1D rods by changing the ratio of the quencher (DMAEMA) in the photo-curable material and laser power, allowing us to fabricate woodpile structures with different dimensions, as shown in Figure 5.3.

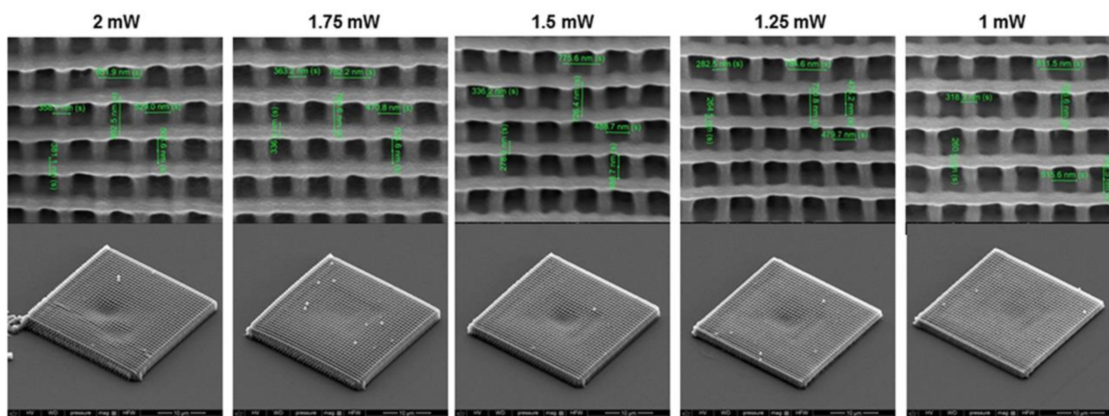

Figure 5.3 SEM images of woodpile structures fabricated by different laser power while maintaining the scanning speed at 20 μm s^{-1}. (Image courtesy of Sangmo Koo, University of California, Berkeley)

5.3.2 Incorporation of BCPs in Woodpile Structures

As shown in Figure 5.4, we devised a method to incorporate BCPs in woodpile structures. First, a single droplet of the BCP solution in the syringe is dropped onto the woodpile structures on the glass substrate (Figure 5.4a). This process results in covering woodpile structures with the BCP solution (Figure 5.4b). After several minutes, the solvent is evaporated across the woodpile structures, whereupon the BCP is incorporated into the woodpile (Figure 5.4c–f). We found that the rate of solvent evaporation, and concentration of BCP solutions play key roles in completely filling the woodpile structures with BCPs.

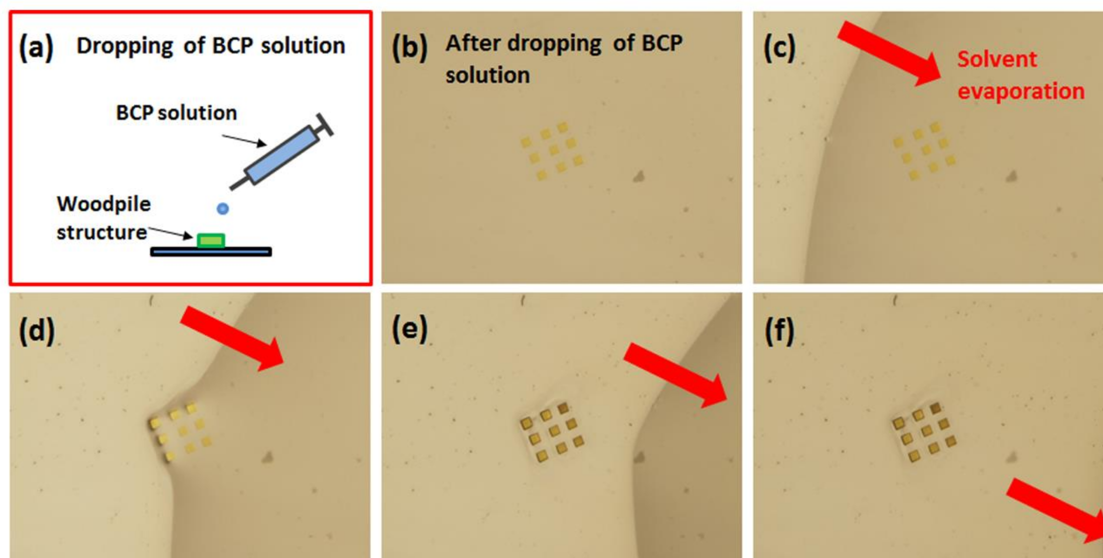

Figure 5.4 Procedure for incorporation of BCPs in woodpile structures. Red arrow in (c–f) indicates the direction of solvent evaporation.

5.3.3 PS-*b*-PMMA Morphologies on Top Layers of Woodpile Structures

Figure 5.5 shows scanning electron microscopy (SEM) images of thermally annealed poly(styrene-*b*-methyl methacrylate) (PS-*b*-PMMA) on top layers of the woodpile structures. To improve the phase contrast between the PS and PMMA blocks, reactive ion etching (RIE) with O_2/Ar plasma was used after thermal annealing. As seen in the inset in Figure 5.5, the DSA of PS-*b*-PMMA amplified the patterns, generating well-defined concentric ring structures with nanoscales on top layers of the woodpile structures.

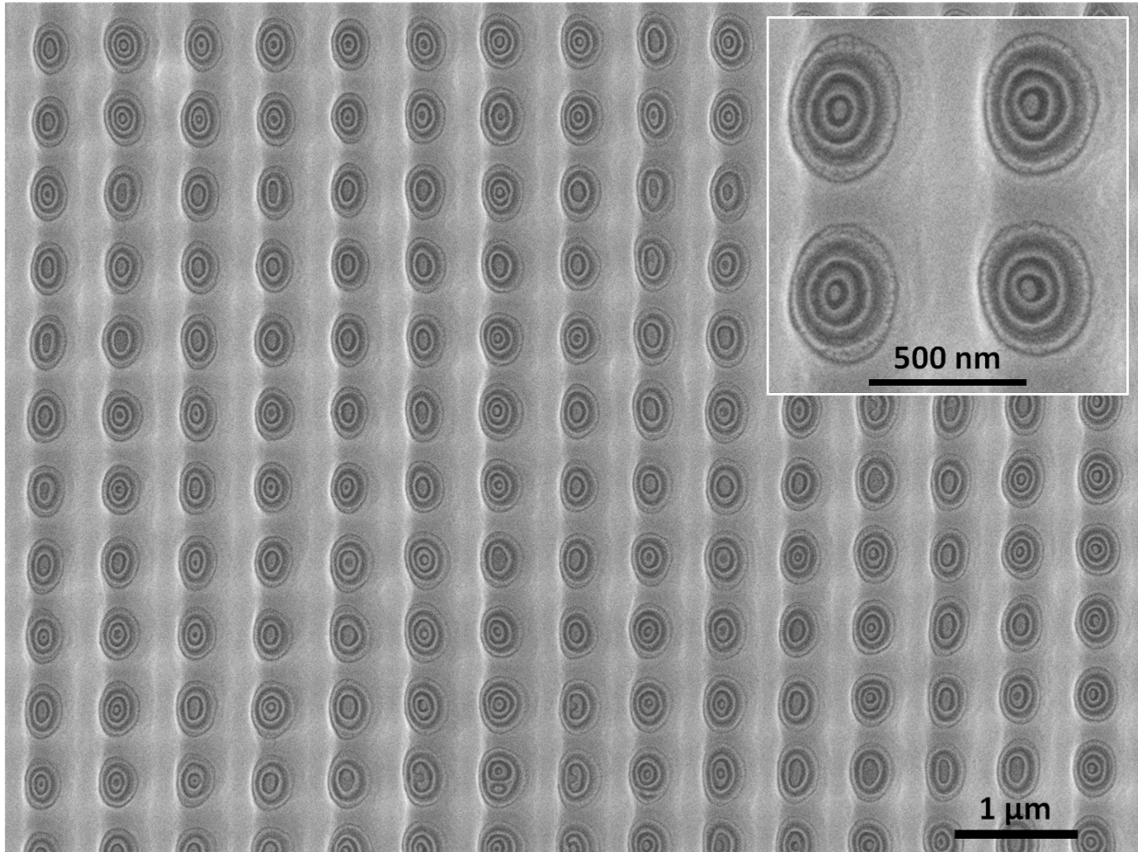

Figure 5.5 SEM images of PS-*b*-PMMA patterns on top layers of woodpile structures with pitch of 650 nm and height of 5 µm. The inset shows a high-magnification image of the concentric ring structures.

The commensurability between the characteristic length scales of woodpile structures and natural period of BCPs (L_0) is important for dictating the BCP morphology within the woodpile structure because this constraint can lead to completely new BCP morphologies.[16-18] We varied the pitch of the woodpile structure to investigate the effect of pattern dimensions on the PS-*b*-PMMA morphology. Interestingly, a slight change in the confinement shape at the identical pitch results in different BCP morphologies on the top layer of woodpile structures. As shown in Figure 5.6, PS-*b*-PMMA microdomains showed concentric rings (Figure 5.6a) or ellipsoidal patterns (Figure 5.6b) for a pitch of 650 nm and trapezoidal (Figure 5.6c) or square patterns for a pitch of 1 µm, depending on the

confinement shape. It is noted that the outermost darker phase in the SEM images corresponds to PMMA, indicating that there are preferential interactions of the PMMA with surface of the woodpile structure. This preferential interaction induces an ordering of the PS-*b*-PMMA microdomains within the confinement areas by conforming to the shape of the confinement.

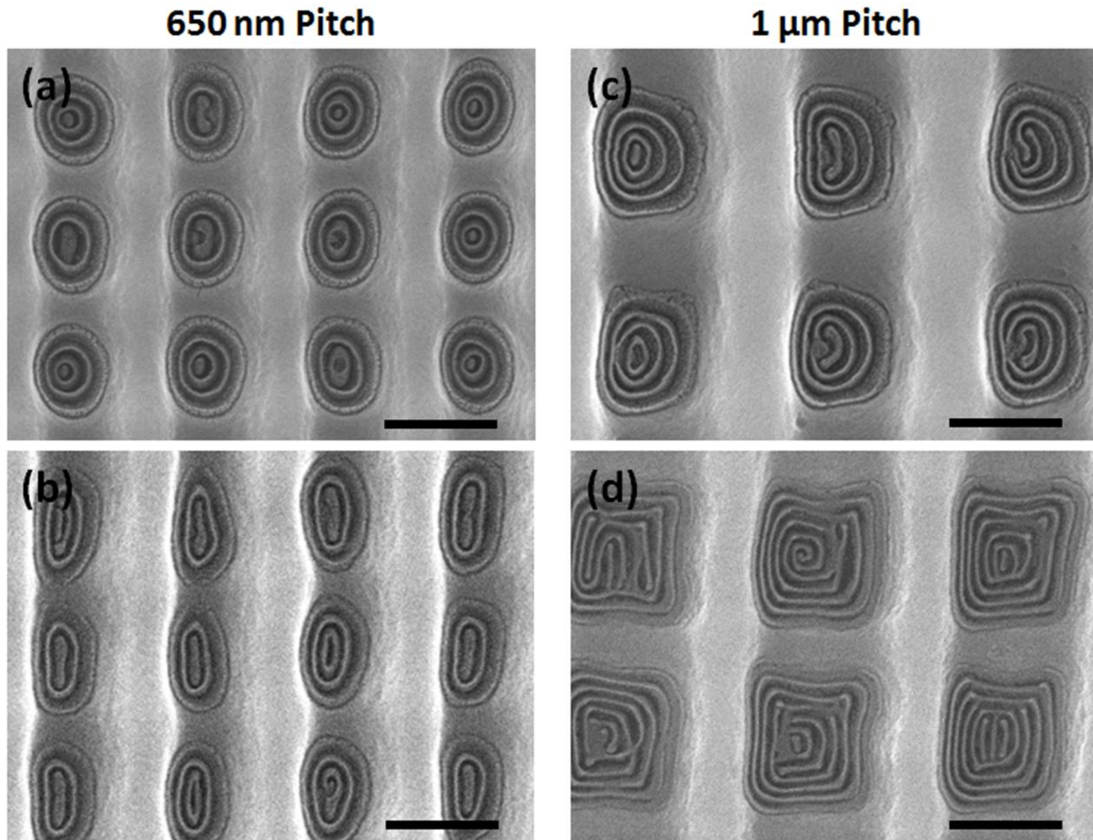

Figure 5.6 SEM images of PS-*b*-PMMA patterns on top layers of woodpile structures with the pitch of (a,b) 650 nm and (c,d) 1 µm. (a) Concentric ring patterns. (b) Ellipsoidal patterns. (c) Trapezoidal patterns. (d) Square patterns. All scale bars are 500 nm.

5.3.4 PS-*b*-PMMA Morphologies Inside of Woodpile Structures

Figure 5.7 shows SEM cross section images of the PS-*b*-PMMA incorporated woodpile structure. To investigate BCP morphologies within the woodpiles, we cleaved the PS-*b*-PMMA embedded woodpile structures, and then applied RIE to the cross section to improve the phase contrast between two blocks, exposing buried PS-*b*-PMMA morphologies within the woodpile structure. As shown in Figure 5.7a, the PS-*b*-PMMA was well-incorporated in the woodpile structure, where the cleaved multi-layered woodpile rods were also observed, indicating that drop-casting method is effective in incorporating the BCPs in woodpile structures. However, as shown in Figure 5.7b, PS-*b*-PMMA morphologies in the woodpile structures were not clear. The reason for this needs to be investigated further.

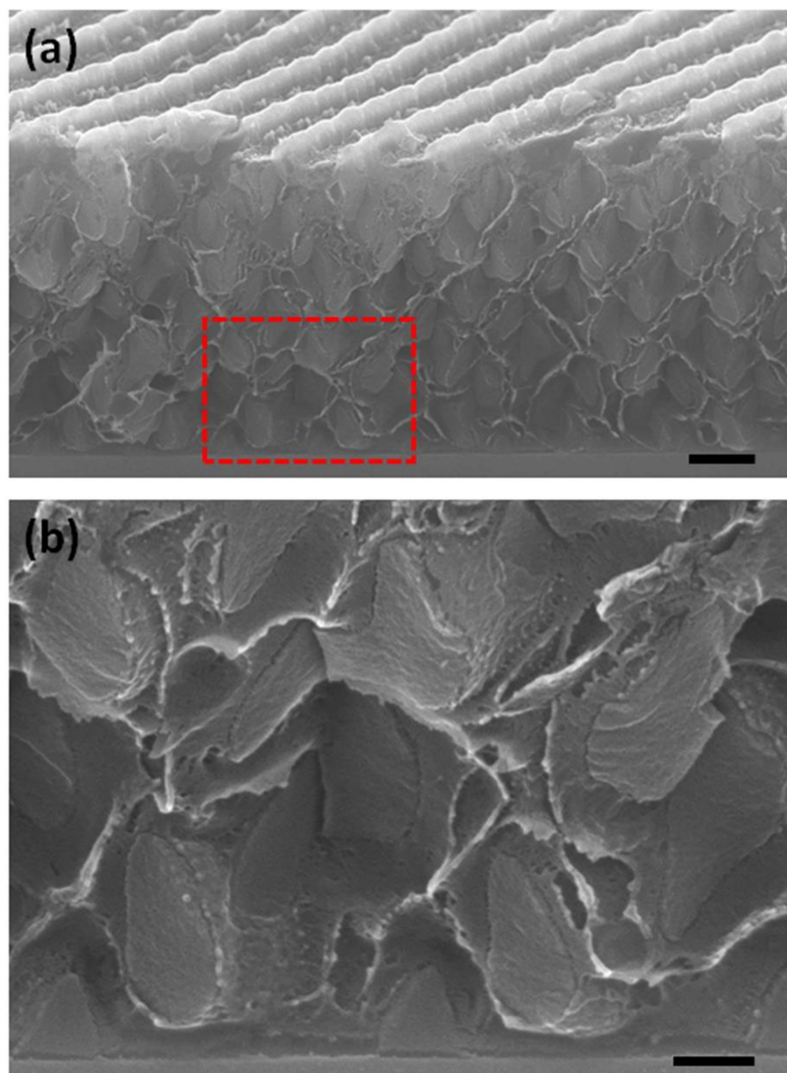

Figure 5.7 (a) SEM cross section images of PS-*b*-PMMA incorporated woodpile structures. Scale bar is 1 μm. (b) Magnified SEM image from the red dashed rectangle in (a). Scale bar is 300 nm.

5.3.5 3D PS-*b*-P2VP Morphologies in Woodpile Structures

Figure 5.8 shows thermally annealed poly(styrene-*b*-2-vinyl pyridine) (PS-*b*-P2VP) inside of the woodpile structure. In this case, the PS-*b*-P2VP did not show any clear morphologies because there was little contrast between the PS and P2VP blocks. To enhance the contrast, PS-*b*-P2VP incorporated woodpile structures were reconstructed by immersion in ethanol, which is a good solvent for the P2VP blocks, but a non-solvent for the PS blocks.[19, 20] During this process, ethanol selectively interacts with the P2VP blocks so that these P2VP blocks are drawn to the surface of the cross section, making height contrasts that can be investigated using SEM.

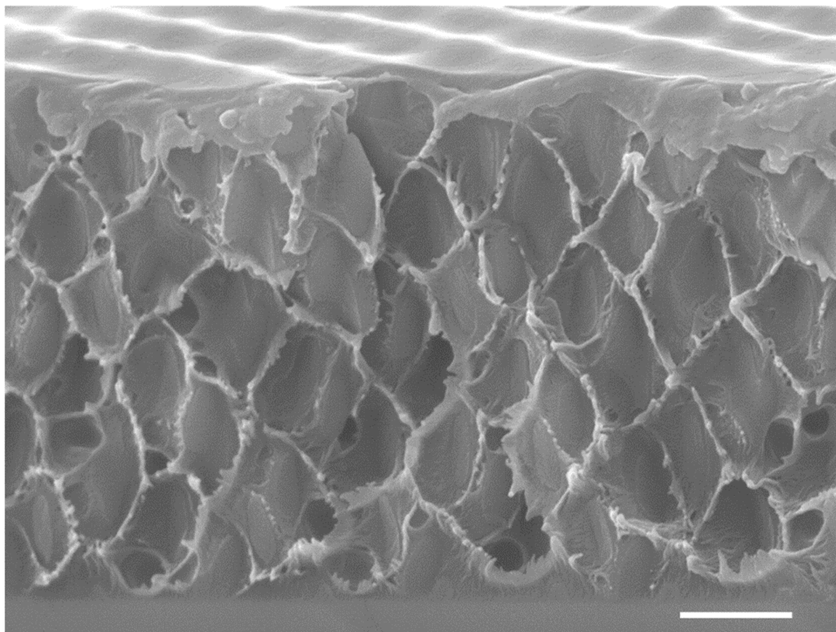

Figure 5.8 SEM cross section image of PS-*b*-P2VP embedded woodpile structures. Scale bar is 1 μm.

Figure 5.9 shows ethanol reconstructed PS-*b*-P2VP microdomains in the woodpile structure. In the magnified SEM image (Figure 5.9b and c), it was clear that the 3D woodpile structure directed the self-assembly of a lamellar-forming PS-*b*-P2VP, generating 3D interconnected lamellar microdomains through void spaces in the woodpile structure. However, 3D lamellar microdomains with large vertical ratio on the cleaved section were collapsed. This is probably due to capillary forces during the wet reconstruction process.[21]

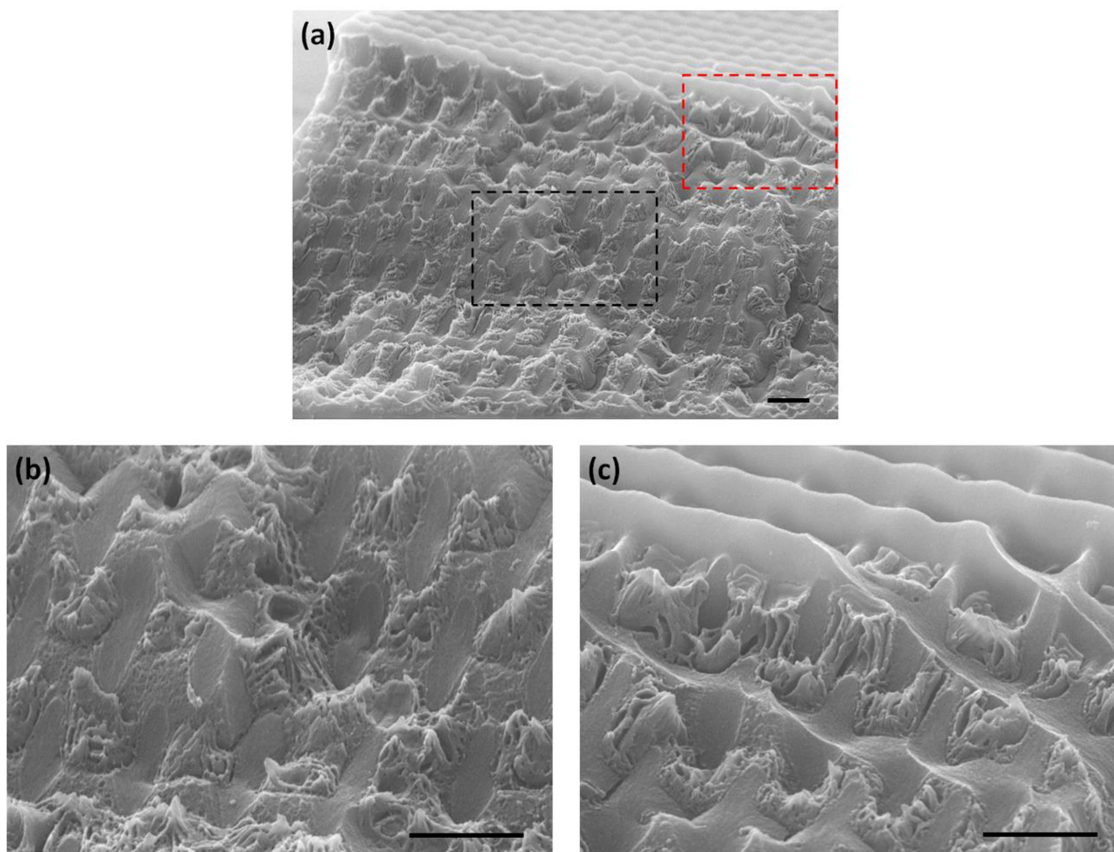

Figure 5.9 SEM images of ethanol reconstructed PS-*b*-P2VP microdomains in woodpile structures. (a) After thermal annealing, PS-*b*-P2VP incorporated woodpile structure was cleaved, and then reconstructed by immersion in ethanol. (b) and (c) are show magnified SEM images from the black and red dashed rectangles in (a), respectively. All scale bars are 1 μm.

By adjusting the concentration of the PS-*b*-P2VP solutions, we investigated how the BCP is drawn into woodpile structures. As mentioned before, when a single droplet of PS-*b*-P2VP solutions is dropped onto the woodpile structures on the glass substrate, the solution covers the woodpile structures. After several minutes, the solvent is evaporated across the woodpile structures, thereby incorporating the BCP within the woodpile structures. As shown in Figure 5.10, the PS-*b*-P2VP was found to penetrate into the woodpile structures laterally rather than vertically, during solvent evaporation. We have found that the rate of solvent evaporation and concentration of BCP solutions are critical to incorporate BCPs in the woodpile structures. In particular, if the concentration of the BCP solution is too high, the woodpile structures will be fully covered with a thick BCP film. However, we note that additional parameters, such as the capillary forces and increased mobility of the polymer during thermal annealing, can also have an effect on BCP loading in woodpile structures.

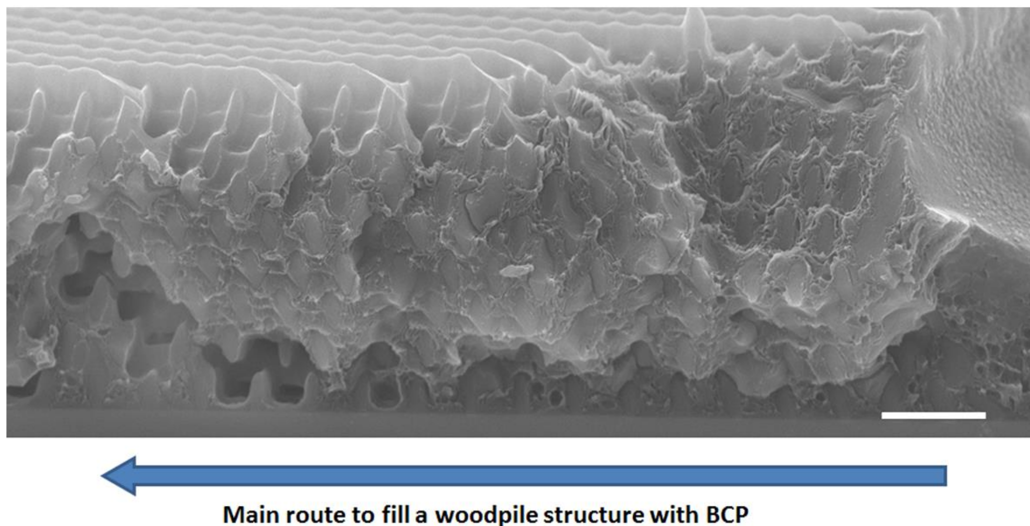

Figure 5.10 Direction of infiltration of PS-*b*-P2VP in woodpile structures.

5.3.6 3D Metallic Nanoscale Patterns in Woodpile Structures

One of the interesting features of PS-*b*-P2VP is that P2VP blocks can be complexed with metal ions,[22] providing the opportunity to fabricate 3D networks of metallic structures within the woodpile structures. Various anionic metal salts, such as $HAuCl_4$, Na_2PdCl_4, Na_2PtCl_4, and $K_3Fe(CN)_6$, can be complexed with the P2VP blocks in the presence of HCl aqueous solutions.[12] From these, we selected Na_2PtCl_4 to fabricate 3D platinum (Pt) patterns in woodpile structures.

To fabricate 3D Pt nanostructures, the cleaved woodpile structures were immersed in Na_2PtCl_4 aqueous solution with HCl. Then, these samples were rinsed with water, followed by drying under a nitrogen stream. To remove the polymer, RIE was used. Figure 5.11a shows SEM cross section of the woodpile structure, which includes Pt nanostructures. It was clear that the PS-*b*-P2VP was fully incorporated in the woodpile structure, showing two distinct shapes of Pt nanostructures inside of the woodpile structure: 1) the shapes of the sunflower and 2) the honeycomb.

Figure 5.11b shows the Pt nanostructures inside of the woodpile structure. It is noted that brighter parts are Pt nanostructures, which are original P2VP microdomains. The elliptical shapes correspond to the cleaved multi-layered woodpile rods. Around these rods, the lamellar PS-*b*-P2VP microdomains (Pt nanostructures) were oriented normal to the rod surface, which can be attributed to the confinement effect by the 3D woodpile structure, so that the microdomains seemed to be emanated from the rods, showing the shapes of the sunflower. The observation of the honeycomb shapes could be related to 3D network of Pt nanostructures inside of the woodpile structure.

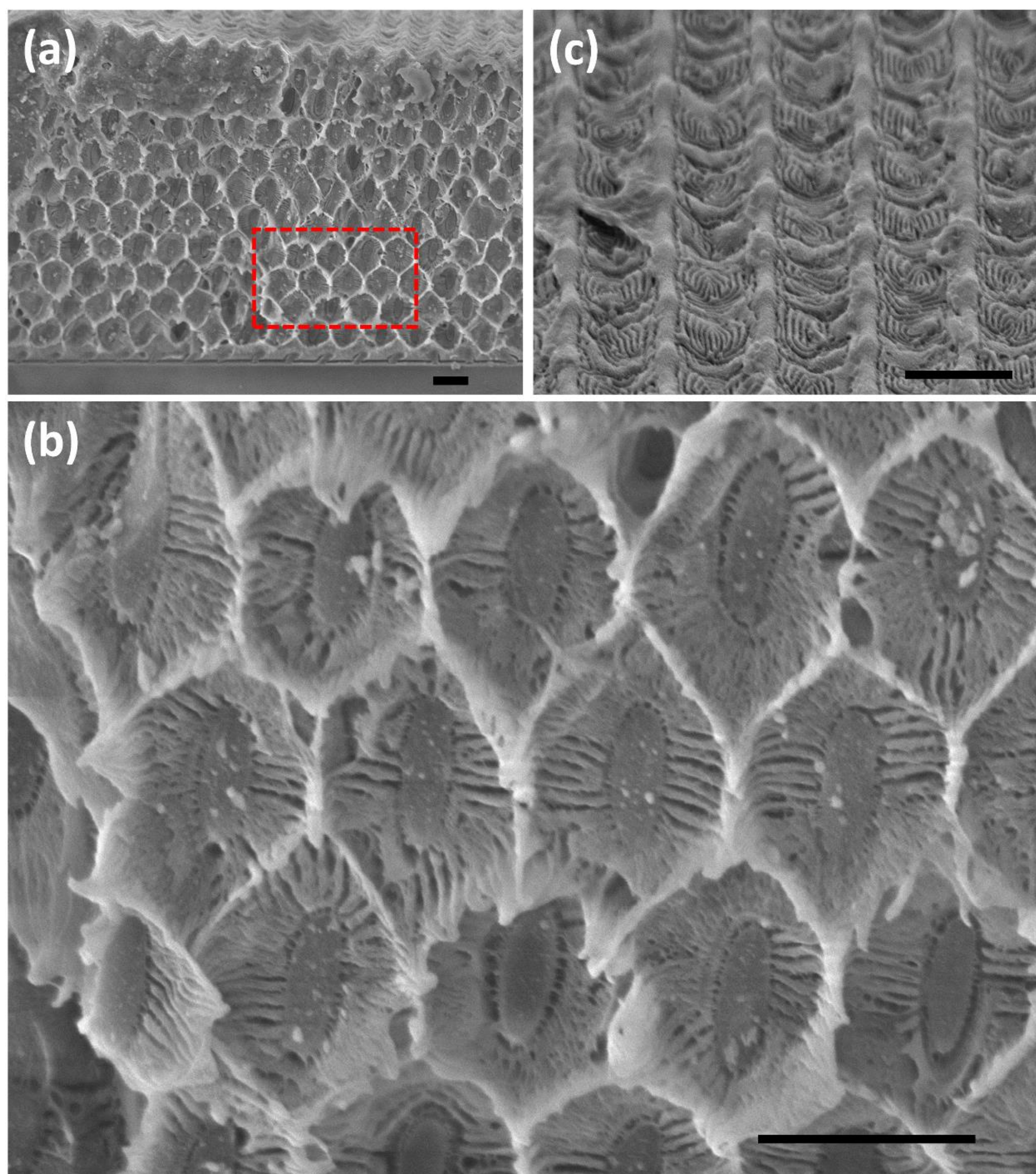

Figure 5.11 (a) SEM cross section (80° tilted) of Pt nanostructures in woodpile structure with the pitch of 1 μm and the height of 10 μm. (b) High magnification of 3D Pt nanostructures inside of the woodpile structure from the red dashed rectangle in (a). (c) Pt line patterns on top layer of woodpile structure. Dark featureless regions correspond to non-etched remaining PS layer. All scale bars are 1 μm.

Figure 5.11c shows Pt line patterns on the top layer of the woodpile structure. Initially, the top surface of the woodpile structure was fully covered by the PS block

because the surface energy of PS at air/BCP interface is lower than that of the P2VP.[23] After removal of this PS block using RIE, Pt line patterns (brighter parts in Figure 5.11c) were observed.

5.4 Conclusions

In summary, we have demonstrated the fabrication of 3D BCP microdomains using 3D woodpile structures as a guiding template. By varying the pitch, different types of PS-*b*-PMMA patterns were achieved on top layers of woodpile structures. For PS-*b*-P2VP, we produced 3D lamellar microdomains in the woodpile structures. In addition, we generated 3D Pt nanostructures by using deposition of metal salts in the P2VP blocks. The approach presented here provides a powerful platform for building 3D nanosystems with tailored functionality.

5.5 References

1. Kim, H.-C.; Park, S.-M.; Hinsberg, W. D. Block Copolymer Based Nanostructures: Materials, Processes, and Applications to Electronics. *Chem. Rev.* **2010**, *110*, 146-177.

2. Bates, F. S.; Fredrickson, G. H. Block Copolymers-Designer Soft Materials. *Phys. Today* **1999**, *52*, 32-38.

3. Segalman, R. A. Patterning with Block Copolymer Thin Films. *Mater. Sci. Eng. R* **2005**, *48*, 191-226.

4. Morris, M. A. Directed Self-Assembly of Block Copolymers for Nanocircuitry Fabrication. *Microelectron. Eng.* **2015**, *132*, 207-217.

5. Xiao, S.; Yang, X.; Steiner, P.; Hsu, Y.; Lee, K.; Wago, K.; Kuo, D. Servo-Integrated Patterned Media by Hybrid Directed Self-Assembly. *ACS Nano* **2014**, *8*, 11854-11859.

6. Mansky, P.; haikin, P.; Thomas, E. L. Monolayer Films of Diblock Copolymer Microdomains for Nanolithographic Applications. *J. Mater. Sci.* **1995**, *30*, 1987-1992.

7. Mansky, P.; Harrison, C. K.; Chaikin, P. M.; Register, R. A.; Yao, N. Nanolithographic Templates from Diblock Copolymer Thin Films. *Appl. Phys. Lett.* **1996**, *68*, 2586-2588.

8. Park, M.; Harrison, C.; Chaikin, P. M.; Register, R. A.; Adamson, D. H. Block Copolymer Lithography: Periodic Arrays of ~10^{11} Holes in 1 Square Centimeter. *Science* **1997**, *276*, 1401-1404.

9. Tavakkoli K. G., A.; Gotrik, K. W.; Hannon, A. F.; Alexander-Katz, A.; Ross, C. A.; Berggren, K. K. Templating Three-Dimensional Self-Assembled Structures in Bilayer Block Copolymer Films. *Science* **2012**, *336*, 1294-1298.

10. Gu, X.; Gunkel, I.; Russell, T. P. Pattern Transfer Using Block Copolymers. *Phil. Trans. R. Soc. A* **2013**, *371*.

11. Tsai, H.; Pitera, J. W.; Miyazoe, H.; Bangsaruntip, S.; Engelmann, S. U.; Liu, C.-C.; Cheng, J. Y.; Bucchignano, J. J.; Klaus, D. P.; Joseph, E. A.; Sanders, D. P.; Colburn, M. E.; Guillorn, M. A. Two-Dimensional Pattern Formation Using Graphoepitaxy of PS-*b*-PMMA Block Copolymers for Advanced FinFET Device and Circuit Fabrication. *ACS Nano* **2014**, *8*, 5227-5232.

12. Chai, J.; Buriak, J. M. Using Cylindrical Domains of Block Copolymers to Self-Assemble and Align Metallic Nanowires. *ACS Nano* **2008**, *2*, 489-501.

13. Chai, J.; Wang, D.; Fan, X.; Buriak, J. M. Assembly of Aligned Linear Metallic Patterns on Silicon. *Nat. Nanotechnol.* **2007**, *2*, 500-506.

14. Sun, Z.; Chen, Z.; Zhang, W.; Choi, J.; Huang, C.; Jeong, G.; Coughlin, E. B.; Hsu, Y.; Yang, X.; Lee, K. Y.; Kuo, D. S.; Xiao, S.; Russell, T. P. Directed Self-Assembly of Poly(2-Vinylpyridine)-*b*-Polystyrene-*b*-Poly(2-Vinylpyridine) Triblock Copolymer with Sub-15 nm Spacing Line Patterns Using a Nanoimprinted Photoresist Template. *Adv. Mater.* **2015**, *27*, 4364-4370.

15. Serbin, J.; Ovsianikov, A.; Chichkov, B. Fabrication of Woodpile Structures by Two-Photon Polymerization and Investigation of Their Optical Properties. *Opt. Express* **2004**, *12*, 5221-5228.

16. Wu, Y.; Cheng, G.; Katsov, K.; Sides, S. W.; Wang, J.; Tang, J.; Fredrickson, G. H.; Moskovits, M.; Stucky, G. D. Composite Mesostructures by Nano-Confinement. *Nat. Mater.* **2004**, *3*, 816-822.

17. Shin, K.; Xiang, H.; Moon, S. I.; Kim, T.; McCarthy, T. J.; Russell, T. P. Curving and Frustrating Flatland. *Science* **2004**, *306*, 76.

18. Xiang, H.; Shin, K.; Kim, T.; Moon, S. I.; McCarthy, T. J.; Russell, T. P. From Cylinders to Helices Upon Confinement. *Macromolecules* **2005**, *38*, 1055-1056.

19. Park, S.; Wang, J.-Y.; Kim, B.; Xu, J.; Russell, T. P. A Simple Route to Highly Oriented and Ordered Nanoporous Block Copolymer Templates. *ACS Nano* **2008**, *2*, 766-772.

20. Xu, J.; Hong, S. W.; Gu, W.; Lee, K. Y.; Kuo, D. S.; Xiao, S.; Russell, T. P. Fabrication of Silicon Oxide Nanodots with an Areal Density Beyond 1 Teradots Inch^{-2}. *Adv. Mater.* **2011**, *23*, 5755-5761.

21. Ruiz, R.; Dobisz, E.; Albrecht, T. R. Rectangular Patterns Using Block Copolymer Directed Assembly for High Bit Aspect Ratio Patterned Media. *ACS Nano* **2011**, *5*, 79-84.

22. Spatz, J. P.; Mössmer, S.; Hartmann, C.; Möller, M.; Herzog, T.; Krieger, M.; Boyen, H.-G.; Ziemann, P.; Kabius, B. Ordered Deposition of Inorganic Clusters from Micellar Block Copolymer Films. *Langmuir* **2000**, *16*, 407-415.

23. Kim, B. J.; Chiu, J. J.; Yi, G. R.; Pine, D. J.; Kramer, E. J. Nanoparticle-Induced Phase Transitions in Diblock-Copolymer Films. *Adv. Mater.* **2005**, *17*, 2618-2622.

CHAPTER 6

CONCLUSIONS AND OUTLOOK

Directed self-assembly (DSA) of block copolymers (BCPs) based on topographic patterns is one of the most promising strategies for overcoming resolution limitations in the current lithographic process and fabricating the next-generation data storage devices. The main focus of this dissertation is to understand the effect of minimal topographic patterning on guiding the self-assembly of BCPs in 2D and 3D. The use of minimal topographic patterns in the DSA of BCPs provides the following important advantages: 1) full occupancy of the patterned surface by allowing the BCP microdomains to exist both inside and outside of the confinement regions and 2) decreasing the total cost of patterning by minimizing the amount of topographic patterning.

We have explored the minimum amount of topographic patterning necessary to successfully guide the self-assembly of cylinder-forming BCPs. The important observation was the propagation of hexagonal arrays of cylindrical microdomains oriented normal to the film surface away from the edges of a single trench pattern, providing insight into the minimum pitch of the trench necessary to fully order hexagonal arrays. For cylindrical microdomains in BCP thin films, our results showed that the minimally patterned trench surface was more effective in guiding the hexagonal arrays than the line patterns.

We have taken advantage of grazing incidence small angle X-ray scattering (GISAXS) to study the morphological characteristics and lateral ordering of hexagonal arrays on the minimal trench patterns. GISAXS patterns revealed that the hexagonal arrays

on the minimal trench pattern were distorted, deviating from a perfect hexagonal lattice, although the (10) planes of hexagonal arrays of cylindrical microdomains were oriented parallel to the underlying trench direction over macroscopic length scales (~1×1 cm^2). A combination of the absence of topographic constraints in the unconfined direction on the minimal trench pattern with the frustration of BCP microdomains, arising from the incommensurability near the base of the trench, can explain this distortion. It is important to mention that BCP hexagonal arrays with perfect long-range lateral order (orientational and translational) cannot be achieved using 1D topographic patterns, such as the minimal trench pattern discussed here. Therefore, the future study may focus on fabricating 2D topographic patterns that can reduce the distortion, which is observed in 1D topographic patterns, thereby producing perfectly ordered BCP hexagonal arrays.

Using minimal trench patterns, we have introduced the fabrication of orthogonally aligned BCP line patterns over macroscopic distances. This study offers the opportunity to generate multilayer mesh-shaped nanostructure or nanowire arrays, which can be used for the fabrication of integrated circuit interconnects or bit-patterned media (BPM), without the using of a complex lithographic process. Simulation describing this orthogonal alignment is currently underway.

Lastly, we have addressed the fabrication of 3D BCP architectures over large areas using simple woodpile structures as a guiding template. In particular, we successfully produced 3D networks of metallic nanostructures within the woodpile structures, providing a simple but a powerful platform for building 3D nanosystems with tailored functionality. For the future study, we are interested in varying the dimensions of the woodpile structures, characterizing the morphology of the confined BCPs using X-ray scattering and

transmission electron microscopy (TEM) tomography, investigating the optical properties of 3D BCP nanostructures, and studying the computer modeling of 3D BCP nanostructures to predict the behavior of metamaterials.

There has been significant progress in this arena using the DSA of BCPs over the past decade. However, up to now, most efforts have focused on the use of diblock or triblock copolymers as templates and scaffolds for the fabrication of nanoscopic materials. It is evident that the alternative way to achieve perfection in the ordering is to increase the complexity of the polymer chain, i.e. the chain topology, so that the packing of the polymer chains within a specific morphology will provide additional directors in controlling the lateral order. As an example, mikto-arm star terpolymers are one of the more advantageous topologies to pursue. Not only are there a range of symmetries accessible, but the entropic penalties associated with the packing of the chains to ensure a constant segment density (incompressibility and a particularly demanding constant). Unlike diblock or triblock copolymers, with star-shaped terpolymers, the constraints imposed on one chain on the others are in multiple directions which hold the key to perfection in the lateral order when they combine with the DSA process. Further efforts on this area can lead us to unprecedented perfectly ordered 2D or 3D BCP systems, which have not yet been achieved using diblock or triblock copolymers.

BIBLIOGRAPHY

Aissou, K., Mumtaz, M., Fleury, G., Portale, G., Navarro, C., Cloutet, E., Brochon, C., Ross, C. A. and Hadziioannou, G. (2015) "Sub-10 nm Features Obtained from Directed Self-Assembly of Semicrystalline Polycarbosilane-Based Block Copolymer Thin Films", *Adv. Mater.,* 27**,** 261-265.

Aissou, K., Shaver, J., Fleury, G., Pécastaings, G., Brochon, C., Navarro, C., Grauby, S., Rampnoux, J.-M., Dilhaire, S. and Hadziioannou, G. (2013) "Nanoscale Block Copolymer Ordering Induced by Visible Interferometric Micropatterning: A Route Towards Large Scale Block Copolymer 2D Crystals", *Adv. Mater.,* 25**,** 213-217.

Anastasiadis, S. H., Russell, T. P., Satija, S. K. and Majkrzak, C. F. (1989) "Neutron Reflectivity Studies of the Surface-Induced Ordering of Diblock Copolymer Films", *Phys. Rev. Lett.,* 62**,** 1852-1855.

Angelescu, D. E., Harrison, C. K., Trawick, M. L., Register, R. A. and Chaikin, P. M. (2005) "Two-Dimensional Melting Transition Observed in a Block Copolymer", *Phys. Rev. Lett.,* 95**,** 025702.

Angelescu, D. E., Waller, J. H., Adamson, D. H., Deshpande, P., Chou, S. Y., Register, R. A. and Chaikin, P. M. (2004) "Macroscopic Orientation of Block Copolymer Cylinders in Single-Layer Films by Shearing", *Adv. Mater.,* 16**,** 1736-1740.

Auzelyte, V., Dais, C., Farquet, P., Grützmacher, D., Heyderman, L. J., Luo, F., Olliges, S., Padeste, C., Sahoo, P. K., Thomson, T., Turchanin, A., David, C. and Solak, H. H. (2009) "Extreme Ultraviolet Interference Lithography at the Paul Scherrer Institut", *J. Micro/Nanolith., MEMS MOEMS,* 8**,** 021204-10.

Bang, J., Bae, J., Löwenhielm, P., Spiessberger, C., Given-Beck, S. A., Russell, T. P. and Hawker, C. J. (2007) "Facile Routes to Patterned Surface Neutralization Layers for Block Copolymer Lithography", *Adv. Mater.,* 19**,** 4552-4557.

Bang, J., Jeong, U., Ryu, D. Y., Russell, T. P. and Hawker, C. J. (2009) "Block Copolymer Nanolithography: Translation of Molecular Level Control to Nanoscale Patterns", *Adv. Mater.,* 21**,** 4769-4792.

Bates, F. S. (1991) "Polymer-Polymer Phase Behavior", *Science,* 251**,** 898-905.

Bates, F. S. and Fredrickson, G. H. (1990) "Block Copolymer Thermodynamics: Theory and Experiment", *Annu. Rev. Phys. Chem.,* 41**,** 525-557.

Bates, F. S. and Fredrickson, G. H. (1999) "Block Copolymers-Designer Soft Materials", *Phys. Today,* 52**,** 32-38.

Berry, B. C., Bosse, A. W., Douglas, J. F., Jones, R. L. and Karim, A. (2007) "Orientational Order in Block Copolymer Films Zone Annealed Below the Order−Disorder Transition Temperature", *Nano Lett.,* 7**,** 2789-2794.

Berry, B. C., Singh, G., Kim, H.-C. and Karim, A. (2013) "Highly Aligned Block Copolymer Thin Films by Synergistic Coupling of Static Graphoepitaxy and Dynamic Thermal Annealing Fields", *ACS Macro Lett.,* 2**,** 346-350.

Bita, I., Yang, J. K. W., Jung, Y. S., Ross, C. A., Thomas, E. L. and Berggren, K. K. (2008) "Graphoepitaxy of Self-Assembled Block Copolymers on Two-Dimensional Periodic Patterned Templates", *Science,* 321**,** 939-943.

Blachut, G., Sirard, S. M., Maher, M. J., Asano, Y., Someya, Y., Lane, A. P., Durand, W. J., Bates, C. M., Dinhobl, A. M., Gronheid, R., Hymes, D., Ellison, C. J. and Willson, C. G. (2016) "A Hybrid Chemo-/Grapho-Epitaxial Alignment Strategy for Defect Reduction in Sub-10 nm Directed Self-Assembly of Silicon-Containing Block Copolymers", *Chem. Mater.*

Black, C. T. (2005) "Self-Aligned Self Assembly of Multi-Nanowire Silicon Field Effect Transistors", *Appl. Phys. Lett.,* 87**,** 163116-3.

Black, C. T. and Bezencenet, O. (2004) "Nanometer-Scale Pattern Registration and Alignment by Directed Diblock Copolymer Self-Assembly", *IEEE Trans. Nanotechnol.,* 3**,** 412-415.

Borah, D., Shaw, M. T., Holmes, J. D. and Morris, M. A. (2013) "Sub-10 nm Feature Size PS-*b*-PDMS Block Copolymer Structures Fabricated by a Microwave-Assisted Solvothermal Process", *ACS Appl. Mater. Interfaces,* 5**,** 2004-2012.

Brandrup, J., Immergut, E. H. and Grulke, E. A. (1999) *Polymer Handbook,* New York, John Wiley & Sons.

Brown, G. and Chakrabarti, A. (1995) "Ordering of Block Copolymer Melts in Confined Geometry", *J. Chem. Phys.,* 102**,** 1440-1448.

Cai, Z. h., Huang, K., Montano, P. A., Russell, T. P., Bai, J. M. and Zajac, G. W. (1993) "Experimental Study of the Surface Structure of Diblock Copolymer Films Using Microscopy and X-Ray Scattering", *J. Chem. Phys.,* 98**,** 2376-2386.

Chai, J. and Buriak, J. M. (2008) "Using Cylindrical Domains of Block Copolymers to Self-Assemble and Align Metallic Nanowires", *ACS Nano,* 2**,** 489-501.

Chai, J., Wang, D., Fan, X. and Buriak, J. M. (2007) "Assembly of Aligned Linear Metallic Patterns on Silicon", *Nat. Nanotechnol.,* 2**,** 500-506.

Chang, J.-B., Choi, H. K., Hannon, A. F., Alexander-Katz, A., Ross, C. A. and Berggren, K. K. (2014) "Design Rules for Self-Assembled Block Copolymer Patterns Using Tiled Templates", *Nat. Commun.,* 5**,** Article number: 3305, 1-9.

Chang, J.-B., Son, J. G., Hannon, A. F., Alexander-Katz, A., Ross, C. A. and Berggren, K. K. (2012) "Aligned Sub-10-nm Block Copolymer Patterns Templated by Post Arrays", *ACS Nano,* 6**,** 2071-2077.

Chang, S.-W., Chuang, V. P., Boles, S. T., Ross, C. A. and Thompson, C. V. (2009) "Densely Packed Arrays of Ultra-High-Aspect-Ratio Silicon Nanowires Fabricated Using Block-Copolymer Lithography and Metal-Assisted Etching", *Adv. Funct. Mater.,* 19**,** 2495-2500.

Cheng, J. Y., Mayes, A. M. and Ross, C. A. (2004) "Nanostructure Engineering by Templated Self-Assembly of Block Copolymers", *Nat. Mater.,* 3**,** 823-828.

Cheng, J. Y., Pitera, J., Park, O.-H., Flickner, M., Ruiz, R., Black, C. T. and Kim, H.-C. (2007) "Rapid Directed Self Assembly of Lamellar Microdomains from a Block Copolymer Containing Hybrid", *Appl. Phys. Lett.,* 91**,** 143106-3.

Cheng, J. Y., Rettner, C. T., Sanders, D. P., Kim, H.-C. and Hinsberg, W. D. (2008) "Dense Self-Assembly on Sparse Chemical Patterns: Rectifying and Multiplying Lithographic Patterns Using Block Copolymers", *Adv. Mater.,* 20**,** 3155-3158.

Cheng, J. Y., Ross, C. A., Smith, H. I. and Thomas, E. L. (2006) "Templated Self-Assembly of Block Copolymers: Top-Down Helps Bottom-Up", *Adv. Mater.,* 18**,** 2505-2521.

Cheng, J. Y., Ross, C. A., Thomas, E. L., Smith, H. I. and Vancso, G. J. (2002) "Fabrication of Nanostructures with Long-Range Order Using Block Copolymer Lithography", *Appl. Phys. Lett.,* 81**,** 3657-3659.

Cheng, J. Y., Ross, C. A., Thomas, E. L., Smith, H. I. and Vancso, G. J. (2003) "Templated Self-Assembly of Block Copolymers: Effect of Substrate Topography", *Adv. Mater.,* 15**,** 1599-1602.

Cheng, J. Y., Zhang, F., Chuang, V. P., Mayes, A. M. and Ross, C. A. (2006) "Self-Assembled One-Dimensional Nanostructure Arrays", *Nano Lett.,* 6**,** 2099-2103.

Cheng, J. Y., Zhang, F., Smith, H. I., Vancso, G. J. and Ross, C. A. (2006) "Pattern Registration between Spherical Block-Copolymer Domains and Topographical Templates", *Adv. Mater.,* 18**,** 597-601.

Choi, E., Park, S., Ahn, H., Lee, M., Bang, J., Lee, B. and Ryu, D. Y. (2014) "Substrate-Independent Lamellar Orientation in High-Molecular-Weight Polystyrene-*b*-Poly(Methyl Methacrylate) Films: Neutral Solvent Vapor and Thermal Annealing Effect", *Macromolecules,* 47**,** 3969-3977.

Choi, J., Huh, J., Carter, K. R. and Russell, T. P. (2016) "Directed Self-Assembly of Block Copolymer Thin Films Using Minimal Topographic Patterns", *ACS Nano,* 10**,** 7915-7925.

Chou, S. Y., Krauss, P. R. and Renstrom, P. J. (1996) "Nanoimprint Lithography", *J. Vac. Sci. Technol. B,* 14**,** 4129-4133.

Chuang, V. P., Cheng, J. Y., Savas, T. A. and Ross, C. A. (2006) "Three-Dimensional Self-Assembly of Spherical Block Copolymer Domains into V-Shaped Grooves", *Nano Lett.,* 6**,** 2332-2337.

Chuang, V. P., Gwyther, J., Mickiewicz, R. A., Manners, I. and Ross, C. A. (2009) "Templated Self-Assembly of Square Symmetry Arrays from an ABC Triblock Terpolymer", *Nano Lett.,* 9**,** 4364-4369.

Coulon, G., Russell, T. P., Deline, V. R. and Green, P. F. (1989) "Surface-Induced Orientation of Symmetric, Diblock Copolymers: A Secondary Ion Mass-Spectrometry Study", *Macromolecules,* 22**,** 2581-2589.

Cushen, J., Wan, L., Blachut, G., Maher, M. J., Albrecht, T. R., Ellison, C. J., Willson, C. G. and Ruiz, R. (2015) "Double-Patterned Sidewall Directed Self-Assembly and Pattern Transfer of Sub-10 nm PTMSS-*b*-PMOST", *ACS Appl. Mater. Interfaces,* 7**,** 13476-13483.

Dobriyal, P., Xiang, H., Kazuyuki, M., Chen, J.-T., Jinnai, H. and Russell, T. P. (2009) "Cylindrically Confined Diblock Copolymers", *Macromolecules,* 42**,** 9082-9088.

Edwards, E. W., Stoykovich, M. P., Solak, H. H. and Nealey, P. F. (2006) "Long-Range Order and Orientation of Cylinder-Forming Block Copolymers on Chemically Nanopatterned Striped Surfaces", *Macromolecules,* 39**,** 3598-3607.

Farhoud, M., Ferrera, J., Lochtefeld, A. J., Murphy, T. E., Schattenburg, M. L., Carter, J., Ross, C. A. and Smith, H. I. (1999) "Fabrication of 200 nm Period Nanomagnet Arrays Using Interference Lithography and a Negative Resist", *J. Vac. Sci. Technol. B,* 17**,** 3182-3185.

Fasolka, M. J., Harris, D. J., Mayes, A. M., Yoon, M. and Mochrie, S. G. J. (1997) "Observed Substrate Topography-Mediated Lateral Patterning of Diblock Copolymer Films", *Phys. Rev. Lett.,* 79**,** 3018-3021.

Ferrarese Lupi, F., Aprile, G., Giammaria, T. J., Seguini, G., Zuccheri, G., De Leo, N., Boarino, L., Laus, M. and Perego, M. (2015) "Thickness and Microdomain Orientation of Asymmetric PS-*b*-PMMA Block Copolymer Films inside Periodic Gratings", *ACS Appl. Mater. Interfaces,* 7**,** 23615-23622.

Ferrarese Lupi, F., Giammaria, T. J., Seguini, G., Laus, M., Enrico, E., De Leo, N., Boarino, L., Ober, C. K. and Perego, M. (2014) "Thermally Induced Orientational Flipping of Cylindrical Phase Diblock Copolymers", *Journal of Materials Chemistry C,* 2**,** 2175-2182.

Fitzgerald, T. G., Farrell, R. A., Petkov, N., Bolger, C. T., Shaw, M. T., Charpin, J. P. F., Gleeson, J. P., Holmes, J. D. and Morris, M. A. (2009) "Study on the Combined Effects of Solvent Evaporation and Polymer Flow Upon Block Copolymer Self-Assembly and Alignment on Topographic Patterns", *Langmuir,* 25**,** 13551-13560.

Gabai, R., Ismach, A. and Joselevich, E. (2007) "Nanofacet Lithography: A New Bottom-up Approach to Nanopatterning and Nanofabrication by Soft Replication of Spontaneously Faceted Crystal Surfaces", *Adv. Mater.,* 19**,** 1325-1330.

Gates, B. D., Xu, Q., Stewart, M., Ryan, D., Willson, C. G. and Whitesides, G. M. (2005) "New Approaches to Nanofabrication: Molding, Printing, and Other Techniques", *Chem. Rev.,* 105**,** 1171-1196.

Geis, M. W., Flanders, D. C. and Smith, H. I. (1979) "Crystallographic Orientation of Silicon on an Amorphous Substrate Using an Artificial Surface-Relief Grating and Laser Crystallization", *Appl. Phys. Lett.,* 35**,** 71-74.

Geissler, M. and Xia, Y. (2004) "Patterning: Principles and Some New Developments", *Adv. Mater.,* 16**,** 1249-1269.

Grigorescu, A. E. and Hagen, C. W. (2009) "Resists for Sub-20-nm Electron Beam Lithography with a Focus on HSQ: State of the Art", *Nanotechnology,* 20**,** 292001.

Gu, X., Gunkel, I., Hexemer, A., Gu, W. and Russell, T. P. (2014) "An in Situ Grazing Incidence X-Ray Scattering Study of Block Copolymer Thin Films During Solvent Vapor Annealing", *Adv. Mater.,* 26**,** 273-281.

Gu, X., Gunkel, I. and Russell, T. P. (2013) "Pattern Transfer Using Block Copolymers", *Phil. Trans. R. Soc. A,* 371.

Hammond, M. R., Cochran, E., Fredrickson, G. H. and Kramer, E. J. (2005) "Temperature Dependence of Order, Disorder, and Defects in Laterally Confined Diblock Copolymer Cylinder Monolayers", *Macromolecules,* 38**,** 6575-6585.

Hammond, M. R. and Kramer, E. J. (2006) "Edge Effects on Thermal Disorder in Laterally Confined Diblock Copolymer Cylinder Monolayers", *Macromolecules,* 39**,** 1538-1544.

Han, E., In, I., Park, S. M., La, Y. H., Wang, Y., Nealey, P. F. and Gopalan, P. (2007) "Photopatternable Imaging Layers for Controlling Block Copolymer Microdomain Orientation", *Adv. Mater.,* 19**,** 4448-4452.

Han, E., Kang, H., Liu, C.-C., Nealey, P. F. and Gopalan, P. (2010) "Graphoepitaxial Assembly of Symmetric Block Copolymers on Weakly Preferential Substrates", *Adv. Mater.,* 22**,** 4325-4329.

Hannon, A. F., Ding, Y., Bai, W., Ross, C. A. and Alexander-Katz, A. (2014) "Optimizing Topographical Templates for Directed Self-Assembly of Block Copolymers via Inverse Design Simulations", *Nano Lett.,* 14**,** 318-325.

Hatzakis, M. (1969) "Electron Resists for Microcircuit and Mask Production", *J. Electrochem. Soc.,* 116**,** 1033-1037.

Hawker, C. J., Elce, E., Dao, J., Volksen, W., Russell, T. P. and Barclay, G. G. (1996) "Well-Defined Random Copolymers by a “Living” Free-Radical Polymerization Process", *Macromolecules,* 29**,** 2686-2688.

Hawker, C. J. and Russell, T. P. (2005) "Block Copolymer Lithography: Merging “Bottom-up” with “Top-Down” Processes", *MRS Bull.,* 30**,** 952-966.

Haynes, W. M. (2012) *Crc Handbook of Chemistry and Physics 98rd Edition,* Boca Raton, CRC Press.

He, X., Song, M., Liang, H. and Pan, C. (2001) "Self-Assembly of the Symmetric Diblock Copolymer in a Confined State: Monte Carlo Simulation", *J. Chem. Phys.,* 114**,** 10510-10513.

Hexemer, A., Bras, W., Glossinger, J., Schaible, E., Gann, E., Kirian, R., MacDowell, A., Church, M., Rude, B. and Padmore, H. (2010) "A SAXS/WAXS/GISAXS Beamline with Multilayer Monochromator", *J. Phys. Conf. Ser.,* 247**,** 012007.

Hexemer, A., Stein, G. E., Kramer, E. J. and Magonov, S. (2005) "Block Copolymer Monolayer Structure Measured with Scanning Force Microscopy Moiré Patterns", *Macromolecules,* 38**,** 7083-7089.

Hoheisel, T. N., Hur, K. and Wiesner, U. B. (2015) "Block Copolymer-Nanoparticle Hybrid Self-Assembly", *Prog. Polym. Sci.,* 40**,** 3-32.

Hong, S. W., Gu, X., Huh, J., Xiao, S. and Russell, T. P. (2011) "Circular Nanopatterns over Large Areas from the Self-Assembly of Block Copolymers Guided by Shallow Trenches", *ACS Nano,* 5**,** 2855-2860.

Hong, S. W., Huh, J., Gu, X., Lee, D. H., Jo, W. H., Park, S., Xu, T. and Russell, T. P. (2012) "Unidirectionally Aligned Line Patterns Driven by Entropic Effects on Faceted Surfaces", *Proc. Natl. Acad. Sci.,* 109**,** 1402-1406.

Hong, S. W., Voronov, D. L., Lee, D. H., Hexemer, A., Padmore, H. A., Xu, T. and Russell, T. P. (2012) "Controlled Orientation of Block Copolymers on Defect-Free Faceted Surfaces", *Adv. Mater.,* 24**,** 4278-4283.

Hu, H., Gopinadhan, M. and Osuji, C. O. (2014) "Directed Self-Assembly of Block Copolymers: A Tutorial Review of Strategies for Enabling Nanotechnology with Soft Matter", *Soft Matter,* 10**,** 3867-3889.

Huang, E., Mansky, P., Russell, T. P., Harrison, C., Chaikin, P. M., Register, R. A., Hawker, C. J. and Mays, J. (2000) "Mixed Lamellar Films: Evolution, Commensurability Effects, and Preferential Defect Formation", *Macromolecules,* 33**,** 80-88.

Huang, E., Pruzinsky, S., Russell, T. P., Mays, J. and Hawker, C. J. (1999) "Neutrality Conditions for Block Copolymer Systems on Random Copolymer Brush Surfaces", *Macromolecules,* 32**,** 5299-5303.

Huang, E., Russell, T. P., Harrison, C., Chaikin, P. M., Register, R. A., Hawker, C. J. and Mays, J. (1998) "Using Surface Active Random Copolymers to Control the Domain Orientation in Diblock Copolymer Thin Films", *Macromolecules,* 31**,** 7641-7650.

Husseman, M., Malmström, E. E., McNamara, M., Mate, M., Mecerreyes, D., Benoit, D. G., Hedrick, J. L., Mansky, P., Huang, E., Russell, T. P. and Hawker, C. J. (1999) "Controlled Synthesis of Polymer Brushes by “Living” Free Radical Polymerization Techniques", *Macromolecules,* 32**,** 1424-1431.

Huth, M., Ritley, K. A., Oster, J., Dosch, H. and Adrian, H. (2002) "Highly Ordered Fe and Nb Stripe Arrays on Facetted A-$Al_{2}o_{3}$ (1010)", *Adv. Funct. Mater.,* 12**,** 333-338.

ITRS (2013) "International Technology Roadmap for Semiconductors (ITRS) 2013 Edition", *http://http://www.itrs2.net/2013-itrs.html.*

Jeong, J. W., Park, W. I., Do, L.-M., Park, J.-H., Kim, T.-H., Chae, G. and Jung, Y. S. (2012) "Nanotransfer Printing with Sub-10 nm Resolution Realized Using Directed Self-Assembly", *Adv. Mater.,* 24**,** 3526-3531.

Jeong, J. W., Park, W. I., Kim, M.-J., Ross, C. A. and Jung, Y. S. (2011) "Highly Tunable Self-Assembled Nanostructures from a Poly(2-Vinylpyridine-*b*-Dimethylsiloxane) Block Copolymer", *Nano Lett.,* 11**,** 4095-4101.

Jeong, S.-J., Kim, J. E., Moon, H.-S., Kim, B. H., Kim, S. M., Kim, J. B. and Kim, S. O. (2009) "Soft Graphoepitaxy of Block Copolymer Assembly with Disposable Photoresist Confinement", *Nano Lett.,* 9**,** 2300-2305.

Jeong, S.-J., Moon, H.-S., Kim, B. H., Kim, J. Y., Yu, J., Lee, S., Lee, M. G., Choi, H. and Kim, S. O. (2010) "Ultralarge-Area Block Copolymer Lithography Enabled by Disposable Photoresist Prepatterning", *ACS Nano,* 4**,** 5181-5186.

Jeong, S.-J., Moon, H.-S., Shin, J., Kim, B. H., Shin, D. O., Kim, J. Y., Lee, Y.-H., Kim, J. U. and Kim, S. O. (2010) "One-Dimensional Metal Nanowire Assembly via Block Copolymer Soft Graphoepitaxy", *Nano Lett.,* 10**,** 3500-3505.

Ji, S., Wan, L., Liu, C.-C. and Nealey, P. F. (2016) "Directed Self-Assembly of Block Copolymers on Chemical Patterns: A Platform for Nanofabrication", *Prog. Polym. Sci.,* 54–55**,** 76-127.

Jung, Y. S., Chang, J. B., Verploegen, E., Berggren, K. K. and Ross, C. A. (2010) "A Path to Ultranarrow Patterns Using Self-Assembled Lithography", *Nano Lett.,* 10**,** 1000-1005.

Jung, Y. S., Jung, W. and Ross, C. A. (2008) "Nanofabricated Concentric Ring Structures by Templated Self-Assembly of a Diblock Copolymer", *Nano Lett.,* 8**,** 2975-2981.

Jung, Y. S., Jung, W., Tuller, H. L. and Ross, C. A. (2008) "Nanowire Conductive Polymer Gas Sensor Patterned Using Self-Assembled Block Copolymer Lithography", *Nano Lett.,* 8**,** 3776-3780.

Jung, Y. S. and Ross, C. A. (2007) "Orientation-Controlled Self-Assembled Nanolithography Using a Polystyrene−Polydimethylsiloxane Block Copolymer", *Nano Lett.,* 7**,** 2046-2050.

Kao, J., Jeong, S.-J., Jiang, Z., Lee, D. H., Aissou, K., Ross, C. A., Russell, T. P. and Xu, T. (2014) "Direct 3-D Nanoparticle Assemblies in Thin Films via Topographically Patterned Surfaces", *Adv. Mater.,* 26**,** 2777-2781.

Kellogg, G. J., Walton, D. G., Mayes, A. M., Lambooy, P., Russell, T. P., Gallagher, P. D. and Satija, S. K. (1996) "Observed Surface Energy Effects in Confined Diblock Copolymers", *Phys. Rev. Lett.,* 76**,** 2503-2506.

Kikuchi, M. and Binder, K. (1993) "Monte Carlo Study of Thin Films of the Symmetric Diblock-Copolymer Melt", *Europhys. Lett.,* 21**,** 427.

Kim, B. H., Choi, Y., Kim, J. Y., Shin, H., Kim, S., Son, S.-W., Kim, S. O. and Kim, P. (2014) "Wrinkle-Directed Self-Assembly of Block Copolymers for Aligning of Nanowire Arrays", *Adv. Mater.,* 26**,** 4665-4670.

Kim, B. J., Chiu, J. J., Yi, G. R., Pine, D. J. and Kramer, E. J. (2005) "Nanoparticle-Induced Phase Transitions in Diblock-Copolymer Films", *Adv. Mater.,* 17**,** 2618-2622.

Kim, E., Ahn, H., Park, S., Lee, H., Lee, M., Lee, S., Kim, T., Kwak, E.-A., Lee, J. H., Lei, X., Huh, J., Bang, J., Lee, B. and Ryu, D. Y. (2013) "Directed Assembly of High Molecular Weight Block Copolymers: Highly Ordered Line Patterns of Perpendicularly Oriented Lamellae with Large Periods", *ACS Nano,* 7**,** 1952-1960.

Kim, G. and Libera, M. (1998) "Kinetic Constraints on the Development of Surface Microstructure in SBS Thin Films", *Macromolecules,* 31**,** 2670-2672.

Kim, G. and Libera, M. (1998) "Morphological Development in Solvent-Cast Polystyrene−Polybutadiene−Polystyrene (SBS) Triblock Copolymer Thin Films", *Macromolecules,* 31**,** 2569-2577.

Kim, H.-C., Park, S.-M. and Hinsberg, W. D. (2010) "Block Copolymer Based Nanostructures: Materials, Processes, and Applications to Electronics", *Chem. Rev.,* 110**,** 146-177.

Kim, H.-C., Rettner, C., T. and Sundström, L. (2008) "Fabrication of 20 nm Half-Pitch Gratings by Corrugation-Directed Self-Assembly", *Nanotechnology,* 19**,** 235301.

Kim, H.-C. and Russell, T. P. (2001) "Ordering in Thin Films of Asymmetric Diblock Copolymers", *J. Polym. Sci., Part B: Polym. Phys.,* 39**,** 663-668.

Kim, M., Han, E., Sweat, D. P. and Gopalan, P. (2013) "Interplay of Surface Chemical Composition and Film Thickness on Graphoepitaxial Assembly of Asymmetric Block Copolymers", *Soft Matter,* 9**,** 6135-6141.

Kim, S., Nealey, P. F. and Bates, F. S. (2013) "Directed Assembly of Lamellae Forming Block Copolymer Thin Films near the Order–Disorder Transition", *Nano Lett.,* 14**,** 148-152.

Kim, S., Shin, D. O., Choi, D.-G., Jeong, J.-R., Mun, J. H., Yang, Y.-B., Kim, J. U., Kim, S. O. and Jeong, J.-H. (2012) "Graphoepitaxy of Block-Copolymer Self-Assembly Integrated with Single-Step Zno Nanoimprinting", *Small,* 8**,** 1563-1569.

Kim, S. H., Misner, M. J. and Russell, T. P. (2004) "Solvent-Induced Ordering in Thin Film Diblock Copolymer/Homopolymer Mixtures", *Adv. Mater.,* 16**,** 2119-2123.

Kim, S. H., Misner, M. J., Xu, T., Kimura, M. and Russell, T. P. (2004) "Highly Oriented and Ordered Arrays from Block Copolymers via Solvent Evaporation", *Adv. Mater.,* 16**,** 226-231.

Kim, S. O., Solak, H. H., Stoykovich, M. P., Ferrier, N. J., de Pablo, J. J. and Nealey, P. F. (2003) "Epitaxial Self-Assembly of Block Copolymers on Lithographically Defined Nanopatterned Substrates", *Nature,* 424**,** 411-414.

Knoll, A., Horvat, A., Lyakhova, K. S., Krausch, G., Sevink, G. J. A., Zvelindovsky, A. V. and Magerle, R. (2002) "Phase Behavior in Thin Films of Cylinder-Forming Block Copolymers", *Phys. Rev. Lett.,* 89**,** 035501.

Koneripalli, N., Singh, N., Levicky, R., Bates, F. S., Gallagher, P. D. and Satija, S. K. (1995) "Confined Block Copolymer Thin Films", *Macromolecules,* 28**,** 2897-2904.

Koo, K., Ahn, H., Kim, S.-W., Ryu, D. Y. and Russell, T. P. (2013) "Directed Self-Assembly of Block Copolymers in the Extreme: Guiding Microdomains from the Small to the Large", *Soft Matter,* 9**,** 9059-9071.

Kurihara, K., Iwadate, K., Namatsu, H., Nagase, M., Takenaka, H. and Murase, K. (1995) "An Electron Beam Nanolithography System and its Application to Si Nanofabrication", *Jpn. J. Appl. Phys.,* 34**,** 6940.

La, Y.-H., Edwards, E. W., Park, S.-M. and Nealey, P. F. (2005) "Directed Assembly of Cylinder-Forming Block Copolymer Films and Thermochemically Induced Cylinder to Sphere Transition: A Hierarchical Route to Linear Arrays of Nanodots", *Nano Lett.,* 5**,** 1379-1384.

Lambooy, P., Russell, T. P., Kellogg, G. J., Mayes, A. M., Gallagher, P. D. and Satija, S. K. (1994) "Observed Frustration in Confined Block Copolymers", *Phys. Rev. Lett.,* 72**,** 2899-2902.

Lee, B., Park, I., Yoon, J., Park, S., Kim, J., Kim, K.-W., Chang, T. and Ree, M. (2005) "Structural Analysis of Block Copolymer Thin Films with Grazing Incidence Small-Angle X-Ray Scattering", *Macromolecules,* 38**,** 4311-4323.

Li, W. and Müller, M. (2016) "Directed Self-Assembly of Block Copolymers by Chemical or Topographical Guiding Patterns: Optimizing Molecular Architecture, Thin-Film Properties, and Kinetics", *Prog. Polym. Sci.,* 54–55**,** 47-75.

Li, Y., Peterson, J. J., Jhaveri, S. B. and Carter, K. R. (2013) "Patterned Polymer Films via Reactive Silane Infusion-Induced Wrinkling", *Langmuir,* 29**,** 4632-4639.

Lin, Z. Q., Kim, D. H., Wu, X. D., Boosahda, L., Stone, D., LaRose, L. and Russell, T. P. (2002) "A Rapid Route to Arrays of Nanostructures in Thin Films", *Adv. Mater.,* 14**,** 1373-1376.

Liu, C.-C., Nealey, P. F., Raub, A. K., Hakeem, P. J., Brueck, S. R. J., Han, E. and Gopalan, P. (2010) "Integration of Block Copolymer Directed Assembly with 193 Immersion Lithography", *J. Vac. Sci. Technol. B,* 28**,** C6B30-C6B34.

Liu, C.-C., Ramírez-Hernández, A., Han, E., Craig, G. S. W., Tada, Y., Yoshida, H., Kang, H., Ji, S., Gopalan, P., de Pablo, J. J. and Nealey, P. F. (2013) "Chemical Patterns for Directed Self-Assembly of Lamellae-Forming Block Copolymers with Density Multiplication of Features", *Macromolecules,* 46**,** 1415-1424.

Long, B. K., Keitz, B. K. and Willson, C. G. (2007) "Materials for Step and Flash Imprint Lithography (S-Fil®)", *J. Mater. Chem.,* 17**,** 3575-3580.

Luo, M. and Epps, T. H. (2013) "Directed Block Copolymer Thin Film Self-Assembly: Emerging Trends in Nanopattern Fabrication", *Macromolecules,* 46**,** 7567-7579.

Majewski, P. W. and Yager, K. G. (2015) "Latent Alignment in Pathway-Dependent Ordering of Block Copolymer Thin Films", *Nano Lett.,* 15**,** 5221-5228.

Mansky, P., haikin, P. and Thomas, E. L. (1995) "Monolayer Films of Diblock Copolymer Microdomains for Nanolithographic Applications", *J. Mater. Sci.,* 30**,** 1987-1992.

Mansky, P., Harrison, C. K., Chaikin, P. M., Register, R. A. and Yao, N. (1996) "Nanolithographic Templates from Diblock Copolymer Thin Films", *Appl. Phys. Lett.,* 68**,** 2586-2588.

Mansky, P., Liu, Y., Huang, E., Russell, T. P. and Hawker, C. (1997) "Controlling Polymer-Surface Interactions with Random Copolymer Brushes", *Science,* 275**,** 1458-1460.

Mansky, P., Russell, T. P., Hawker, C. J., Mays, J., Cook, D. C. and Satija, S. K. (1997) "Interfacial Segregation in Disordered Block Copolymers: Effect of Tunable Surface Potentials", *Phys. Rev. Lett.,* 79**,** 237-240.

Mansky, P., Russell, T. P., Hawker, C. J., Pitsikalis, M. and Mays, J. (1997) "Ordered Diblock Copolymer Films on Random Copolymer Brushes", *Macromolecules,* 30**,** 6810-6813.

Mansky, P., Tsui, O. K. C., Russell, T. P. and Gallot, Y. (1999) "Phase Coherence and Microphase Separation Transitions in Diblock Copolymer Thin Films", *Macromolecules,* 32**,** 4832-4837.

Maret, M., Tiron, R., Chevalier, X., Gergaud, P., Gharbi, A., Lapeyre, C., Pradelles, J., Jousseaume, V., Fleury, G., Hadziioannou, G., Boudet, N. and Navarro, C. (2014) "Probing Self-Assembly of Cylindrical Morphology Block Copolymer Using in Situ and ex Situ Grazing Incidence Small-Angle X-Ray Scattering: The Attractive Case of Graphoepitaxy", *Macromolecules,* 47**,** 7221-7229.

Marrian, C. R. K. and Tennant, D. M. (2003) "Nanofabrication", *J. Vac. Sci. Technol. A,* 21**,** S207-S215.

McCord, M. A. and Rooks, M. J. (1997) *Handbook of Microlithography, Micromachining, and Microfabrication. Volume 1: Microlithography,* Bellingham, SPIE.

Menelle, A., Russell, T. P., Anastasiadis, S. H., Satija, S. K. and Majkrzak, C. F. (1992) "Ordering of Thin Diblock Copolymer Films", *Phys. Rev. Lett.,* 68**,** 67-70.

Mikulík, P., Jergel, M., Baumbach, T., Majková, E., Pincík, E., Luby, S., Ortega, L., Tucoulou, R., Hudek, P. and Kostic, I. (2001) "Coplanar and Non-Coplanar X-Ray Reflectivity Characterization of Lateral W/Si Multilayer Gratings", *J. Phys. D: Appl. Phys.,* 34**,** A188.

Mishra, V., Fredrickson, G. H. and Kramer, E. J. (2012) "Effect of Film Thickness and Domain Spacing on Defect Densities in Directed Self-Assembly of Cylindrical Morphology Block Copolymers", *ACS Nano,* 6**,** 2629-2641.

Mokarian-Tabari, P., Collins, T. W., Holmes, J. D. and Morris, M. A. (2011) "Cyclical “Flipping” of Morphology in Block Copolymer Thin Films", *ACS Nano,* 5**,** 4617-4623.

Morris, M. A. (2015) "Directed Self-Assembly of Block Copolymers for Nanocircuitry Fabrication", *Microelectron. Eng.,* 132**,** 207-217.

Murphy, J. N., Harris, K. D. and Buriak, J. M. (2015) "Automated Defect and Correlation Length Analysis of Block Copolymer Thin Film Nanopatterns", *PLoS ONE,* 10**,** e0133088.

Namatsu, H., Takahashi, Y., Yamazaki, K., Yamaguchi, T., Nagase, M. and Kurihara, K. (1998) "Three-Dimensional Siloxane Resist for the Formation of Nanopatterns with Minimum Linewidth Fluctuations", *J. Vac. Sci. Technol. B,* 16**,** 69-76.

Nishida, T., Notomi, M., Iga, R. and Tamamura, T. (1992) "Quantum Wire Fabrication by E-Beam Elithography Using High-Resolution and High-Sensitivity E-Beam Resist ZEP-520", *Jpn. J. Appl. Phys.,* 31**,** 4508-4514.

Paik, M. Y., Bosworth, J. K., Smilges, D.-M., Schwartz, E. L., Andre, X. and Ober, C. K. (2010) "Reversible Morphology Control in Block Copolymer Films via Solvent Vapor Processing: An in Situ GISAXS Study", *Macromolecules,* 43**,** 4253-4260.

Pandav, G., Durand, W. J., Ellison, C. J., Willson, C. G. and Ganesan, V. (2015) "Directed Self Assembly of Block Copolymers Using Chemical Patterns with Sidewall Guiding Lines, Backfilled with Random Copolymer Brushes", *Soft Matter,* 11**,** 9107-9114.

Park, C., Cheng, J. Y., Fasolka, M. J., Mayes, A. M., Ross, C. A., Thomas, E. L. and De Rosa, C. (2001) "Double Textured Cylindrical Block Copolymer Domains via Directional Solidification on a Topographically Patterned Substrate", *Appl. Phys. Lett.,* 79**,** 848-850.

Park, H.-H., Law, W. L., Zhang, X., Hwang, S.-Y., Jung, S. H., Shin, H.-B., Kang, H. K., Park, H.-H., Hill, R. H. and Ko, C. K. (2012) "Facile Size-Tunable Fabrication of Functional Tin Dioxide Nanostructures by Multiple Size Reduction Lithography", *ACS Appl. Mater. Interfaces,* 4**,** 2507-2514.

Park, M., Harrison, C., Chaikin, P. M., Register, R. A. and Adamson, D. H. (1997) "Block Copolymer Lithography: Periodic Arrays of ~10^{11} Holes in 1 Square Centimeter", *Science,* 276**,** 1401-1404.

Park, S.-M., Berry, B. C., Dobisz, E. and Kim, H.-C. (2009) "Observation of Surface Corrugation-Induced Alignment of Lamellar Microdomains in PS-*b*-PMMA Thin Films", *Soft Matter,* 5**,** 957-961.

Park, S.-M., Craig, G. S. W., Liu, C.-C., La, Y.-H., Ferrier, N. J. and Nealey, P. F. (2008) "Characterization of Cylinder-Forming Block Copolymers Directed to Assemble on Spotted Chemical Patterns", *Macromolecules,* 41**,** 9118-9123.

Park, S.-M., Park, O.-H., Cheng, J. Y., Rettner, C. T. and Kim, H.-C. (2008) "Patterning Sub-10 nm Line Patterns from a Block Copolymer Hybrid", *Nanotechnology,* 19**,** 455304.

Park, S.-M., Rettner, C. T., Pitera, J. W. and Kim, H.-C. (2009) "Directed Self-Assembly of Lamellar Microdomains of Block Copolymers Using Topographic Guiding Patterns", *Macromolecules,* 42**,** 5895-5899.

Park, S.-M., Stoykovich, M. P., Ruiz, R., Zhang, Y., Black, C. T. and Nealey, P. F. (2007) "Directed Assembly of Lamellae-Forming Block Copolymers by Using Chemically and Topographically Patterned Substrates", *Adv. Mater.,* 19**,** 607-611.

Park, S., Kim, B., Yavuzcetin, O., Tuominen, M. T. and Russell, T. P. (2008) "Ordering of PS-*b*-P4VP on Patterned Silicon Surfaces", *ACS Nano,* 2**,** 1363-1370.

Park, S., Lee, D. H. and Russell, T. P. (2010) "Self-Assembly of Block Copolymers on Flexible Substrates", *Adv. Mater.,* 22**,** 1882-1884.

Park, S., Lee, D. H., Xu, J., Kim, B., Hong, S. W., Jeong, U., Xu, T. and Russell, T. P. (2009) "Macroscopic 10-Terabit-Per-Square-Inch Arrays from Block Copolymers with Lateral Order", *Science,* 323**,** 1030-1033.

Park, S., Wang, J.-Y., Kim, B., Xu, J. and Russell, T. P. (2008) "A Simple Route to Highly Oriented and Ordered Nanoporous Block Copolymer Templates", *ACS Nano,* 2**,** 766-772.

Peng, M., Ma, S., Hu, J. and Wang, R. (2015) "Hierarchical Nanostructures of Diblock Copolymer Thin Films Directed by a Saw-Toothed Substrate", *Soft Matter,* 11**,** 6642-6651.

Perego, M., Andreozzi, A., Vellei, A., Lupi, F. F. and Seguini, G. (2013) "Collective Behavior of Block Copolymer Thin Films within Periodic Topographical Structures", *Nanotechnology,* 24**,** 245301.

Qiang, Z., Zhang, L., Stein, G. E., Cavicchi, K. A. and Vogt, B. D. (2014) "Unidirectional Alignment of Block Copolymer Films Induced by Expansion of a Permeable Elastomer During Solvent Vapor Annealing", *Macromolecules,* 47**,** 1109-1116.

Ree, M. (2014) "Probing the Self-Assembled Nanostructures of Functional Polymers with Synchrotron Grazing Incidence X-Ray Scattering", *Macromol. Rapid Commun.,* 35**,** 930-959.

Rho, Y., Aissou, K., Mumtaz, M., Kwon, W., Pécastaings, G., Mocuta, C., Stanecu, S., Cloutet, E., Brochon, C., Fleury, G. and Hadziioannou, G. (2015) "Laterally Ordered Sub-10 nm Features Obtained from Directed Self-Assembly of Si-Containing Block Copolymer Thin Films", *Small,* 11**,** 6377-6383.

Rhys Alun, G., Aled, W., Chloe, O., Jonathan, R., Aravind, V. and Thomas, T. (2013) "Directed Self-Assembly of Block Copolymers for Use in Bit Patterned Media Fabrication", *J. Phys. D: Appl. Phys.,* 46**,** 503001.

Rockford, L., Liu, Y., Mansky, P., Russell, T. P., Yoon, M. and Mochrie, S. G. J. (1999) "Polymers on Nanoperiodic, Heterogeneous Surfaces", *Phys. Rev. Lett.,* 82**,** 2602-2605.

Rockford, L., Mochrie, S. G. J. and Russell, T. P. (2001) "Propagation of Nanopatterned Substrate Templated Ordering of Block Copolymers in Thick Films", *Macromolecules,* 34**,** 1487-1492.

Ross, C. A. and Cheng, J. Y. (2008) "Patterned Magnetic Media Made by Self-Assembled Block-Copolymer Lithography", *MRS Bull.,* 33**,** 838-845.

Rueda, D. R., Martín-Fabiani, I., Soccio, M., Alayo, N., Pérez-Murano, F., Rebollar, E., García-Gutiérrez, M. C., Castillejo, M. and Ezquerra, T. A. (2012) "Grazing-Incidence Small-Angle X-Ray Scattering of Soft and Hard Nanofabricated Gratings", *J. Appl. Crystallogr.,* 45**,** 1038-1045.

Ruiz, R., Dobisz, E. and Albrecht, T. R. (2011) "Rectangular Patterns Using Block Copolymer Directed Assembly for High Bit Aspect Ratio Patterned Media", *ACS Nano,* 5**,** 79-84.

Ruiz, R., Kang, H., Detcheverry, F. A., Dobisz, E., Kercher, D. S., Albrecht, T. R., de Pablo, J. J. and Nealey, P. F. (2008) "Density Multiplication and Improved Lithography by Directed Block Copolymer Assembly", *Science,* 321**,** 936-939.

Ruiz, R., Ruiz, N., Zhang, Y., Sandstrom, R. L. and Black, C. T. (2007) "Local Defectivity Control of 2D Self-Assembled Block Copolymer Patterns", *Adv. Mater.,* 19**,** 2157-2162.

Russell, T. P., Coulon, G., Deline, V. R. and Miller, D. C. (1989) "Characteristics of the Surface-Induced Orientation for Symmetric Diblock PS/PMMA Copolymers", *Macromolecules,* 22**,** 4600-4606.

Russell, T. P., Thurn-Albrecht, T., Tuominen, M., Huang, E. and Hawker, C. J. (2000) "Block Copolymers as Nanoscopic Templates", *Macromol. Symp.,* 159**,** 77-88.

Ryu, D. Y., Shin, K., Drockenmuller, E., Hawker, C. J. and Russell, T. P. (2005) "A Generalized Approach to the Modification of Solid Surfaces", *Science,* 308**,** 236-239.

Ryu, D. Y., Wang, J.-Y., Lavery, K. A., Drockenmuller, E., Satija, S. K., Hawker, C. J. and Russell, T. P. (2007) "Surface Modification with Cross-Linked Random Copolymers: Minimum Effective Thickness", *Macromolecules,* 40**,** 4296-4300.

Salaun, M., Zelsmann, M., Archambault, S., Borah, D., Kehagias, N., Simao, C., Lorret, O., Shaw, M. T., Sotomayor Torres, C. M. and Morris, M. A. (2013) "Fabrication of Highly Ordered Sub-20 nm Silicon Nanopillars by Block Copolymer Lithography Combined with Resist Design", *J. Mater. Chem. C,* 1**,** 3544-3550.

Savas, T. A., Schattenburg, M. L., Carter, J. M. and Smith, H. I. (1996) "Large-Area Achromatic Interferometric Lithography for 100 nm Period Gratings and Grids", *J. Vac. Sci. Technol. B,* 14**,** 4167-4170.

Segalman, R. A. (2005) "Patterning with Block Copolymer Thin Films", *Mater. Sci. Eng. R,* 48**,** 191-226.

Segalman, R. A., Hexemer, A., Hayward, R. C. and Kramer, E. J. (2003) "Ordering and Melting of Block Copolymer Spherical Domains in 2 and 3 Dimensions", *Macromolecules,* 36**,** 3272-3288.

Segalman, R. A., Hexemer, A. and Kramer, E. J. (2003) "Edge Effects on the Order and Freezing of a 2D Array of Block Copolymer Spheres", *Phys. Rev. Lett.,* 91**,** 196101.

Segalman, R. A., Hexemer, A. and Kramer, E. J. (2003) "Effects of Lateral Confinement on Order in Spherical Domain Block Copolymer Thin Films", *Macromolecules,* 36**,** 6831-6839.

Segalman, R. A., Yokoyama, H. and Kramer, E. J. (2001) "Graphoepitaxy of Spherical Domain Block Copolymer Films", *Adv. Mater.,* 13**,** 1152-1155.

Serbin, J., Ovsianikov, A. and Chichkov, B. (2004) "Fabrication of Woodpile Structures by Two-Photon Polymerization and Investigation of Their Optical Properties", *Opt. Express,* 12**,** 5221-5228.

Sevink, G. J. A., Zvelindovsky, A. V., Fraaije, J. G. E. M. and Huinink, H. P. (2001) "Morphology of Symmetric Block Copolymer in a Cylindrical Pore", *J. Chem. Phys.,* 115**,** 8226-8230.

Shin, K., Xiang, H., Moon, S. I., Kim, T., McCarthy, T. J. and Russell, T. P. (2004) "Curving and Frustrating Flatland", *Science,* 306**,** 76.

Smith, H. I. and Flanders, D. C. (1978) "Oriented Crystal Growth on Amorphous Substrates Using Artificial Surface-Relief Gratings", *Appl. Phys. Lett.,* 32**,** 349-350.

Son, J. G., Gotrik, K. W. and Ross, C. A. (2012) "High-Aspect-Ratio Perpendicular Orientation of PS-*b*-PDMS Thin Films under Solvent Annealing", *ACS Macro Lett.,* 1**,** 1279-1284.

Song, S. and Mochrie, S. G. J. (1995) "Attractive Step-Step Interactions, Tricriticality, and Faceting in the Orientational Phase Diagram of Silicon Surfaces between [113] and [114]", *Phys. Rev. B,* 51**,** 10068-10084.

Song, S., Mochrie, S. G. J. and Stephenson, G. B. (1995) "Faceting Kinetics of Stepped Si(113) Surfaces: A Time-Resolved X-Ray Scattering Study", *Phys. Rev. Lett.,* 74**,** 5240-5243.

Spatz, J. P., Mössmer, S., Hartmann, C., Möller, M., Herzog, T., Krieger, M., Boyen, H.-G., Ziemann, P. and Kabius, B. (2000) "Ordered Deposition of Inorganic Clusters from Micellar Block Copolymer Films", *Langmuir,* 16**,** 407-415.

Stein, G. E., Kramer, E. J., Li, X. and Wang, J. (2007) "Single-Crystal Diffraction from Two-Dimensional Block Copolymer Arrays", *Phys. Rev. Lett.,* 98**,** 086101.

Stein, G. E., Lee, W. B., Fredrickson, G. H., Kramer, E. J., Li, X. and Wang, J. (2007) "Thickness Dependent Ordering in Laterally Confined Monolayers of Spherical-Domain Block Copolymers", *Macromolecules,* 40**,** 5791-5800.

Stoykovich, M. P., Kang, H., Daoulas, K. C., Liu, G., Liu, C.-C., de Pablo, J. J., Müller, M. and Nealey, P. F. (2007) "Directed Self-Assembly of Block Copolymers for Nanolithography: Fabrication of Isolated Features and Essential Integrated Circuit Geometries", *ACS Nano,* 1**,** 168-175.

Stoykovich, M. P., Müller, M., Kim, S. O., Solak, H. H., Edwards, E. W., de Pablo, J. J. and Nealey, P. F. (2005) "Directed Assembly of Block Copolymer Blends into Nonregular Device-Oriented Structures", *Science,* 308**,** 1442-1446.

Stoykovich, M. P. and Nealey, P. F. (2006) "Block Copolymers and Conventional Lithography", *Mater. Today,* 9**,** 20-29.

Sun, Z., Chen, Z., Zhang, W., Choi, J., Huang, C., Jeong, G., Coughlin, E. B., Hsu, Y., Yang, X., Lee, K. Y., Kuo, D. S., Xiao, S. and Russell, T. P. (2015) "Directed Self-Assembly of Poly(2-Vinylpyridine)-*b*-Polystyrene-*b*-Poly(2-Vinylpyridine) Triblock Copolymer with Sub-15 nm Spacing Line Patterns Using a Nanoimprinted Photoresist Template", *Adv. Mater.,* 27**,** 4364-4370.

Sundrani, D., Darling, S. B. and Sibener, S. J. (2004) "Guiding Polymers to Perfection: Macroscopic Alignment of Nanoscale Domains", *Nano Lett.,* 4**,** 273-276.

Sundrani, D., Darling, S. B. and Sibener, S. J. (2004) "Hierarchical Assembly and Compliance of Aligned Nanoscale Polymer Cylinders in Confinement", *Langmuir,* 20**,** 5091-5099.

Sundrani, D. and Sibener, S. J. (2002) "Spontaneous Spatial Alignment of Polymer Cylindrical Nanodomains on Silicon Nitride Gratings", *Macromolecules,* 35**,** 8531-8539.

Tada, Y., Akasaka, S., Yoshida, H., Hasegawa, H., Dobisz, E., Kercher, D. and Takenaka, M. (2008) "Directed Self-Assembly of Diblock Copolymer Thin Films on Chemically-Patterned Substrates for Defect-Free Nano-Patterning", *Macromolecules,* 41**,** 9267-9276.

Tavakkoli K. G, A., Nicaise, S. M., Gadelrab, K. R., Alexander-Katz, A., Ross, C. A. and Berggren, K. K. (2016) "Multilayer Block Copolymer Meshes by Orthogonal Self-Assembly", *Nat. Commun.,* 7**,** 10518.

Tavakkoli K. G., A., Gotrik, K. W., Hannon, A. F., Alexander-Katz, A., Ross, C. A. and Berggren, K. K. (2012) "Templating Three-Dimensional Self-Assembled Structures in Bilayer Block Copolymer Films", *Science,* 336**,** 1294-1298.

Tsai, H., Pitera, J. W., Miyazoe, H., Bangsaruntip, S., Engelmann, S. U., Liu, C.-C., Cheng, J. Y., Bucchignano, J. J., Klaus, D. P., Joseph, E. A., Sanders, D. P., Colburn, M. E. and Guillorn, M. A. (2014) "Two-Dimensional Pattern Formation Using Graphoepitaxy of PS-*b*-PMMA Block Copolymers for Advanced FinFET Device and Circuit Fabrication", *ACS Nano,* 8**,** 5227-5232.

Turner, M. S. (1992) "Equilibrium Properties of a Diblock Copolymer Lamellar Phase Confined between Flat Plates", *Phys. Rev. Lett.,* 69**,** 1788-1791.

Wagner, C. and Harned, N. (2010) "Euv Lithography: Lithography Gets Extreme", *Nat. Photonics,* 4**,** 24-26.

Walton, D. G., Kellogg, G. J., Mayes, A. M., Lambooy, P. and Russell, T. P. (1994) "A Free Energy Model for Confined Diblock Copolymers", *Macromolecules,* 27**,** 6225-6228.

Welander, A. M., Craig, G. S. W., Tada, Y., Yoshida, H. and Nealey, P. F. (2013) "Directed Assembly of Block Copolymers in Thin to Thick Films", *Macromolecules,* 46**,** 3915-3921.

Welander, A. M., Nealey, P. F., Cao, H. and Bristol, R. (2008) "Impact of Trench Width Roughness on the Graphoepitaxial Assembly of Block Copolymers", *J. Vac. Sci. Technol. B,* 26**,** 2484-2488.

Wu, Y., Cheng, G., Katsov, K., Sides, S. W., Wang, J., Tang, J., Fredrickson, G. H., Moskovits, M. and Stucky, G. D. (2004) "Composite Mesostructures by Nano-Confinement", *Nat. Mater.,* 3**,** 816-822.

Xia, Y. and Whitesides, G. M. (1998) "Soft Lithography", *Annu. Rev. Mater. Sci.,* 28**,** 153-184.

Xiang, H., Shin, K., Kim, T., Moon, S., McCarthy, T. J. and Russell, T. P. (2005) "The Influence of Confinement and Curvature on the Morphology of Block Copolymers", *J. Polym. Sci., Part B: Polym. Phys.,* 43**,** 3377-3383.

Xiang, H., Shin, K., Kim, T., Moon, S. I., McCarthy, T. J. and Russell, T. P. (2004) "Block Copolymers under Cylindrical Confinement", *Macromolecules,* 37**,** 5660-5664.

Xiang, H., Shin, K., Kim, T., Moon, S. I., McCarthy, T. J. and Russell, T. P. (2005) "From Cylinders to Helices Upon Confinement", *Macromolecules,* 38**,** 1055-1056.

Xiao, S., Yang, X., Edwards, E. W., La, Y.-H. and Nealey, P. F. (2005) "Graphoepitaxy of Cylinder-Forming Block Copolymers for Use as Templates to Pattern Magnetic Metal Dot Arrays", *Nanotechnology,* 16**,** S324-S329.

Xiao, S., Yang, X., Hwu, J. J., Lee, K. Y. and Kuo, D. (2014) "A Facile Route to Regular and Nonregular Dot Arrays by Integrating Nanoimprint Lithography with Sphere-Forming Block Copolymer Directed Self-Assembly", *J. Polym. Sci., Part B: Polym. Phys.,* 52**,** 361-367.

Xiao, S., Yang, X., Park, S., Weller, D. and Russell, T. P. (2009) "A Novel Approach to Addressable 4 Teradot/In.^{2} Patterned Media", *Adv. Mater.,* 21**,** 2516-2519.

Xiao, S., Yang, X., Steiner, P., Hsu, Y., Lee, K., Wago, K. and Kuo, D. (2014) "Servo-Integrated Patterned Media by Hybrid Directed Self-Assembly", *ACS Nano,* 8**,** 11854-11859.

Xu, J., Hong, S. W., Gu, W., Lee, K. Y., Kuo, D. S., Xiao, S. and Russell, T. P. (2011) "Fabrication of Silicon Oxide Nanodots with an Areal Density Beyond 1 Teradots Inch^{-2}", *Adv. Mater.,* 23**,** 5755-5761.

Xu, J., Park, S., Wang, S., Russell, T. P., Ocko, B. M. and Checco, A. (2010) "Directed Self-Assembly of Block Copolymers on Two-Dimensional Chemical Patterns Fabricated by Electro-Oxidation Nanolithography", *Adv. Mater.,* 22**,** 2268-2272.

Xu, T., Hawker, C. J. and Russell, T. P. (2005) "Interfacial Interaction Dependence of Microdomain Orientation in Diblock Copolymer Thin Films", *Macromolecules,* 38**,** 2802-2805.

Yamaguchi, T. and Yamaguchi, H. (2006) "Resist-Pattern Guided Self-Assembly of Symmetric Diblock Copolymer", *J. Photopolym. Sci. Technol.,* 19**,** 385-388.

Yamaguchi, T. and Yamaguchi, H. (2008) "Two-Dimensional Patterning of Flexible Designs with High Half-Pitch Resolution by Using Block Copolymer Lithography", *Adv. Mater.,* 20**,** 1684-1689.

Yan, M. and Gibaud, A. (2007) "On the Intersection of Grating Truncation Rods with the Ewald Sphere Studied by Grazing-Incidence Small-Angle X-Ray Scattering", *J. Appl. Crystallogr.,* 40**,** 1050-1055.

Yang, G.-W., Wu, G.-P., Chen, X., Xiong, S., Arges, C. G., Ji, S., Nealey, P. F., Lu, X.-B., Darensbourg, D. J. and Xu, Z.-K. (2017) "Directed Self-Assembly of Polystyrene-*b*-Poly(Propylene Carbonate) on Chemical Patterns via Thermal Annealing for Next Generation Lithography", *Nano Lett.,* 17**,** 1233-1239.

Yang, J. K. W., Jung, Y. S., Chang, J.-B., Mickiewicz, R. A., Alexander Katz, A., Ross, C. A. and Berggren, K. K. (2010) "Complex Self-Assembled Patterns Using Sparse Commensurate Templates with Locally Varying Motifs", *Nat. Nanotechnol.,* 5**,** 256-260.

Yang, X., Wan, L., Xiao, S., Xu, Y. and Weller, D. K. (2009) "Directed Block Copolymer Assembly versus Electron Beam Lithography for Bit-Patterned Media with Areal Density of 1 Terabit/Inch^2 and Beyond", *ACS Nano,* 3**,** 1844-1858.

Yang, X., Xiao, S., Liu, C., Pelhos, K. and Minor, K. (2004) "Nanoscopic Templates Using Self-Assembled Cylindrical Diblock Copolymers for Patterned Media", *J. Vac. Sci. Technol. B,* 22**,** 3331-3334.

Zhang, X., De Paoli Lacerda, S. H., Yager, K. G., Berry, B. C., Douglas, J. F., Jones, R. L. and Karim, A. (2009) "Target Patterns Induced by Fixed Nanoparticles in Block Copolymer Films", *ACS Nano,* 3**,** 2115-2120.

Zhang, X., Harris, K. D., Wu, N. L. Y., Murphy, J. N. and Buriak, J. M. (2010) "Fast Assembly of Ordered Block Copolymer Nanostructures through Microwave Annealing", *ACS Nano,* 4**,** 7021-7029.